Analysis of Off-Road Tire-Soil Interaction through Analytical and Finite Element Methods

Vom Fachbereich Maschinenbau und Verfahrenstechnik
der Technischen Universität Kaiserslautern
zur Verleihung des akademischen Grades

Doktor-Ingenieur (Dr.-Ing.)

genehmigte Dissertation

von

M.Sc. Hao Li
aus Yushan, China

Vorsitzender:	Prof. Dr.-Ing. Bernd Sauer
Berichterstatter:	Prof. Dr.-Ing. Christian Schindler
	Prof. Robert K. Paasch
Dekan:	Prof. Dr.-Ing. Bernd Sauer

Tag der Einreichung:	09. April 2013
Tag der Mündlichen Prüfung:	30. Juli 2013

Kaiserslautern, Oktober 2013

D 386

Acknowledgements

This dissertation was completed based on the research work at the Chair of Design in Mechanical Engineering (KIMA), University of Kaiserslautern, Germany. I had a lot of supports and advices for the completion of this work.

First of all, I would like to express my sincere gratitude to my supervisor Prof. Dr.-Ing. Christian Schindler. His invaluable suggestions, excellent guidance and continuous engagement are a great source of inspiration for this work. Without his guidance and persistent help my dissertation would not have been finished.

I wish to thank Prof. Robert Paasch from Oregon State University for his patience and willingness to review my dissertation, and for bringing me new aspects to my work. I would like to express my gratitude to Prof. Dr.-Ing. Bernd Sauer who chaired the defense committee as a chairman.

I would like to thank all of my colleges at this Chair, especially Nureddin Bennett and Michael Kremb for the great suggestions and enormous help during the field tests; Martin Schwickert and Karsten Hilbert for the ideas of improving the design of the test rig. Special acknowledgement goes to Dr. Peter Bach and Martin Frank for spending time and providing facilities to carry out the field tests at Volvo Construction Equipment Germany, Konz. I am grateful to Prof. Dr.-Ing. Christos Vrettos, Dr. Andreas Bekker, Roland Günther who offered instruments for the measurement of soil parameters.

Finally I would like to thank my wife Xiaojing for her understanding and care during the past few years that we have been spending together. Her support and encouragement are always the working impetus. My father, mother and brother receive my deepest gratitude and love for their dedication and encouragement during my life and studies.

Kaiserslautern, August 2013 Hao Li

Contents

Nomenclature

A	[N/mm^2]	Oscillation amplitude
A_c	[mm^2]	Contact area
A_R	[mm^2]	Cross section area
B	[-]	Stiffness factor
C	[-]	Shape factor
C_{10}	[-]	Material constant
C_i	[-]	Cone index value
CC	[-]	Compaction capacity
D	[-]	Peak factor
D_1	[MPa]	Material constant
D_t	[N·s/mm]	Tire damping coefficient
E	[-]	Curvature factor
F_x	[N]	longitudinal force
F_y	[N]	Lateral force
F_z, F_{zr}, F_{zd}	[N]	Vertical force
Fa_c	[N/mm^2]	Cap failure
Fa_s	[N/mm^2]	Shear failure
G	[-]	Sand penetration resistance gradient
I_1	[-]	The first invariant of the left Cauchy-Green deformation tensor
$\overline{I}_1$	[-]	The first invariant of the deviatoric part of the left Cauchy-Green deformation tensor
J	[-]	Volume ratio
K	[mm]	Shear deformation modulus

K_0	[N/mm^2]	Bulk modulus
K_1, K_2	[-]	Empirical constants
K_{bg}	[-]	Bogie factor
K_{cl}	[-]	Clearance factor
K_{cp}	[-]	Contact pressure factor
K_{en}	[-]	Engine factor
K_g	[-]	Grouser factor
K_t	[N/mm]	Tire vertical stiffness
K_{tr}	[-]	Track factor
K_{tra}	[-]	Transmission factor
K_r	[-]	Ratio of the residual shear stress to the maximum shear stress
K_R	[-]	Flow stress ratio
K_w	[-]	Weight factor
K_x, K_y	[mm]	Longitudinal and lateral shear deformation modulus
M_y	[N·mm]	Resistance torque
M_z	[N·mm]	Self-aligning torque
MI	[-]	Mobility index
N	[-]	Soil-tire numeric
P_R	[mm]	Rebar position
R	[mm]	Radius of parabolic shape
R_b	[N/mm]	Bulldozing resistance
R_c	[N]	Compaction resistance
R_e	[mm]	Effective rolling radius
R_S	[-]	Cap Eccentricity
S	[mm]	Rebar spacing

$S_h,\ S_v$	[-]	Parameters in the MF model
VCI	[-]	Vehicle cone index value
a	[-]	Transition surface radius
b	[mm]	Smaller dimension of a plate
b_t	[mm]	Tire width
c	[N/mm^2]	Soil cohesion
c_1, c_2	[-]	Coefficients of the angular position
c_s	[N·s/mm]	Soil damping coefficient
d	[mm]	Tire diameter
f_0	[mm]	Tire deformation
f_x, f_y, f_z	[-]	Force and moment coefficients
h	[mm]	Unloaded tire section height
i, s_x	[-]	Longitudinal slip
j	[mm]	Shear displacement
j_0	[mm]	Shear displacement at τ_{max}
j_x, j_y	[mm]	Longitudinal and lateral shear deformation
k	[mm/N$^{1/2}$]	Soil deformation modulus
k_1	[N/mm^{2-n}]	Soil stiffness
k_ϕ	[N/mm^{2-n}]	Pressure-sinkage parameters in the Bekker equation
k_c	[N/mm^{1-n}]	Pressure-sinkage parameters in the Bekker equation
k_{ca}	[N/mm^2]	Carcass stiffness
$k_c',\ k_\phi'$	[-]	Pressure-sinkage parameters in the Reece equation
k_u	[N/mm^3]	Soil unloading stiffness
k_r	[mm]	Tire sinkage ratio
k', n', m	[-]	Pressure-sinkage parameters in the MG equation

l_{con}	[mm]	Length of the tire-soil contact interface
m_t	[kg]	Tire mass
n	[-]	Sinkage exponent
p	[N/mm^2]	Loading pressure
p_e	[N/mm^2]	Equivalent pressure stress
p_{gcr}	[N/mm^2]	Critical ground pressure
p_i	[N/mm^2]	Inflation pressure
r	[mm]	Radius of rigid tire
v_r	[mm/s]	Tire penetrating rate in the radial direction
v_x	[mm/s]	Tire longitudinal velocity
v_y	[mm/s]	Tire lateral velocity
t	[N/mm^2]	Deviatoric stress
t_i	[s]	Time
z	[mm]	Soil sinkage
$z_r,\ z_e$	[mm]	Maximum soil sinkage in the rigid and elastic mode
z_A	[mm]	Sinkage when unloading begins
α	[°]	Slip angle
β	[°]	Friction angle
γ_s	[N/mm^3]	Soil weight density
δ	[mm]	Tire deflection
θ_m	[°]	Angular position of the maximum radial stress
θ_0	[°]	Contact angle of the tire
θ_1, θ_2	[°]	Entry angle and exit angle
θ_r, θ_f	[°]	Locations where radial stresses are identical in the rear and front regions
λ_i	[-]	Principal stretches

μ_0	[N/mm^2]	Shear modulus
ρ_{dc}	[kg/mm^3]	Critical dry density
ρ_{ds}	[kg/mm^3]	Average dry density
σ	[N/mm^2]	Radial stress
σ_1, σ_2	[N/mm^2]	Radial stress in the front and rear region
σ_d	[N/mm^2]	Damping stress
σ_i	[N/mm^2]	The principal stress
σ_v	[N/mm^2]	The Mises equivalent stress
σ_T	[N/mm^2]	Radial stress in the new analytical model
τ, τ_{max}	[N/mm^2]	Shear stress and the maximum shear stress
τ_x, τ_y	[N/mm^2]	Longitudinal and lateral shear stress
ϕ	[°]	Angle of internal friction
φ	[rad]	Optional phase shift
ω	[s^{-1}]	Rotation velocity

Abbreviation

ATV	All-Terrain Vehicle
CC	Cam-Clay model
CDTire	Comfort and Durability Tire
CI	Cone Index
DE	Discrete Element
DEM	Discrete Element Method
DP	Drucker-Prager
FE	Finite Element
FEM	Finite Element Method
FTire	Flexible Ring Tire
HSRI	Highway Safety Research Institute
MBS	Multibody simulation
MC	Mohr Coulomb
MDPC	Modified Drucker-Prager/Cap
MER	Mars Exploration Rover
MF	Magic Formula
MI	Mobility Index
NSDL	National Soil Dynamic Laboratory
PTO	Power Take Off
RCI	Rating Cone Index
SCM	Soil Contact Model
SST	Stress State Transducer
SWIFT	Short Wave Intermediate Frequency Tire
VCI	Vehicle Cone Index
WES	Waterways Experiment Station
WFTV	Wide Frame Tractive Vehicle

Abstract

Tire-soil interaction is important for the performance of off-road vehicles and the soil compaction in the agricultural field. With an analytical model, which is integrated in multibody-simulation software, and a Finite Element model, the forces and moments generated on the tire-soil contact patch were studied to analyze the tire performance. Simulations with these two models for different tire operating conditions were performed to evaluate the mechanical behaviors of an excavator tire. For the FE model validation a single wheel tester connected to an excavator arm was designed. Field tests were carried out to examine the tire vertical stiffness, the contact pressure on the tire – hard ground interface, the longitudinal/vertical force and the compaction of the sandy clay from the test field under specified operating conditions. The simulation and experimental results were compared to evaluate the model quality. The Magic Formula was used to fit the curves of longitudinal and lateral forces. A simplified tire-soil interaction model based on the fitted Magic Formula could be established and further applied to the simulation of vehicle-soil interaction.

Kurzzusammenfassung

Die Reifen-Boden-Interaktion ist wichtig für die Leistungsfähigkeit von Geländefahrzeugen und die Bodenverdichtung landwirtschaftlicher Nutzflächen. Mit Hilfe einen analytischen Models, das in eine Mehrkörpersimulation Software integriert wird, und der Finite Elemente (FE) Modell, werden die Kräfte und Drehmomente für die Analyse des Reifenverhaltens ermittelt. Es wurden Simulationen bei unterschiedlichen Betriebszuständen eines Baggerreifens durchgeführt und das mechanische Verhalten ausgewertet. Um das FE-Modell zu validieren, wurde ein Einzelrad-Tester entwickelt, welcher an einen Baggerarm angekuppelt wurde. In Feldversuchen wurden die Reifensteifigkeit, die Spannung in der Reifen-Hartboden-Kontaktfläche, sowie die longitudinalen und vertikalen Kräfte und die Verdichtung des Sandigen Lehmbodens in Abhängigkeit von vorgegeben Reifenbetriebszuständen untersucht. Für die Bewertung der Modellqualität werden die Ergebnisse von Simulationen und Experimenten verglichen. Das Magic Formula wurde heraufgezogen, um die Kurven der longitudinalen und queren Kräfte anzupassen. Mittels die Magic-Formula-Funktion wird ein Modell der vereinfachtes Reifen-Boden-Interaktion zur Verfügung steht, mit dem könnte die Fahrzeug-Boden-Interaktion simuliert werden kann.

Zusammenfassung

Im Gegensatz zu Straßenfahrzeugen, wie PKW und LKW des Langstrecken- und Verteilerverkehres, werden viele Nutzfahrzeuge auch oder sogar zum Großteil im Gelände, also Off-Road, eingesetzt. In der Fahrzeugentwicklung nutzt man seit Jahrzehnten die numerische Simulation zu Untersuchungen des dynamischen Fahrzeugverhaltens. Dazu ist eine genaue Kenntnis und Beschreibung der Reifen-Fahrweg-Interaktion notwendig. Für die Kombination Reifen und feste Fahrbahn sind dazu viele Modelle beschrieben und etabliert. Die Modellierung des Reifens auf nicht festem Boden ist dagegen ungleich schwieriger, nicht zuletzt wegen der viele unterschiedlichen Bodenarten.

Ziel dieser Dissertation ist es, die Reifen-Boden-Interaktion mit zuverlässigen Modellen zu simulieren und die Auswirkungen von Achslast und Fülldruck auf die Bodenverdichtung und die Reifenverhalten zu analysieren. Zwei unterschiedliche Methoden (eine analytische Methode und die Finite-Elemente-Methode) wurden angewendet, um die Reifen-Boden-Interaktion zu modellieren. Dazu wurden Simulationen und Versuche durchgeführt, um die Modelle, die mit diesen zwei Methoden entwickelt wurden, zu verifizieren und zu validieren. Der Grund für die Anwendung zwei unterschiedlicher Methoden (der analytischen Methode und Finite-Elemente-Methode) sind die jeweiligen Vor- und Nachteile der Verfahren:

Bei der analytischen Methode, kann das Modell der Reifen-Boden-Interaktion infolge der notwendigen Vereinfachungen einige Faktoren, z.B. das Reifenprofil und die Reifenkarkasse nicht oder nicht ausreichend genau berücksichtigen. Das Modell kann allerdings in eine MKS-Software integriert werden. Dadurch wird die Berechnungszeit verkürzt und die Simulationsdurchführung wird effizienter. Auch ist es möglich dynamische Untersuchungen der Fahrzeug-Boden-Interaktion mit einem Gesamtfahrzeugmodell in der MKS-Software durchzuführen, bei denen das entwickelte analytische Reifenmodell eingesetzt wird.

Bei der FEM können hingegen alle Komponenten des Reifens deutlich genauer modelliert werden, weshalb die Simulation der Reifen-Boden-Interaktion die Realität besser widerspiegelt als die analytische Methode. Die Berechnungen der Reifen- und Bodenbeanspruchungen können nur mittels der FEM erfolgen, sie ermöglicht den Einblick in die Beanspruchung der Reifen-Boden-Kontaktfläche. Für dynamische

Untersuchungen der Fahrzeug-Boden-Interaktion wird diese Methode jedoch wegen des intensiven Berechnungsaufwands selten angewendet.

Nach der Validierung des FEM Modells anhand der Messwerte aus dem Versuch, werden die Simulationsergebnisse aus den beiden Simulationsmethoden verglichen, um so die Validität des analytischen Modells zu ermitteln. Das validierte analytische Modell könnte in weitere Simulationsgebieten, z. B. die Gesamtfahrzeugsimulationen zur Anwendung kommen.

Den Schwerpunkt in der Reifen-Boden-Interaktion bei der analytischen Methode bilden die Kontaktflächen und Kontaktspannungen. Diese beiden Größen können durch mathematische Gleichungen beschrieben werden. Daraus können die Kinematik, sowie die Kräfte und Drehmomente des Reifens abgeleitet werden. Bei dieser Methode werden die Radialspannungen als nicht-lineare Feder-Dämpfer-Elemente und die Tangentialspannungen als Reibungsspannungen dargestellt. Die geometrischen Eigenschaften der Kontaktfläche und des deformierten Reifens werden mit empirischen Gleichungen beschrieben. Das analytische Modell wurde in die Mehrkörpersimulation (MKS) Software MSC Adams integriert. Es wurden verschiedene Simulationen durchgeführt, um das analytische Modell zu verifizieren.

Die zweite angewendete Modellierungsmethode ist die der Finite-Elemente-Methode (FEM). Damit werden Reifen und Boden als Kontinuum modelliert. Um die äußere Gestalt und die innere Struktur des Reifens zu modellieren, wurde ein Baggerreifen zerlegt und seine Bestandteile analysiert. Die Hauptmaterialien des Reifens sind Gummi und Stahl. Das Gummi wird im Modell mittels hyperelastischer Formänderungsenergiefunktionen beschrieben. Der Stahl ist als elastisches Material dargestellt. Der Boden, der elasto-plastisches Materialverhalten zeigt, wird mittels des Modifizierten Drucker-Prager Modells (MDPC) mit elastischem Material modelliert.

Um die FE-Modelle der Reifen-Boden-Interaktion zu validieren, wurde ein Einzelrad-Tester konstruiert. Zur Messung von Reifensteifigkeit, Kontaktspannung, Bodenreaktionskräften und Bodenverdichtung wurden unterschiedliche Experimente mit diesem Prüfgerät durchgeführt. Als Messequipment wurden Kraftsensoren, Druckmessfolien und eine 3D-Kamera eingesetzt. Die auf das Rad wirkenden Kräfte, sowie die Reifen- und Bodendeformation konnten als digitales Signal erfasst und aufgezeichnet werden. Zum Schluss wurden die Versuchsdaten analysiert und mit

den Ergebnissen der FE-Simulationen verglichen. Die Simulationsergebnisse wurden tendenziell durch die Versuchsergebnisse bestätigt.

Mit dem so validierten FE-Modell wurden Parameteruntersuchungen durchgeführt. Die durchschnittliche Kontaktspannung zwischen dem vorgegebenen Reifen und Boden ist abhängig von der Radlast und dem Fülldruck. Mit steigender Radlast und zunehmendem Fülldruck erhöht sich auch die durchschnittliche Kontaktspannung. Ab einem bestimmten Wert für die Radlast ist die Kontaktspannung überwiegend von Fülldruck abhängig.

Bei der Betrachtung der Bodenbeanspruchung ist es auffällig, dass sich die Radlast auf der Unterfläche und der Fülldruck auf der Oberfläche auswirken. Traktion und Handling hängen von der Radlast, dem Fülldruck, sowie vom Schlupf und dem Schräglaufwinkel ab. Ähnlich wie bei Reifenmodelle für Straßenfahrzeuge, können die Longitudinalkraft-Schlupf- und Seitenkraft-Schräglaufwinkel-Kurven aus der FE-Analyse mittels Magic-Formula-Funktionen dargestellt werden. Diese Funktionen können wieder in MKS Modelle integriert werden und dies führt zu vereinfachten Modellen für die Reifen-Boden-Interaktion. Bei vorgegebener Radlast und festgelegtem Fülldruck, sinkt die Seitenkraft mit steigender Longitudinalkraft. Bei vorgegebenen Werten für die Radlast, den Schlupf und der Schräglaufwinkel, führt der niedrigere Fülldruck zu einer höheren Longitudinal- und Seitenkraft. Die Simulationsergebnisse zeigen, dass durch die Wahl des Reifenfülldrucks ein Beitrag zur Verringerung der Bodendeformation und zur Erhöhung der Leistungsfähigkeit des Reifens erreicht wird.

1 Introduction

As one of the most complicated subsystems of a vehicle, tires play an important role in the vehicle ride and handling performance, especially for maneuvers such as accelerating, braking and cornering [1]. Simulations with a robust and accurate tire model can offer credible predictions of the mechanical response of vehicles and shorten the period of developing vehicles with new design features and higher performance. Since decades lots of research work has been carried out to develop tire models for estimating the performance of road vehicles such as passenger cars and trucks running on hard ground [2]. Off-road vehicles such as excavators and wheel loaders often work at the construction sites and tractors often work on agricultural fields and dirt roads where the terrain might be soft and muddy. Compared to the tire models of the road vehicles, to establish tire models for the prediction of the ride and handling performance of the off-road vehicles running on the terrain is more difficult due to the complex mechanical properties of the terrain [3]. More research work has to be done to contribute to the development of the off-road tire models with which the dynamic performance of tires used on the terrain under different operating conditions can be analyzed.

The primary objectives of this dissertation are to explore current and emerging approaches to modeling the rigid and deformable tire vs. hard ground and soil interaction in order to understand the mechanism of tire and soil models; to contribute to the modeling of the deformable tire – soil interaction by developing novel and reliable models with an analytical method and the finite element method (FEM); to guarantee the accuracy of simulation results by validating these models; to study the influence of operating conditions such as wheel load and inflation pressure on the tire handling performance and the soil compaction.

To achieve these objectives, the analytical method utilizing the principles of terramechanics and the finite element method were applied to develop the models of the deformable tire – soil interaction; experiments in the test field with a single wheel tester were conducted for the model validation; Simulations for different tire maneuvers such as pure longitudinal and lateral slipping were performed at different wheel loads and inflation pressures to study their influence on the tire handling performance and the soil compaction.

The reasons of using the analytical method and the FEM for the modeling are addressed as follows:

With the analytical method some simplifications are required to develop the tire-soil interaction model, for example the complicate tire tread and the reinforcement layers such belt and carcass are either simplified or neglected in the modeling, and these simplifications might affect the accuracy of simulation results. The analytical tire-soil interaction model can be integrated into the MBS software, and further applied to analyze dynamic behaviors of a vehicle running on the soil [4]. Compared to the FE model, the computation time is shorter and the simulation is more efficient with the analytical model.

With the FEM all the components of a tire can be more accurately modeled, and the FE model of the tire-soil interaction provides more credible simulation results compared to the analytical model. With a validated FE model of the tire-soil interaction, it is possible to evaluate the quality of the analytical model by comparing simulation results such as drawbar pull and cornering force obtained from these two models. Besides, the computation of the stress distribution in the tire and the soil is only available with the FE model, and the index of tire performance such tire fatigue and abrasion can be studied [5-7]. However, the FEM is not appropriate for the study of the vehicle-soil interaction due to the fact that the FE vehicle model is quite complex and simulating the vehicle-soil interaction is quite time-consuming.

In conclusion the application of the analytical method and the FEM is necessary for developing the models of the deformable tire – soil interaction, since the advantages and disadvantages of these two methods indicate that they are complementary with each other.

The major contributions of this dissertation are the novelties of modeling the deformable tire – soil interaction with the analytical method and the FEM, and of analyzing simulation results with a curve fitting method.

With the analytical method the soil damping effect which is never considered before was introduced in the modeling, and non-linear spring-damper elements were used to describe the normal stress and shear stress elements were used to describe the tangential stress on the tire-soil interaction interface. With the FEM the tire tread and inner reinforcement layers which were neglected or simplified by the other researchers are considered in the FE model. The tire tread was modeled with solid elements, and the inner reinforcement layers of rubber-cord composite embedded in

the tire were modeled with shell elements. To analyze the simulation results, the Magic Formula (MF) was applied to fit the curves of the drawbar pull, the cornering force and the aligning torque for the deformable tire – soil interaction. A simplified model could be established based on the fitted MF and integrated into the MBS software Adams for the storage of simulation results as look-up tables.

The novelties of the analytical and FE models can potentially bring more accurate simulation results compared to the models established in the previous research work, and the novelties of analyzing simulation results can provide a better understanding of the handling performance such as drawbar pull and cornering force of a tire running on the soil and a better approach to restore simulation results for the further application.

2 State of the Art

The tire operating environments, including a large diversity of road conditions from hard ground through soft mud to fresh snow, may limit the tire mobility. From the last century, lots of efforts have been focused on exploring and extending the knowledge of the mechanic properties of the interaction between the tire and the road with hard ground/soil.

2.1 Empirical methods

2.1.1 Soil characterization

At the US Army Waterways Experiment Station (WES), an empirical method was initially developed during the Second World War to provide the assessment of the soil trafficability and the vehicle mobility. This approach was supported by the hand-held cone penetrometer as shown in Fig. 2.1. A cone penetrometer is comprised of a proving ring, a rod in the diameter of 1.59 cm, a cone with an apex angle of 30°, a base area (the cross-sectional area at the base of the cone) of 323 mm^2 and a dial gauge to display the force which is required to press the cone through the soil layers. As an indication of the soil strength, the CI is the force per unit the cone base area. It is concluded that the soil strengths including shear, compression and tension strength vary with penetration velocity, water content, bulk density, root density, soil structure, and soil type [8-12].

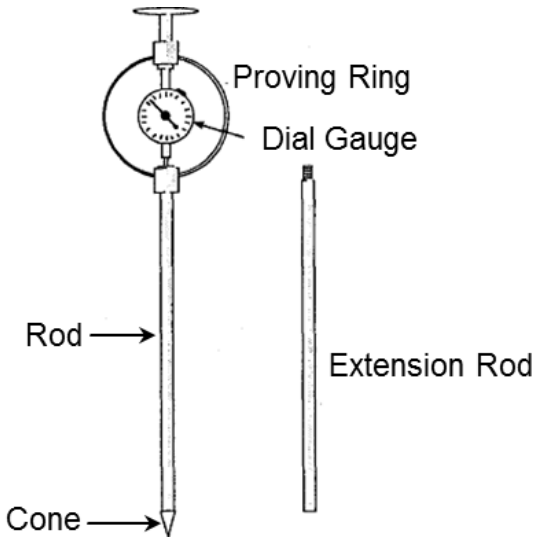

Fig. 2.1: Hand-held cone penetrometer [13]

Due to the large progress made in the industry field, tools of the force requisition and recording for the penetrometer have been developed. Electrical sensors such as

strain gauges were applied to measure the penetration force [14, 15]. A new cone penetrometer called ‘dynamic cone penetrometer’ was designed in 1993 during the Minnesota Road Research Project. To operate the dynamic cone penetrometer, a hammer with a fixed mass on the top of the device is lifted to a height and then dropped driving the cone into the soil. The soil strength is calculated as the energy needed by the soil to stop the movement of the penetrometer divided by the distance the penetrometer travels. [16]

In 1960 Bekker [17-19] initiated the bevameter technique to measure the normal and shear strengths of the soil to predict the vehicle mobility. To simulate the tire-soil interaction in the normal and shear direction, the bevameter is used to carry out two sets of tests. One is a set of plate sinkage tests and the other is a set of shear tests. In the plate sinkage tests, rectangular or circular plates of different sizes are forced into the soil to simulate the vehicle-soil interaction in the vertical direction, and the plate sizes should be comparable to that of the contact area of a tire [20]. The pressure-sinkage relationship is measured for the prediction of normal stress distribution on the tire-soil interface. In the shear tests, shear rings or shear plates are used to simulate the shear action of a tire or a track link. The shear stress-displacement relationship is measured for the prediction of the shear stress distribution on the tire-soil interface.

A basic bevameter designed to perform the tests is illustrated in Fig. 2.2. In the bevameter, a hydraulic ram for the generation of normal loads on the sinkage plate is mounted at one end of the bevameter frame. The pressures applied on the sinkage plate and the plate sinkages are recorded during the pressure-sinkage tests. Shear rings or shear plates with 8 grouses mounted at the other end of the bevameter frame are pressed by the hydraulic ram and rotated by the torque motor. The torques applied on the shear rings or plates and the angular displacements are recorded during the shear tests.

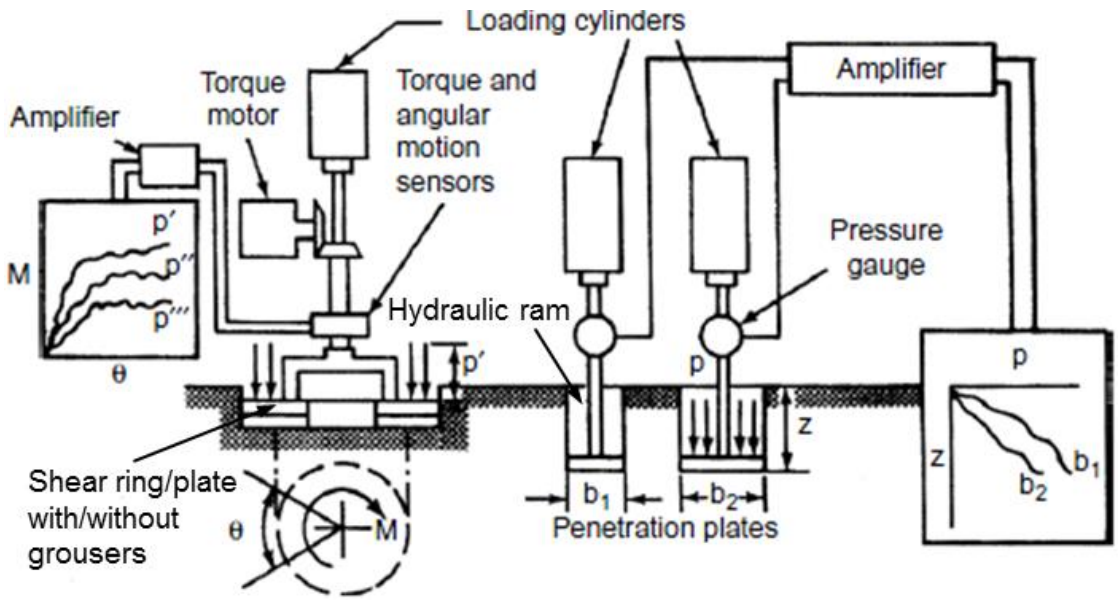

Fig. 2.2: Schematic view of a bevameter [13]

2.1.2 WES methods

Freitag [21] attempted to develop an empirical model using a simple soil-tire numeric *N*, which describes the relationship between the contact pressure and the soil bearing capability as displayed in Eq. (2.1).

$$N = \frac{C_i b_t d}{F_z}\sqrt{\frac{\delta}{h}} \tag{2.1}$$

Where

C_i	cone index value	b_t	tire width
d	tire diameter	δ	tire deflection
F_z	vertical force	h	unloaded tire section height

Turnage [22, 23] revised the soil-tire numeric to fit the specific types of soil, such as N_c for purely cohesive soil (near-saturated clay) and N_s for purely frictional soil (air-dry sand).

$$N_C = \frac{C_i b_t d}{F_z\left(1 + b_t / 2d\right)}\sqrt{\frac{\delta}{h}} \tag{2.2}$$

$$N_S = \frac{G\left(b_t d\right)^{3/2}}{F_z}\frac{\delta}{h} \tag{2.3}$$

Where G is the sand penetration resistance gradient.

Wismer and Luth [24, 25] defined a soil-tire numeric N_{cs} for the tires operated in cohesive-frictional soil.

$$N_{CS} = \frac{C_i b_t d}{F_z} \tag{2.4}$$

As shown in Fig. 2.3, the soil-tire numerics were linked to drawbar coefficient and efficiency based on tests performed in the laboratory. The drawbar coefficient μ is defined as the ratio of drawbar pull to the vertical load on the tire, and the drawbar efficiency η is defined as the ratio of drawbar power to power input to the tire [23].

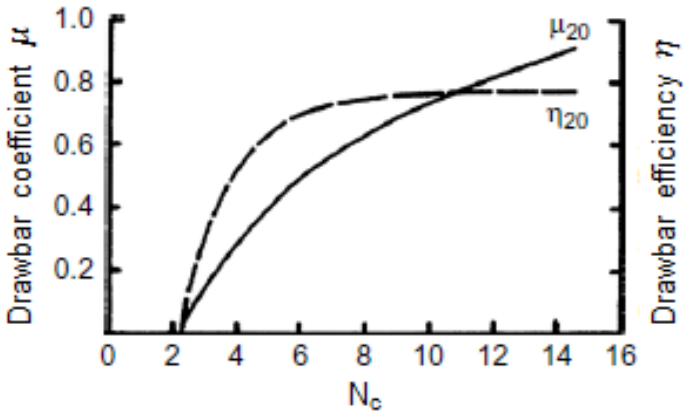

Fig. 2.3: Empirical relationships between the clay-tire numeric N_c and drawbar characteristics at the slip of 20% [23]

Rula and Nuttall [26] proposed an empirical model known as the vehicle cone index (VCI) model to predict vehicle performance and soil trafficability. As given in Eq. (2.5) and (2.6), the VCI is an index to predict the minimum soil strength in the critical layer for a vehicle to drive over the soil with a certain number of passes. The critical layer mentioned above is determined by the type and weight of vehicle and by soil strength profile. For fine-grained soils and poorly drained sands, it's usually in the layer of the depth of 0–15 cm layer for one pass and of the depth of 15–30 cm for 50 passes. As described by Eq. (2.7), the mobility index (MI) was developed to account for the effects of vehicle design features on the VCI. K_{cp} is the contact pressure factor which equals to the value of vehicle gross weight (lb) by contact area (in^2), K_w is the weight factor which equals to 1 when the vehicle weight is below 22.24 tons, equals to 1.2 when the vehicle weight ranges from 22.24 to 31.14 tons, equals to 1.4 when the vehicle weight ranges from 31.14 to 44.48 tons and equals to 1.8 when the vehicel weight is larger than 44.48 tons. K_t is the track factor which equals to the value of track width (in) divided by 100. K_g is the grouser factor which equals to 1 when the

height of grousers is less than 3.8 cm and equals to 1.1 when the height of grousers is more than 3.8 cm. K_{bg} is bogie factor which equals to the value of vehicle gross weight (lb) divided by 10, total numbers of bogies in contact with ground and area of one track shoe. K_{cl} is the clearance factor which equals to the value of clearance (in) divided by 10, K_{en} is the engine factor which equals to 1 when the engine power divided by the vehicle weight is larger than 8.2 kW/tonne and equals to 1.05 when this value is less than 8.2 kW/tonne, K_{tr} is the transmission factor which equals to 1 for automatic transmissions and to 1.05 for manual transmissions.

$$VCI_1 = 7.0 + 0.2MI - (\frac{39.2}{MI + 5.6}) \tag{2.5}$$

$$VCI_{50} = 19.72 + 0.43MI - (\frac{125.79}{MI + 7.08}) \tag{2.6}$$

$$MI = \left(\frac{K_{cp} \times K_w}{K_t \times K_g} + K_{bg} - K_{cl} \right) \times K_{en} \times K_{tr} \tag{2.7}$$

Where

VCI_1 vehicle cone index for one pass

VCI_{50} vehicle cone index for fifty passes

After the values of the VCI and the CI have been identified, the vehicle performance such as the net maximum drawbar pull coefficient can be determined based on the number of passes and the excess value of CI minus VCI, as displayed in Fig. 2.4.

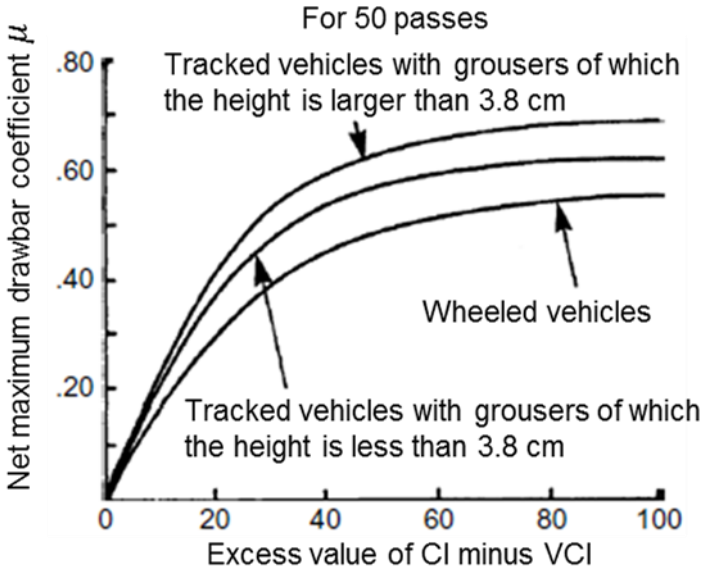

Fig. 2.4 Variations of the net maximum drawbar pull coefficient with the excess value of CI minus VCI [26]

The WES methods are applicable to assess the performance of vehicles which are similar to those tested under the similar conditions. However as vehicles with new features and new environments are frequently encountered, the limitations of the empirical method are obvious as well. Reece and Peca [27] pointed out that the evaluation of the tire performance with an empirical method was not appropriate for certain types of sand. Gee-Clough [28] reported that the prediction of certain performances of tires couldn't be adequately accurate an empirical method.

Grecenko and Prikner [29] proposed the Compaction Capacity (CC) rating to quantify the soil compaction due to the axle load at various inflation pressures.

$$CC = 1000\left(\frac{\rho_{ds}}{\rho_{dc}} - 1\right) \tag{2.8}$$

Where ρ_{ds} is the dry density defined as the average value of density after loading in the depth range from 20 to 50 cm, ρ_{dl} is the critical value of dry density limiting the growth of field crops on loamy soils.

2.1.3 Pressure-sinkage relationship

Bernstein [30] established an empirical sinkage model for the assessment of the relationship between the loading pressure and the sinkage as displayed in Eq. (2.9).

$$z = k\sqrt{p} \tag{2.9}$$

Where

z	soil sinkage	k	soil deformation modulus
p	loading pressure		

Goriatchkin [31] revised the Bernstein pressure-sinkage model as follows.

$$p = k_1 z^n \tag{2.10}$$

Where k_1 is the soil stiffness.

By modifying the Bernstein-Goriatchkin model, Bekker [17] developed the pressure-sinkage relationship for homogeneous soils supported by the bevameter technique. The parameters k_c and k_φ have variable dimensions depending on the exponent *n*.

$$p = \left(k_c / b + k_\phi\right) z^n \tag{2.11}$$

Where b is the smaller dimension of a sinking plate.

Reece [32] developed the non-dimensional k_c' and k_φ' parameters based on the experimental results as displayed in Eq. (2.12). It was notice that the effects of k_c' on the loading pressure could be ignored for dry and cohesionless sand, and the effects of k_φ' on that pressure could be ignored for frictionless and cohesive clay.

$$p = \left(ck_c^{'} + \gamma_s b\, k_\varphi^{'}\right)\left(z/b\right)^n \tag{2.12}$$

Where

c soil cohesion γ_s soil weight density

Based on the experimental data of five different tires, Meirion-Griffith and Spenko [33] modified the classic pressure-sinkage models for small tires as shown in Eq. (2.13). The new model indicates that the tire diameter plays an important role in the pressure-sinkage relationship.

$$p = k' z^{n'} d^{m} \tag{2.13}$$

Where k', n', m are the pressure-sinkage parameters in the MG equation.

When the multi-axle vehicles drive over soft soils, the multi-passing causes the soils being repetitively loaded. The response of a mineral soil to the loading-unloading-reloading action was measured, and the pressure-sinkage relationship was displayed in Fig. 2.5. Wong [34, 35] established an equation for describing the soil responding to the repetitive loading, as shown in Eq. (2.14).

$$p = (k_c / b + k_\phi) z_A^{\,n} - k_u (z_A - z) \tag{2.14}$$

Where z_A is the soil sinkage when the unloading begins.

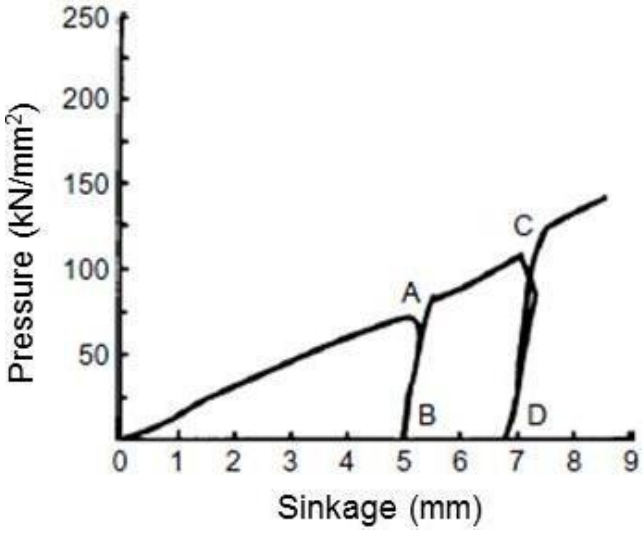

Fig. 2.5: Soil response to repetitive loading [34]

2.1.4 Shear stress-displacement relationship

The shear stress-displacement model is intended for the identification of the shear strength and the prediction of the tractive performance of the vehicles running over unprepared soils. Bekker [17] proposed Eq. (2.15) to describe the shear stress-displacement relationship for brittle soils which contains a hump of maximum shear stress.

$$\tau / \tau_{\max} = \frac{e^{(-K_2+\sqrt{K_2^2-1})K_1 j} - e^{(-K_2-\sqrt{K_2^2-1})K_1 j}}{e^{(-K_2+\sqrt{K_2^2-1})K_1 j_0} - e^{(-K_2-\sqrt{K_2^2-1})K_1 j_0}} \tag{2.15}$$

Where

τ shear stress

τ_{max} maximum shear stress

K_1 empirical parameter in the Bekker shear equation

K_2 empirical parameter in the Bekker shear equation

j shear displacement

j_0 shear displacement at τ_{max}

Janosi and Hanamoto [36, 37] established a modified shear stress-displacement equation based on the Bekker equation. This modified equation is widely used due to the simplicity that only one constant is included.

$$\tau / \tau_{\max} = 1 - e^{(-j/K)} \tag{2.16}$$

Where K is the shear deformation modulus.

Wong and Preston-Thomas [38] reported that Eq. (2.16) was quite suitable to describe the shear stress-displacement relationship for certain types of sandy soils, saturated clay, fresh snow and peat. The curve exhibits that the shear stress increases with the shear displacement and approaches a constant value as the shear displacement increases further, as shown in Fig. 2.6.

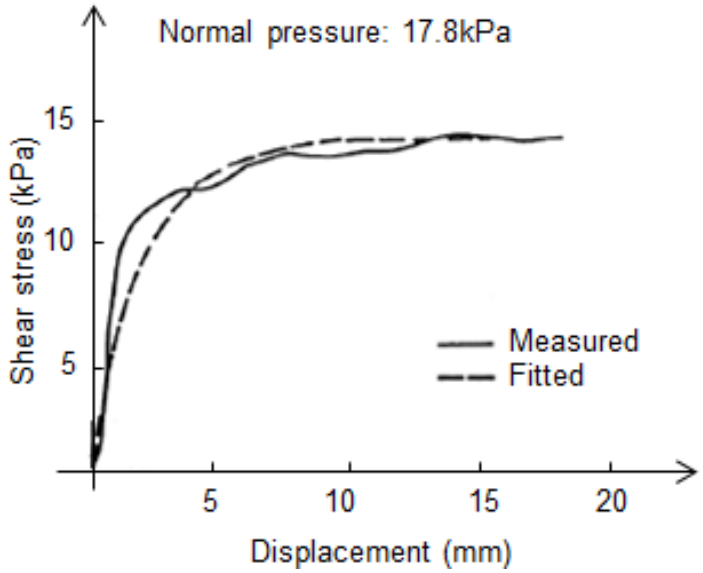

Fig. 2.6: Shear curve in an exponential form for a saturated clay [20]

Shear curves of snow covered soils and certain types of loam display a hump of maximum shear stress at a certain shear displacement and the shear stress tends to decrease with the further increase of shear displacement to a constant value of residual stress, as shown in Fig. 2.7.

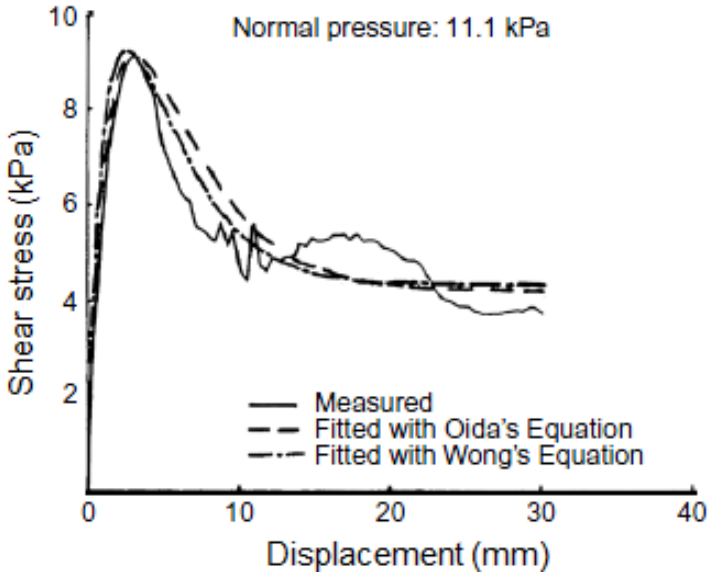

Fig. 2.7: Shear curve with a peak and constant residual shear stress for a loam [20]

Based on the research of Kacigin and Guskov [40], Oida [41] proposed a shear stress-displacement equation for this type of shear stress curve as shown in Eq. (2.17). The identification of the constants in the Oida's equation is a quite complicated and time consuming process due to the non-linear feature. Wong [39] modified the Oida's equation to simplify the constant identification as shown in Eq. (2.18).

$$\tau / \tau_{\max} = K_r \left[1 - \frac{\sqrt{1-K_r}\left[1+\left(\sqrt{1-K_r}-1\right)/K_r\right]^{j/j_0}}{\sqrt{1-K_r}(1-2/K_r)+2/K_r-2} \right] \left[1-\left[1+\left(\sqrt{1-K_r}-1\right)/K_r\right]^{j/j_0} \right] \quad (2.17)$$

$$\tau / \tau_{\max} = K_r \left(1+\left(1/K_r(1-1/e)-1\right)e^{1-j/j_0}\right)\left(1-e^{1-j/j_0}\right) \quad (2.18)$$

Where K_r is the ratio of the residual shear stress to the maximum shear stress.

The shear curve of a muskeg soil exhibits the features that the shear stress increases with shear displacement, reaches a hump of maximum shear stress, and decreases with a further increase of the shear displacement, as shown in Fig. 2.8.

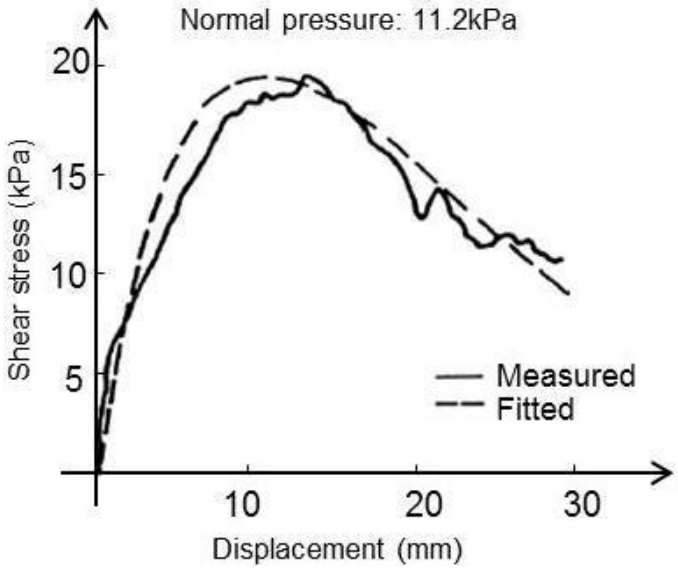

Fig. 2.8: Shear curve with a peak and decreasing residual shear stress for a muskeg soil [20]

Wong and Preston-Thomas [38] pointed out that Eq. (2.19) may be used to fit this type of shear stress curve.

$$\tau / \tau_{\max} = (j / j_0) e^{(1-j/j_0)} \quad (2.19)$$

The maximum shear stress τ_{max}, an index representing soil shear stress, was described with the Mohr-Coulomb equation as shown in Eq. (2.20).

$$\tau_{\max} = c + p \tan\phi \quad (2.20)$$

Where

c soil cohesion ϕ angle of internal friction

p loading pressure

As shown in Fig. 2.9, Wills [42] measured the soil shear strength with different shearing devices to obtain the constants in the maximum shear stress equation.

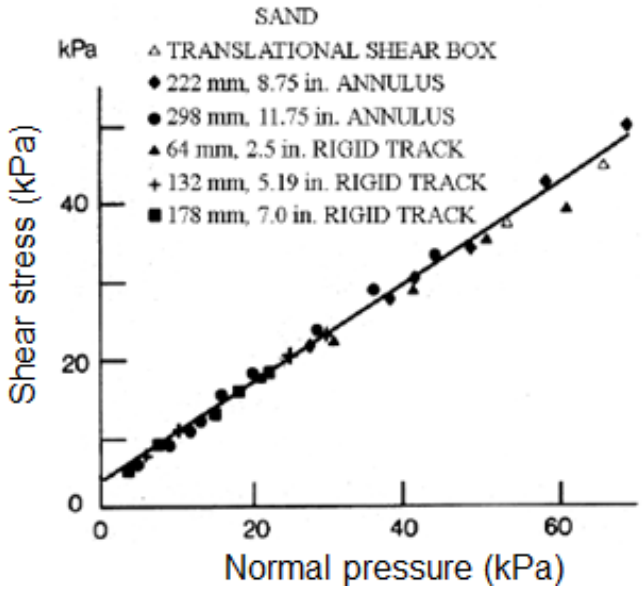

Fig. 2.9: Relationship between normal pressure and shear stress for sand [42]

2.2 Analytical Methods

Under the support of the experiments carried out with the bevameter, Bekker [17, 18] initially developed an analytical method for predicting rigid tire performance on unprepared soils. The analytical method was further improved and extended for predicting deformable tire performance.

2.2.1 Deformable tire – rigid road interaction

During the last century several types of tire models have been developed to describe the generation of forces and moments when the tire rolls on a rigid road. The models describing the tire behavior are mainly distinguished into steady-state and transient dynamics models. The steady-state refers to the situation in which all motions of the tire structure are fixed and not vary with time. In this case, all the vehicle states such as speed, yaw rate and path curvature, remain constant. This aspect is more devoted to pure tire characteristics studies. On the other hand, the transient state refers to the situation in which the motions of the vehicle are varying with time. Thus, the transient investigations deal with forces and deformations at the tire-road interface affected by road roughness, tire-wheel assembly, non-uniformities and operating conditions [43].

The Fiala tire model approximates a parabolic normal pressure distribution on the contact patch with a rectangular shape [44]. The instantaneous value of the tire-road friction coefficient is determined by a linear interpolation in terms of the resultant slip

and the static friction coefficient. The influence of a camber angle on lateral force and aligning moment is not considered.

Three versions of tire models were developed at the United States Highway Safety Research Institute (HSRI), Arlington. The models represent the tire tread as an array of elastic rectangular blocks radially attached to an elastic or rigid ring, as displayed in Fig. 2.10. The ring stands for the tire carcass which has bending stiffness. The tire carcass may be attached to the mounting rim or separated from the rim by a spring foundation which allows the carcass motion in the longitudinal and lateral directions [45]. The first version of the HSRI tire model assumes a rectangular contact patch comprised of adhesion and sliding regions. The friction coefficient is assumed to be a linearly decreasing function of sliding speed. However this model isn't capable of providing an accurate prediction of the tire characteristics, especially the self-aligning torque. Hence the second version, which introduces a transition region between the adhesion and sliding regions, is proposed. The assumption of the normal pressure uniformly distributed on the contact patch is not adequately realistic. Hence the third version, which supposes a parabolic normal pressure distribution, is proposed. The generation of forces and moments under pure and combined slip conditions can be obtained.

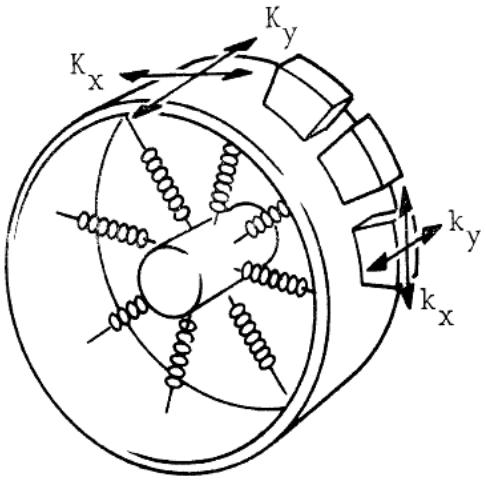

Fig. 2.10: HSRI tire models [45]

The brush model presents the tire tread patterns by elastic brush elements attached to a belt [46-49]. The belt which has an infinite lateral stiffness is connected to the rim. When the tire is in the free rolling status, the tread elements from the leading edge to the trailing edge remain vertical to the road surface, and no longitudinal or lateral force is generated. When a lateral slip occurs, the tire deflections in the lateral direction are developed and corresponding forces and moments appear. To analyze

the longitudinal force caused by the longitudinal slip ratio, it is assumed that the longitudinal and lateral stiffness of the tread elements are equal. When the tire brakes at a given slip angle, the deflection of the tread elements are opposite to the slip speed in the sticking and sliding regions. The longitudinal and lateral forces can be calculated by integrating the contact force on each tread element caused by the deflection in the sticking and sliding regions. The force distribution on the contact patch is presented in Fig. 2.11.

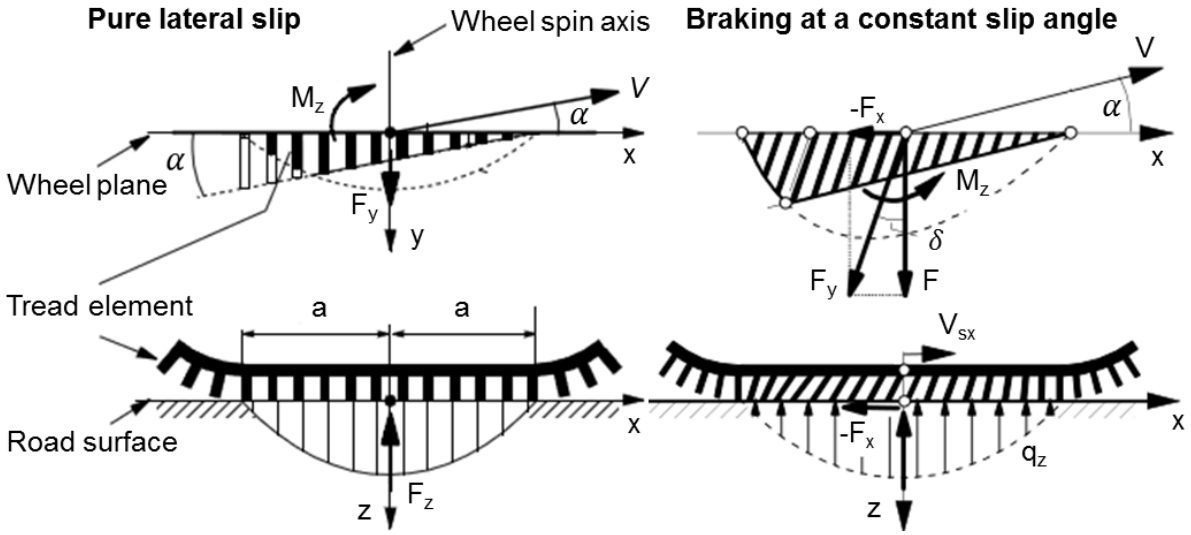

Fig. 2.11: Brush model at pure lateral slip and combined slip [49]

The Magic Formula (MF) tire model is well established based on the work by Pacejka. This model is not considered as a predictive tire model, but is applied to demonstrate the tire force and moment curves in terms of longitudinal slip and slip angle. The original MF tire model established by Bakker applies a formula of Fourier series to represent the force and moment curves. The major disadvantage of this model is that the formula coefficients have no engineering significance related to the tire properties and no connection to the improvement of the tire performance in reality [50]. The MF tire model improved by Pacejka was tested at Michelin and came to general acceptance in the automotive field [51, 52]. The main feature of the MF tire model is that it relates the lateral force and the aligning moment as functions of the slip angle, and the longitudinal force as a function of the longitudinal slip. It is capable of dealing with the complicated situation of combined slip. The MF tire model is still undergoing continual development, and is reflected in the further publications [53-55].

The models introduced so far belong to the group of steady state models. Due to the flexible structure, tire forces and moments don't develop instantaneously, but a certain rolling distance is required for the action generation. Pacejka [55] and von

Schlippe [56] introduced the concept of a stretched string model. This model is based on the assumption that the tire tread is equivalent to a stretched string restrained by lateral springs representing the side wall, and the wheel rim acts as the spring base, as displayed in Fig. 2.12. Fromm [57] introduced the point contact theory, which related the cornering force to a linear combination of slip angle, tire deflection and their time derivative.

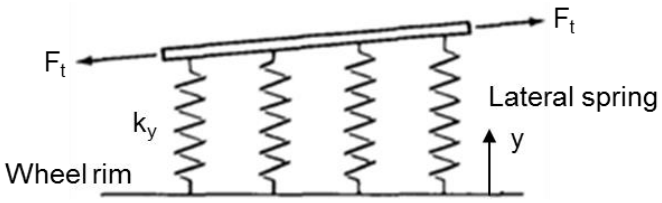

Fig. 2.12 Stretched string model [69]

Developed at TU Delft and TNO Helmond, the Short Wavelength Intermediate Frequency Tire (SWIFT) is a collection of methods employed to extend the MF tire concept with dynamic properties. It presents an ability to deal with the tire performance on uneven roads. The tire carcass is modeled as a rigid ring with inertia. The ring has a flexible linkage to the rim, with stiffness in all directions. It is able to describe the tire dynamic behavior at high frequencies and short road obstacles [58].

In the Flexible Ring Tire (FTire) model established by Gipser, the tire carcass is represented by an extensible and flexible ring with bending stiffness [59]. As displayed in Fig. 2.13, the ring, which is approximated as a collection of belt elements, is attached to the rim. A number of tread blocks, which have nonlinear stiffness and damping properties in radial, tangential and lateral directions, are associated to the belt elements. The FTire is able to simulate the forces and moments development.

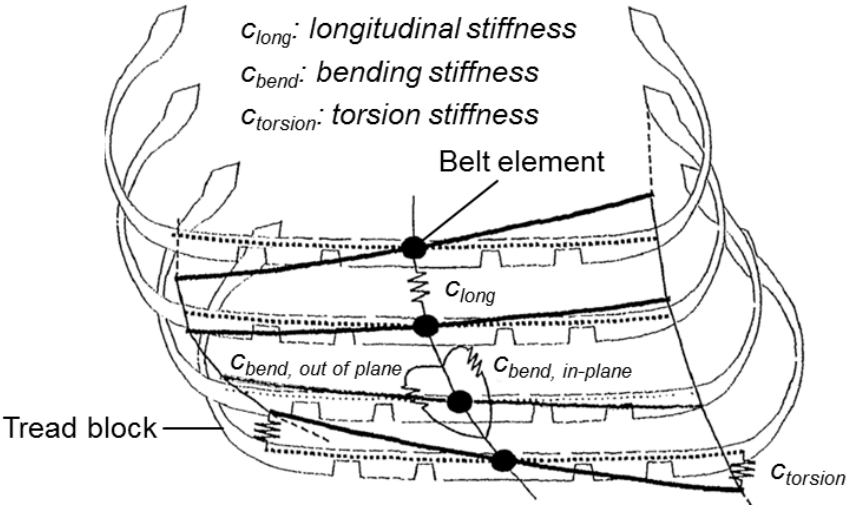

Fig. 2.13 Schematic structure of FTire [59]

Applied at the Fraunhofer Institute for Industrial Mathematics (ITWM), the Comfort and Durability Tire (CDTire) model is a family of four models (CDTire 20, CDTire30, CDTire40 and CDTMC), which use different physical models for belt, sidewall and tread to evaluate the dynamic tire forces and moments [60].

2.2.2 Rigid tire – soil interaction

To simplify the tire-soil model, the pneumatic tire was first handled as a rigid tire running on soft soils. This is valid as long as the inflation pressure is sufficiently high. This model was modified during the development of terramechanics, and the mechanics of the rigid tire – soft soil was established. The reason why this type of interaction is still of great interest is that, the rigid tire is still in use on the rovers for the exploration of Moon, Mars and other planets [17].

As displayed in Fig. 2.14, the original rigid tire – soil interaction model established by Bekker [17] is based on the assumption that the soil reaction is radial and no shear stress exists in the contact patch. The radial stress equals to the normal pressure under the sinkage plate at the same depth in the pressure-sinkage test. Since the forces applied on the rigid tires are in the equilibrium status, the following equations were proposed for the description of compacting resistance and vertical load [17].

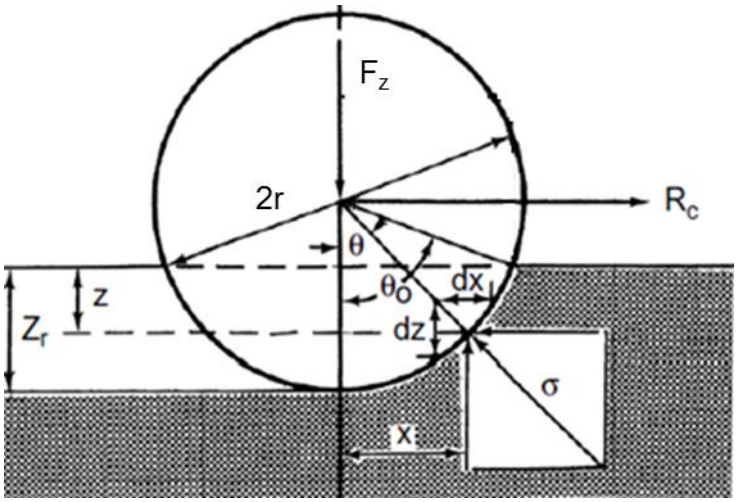

Fig. 2.14: Simplified rigid tire – soil interaction model [17]

$$R_c = b_t\left(\frac{k_c}{b_t} + k_\phi\right)\frac{z_r^{n+1}}{n+1} \tag{2.21}$$

$$F_z = \frac{b_t\left(k_c / b_t + k_\phi\right)\sqrt{2z_r r}}{3} z_r^n\left(3-n\right) \tag{2.22}$$

Where

R_c	motion resistance	z_r	maximum soil sinkage
F_z	vertical force	r	tire radius
b_t	tire width	n	Sinkage exponent

k_ϕ pressure-sinkage parameter in the Bekker equation

k_c pressure-sinkage parameter in the Bekker equation

Eq. (2.21) implies that the motion resistance R_c of a rigid tire is equal to the vertical work per unit length in compressing the sinkage plate into a depth of z_r. Therefore the motion resistance is usually considered as the compacting resistance.

The predictions of tire performance with the application of Eq. (2.21) and (2.22) are acceptable when the sinkage is relatively moderate. Bekker [13] concluded that the larger the value of the tire diameter divided by the sinkage is, the more accurate the predictions will be. Assuming that the motion resistance is independent of the slip, the equations mentioned above, only explain the contribution of radial stress to the rigid tire – soil interaction. The slip also plays an important role in the rigid tire – soil interaction. Theoretically the maximum radial stress on the contact interface should occur at the lowest point of tire contact where the sinkage is maximized. However the measured radial stress distribution on the contact interface varies at different slips [61, 62]. Concluded from experimental data on sand, it was found that the location of the maximum radial stress could be described by the following equation:

$$\theta_m = \theta_0 (c_1 + c_2 i) \tag{2.23}$$

The normal component of the shear stress accounts for partly supporting the wheel load. Due to the fact that the shear stress tends to increase with the increasing of slip, the contribution of the shear stress to the wheel load becomes larger, which results in the decrease of the radial stress. Concluded from Fig. 2.15, the measured angular position of the maximum stress is different with that derived from the simplified rigid tire – soil interaction model.

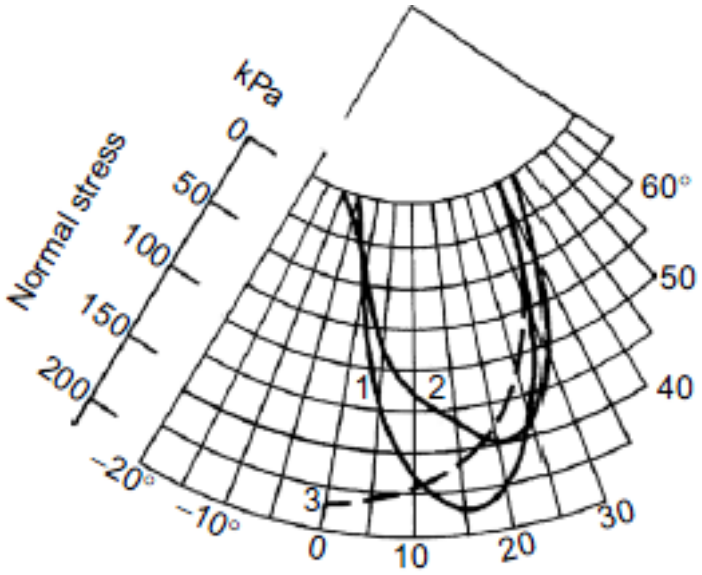

Fig. 2.15: Radial stress distribution on a rigid tire – sand interface (1-at 3.1% slip; 2-35.1%; 3-predicted with Eq. (2.22)) [20]

Yoshida [63, 64] established a rigid tire – soil traction model for lunar planetary exploration rovers. The lateral force of the rigid tire on loose soil during the rover motions was investigated. As displayed in Fig. 2.16, the stress distribution beneath the rigid tire was demonstrated. For the deformable tire – rigid road interaction, the application point of the lateral force is behind the tire central point O, it indicates that the torque caused by the lateral force tends to bring the tire back to its original position, and this effect is called as “self-aligning torque”. [64] For the rigid tire – soil interaction, the application point of the lateral force is in the front of the tire central point O, it indicates that the torque caused by the lateral force tends to increase the slip angle, and this effect is called as “anti-aligning torque”.

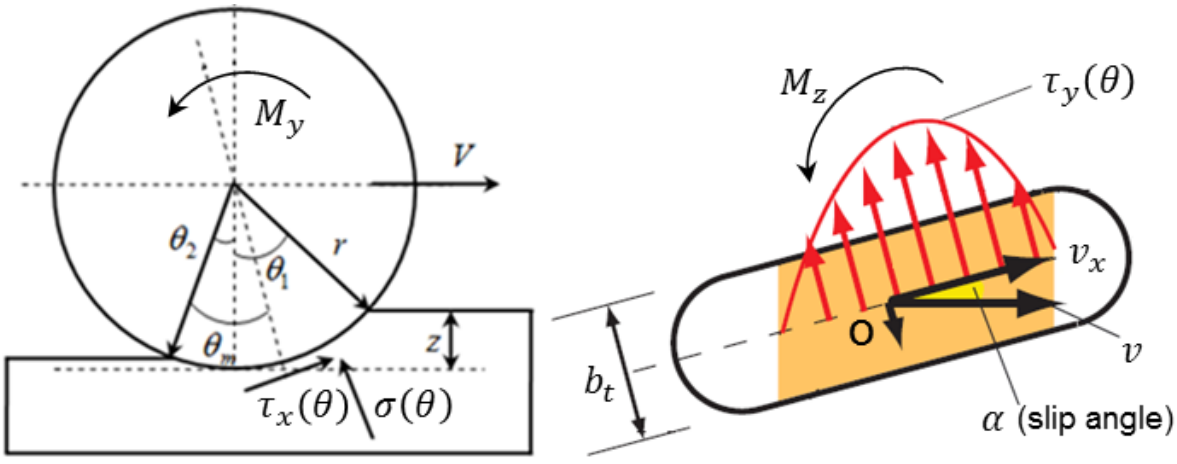

Fig. 2.16: Stress on the rigid tire-soil interface with anti-aligning torque [64]

The radial stress distribution within the contact area was divided into the front and rear area according to θ_m where the maximum radial stress occurs, as shown in Fig. 2.17. Therefore the angular positions of the radial stresses with the same magnitudes in the two regions were correlated with Eq. (2.24), and the angular position of the maximum radial stress was determined by Eq. (2.23).

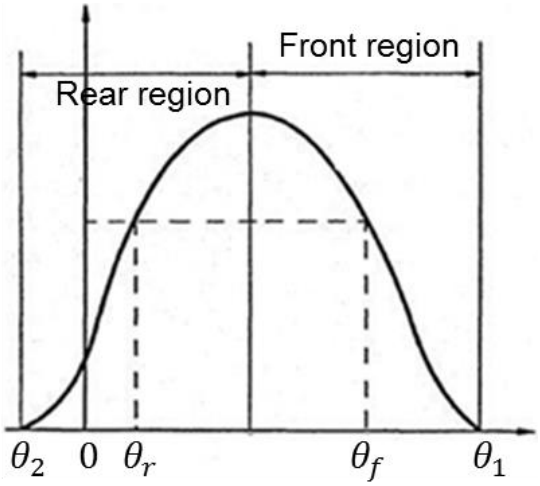

Fig. 2.17: Distribution of radial stress on the contact interface

$$\frac{\theta_r-\theta_2}{\theta_m-\theta_2}=\frac{\theta_1-\theta_f}{\theta_1-\theta_m}\Rightarrow\theta_f=\theta_1-(\theta_1-\theta_m)\frac{\theta_r-\theta_2}{\theta_m-\theta_2} \tag{2.24}$$

Where

θ_1 entry angle θ_2 exit angle

θ_r, θ_f location where radial stresses are identical in the rear and front regions

Deriving from the pressure-sinkage relationship, the radial stress at an arbitrary contact point $z(\theta)$ is determined by the following equations:

$$\sigma(\theta)=\begin{cases}\left(\dfrac{k_c}{b_t}+k_\phi\right)\left(r(\cos\theta-\cos\theta_1)\right)^n & (\theta_m<\theta\le\theta_1)\\ \left(\dfrac{k_c}{b_t}+k_\phi\right)\left\{r\left(\cos\left(\theta_1-(\theta_1-\theta_m)\left(\dfrac{\theta-\theta_2}{\theta_m-\theta_2}\right)\right)-\cos\theta_1\right)\right\}^n & (\theta_2\le\theta\le\theta_m)\end{cases} \tag{2.25}$$

$$\theta_1=\cos^{-1}\left(1-\frac{z}{r}\right) \tag{2.26}$$

$$\theta_2 = \cos^{-1}\left(1 - \frac{k_r z}{r}\right) \tag{2.27}$$

Where

z	soil sinkage	k_r	Tire sinkage ratio
r	tire radius	σ	radial stress

Based on Eq. (2.16) proposed by Janosi and Hanamoto [37], Yoshida and Ishigami [64] developed the following equations for predicting the shear stress in the longitudinal and the lateral direction by introducing the longitudinal shear deformation $j_x(\theta)$ and the lateral shear deformation $j_y(\theta)$.

$$j_x(\theta) = \int_{\theta}^{\theta_1} r\left[1-(1-i)\cos\theta\right]d\theta = r\left[(\theta_1-\theta)-(1-i)(\sin\theta_1-\sin\theta)\right] \tag{2.28}$$

$$j_y(\theta) = \int_{\theta}^{\theta_1} r(1-i)\tan\alpha\, d\theta = r(1-i)(\theta_1-\theta)\tan\alpha \tag{2.29}$$

$$\tau_x(\theta) = \left[c+\sigma(\theta)\tan\phi\right]\left(1-e^{-j_x(\theta)/K_x}\right) \tag{2.30}$$

$$\tau_y(\theta) = \left[c+\sigma(\theta)\tan\phi\right]\left(1-e^{-j_y(\theta)/K_y}\right) \tag{2.31}$$

Where

i	longitudinal slip ratio	α	slip angle
K_x, K_y	longitudinal and lateral shear deformation modulus		
τ_x, τ_y	longitudinal and lateral shear stresses		

The drawbar pull F_x and the vertical force F_z were obtained by integrating the component of the radial and shear stress in the longitudinal direction (x axis) or the vertical direction (z axis) respectively from the entry angle to the exit angle.

$$F_x = b_t r\int_{\theta_2}^{\theta_1}\left(\tau_x(\theta)\cos\theta - \sigma(\theta)\sin\theta\right)d\theta \tag{2.32}$$

$$F_z = b_t r\int_{\theta_2}^{\theta_1}\left(\tau_x(\theta)\sin\theta + \sigma(\theta)\cos\theta\right)d\theta \tag{2.33}$$

The lateral force F_y and the anti-aligning torque M_z were obtained by integrating the stress in the lateral direction (y axis). The resistance torque M_y was obtained by integrating the longitudinal shear stress.

$$F_y = \int_{\theta_2}^{\theta_1} b_t r\tau_y(\theta) + R_b\left(r - z(\theta)\cos\theta\right)d\theta \tag{2.34}$$

$$M_z = b_t r^2 \int_{\theta_2}^{\theta_1} \tau_y(\theta) \sin\theta d\theta \tag{2.35}$$

$$M_y = b_t r^2 \int_{\theta_2}^{\theta_1} \tau_x(\theta) d\theta \tag{2.36}$$

As displayed in Fig. 2.18, Karafiath and Nowatzki [65] established equations to account for the radial stress distribution under the tires with grousers or lugs.

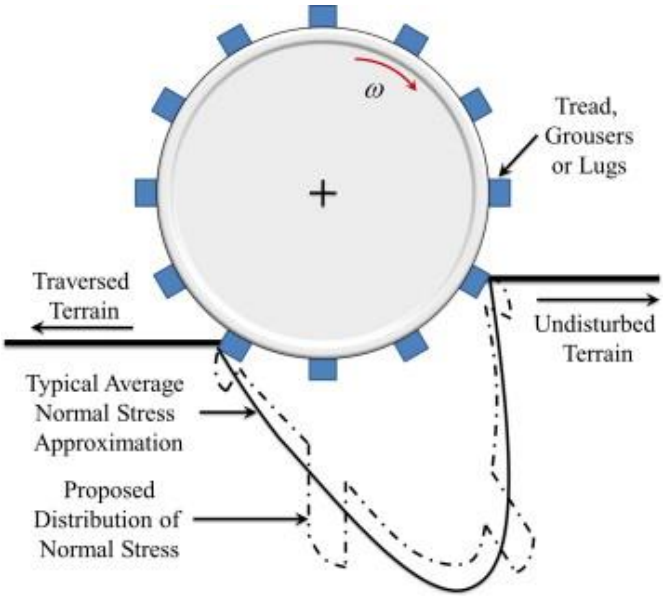

Fig. 2.18: Normal stress distribution beneath the tires with grousers or lugs [66]

Irani [66] developed a validated terramechanic model for rigid tires with grousers which might be applied on planetary and terrestrial mobile robots. The advantage of this model is the capability of predicting the dynamic oscillations caused by grousers. The distinct feature of the model is an item accounting for the oscillation and it is introduced into the equation of the pressure-sinkage relationship. It was assumed that the frequency ω is related to the spacing of the grouser blade and the rotation velocity. The oscillation amplitude is affected by two main factors. One factor is the active and passive stresses due to the grousers or lugs, and the other is the changing in the local soil density around the tire and the grousers due to the soil compaction.

$$p = (k_c / b + k_\phi) z^n + A\sin(\omega t_i + \varphi) \tag{2.37}$$

Where A is the oscillation amplitude, and φ is the optional phase shift.

Krenn and Hirzinger [67] established a new simulation tool called Soil Contact Model (SCM) for the prediction and verification of the rigid tire performances of the ExoMars

(ESA) rover at DLR Institute of Robotics and Mechatronics, Oberpfaffenhofen-Wessling, Germany. SCM applies the classical terramechanics theory of Bekker and Wong and enables the 3D simulation and visualization of the rigid tire – soil interaction phenomena. As a subroutine integrated in SIMPACK, the soil contact model is first initialized before the simulation starts, then the forces and torques acting on the contact bodies are calculated based on the classical terramechanics theory. SCM is able to compute the drawbar pull, the lateral force and the multi-pass effect.

2.2.3 Deformable tire – soil interaction

Wong [68, 69] proposed a model for the deformable tire – soil interaction when the inflation pressure of a pneumatic tire is low, as dsiplaye in Fig. 2.19. The principle is that if the sum of the inflation pressure p_i and the carcass stiffness k_{ca} is larger than the critical ground pressure p_{gcr} at the tire-soil interface, the tire behaves like a rigid rim; otherwise the bottom part of the tire is flattened. Theoretically two operating modes are defined as following: the rigid mode and the elastic mode. Wong [69] proposed the following equation for calculating the critical ground pressure.

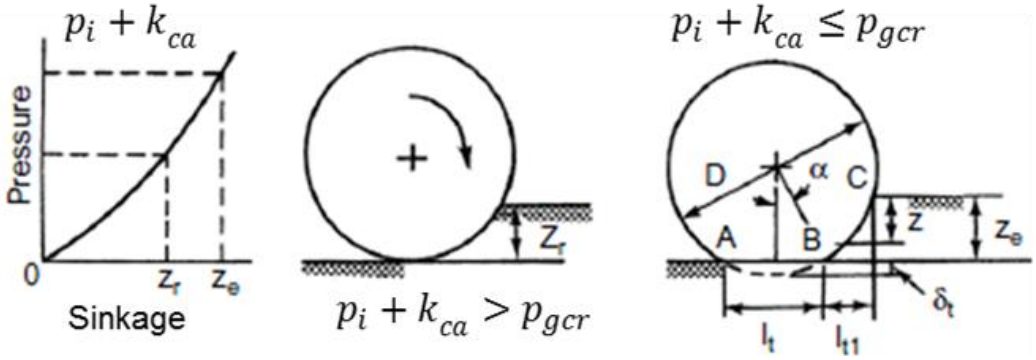

Fig. 2.19: Behavior of a pneumatic tire in different operating modes [69]

$$p_{gcr} = (k_c / b + k_\phi)^{1/(2n+1)} \left(3W / (3-n) b_t \sqrt{D}\right)^{2n/(2n+1)} \tag{2.38}$$

If the tire is in the rigid mode, the equations for the rigid-soil interaction are used; if the tire is in the elastic mode, the following equations are used.

$$z_e = \left(\frac{p_i + p_c}{k_c / b + k_\phi}\right)^{1/n} \tag{2.39}$$

$$R_c = b_t \left(\frac{k_c}{b} + k_\phi\right) \frac{z_e^{n+1}}{n+1} \tag{2.40}$$

Schmid [70] used a parabolic shape to approximate the contact contour of a deformable tire as shown in Fig. 2.20. The radius of the parabolic shape is determined by the following equations.

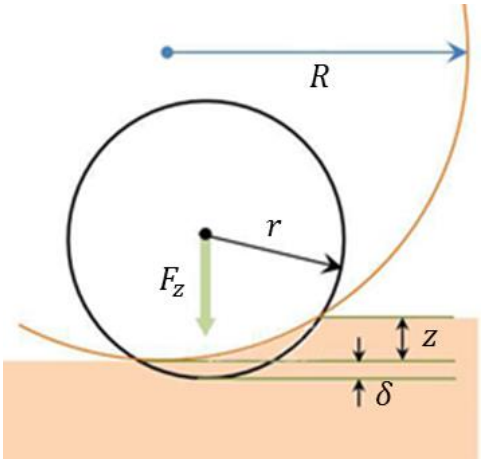

Fig. 2.20: Assumption of the deformable tire – soil contact contour

$$F_z = K_t \delta \tag{2.41}$$

$$\sqrt{R/r} = \sqrt{1+\delta/z} + \sqrt{\delta/z} \tag{2.42}$$

Where

K_t tire vertical stiffness δ tire deformation

R Radius of the parabolic shape

Harnish et al [71] developed a new tire-soil interaction model for MATLAB/Simulink based on the principles introduced in the research field of terramechanics, and a larger substitute circle was adopted to model the behavior of an elastic tire. The effects of slip sinkage and multi-pass were considered in the model.

Based on the plasticity equilibrium theory, Chan and Sandu [72] introduced a flat contact region to mimic the tire deformation geometry. By following Chan's approach, Senatore and Sandu [73] developed an enhanced tire-soil interaction model which is capable of predicting not only the traction performance but also the slip-sinkage and the multi-pass effects.

Favaedi [74] investigated the tractive response of deformable tires mounted on a planetary rover. To model the deformable tire – soil interaction, the tire circumference which is in contact with the soil is divided into three sections as shown in Fig. 2.21. The equations for the description of drawbar pull and vertical load in the model are similar to those in the Yoshida rigid tire – soil interaction model, and the effects of

grousers are considered as well. This analytical model could be applied in the design of optimal traction control strategy for planetary rovers and in the optimization of deformable tires.

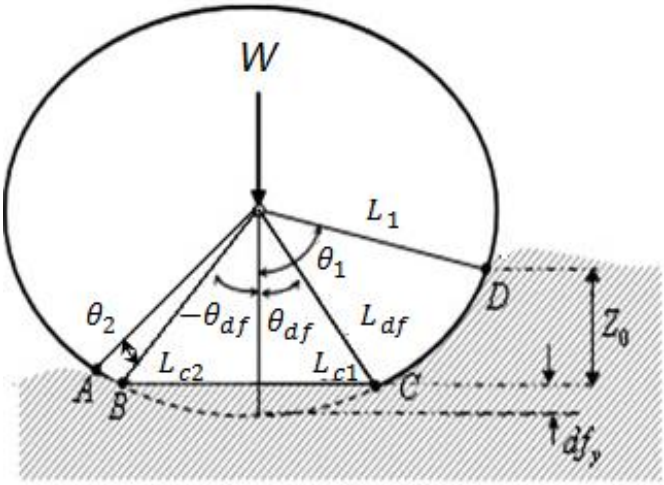

Fig. 2.21: Schematic diagram of tire deformation [74]

The deformable tire – soil model developed in the Adams/Tire module provides a basic model to describe the forces and moments of the tire-soil interaction for the tire running on elastic/plastic ground [75]. This model is established based on the classic terramechanics theory of Bekker and Wong. The steady contact forces and moments generated on the tire-soil interface can be obtained by performing simulations with Adams/Tire. For the deformable – soil interaction, the torque caused by the lateral force could be either self or anti-aligning torque, and the direction of this torque is determined by tire and soil properties.

2.3 Numerical simulation methods

The empirical and analytical methods may not be capable of offering the insights into the stress distribution on the tire-soil interface and the soil deformation at different layers. The finite element method (FEM), initially intended for solving the problems of structural analysis and complex elasticity, and the discrete element method (DEM), originated from the need of modeling a granular material as a continuum for rock mechanics, have been widely applied in the investigation of tire-soil interaction.

2.3.1 Finite element method

For the investigation of the stress distribution and the soil deformation under the axle load of a tractor, the two dimensional (2D) FEM model was first introduced in the analysis of tire-soil interaction by Perumpral [76].

Yong et al [77, 78] developed 2D models for the analysis of rigid/elastic tire-soil interaction. The models required the normal stress, the shear stress and the contact properties as input for the initialization. Pi [79] developed a 2D model of elastic tire-viscoelastic soil interaction for the improvement of aircraft ground operation. The contact pressure distribution, the soil deformation and the tire footprint area were predicted with this model. Foster et al. [80] developed a 2D model of rigid tire – soil interaction to investigate soil stresses and deformations. Liu and Wong [81] confirmed that the prediction of the tire-soil interaction behavior is in the acceptable range by comparing the results from 2D FEM simulation with the experimental data on several types of soil. As shown in Fig. 2.22, Aubel [82] developed a 2D model to study soil compaction and tire dynamic performance at IKK in Hamburg, Germany. Fervers [83, 84] modified this model to investigate the influence of different tread patterns, inflation pressures and slips on the tire performance. The FEM program VENUS developed at IKK offers the opportunities to simulate the tire deflection, the displacement of the soil surface and the bulldozing effect, as displayed in Fig. 2.23.

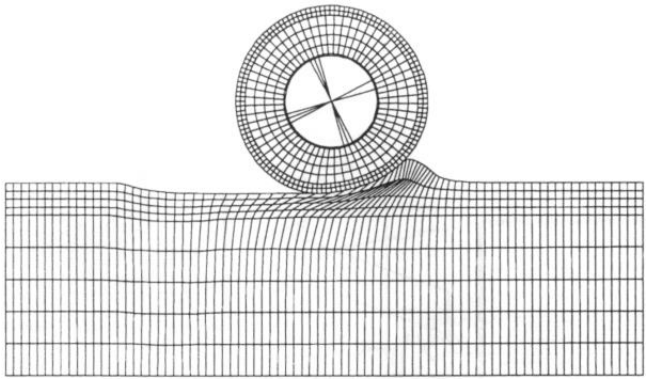

Fig. 2.22: 2D model of tire-soil interaction with bulldozing effect [83]

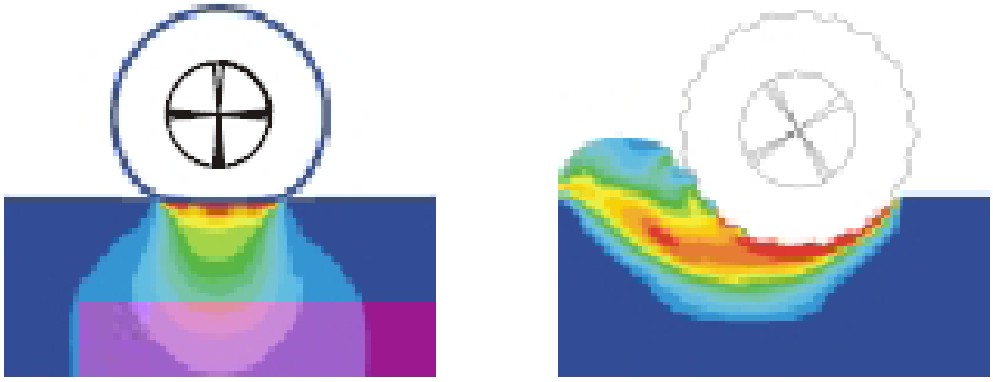

Fig. 2.23: Simulation of pressure distribution in the soil [84]

Shoop [85] proposed a 3D tire-snow interaction model to simulate a tire running through fresh snow of various depths. The tire was assumed to be rigid. Darnell and

Shoop [86, 87] developed a three dimensional (3D) deformable tire-soft soil interaction model for the exploration of vehicle mobility and soil deformation. Zhang [88] developed a 3D tire-soil interaction model for the analysis of the stress distribution on the contact interface. Curve fitting techniques were applied to generate equations for the prediction of pressure distribution in terms of the normal load and the inflation pressure.

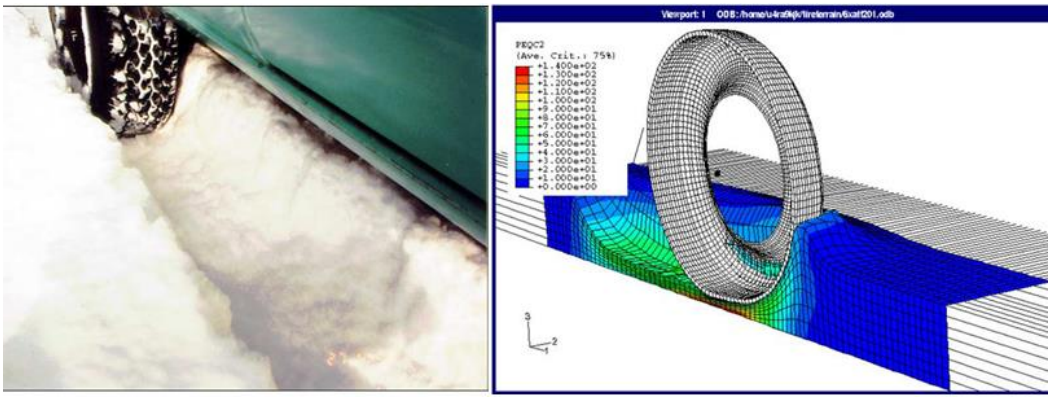

Fig. 2.24: Rigid tire rolling through 20 cm of fresh snow [85]

Poodt [89] applied the finite element method to analyze the subsoil compaction caused by heavy sugarbeet harvesters. Cui [90] employed the FEM models based on the PLAXIS code to investigate the vertical stress distribution at the tire-soil interface. PLAXIS is a 2 dimensional FEM model package originally developed for analyzing deformation and stability in geotechnical engineering [91]. By modeling a pavement as 2D four-layer stratum with a commercial FEM software-Ansys, Mulungye [92] studied the effect of tire pressure, tire configuration and axle load on the structural performance of a flexible road pavement, as shown in Fig. 2.25.

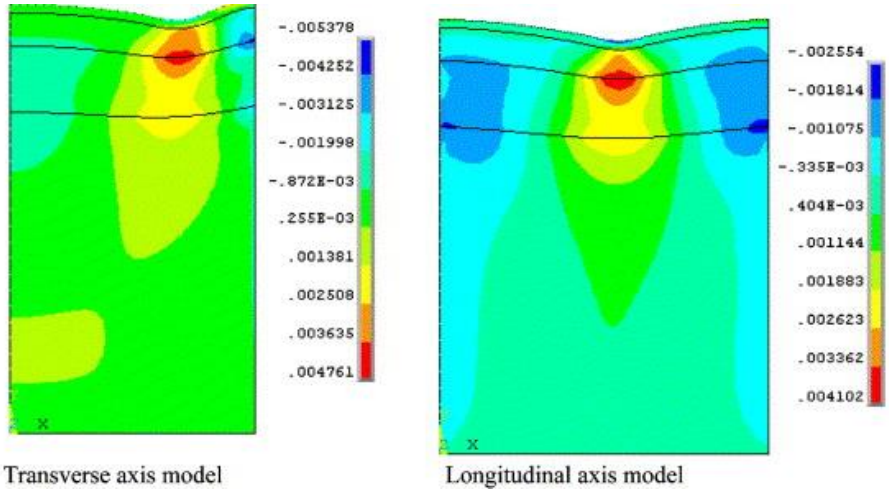

Fig. 2.25: Lateral and longitudinal strain output corresponding to front single wheel load of 31.7 kN at the tire inflation pressure of 630 kPa [92]

Hambleton and Drescher [93, 94] predicted the axle load-soil penetration relationship for the steady-state rolling of rigid cylindrical wheels on cohesive soil with analytical and finite element models. The axle load-sinkage curves predicted with these two approaches show the same trend. Quantitative agreement between the predicted and experimental results was observed as well.

As displayed in Fig. 2.26, Mohsenimanesh [95] modeled a pneumatic tractor tire with non-linear 3D finite elements and validated the tire model by comparing the dimensions of the tire-road contact interface with the simulation results. The interaction between the tractor tire and a multi-layered soil was studied with the application of Ansys, and the influence of the tire load and the inflation pressure on the contact stress distribution was analyzed as displayed in Fig. 2.27. To simplify the structure of the FEM tire model, the tread patterns were assumed as straight ribs.

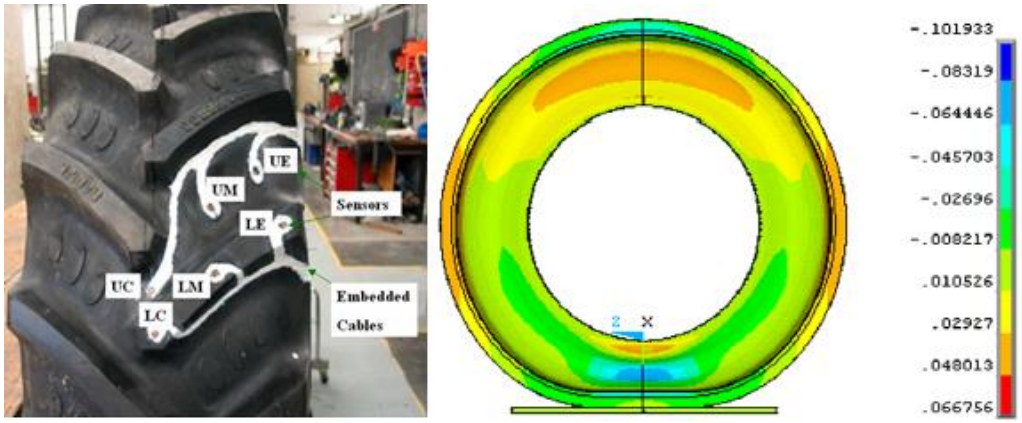

Fig. 2.26: Vertical components of strain at the load of 15 kN and the inflation pressure of 100 kPa for a 16.9R38 tractor tire [95]

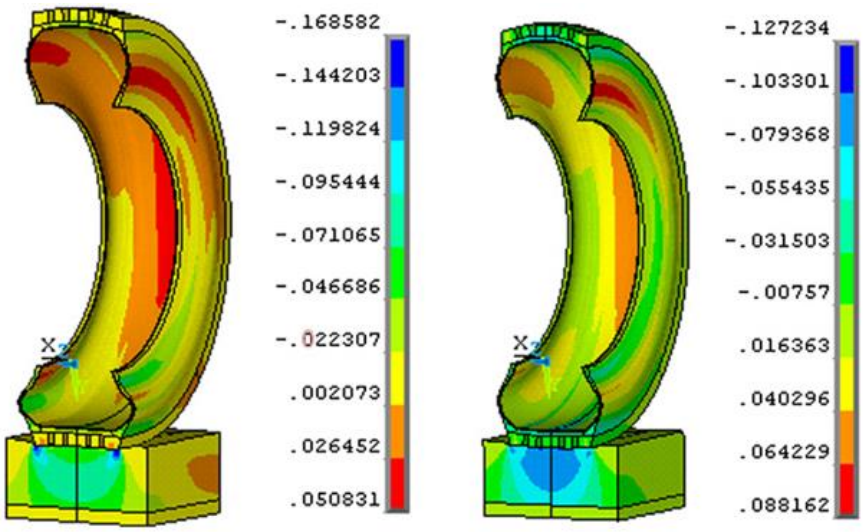

Fig. 2.27: Vertical components of natural strain derived from the FE simulation at the load of 15 kN, inflation pressure of 70 kPa and 150 kPa [95]

Xia [96] applied the modified Drucker-Prager/Cap model (refer to Chapter 5.2.2) to describe the soil plasticity, and incompressible rubber material to model a tire ignoring the tread part in a commercial FEM software-Abaqus, as shown in Fig. 2.28. The influence of the inflation pressure, the wheel load and the travelling velocity on the soil compaction and the tire mobility was investigated.

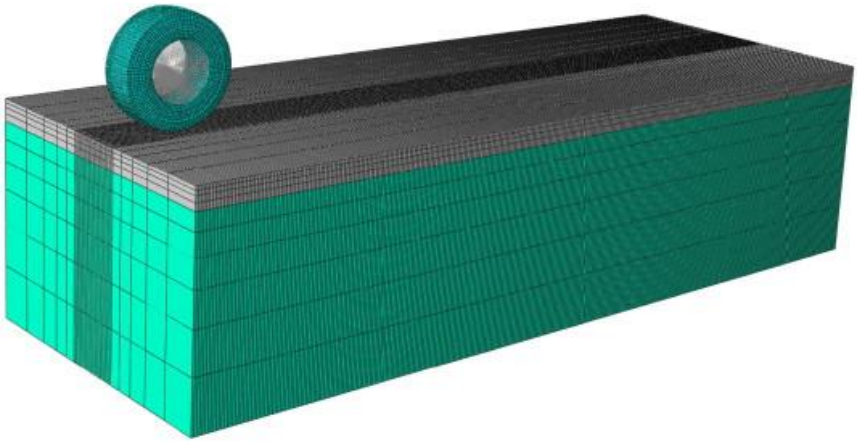

Fig. 2.28: Finite element model of tire-soil interaction [96]

As shown in Fig. 2.29, Biris [97] applied the finite element method to study the influence of the inflation pressure on the tire stress and the strain distribution for a tractor tire. In the 3D tractor tire model, the tire rubber is described by using the hyperelastic model in Ansys.

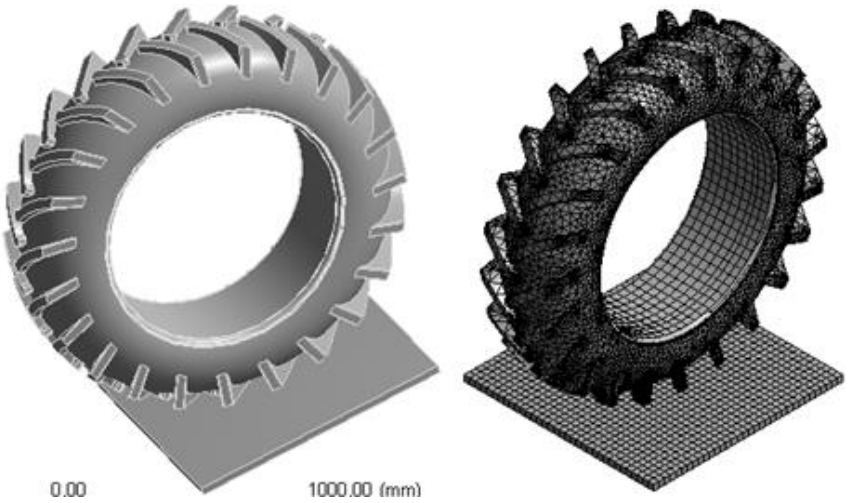

Fig. 2.29: 3D tire model [97]

For solving the problem with the larger deformation occurring in the sand, Pruiksma [98] modeled the sand as a continuum of Eulerian instance and the flexible tire as a Lagrangian instance. The flexible tire-sand interaction model is displayed in Fig. 2.30.

The simulation results of drawbar pull, input torque and tire sinkage were correlated to the slip ratio.

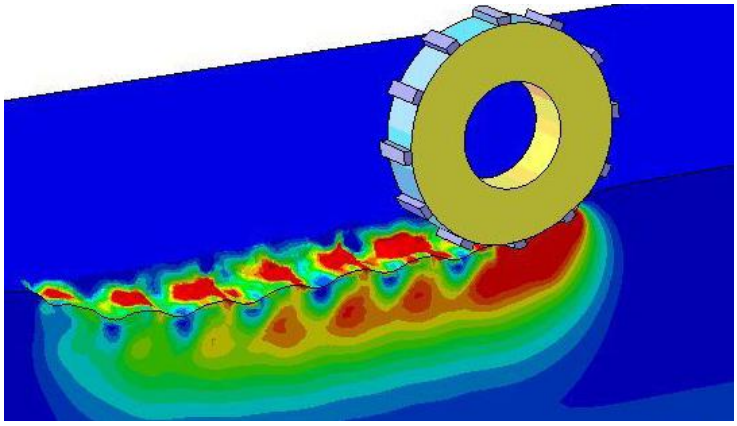

Fig. 2.30: Stress distribution at the flexible tire-sand contact interface [98]

Without considering tread patterns, Lee [99] developed a pneumatic tire model using elastic, viscoelastic and hyperelastic material models and a snow model using the modified Drucker-Prager Cap material model (MDPC). Tire traction, motion resistance, drawbar pull, tire sinkage, tire deflection, snow density, contact pressure and contact shear stresses were linked with longitudinal and lateral slips.

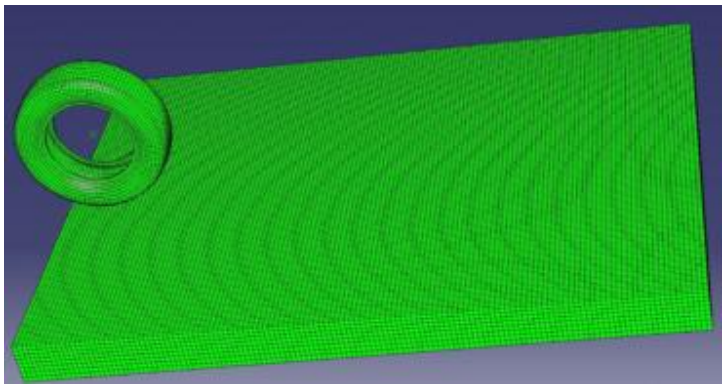

Fig. 2.31: Finite element mesh for tire on snow [99]

Choi [100] investigated the traction and braking performance of an automobile tire on a snow road under the support of the FEM software-MSC/Dytran. The simulation of the tire-snow interaction was carried out through the explicit Euler-Lagrange coupling scheme. Fig. 2.32 displays the snow deformation and the development of the forces generated within the contact patch.

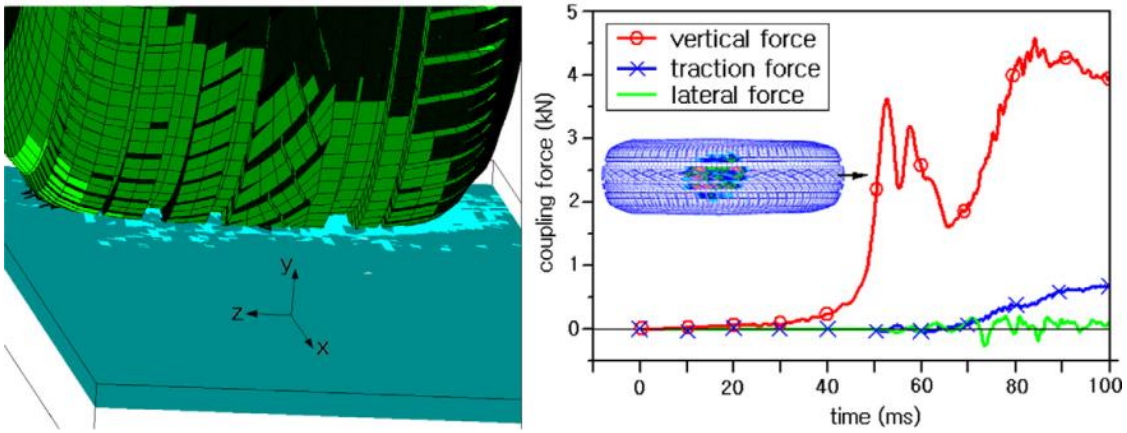

Fig. 2.32: Simulation results for tire-soft snow interaction [100]

2.3.2 Discrete element method and validation

The discrete element method (DEM) is an alternative to the classical continuum mechanics approach for analyzing the mechanics of flow-like solids [101]. The DEM is a promising approach to predict the behavior of discrete assemblies of particles, such as sand. However the foreseeable disadvantage is that enormous computational time is required for the calculation of contact reaction and movement of each particle.

The initial application of the DEM in the tire-soil interaction was presented by Oida [102-104] at the Agricultural System Engineering Laboratory, Kyoto University, Japan. A rigid tire with lugs running over soft soil was analyzed with the DEM as shown in Fig. 2.33.

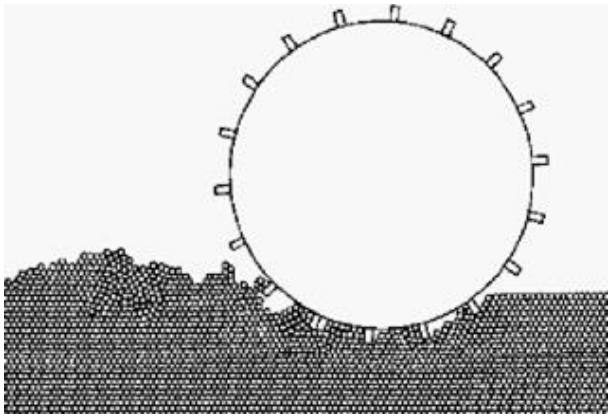

Fig. 2.33: Tire-soil interaction model with DEM [104]

Tanaka et al. [105] decomposed the interaction forces into the normal and tangential directions. As shown in Fig. 2.34, no tension force was defined indicating that the cohesion between each discrete element and the adhesion between the discrete elements and the tire surface were not considered.

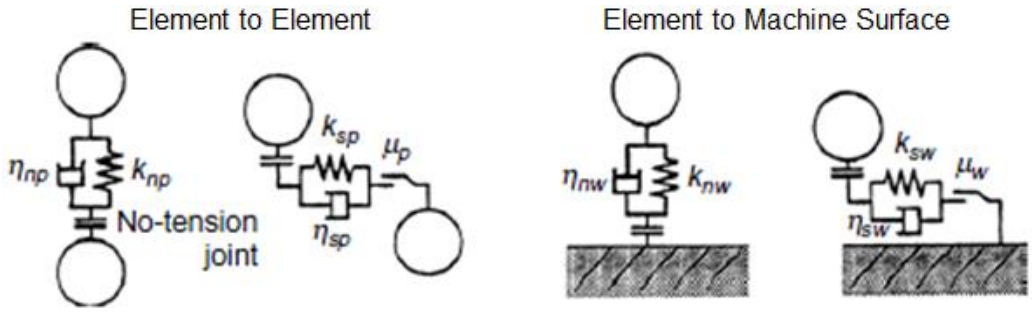

Fig. 2.34: Mechanical interaction model with DEM [105]

Oida and Momozu [106] modified the Tanaka interaction model by introducing a tension spring which represents the soil cohesion. As displayed in Fig. 2.35, the tension force could be calculated when the elements are moving against each other.

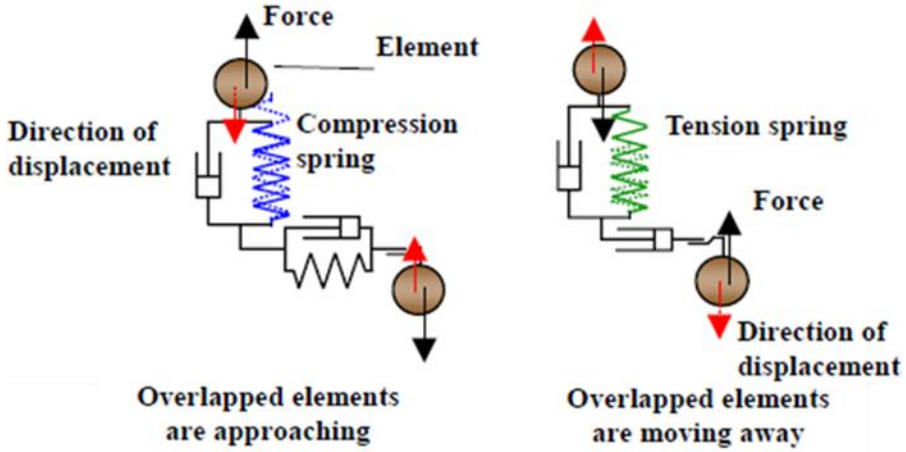

Fig. 2.35: Modified interaction model with DEM [106]

To improve the computational efficiency, Nakashima [107, 108] applied 2D FE elements to model the automobile tire and the bottom soil layer, and DE elements to model the surface soil layer, as shown in Fig. 2.36. The tractive performance of the tires with two different patterns was analyzed by the coupling of FEM and DEM.

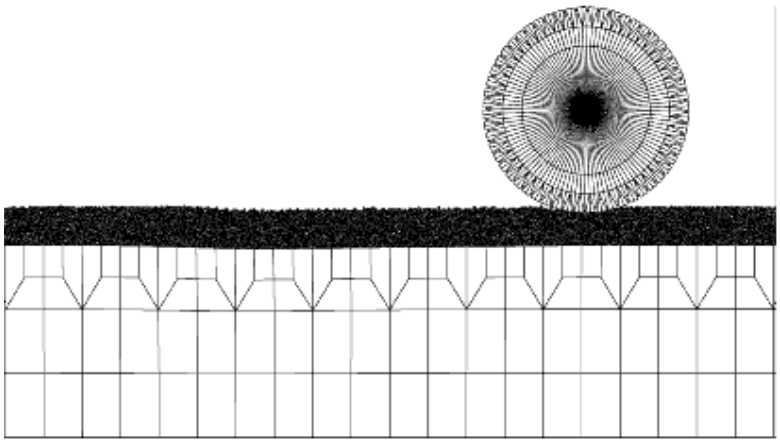

Fig. 2.36: Model of FEM tire and FE-DEM coupled soil [108]

As displayed in see Fig. 2.37, to study the influence of the rigid tire lugs on the tractive performance, the DEM was applied for the contact calculation of soft soil particles by Nakashima [109]. For the comparison of the experimental and simulation results, the test rig designed by Fujii [110] was used to measure the slip and the drawbar pull, as shown in Fig. 2.38.

Fig. 2.37: Rigid lugged tires [109]

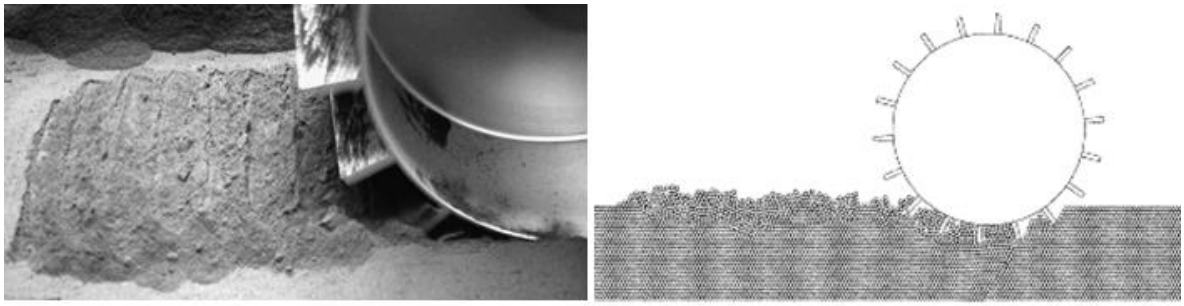

Fig. 2.38: Experimental and simulation results [110]

Khota [111] developed a simulation model using the DEM for the prediction of the deformation of two types of soil at three different vertical loads. The images of the validation experiments captured by video cameras were analyzed and compared with the simulation results. The soil deformations caused by the vertical load of the rigid tire from the simulation and the experiment were displayed in Fig. 2.39.

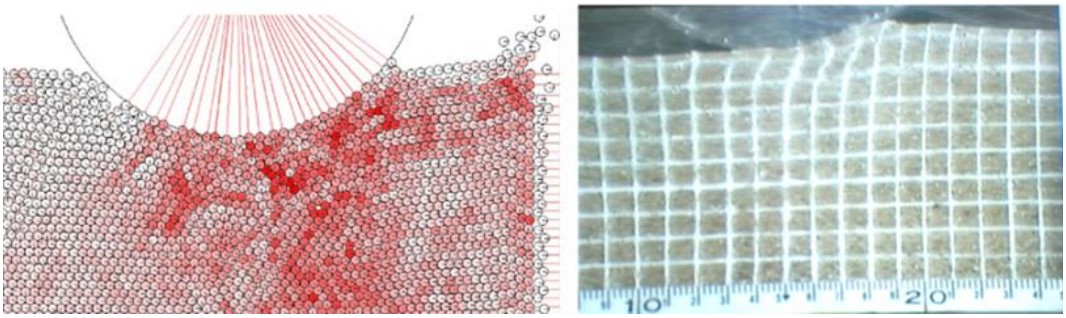

Fig. 2.39: Soil deformation at the vertical load of 14.7 N [111]

Taking into account the environmental gravity, Li [112] examined the rover mobility on the lunar soil at different slips. The electrostatic force, which is a significant non-contact force on the soil particles, was considered in the simulation as well.

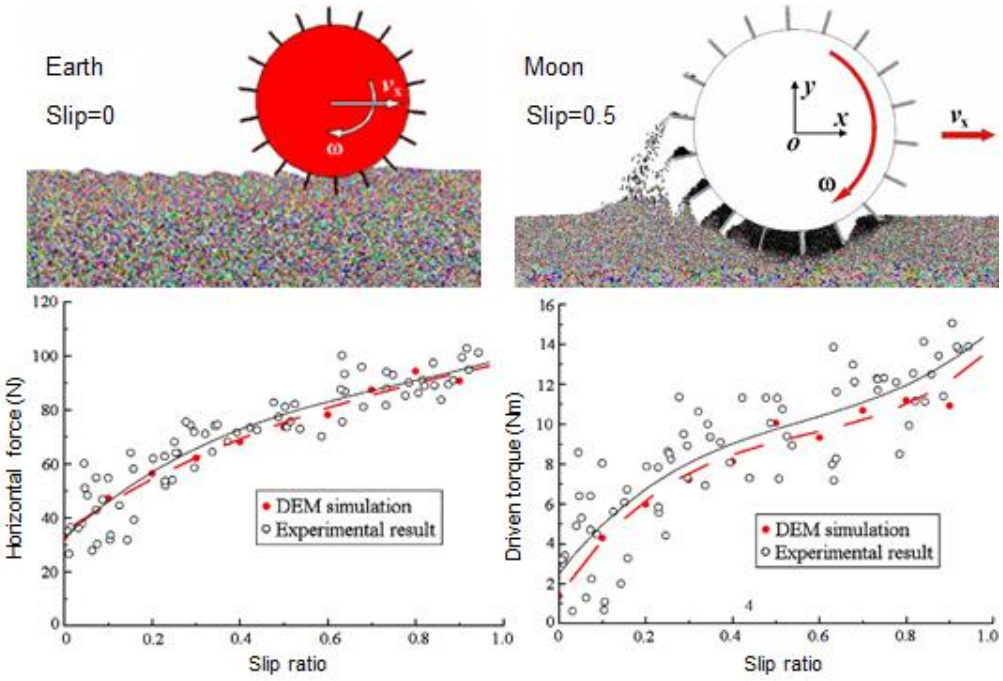

Fig. 2.40: Simulation results at different slips [112]

Knuth [113] analyzed the soil stress/strain to estimate bulk regolith properties and tire propulsion power by performing 3D DEM simulations for the Mars Exploration Rover (MER) mission. These numerical simulations incorporate the unique physical characteristics of the MER rover wheel and enable variation of grain-scale regolith properties such as grain size, shape and inter-particle friction.

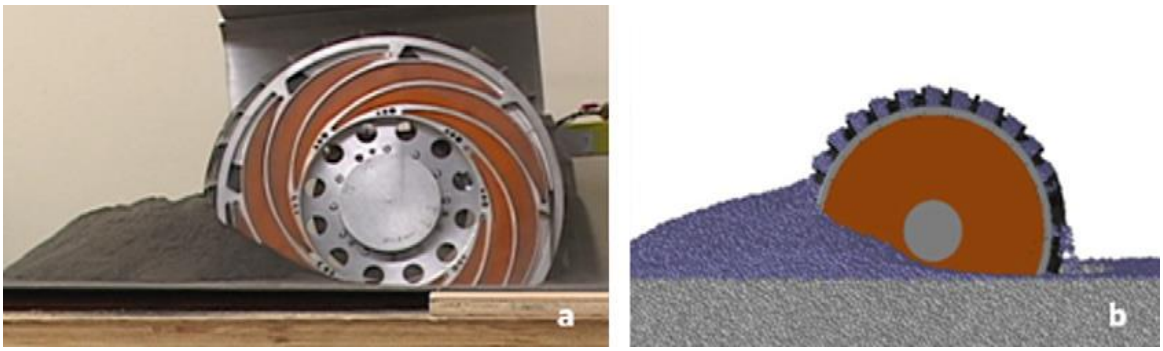

Fig. 2.41: wheel digging test and DEM simulation [113]

2.4 Testing apparatuses for tire-soil interaction

The simulation models developed with different approaches are widely used to predict tire dynamic performance such as drawbar pull, cornering force and rolling

resistance. As classified into indoor testing devices and field testing devices, the specialized testing apparatuses are designed to validate the simulation results and to offer a quantitative insight to the tire-soil interaction. The testing apparatuses mentioned in the chapter 2.3.2 belong to the indoor testing devices.

2.4.1 Indoor testing devices

As shown in Fig. 2.42, a universal loading-test device was designed for measuring the area of the tire-soil interaction interface and the slipping sinkage at the Helmut-Schmidt University, Hamburg [114]. A servo-hydraulic cylinder installed on the frame in the vertical direction was able to offer a maximum force of 660 kN and a maximum extension of 400 mm. A motor mounted on the side was used to rotate the tire and the relationship of slip and tire sinkage could be obtained.

Fig. 2.42: Universal loading-test device [114]

Kawase [115] designed an indoor single wheel tester for the measurement of tire driving torque, drawbar pull and tire sinkage at different slips. The indoor single wheel tester is displayed in Fig. 2.43. Strain gages were attached on the driving shaft to measure the driving torque, and a rotary encoder was used to measure the tire rotational angle. A linear guide, connecting the tire to the single wheel tester carrier, allows the up and down motion of the drive unit. Installed between the driving unit and the linear guide, an extended octagonal ring transducer was used to measure the drawbar pull. Another device with a tiller mounted in the front and a motor-driven roller mounted in the rear was applied for the soil preparation. The device was pulled along rails through a steel wire driven by an electric motor at a constant speed. The inner dimensions of the soil bin were 3015 mm (length), 480 mm (width) and 605 mm (depth).

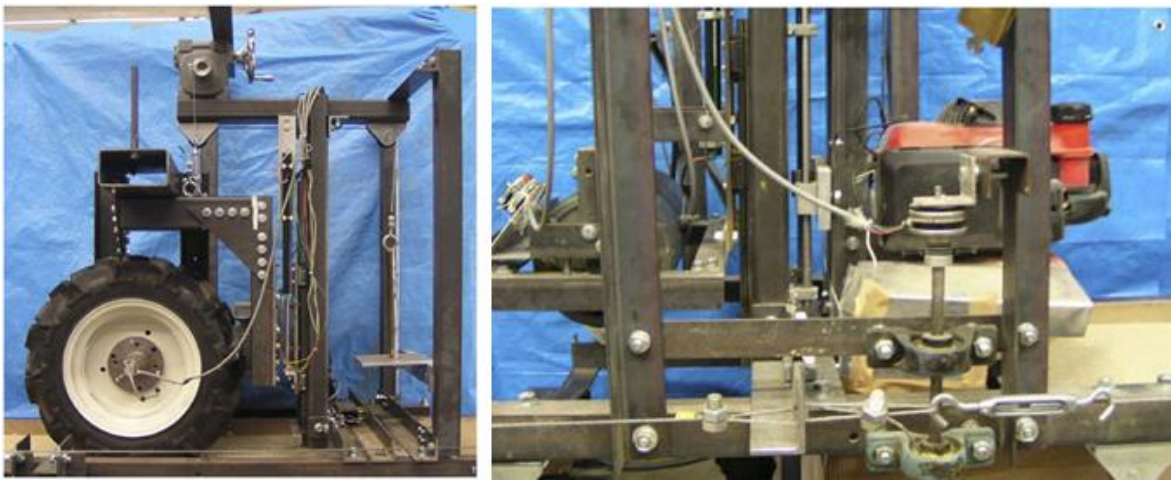

Fig. 2.43: Single wheel tester and a device for soil preparation [115]

Another indoor tire traction testing facility was designed and developed at University Putra, Malaysia, to study the interaction between high-lug agricultural tires and tropical soils [116]. Two sets of tests could be carried out: towing test to measure the tire motion resistance and driving test to measure the tire net traction and tractive efficiency.

Tiwari [117] designed a tire traction testing facility which was comprised of an indoor soil bin, a single wheel tester, a soil processing trolley, a drawbar pull loading device and an instrument unit. This device was capable of testing tires up to 1.5 m in diameter, of providing the vertical load up to 19 kN, the net pull up to 7.2 kN, the torque up to 5.5 kN m and the speed up to 3.5 km/h.

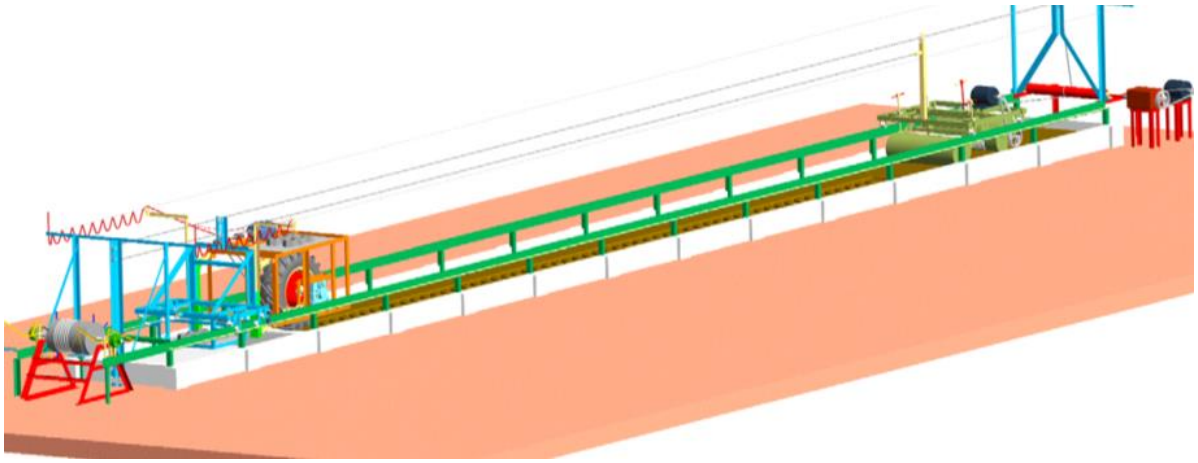

Fig. 2.44: General view of the tire traction testing facility [117]

A test-bed, which contains three motors (driving motor, steering motor and carriage motor), a displacement sensor, six-axis F/T sensors, a driving torque sensor, current sensors and optical encoders, was developed at the Chinese State Key Laboratory of Robotics and System, Harbin Institute of Technology [118]. The driving motor propels

the wheel to move forward. The carriage motor together with a conveyance belt is used to create various slip ratios. The steering motor provides the opportunities to generate various slip angles. A high-precision linear-potentiometer displacement sensor was used to measure the wheel sinkage. The F/T sensors were applied to measure the forces and moments in different directions. The current sensors and optimal encoders were used to measure the current and wheel angular position.

Fig. 2.45: Wheel-soil interaction test-bed [118]

To measure the soil deformation and stress caused by external forces, a measuring system comprised of a stress state transducer (SST) and an optical system was developed at Institute of Agrophysics, Poland [119]. As displayed in Fig. 2.46, the SST comprised of six strain gauge type pressure sensors was used to determine the soil stress state. The six transducers are oriented to measure pressures which can be transformed to the mean stresses and the octahedral shear stresses. The optical system comprised of laser projectors, a shield and a video camera was attached to the SST and mounted to the side wall of the frame. When the investigated soil is loaded and deforms, the movements of the SST and the soil surface are projected on the shield and the images are recorded by the charge-couple device (CCD) monochromatic camera. With this measuring system, soil deformations in the vertical and longitudinal directions as well as soil stress state components can be determined.

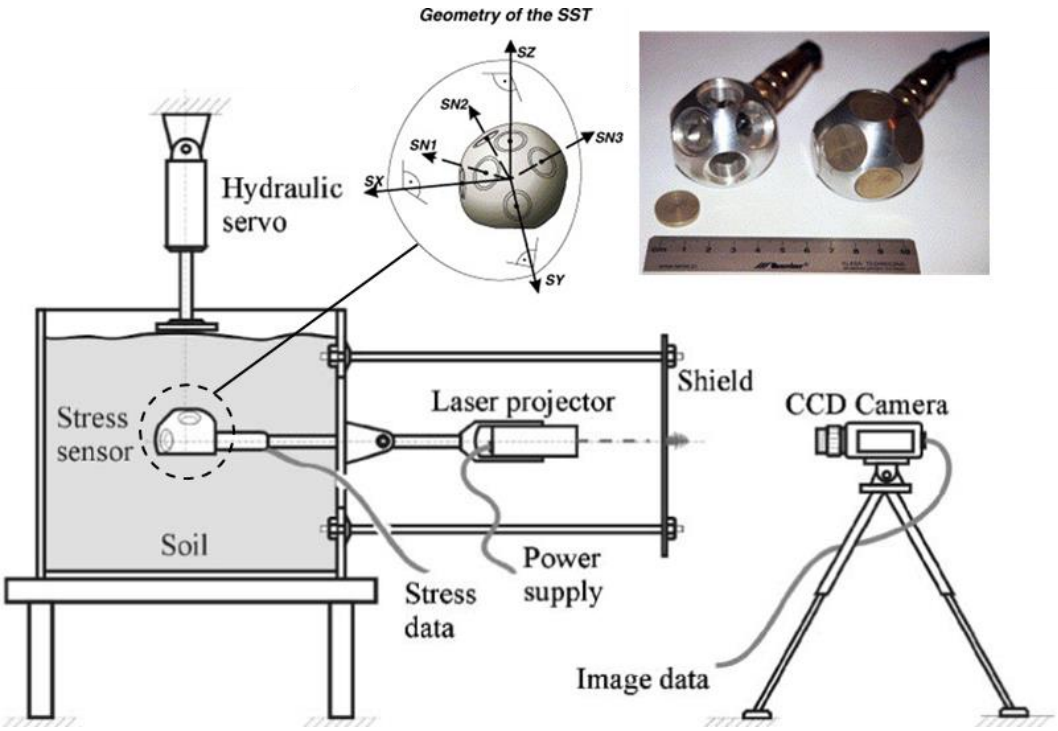

Fig. 2.46 A schematic view of a system to measure soil deformation and stress [119]

2.4.2 Field testing devices

Based on an agricultural tractor, Billington [120] developed a single wheel tester at the National Institute of Agricultural Engineering, Silsoe, Switzerland. The device was hydrostatically controlled and mounted to the tractor through a parallel linkage. A load cell which was free to move in the horizontal direction was placed in front of a carriage to measure the net tractive effort. To supply dynamic wheel loads, weights were added to a rack above the wheel. The maximum wheel load was 2721 kg (6000 lbs), and the maximum torque was 21,964 Nm (16,200 ft-lb). The primary objective of this tester was to explore the relationship between ply rating and tire performance, as well as the performance evaluation of the tires running on variable soils.

As shown in Fig. 2.47, another single-wheel traction testing device was developed to measure the traction performance by Upadhyaya [121] at the department of Agricultural engineering, UC Davis, USA. The tires in the diameter ranging from 18 inches (0.46 m) to 79 inches (2 m) and width up to a maximum of 39 inches (1 m) could be tested with this device. The device could provide a variable vertical load up to a maximum of 6,000 pounds (26.7 kN) and a traction force up to a maximum of 3,000 pounds (13.3 kN).

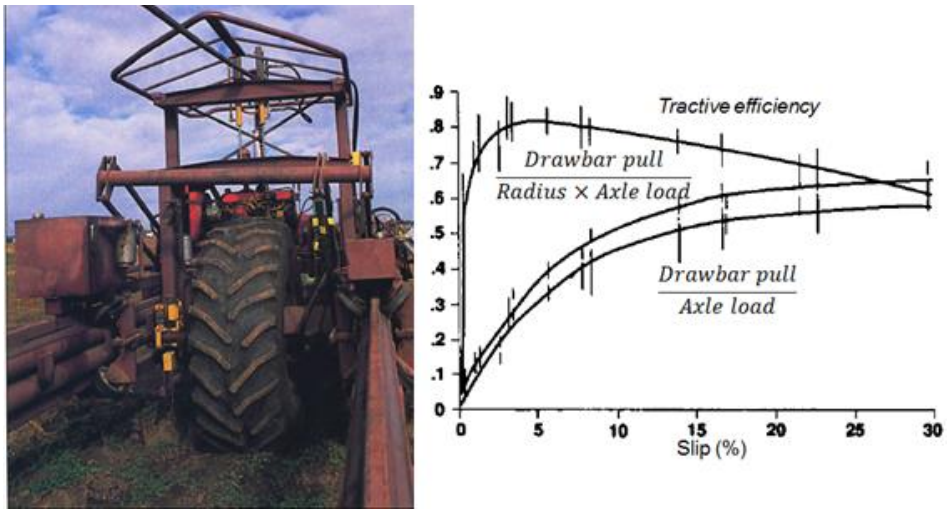

Fig. 2.47: Single-wheel traction testing device [121]

At Institute of Agricultural Engineering, University of Hohenheim, Germany, a single wheel tester designed by Armbruster [122, 123] was able to provide a maximum slip angel of 16°. As displayed in Fig. 2.48, the tested tire mounted on the yellow frame could be either accelerated or braked via a hydraulic system. A 6-component-dynamometer was used to measure the forces and moments on the tested tire. Morhard [124] developed a mobile test rig for the study of grass field and soil protection as shown in Fig. 2.49. Connected to a tractor, the mobile test rig is capable of carrying of the tires in the diameter up to 900 mm and in the width up to 500 mm. A maximum driving torque of 400 Nm and tire load of 5.3 kN could be offered via a hydraulic system. The slip angel ranging from 0 to 40° could be generated via a hydraulic cylinder. The forces and moments acting on the tire could be measured by a 6-componet force sensor. The difference between the tested tire and the reference tire was calculated for the measurement of the slip in the longitudinal direction.

Fig. 2.48: Single wheel tester [122]

Fig. 2.49: Mobile test rig mounted on the tractor [124]

As shown in Fig. 2.50, Nagaoka [125] designed and built a single wheel tester in Brazil which was powered by an agricultural tractor via the power take-off (PTO). A mechanical transmission is used to realize the wheel speed variation along with the engine speed. The mechanical transmission is supplied with 24 speed options up to 540 rpm, and the tire was powered by a tractor rear differential axle. The tester can provide enough space for tires up to 2 m in diameter and 1 m in width. The dynamic wheel load was supplied by using cast iron weights placed on either side of the wheel. To measure the net tractive effort data, a load cell was placed between the inner frame and the outer frame. Several tests were conducted for various tire pressures and soil conditions. The acquired data were utilized for the evaluation of the tractive performance.

Fig. 2.50: Single wheel tester with mechanical transmission [125]

Various designs of the test rig for traction and soil compaction research have been developed at the National Soil Dynamics Laboratory (NSDL) in Auburn, USA. A single-wheel tester designed by Grill and Vanden Berg [125] was applied to measure the drawbar pull of tires through a wide range of wheel slips. Burt [127] redesigned the single wheel tester using the hydraulic system for propulsion. The modified single wheel tester was used to collect tractive performance data.

Way [128] introduced three different single wheel testing machines for traction and soil compaction research at the National Soil Dynamics Laboratory (NSDL) in Auburn, USA. The Traction Research Vehicle is displayed in Fig. 2.51. Electro-hydraulic control is applied to manage forward ground speed, wheel speed, and dynamic wheel load, via a hydraulically powered superstructure and a load cylinder mounted above the tire testing carriage. This device is designed for two operating modes: a) constant slip ratio and b) constant dynamic wheel load. The constant slip ratio can be managed via precisely controlling the wheel speed and the ground speed. The constant dynamic load can be managed via a hydraulic cylinder, and a load cell is coupled to the hydraulic cylinder to measure the dynamic load. The net traction and the torque reaction are measured via the load cells linking the independent carriage to the superstructure. The ability to control wheel speed, ground speed, and dynamic wheel load allows precise control of the independent variables which determines tractive performance.

Fig. 2.51: Single wheel Traction Research Vehicle [128]

The All-Terrain Vehicle tire tester was designed to measure the traction and the motion resistance of all-terrain vehicle (ATV) tires. This device is capable of testing tires in the diameter up to 690 mm and the width up to 280 mm. A maximum dynamic load of 2.7 kN could be offered, and no slip angle could be generated.

Fig. 2.52: All-Terrain Vehicle tire tester [128]

Monroe and Burt [129] developed the NSDL Wide Frame Tractive Vehicle (WFTV) for controlled-traffic research. The WFTV, a heavy and powerful machine that spans a 6 m wide field lane, was mounted to the vehicle working as a mobile platform. The diameter of the largest tire which could be mounted on the machine is 2180 mm. A hydraulic cylinder positioned above the tire center was applied to adjust the vertical load. The forces and moments on the tested tire were measured by load cells and torque transducers.

Fig. 2.53: Wide Frame Tractive Vehicle [129]

3 Motivation

Ranging from entirely empirical to highly numerical, a variety of approaches to model the tire-soil interaction have been developed over the last century. Before recognizing the tire and soil characteristics and the mechanism of the tire-soil interaction, lots of field tests to measure soil properties and tire mobility were carried out and empirical methods were well developed to model the tire-soil interaction. With the development of the discipline of terramechanics, the physical nature of tires and soils were better understood and analytical methods were applied to model the tire-soil interaction by taking into account major tire and soil mechanical characteristics such as tire stiffness, pressure-sinkage and shear stress-displacement relationships. Recently with rapid progress in computation capacity and efficiency as well as the development of computation programs, numerical methods have been introduced to analyze the tire-soil interaction.

Empirical models of the tire-soil interaction can be employed to study vehicle mobility and soil trafficability. Based on the results of tire performance and soil characteristics, simple numerics can be derived for the evaluation of those characteristics. This method is feasible to predict the performance of tires similar to those which have been tested under similar operating conditions. To evaluate new tire designs or to estimate the tire performance in new operating conditions is not feasible with empirical methods.

Analytical methods are developed based on the understanding of the mechanics of the tire-soil interaction and on the principles of Terramechanics. If verified by field tests, this method is capable of evaluating the tire performance on various soils. The fundamental features of the analytical method are the pressure-sinkage and the shear stress-displacement relationships. With the model based on these methods, the forces and the moments generated on the contact interface can be calculated.

Numerical methods such as the finite element method (FEM) or the discrete element method (DEM) can be applied to evaluate the tire performance or the soil compaction. The computation with these methods generally involves a large amount of finite or discrete elements in order to obtain accurate simulation results. Experimental data have to be observed in qualitative agreement with predictions of the tire performance obtained from numerical methods. The stress development inside the contact interface can be studied with the models based on these methods.

Concluded from the state of the art, the following aspects are necessary to be outlined for the further research in the field of tire-soil interaction:

1. The analytical tire-soil interaction models apply the classic terramechanics theory of Bekker and Wong to describe the normal and tangential stresses. The model of the normal stress is well established based on the data obtained from quasi-static experiments, therefore the effect of sinking velocity on the normal stress is not considered. By carrying out penetration experiments with a penetrometer in the test field, it is observed that the sinking velocity has a large influence on the normal resistance of soil [131].
2. The traditional bevameter enables to carry out quasi-static tests for the measurement of the parameters in the Bekker's pressure-sinkage model. To measure the effect of the sinking velocity on the normal resistance of soil, other approaches are required to be proposed.
3. Sufficient data about the tire handling performance on stiff road have been obtained by carrying out lots of experiments and simulations. Referring to the tire response to the driver demands such as steering, accelerating and braking, investigations of the handling performance presented by the slip ratio – longitudinal force, slip angle – lateral force and anti-aligning torque and combined slip plots are still in demand for the tire when rolling on the soil.
4. For the study of the tire – rigid road interaction, the curves of the tire handling performance are analyzed with non-linear regressions and the correlations of each parameter, such as slip ratio, wheel load and longitudinal force, are described by sophisticated functions. However for the study of the tire-soil interaction, such correlations are seldom analyzed and hardly described.
5. Although lots of effects have been put in the finite element analysis of the tire, accurate tire models are still in demand. Due to the complex geometry of the tread structure and the reinforcement layers, it is difficult to establish a precise finite element (FE) tire model. Frequently the tread patterns are neglected or replaced by straight ribbed treads, and the reinforcement layers are simplified by rigid or elastic rings. Such simplified models are not accurate enough to predict the tire performance and can lead to errors in solving the contact problem [150].
6. To validate an FE tire-soil interaction model, it is common that stress state transducers are applied and planted in the soil, and the measured stress data is

compared with that from simulations. However the tire-soil contact area can be so large that lots of stress transducers are required in order to precisely capture the stress distribution in the soil. Therefore better validation approaches are necessary to be proposed.

Concluded from the previous paragraphs, it is obvious that a lot of issues are open to contribute to the modeling of tire-soil interaction and the model validation. To help to solve the problems mentioned above, the proposals in this dissertation are addressed as follows:

1. The effect of the sinking velocity on the normal resistance of soil is recognized as soil damping effect. An analytical model will be elaborated based on the principles of terramechanics. As an improvement to the analytical models introduced in the state of the art, this model taking into account the soil damping effect will be integrated into a MBS program. With the analytical model, simulations with and without the soil damping effect will be performed to demonstrate the improvement of the expanded model. More simulations will be carried out to study the tire handling performance on the soil at the operating conditions such as pure longitudinal slipping, pure cornering and combine slip. The simulation results could be used to determine the correlations of slip ratio, wheel load, longitudinal and lateral forces. The functions of the Magic Formula tire model will be applied to fit the tire handling curves for the establishment of a simplified tire-soil interaction model to be used in MBS simulations. The coefficients of the functions can be estimated through non-linear regressions.
2. As an improvement to the FE models introduced in the state of the art, a FE tire model will be developed by considering the tread structure and the reinforcement layers based on the measured geometry data. The reinforcement layers comprised of rubber-cord composites will be modeled as shell elements, the fiber cords will be modeled as rebar elements embedded in the reinforcement layers. The finite element tire model needs to be validated by comparing the simulation and experimental results.
3. As an improvement to the model validation introduced in the state of the art, the soil plastic deformations obtained from simulations and experiments will be compared instead of comparing the soil stress distribution. By applying a 3D camera, the geometric data of the tire footprints can be measured and exported to Matlab for the evaluation of the soil plastic deformation.

4. Simulations which are similar to the experiments performed by the bevameter will be carried out for the identification of the parameters in the analytical tire-soil interaction model. Several constant sinking velocities will be defined in the simulations to study their effects on the soil normal resistance.

This dissertation is aimed to provide relatively accurate analytical and FE models of the tire-soil interaction, to verify and validate the simulation models, to study tire behaviors and soil compactions under different operating conditions and to provide reliable models for the further simulation of the vehicle-soil interaction.

As displayed in Fig. 3.1, the FE model of the tire-soil interaction will be validated through field tests; simulations with the analytical and FE models will be implemented in the MBS and FEM software; simulation results obtained from these two models will be compared; an empirical Magic Formula tire model will be established by fitting the curves of the simulation results and this empirical tire model can be integrated into the MBS software for the storage of simulation results as look-up tables and further be applied in the vehicle-soil simulation. The main advantages of the application of the empirical tire model in the MBS software are that the computational efficiency is high and the accuracy of simulation results is in an acceptable range.

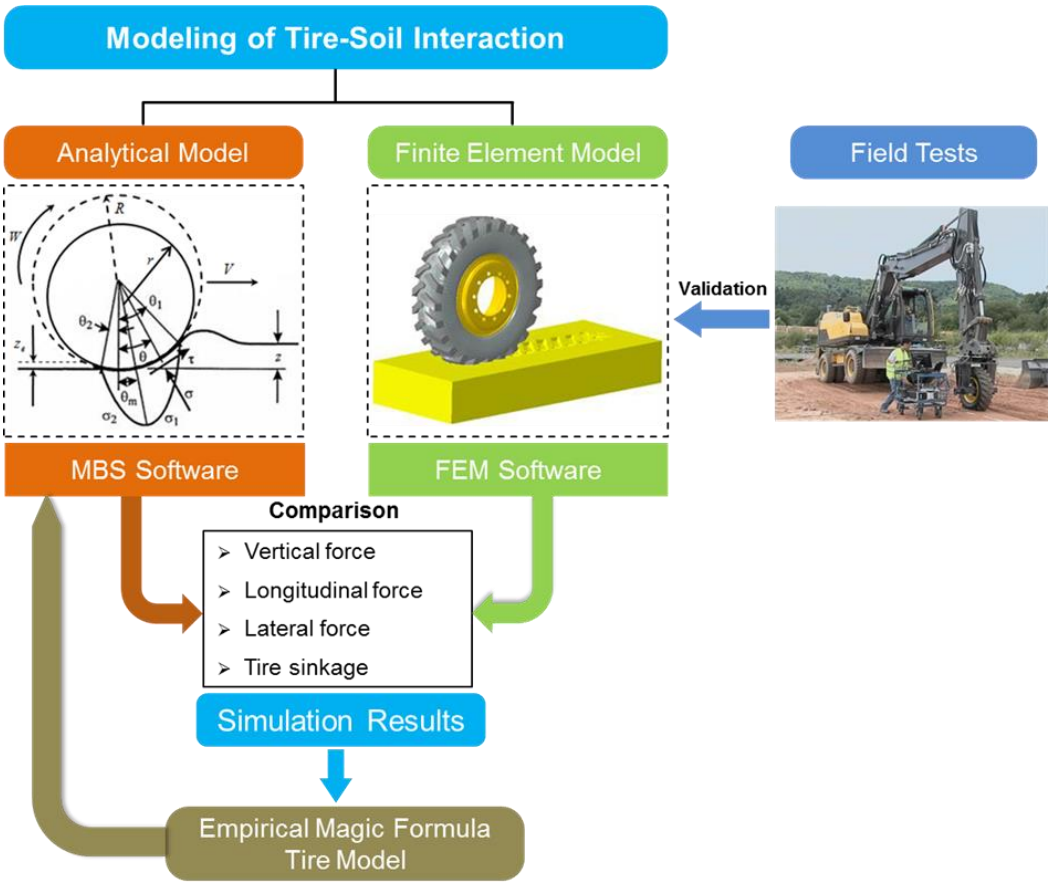

Fig. 3.1 The flowchart of the modeling of tire-soil interaction

Chapter 4 introduces the modeling of tire-soil interaction with the analytical method. This analytical model includes non-linear spring-damper-elements to account for the normal stress developed in the tire-soil contact interface. This model is able to capture the tire quasi-static and transient dynamic behaviors under pure longitudinal slipping, pure cornering and combined slipping conditions.

Chapter 5 discusses the development of the FE tire-soil interaction model, the selection of appropriate material models as well as the loading and boundary definitions in detail. From simulations performed with this model, the insight to the stress and strain development inside the contact interface can be provided.

Chapter 6 presents the structure of a single wheel tester for the outdoor tests, the devices for measuring the forces, tire and soil deformations. In this chapter the identification of the FE soil models is introduced, and the simulation and experimental results are compared as well.

Chapter 7 focuses on identifying parameters of the analytical soil with FEM simulations. The comparison of analytical and FE simulation results of tire-soil interaction is demonstrated as well.

Chapter 8 presents short summaries of this dissertation and recommendations for future studies.

4 Tire-Soil Interaction Modeling with Analytical Method

As mentioned in chapter 2, the state of the art analytical tire-soil interaction models were developed by applying the pressure-sinkage and shear stress displacement relationships. Quasi-static experiments were carried out for determining the parameters in these two relationships through the bevameter, however the penetrating rate of the sinkage plate was not considered. The mechanical behavior of soils, such as soil strength, is influenced by the rate of soil deformation [130-133]. Hence the tire penetrating rate is of great importance to the stress underneath the tire. To accurately study the tire transient behavior, in this work new analytical tire-soil interaction models were established in the MBS software Adams. The equations in the new models were integrated as subroutines in the Adams/Tire module.

4.1 Introduction of the KIMA tire-soil interaction models

Under the condition when the tire is relatively soft and the soil is relatively firm, Wong [69] assumed the shape of the tire-soil interface to be flat. When the deformable tire runs over relatively soft soil, the assumption of a flat contact contour is not acceptable according to the measured deformation shape [134-135]. To realize the mathematic description of the contact contour, a substitute circle in the radius R which is larger than the tire unloaded radius r was adopted to mimic the tire deformation geometry by Schmid [70]. The approximation was proved to be proper in the analysis of deformable tire-relative soft soil interaction. Since the soil deformation is rather limited compared to the tire diameter, the bulldozing effect is not considered in the model. The stresses within the tire-soil interaction interface are divided into the radial and tangential directions, as shown in Fig. 4.1.

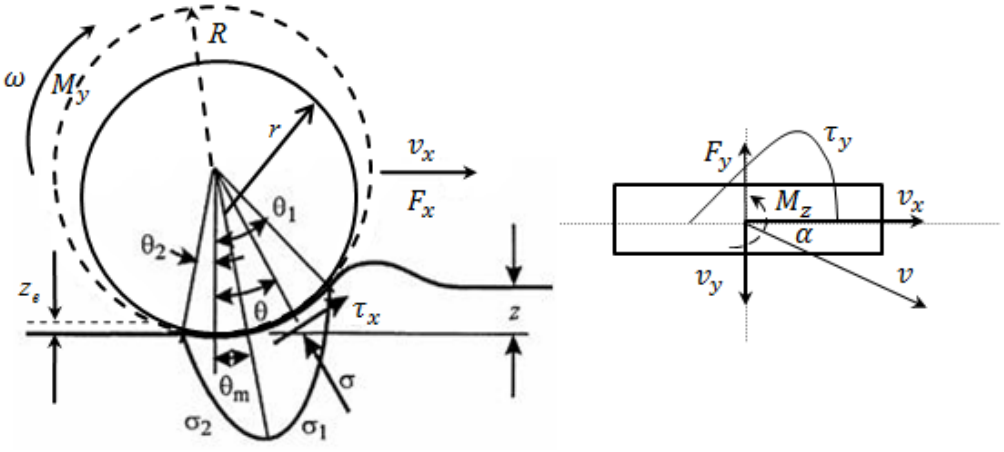

Fig. 4.1: Stress distribution on the tire-soil interface

As an improvement to the analytical models introduced in the state of the art, a new item σ_d described in Eq. (4.3) accounts for the influence of the penetrating rate on the radial stress and the radius R of the substitute circle was used to calculate the tire sinkage. These two parameters were introduced to the equations describing the pressure-sinkage relationship. By replacing the tire unloaded radius r with the substitute circle radius R in Eq. (2.25), (2.26) and (2.27), the radial stress at an arbitrary contact point is determined by the following equations.

$$\sigma_1(\theta)=\left(\frac{k_c}{b_t}+k_\phi\right)\left(R(\cos\theta-\cos\theta_1)\right)^n \tag{4.1}$$

$$\sigma_2(\theta)=\left(\frac{k_c}{b_t}+k_\phi\right)\left(R\left(\cos\left(\theta_1-(\theta_1-\theta_m)\left(\frac{\theta-\theta_2}{\theta_m-\theta_2}\right)\right)-\cos\theta_1\right)\right)^n \tag{4.2}$$

$$\sigma_d(\theta)=c_s v_r(\theta)/b_t l_{con} \tag{4.3}$$

$$\sigma_T(\theta)=\begin{cases}\sigma_1(\theta)+\sigma_d(\theta) & (\theta_m<\theta\le\theta_1)\\ \sigma_2(\theta)+\sigma_d(\theta) & (\theta_2\le\theta\le\theta_m)\end{cases} \tag{4.4}$$

$$\theta_1=\cos^{-1}\left(1-\frac{z}{R}\right) \tag{4.5}$$

$$\theta_2=\cos^{-1}\left(1-\frac{k_r z}{R}\right) \tag{4.6}$$

Where

c_s soil damping coefficient σ_T radial stress

v_r penetrating rate in the radial direction

l_{con} length of the tire-soil contact interface

Deriving from the work of Yoshida and Ishigami [64], the shear stresses in the longitudinal and lateral directions are displayed in the following equations.

$$j_x(\theta)=\int_\theta^{\theta_1} R[1-(1-i)\cos\theta]d\theta=R[(\theta_1-\theta)-(1-i)(\sin\theta_1-\sin\theta)] \tag{4.7}$$

$$j_y(\theta)=\int_\theta^{\theta_1} R(1-i)\tan\alpha d\theta=R(1-i)(\theta_1-\theta)\tan\alpha \tag{4.8}$$

$$\tau_x(\theta) = [c + \sigma_T(\theta)\tan\phi]\left(1 - e^{-j_x(\theta)/K_x}\right) \tag{4.9}$$

$$\tau_y(\theta) = [c + \sigma_T(\theta)\tan\phi]\left(1 - e^{-j_y(\theta)/K_y}\right) \tag{4.10}$$

For the derivation of the drawbar pull and the vertical force, the components of the radial and shear stresses in the longitudinal (x axis) and vertical directions (z axis) were integrated respectively from the entry angle to the exit angle.

$$F_x = b_t R \int_{\theta_2}^{\theta_1} (\tau_x(\theta)\cos\theta - \sigma_T(\theta)\sin\theta) d\theta \tag{4.11}$$

$$F_z = b_t R \int_{\theta_2}^{\theta_1} (\tau_x(\theta)\sin\theta + \sigma_T(\theta)\cos\theta) d\theta \tag{4.12}$$

For the derivation of the lateral force and the aligning torque, the stress was integrated in the lateral direction (y axis). On the tire-hard ground interface, the pneumatic trail is behind the tire central line indicating that the self-aligning torque generated by the lateral shear stress potentially decrease the slip angle. On the tire-soil interface the lateral shear stress is larger in front of the tire central line, and the pneumatic trail is in the front indicating that the anti-aligning torque potentially increases the slip angle.

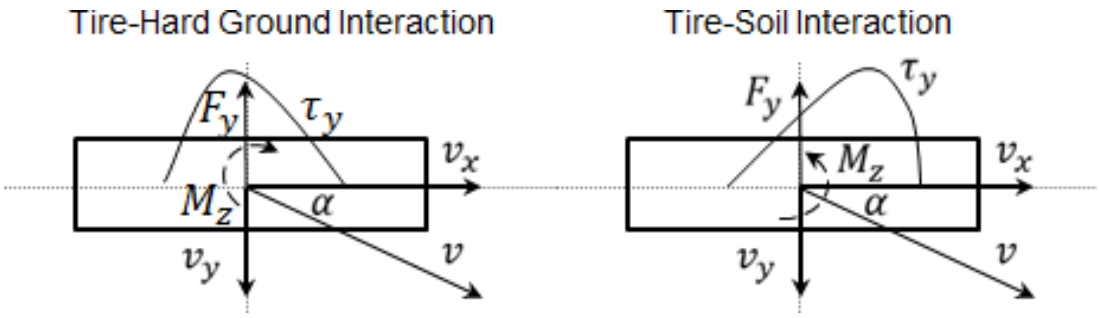

Fig. 4.2: Torque developed on the tire-hard ground/soil interface

For the prediction of the motion resistance, the equations proposed by Bekker [17] were applied.

$$F_y = \int_{\theta_2}^{\theta_1} b_t R \tau_y(\theta) d\theta \tag{4.13}$$

$$M_z = b_t R^2 \int_{\theta_2}^{\theta_1} \tau_y(\theta)\sin\theta d\theta \tag{4.14}$$

$$M_y = b_t R^2 \int_{\theta_2}^{\theta_1} \tau_x(\theta) d\theta \tag{4.15}$$

$$R_c = bR^2 \int_{\theta_2}^{\theta_1} \sigma_T(\theta) \sin\theta d\theta \tag{4.16}$$

Schmid [70] proposed the following equations for determining the radius of the parabolic shape of the contact contour.

$$F_z = K_t \delta + D_t v_t \tag{4.17}$$

$$\sqrt{R/r} = \sqrt{1+\delta/z} + \sqrt{\delta/z} \tag{4.18}$$

It should be noticed that for the modeling of rigid tire – soil interaction, the radius *R* of the parabolic shape equals to that of the rigid tire.

4.2 Subroutines integrated in Adams/Tire

The simulation of the dynamic behavior and the motion analysis of multibody systems can be well performed with multibody simulation software such as Adams. This software enables users to create interactive parts, analyze the distribution of loads and forces throughout mechanical systems, and optimize their performance. The modules incorporated in Adams provide the potentials to solve the problems in specialized fields, such as car dynamics, chassis vibration and engine design. To analyze the mechanical characteristics of the tire-soil interaction, the Adams/Tire module is used.

Adams/Tire is a set of shared object libraries that Adams/Solver can call through different subroutines. These subroutines calculate the forces and moments with respect to the interaction between the tire and the road surface. The tire models can be customized in Adams/Tire by varying the tire properties, such as mass, moments of inertia, stiffness and damping coefficient. By reading the tire property file, the simulation proceeds with Adams/Tire where Adams/Solver automatically selects the default solver or the user-defined solver. The simulation results such as vertical force and displacement, tire velocity and acceleration, can be viewed and processed in Adams/Postprocessor. The procedure how the Adams/Tire module works is described in Fig. 4.3.

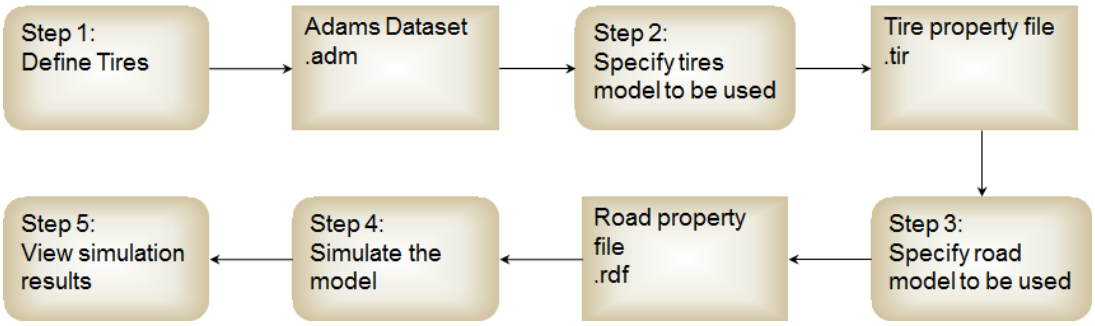

Fig. 4.3: Structure of Adams/Tire working steps

Before the simulation is carried out, Adams/Solver obtains the names of the tire property file and the road property file from the string definition. Tire Object Manager examines the tire and the road property file to determine which tire and road model should be used. The tire and road model is created by reading the tire and road property file to obtain data for calculating tire forces and moments, and then the road model is called to evaluate where the road is relative to the tire. The tire model returns the forces and moments to Adams/Solver. Adams/Solver applies the forces and moments to the wheel part. The process how Adams/Solver and Adams/Tire interactively work is described in Fig. 4.4.

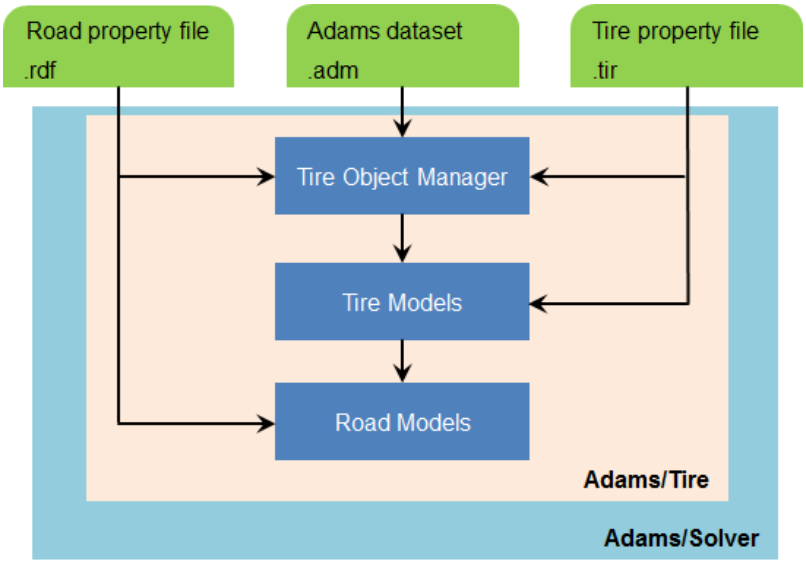

Fig. 4.4: Information flow in Adams/Tire [75]

With the integrated tire and road models, it's only possible to analyze the mechanical characteristics of the tire – rigid road interaction. However Adams/Tire provides an interface to use user-defined tire and road models. For this dissertation two subroutines under the name of TYRSUB and ARCSUB in the user-defined tire and road models were created to extend the capability of Adams/Tire. The equations in section 4.1 describing the analytical model of the rigid/deformable tire – soil

interaction were integrated into the user-defined subroutines. The process how the tire-soil interaction subroutines are executed in Adams is described in Fig. 4.5. After the simulation starts, the property files including the parameters of the tire and soil models are imported as inputs for the next following calculation steps. In the first phase a state-vector at the next time-step is initially estimated. In the second phase the cost function evaluates the set of equations describing constraints (reaction forces and moments), applied forces, and user written differential equations for positions and velocities. The correct value is found by using a modified Newton-Raphson algorithm to minimize the output of the cost function. If the corrector fails in obtaining a corrected value within allowed maximum attempts, the solver returns to the first phase to attempt with a new time-step. In the third phase the difference between the predicted state vector and the corrected state vector is checked. If this difference (error) is within the error requirement, the corrected state vector is accepted. If the corrected state vector fails to comply with the ERROR requirement, the solver returns to the first phase to attempt once again with a smaller time increment.

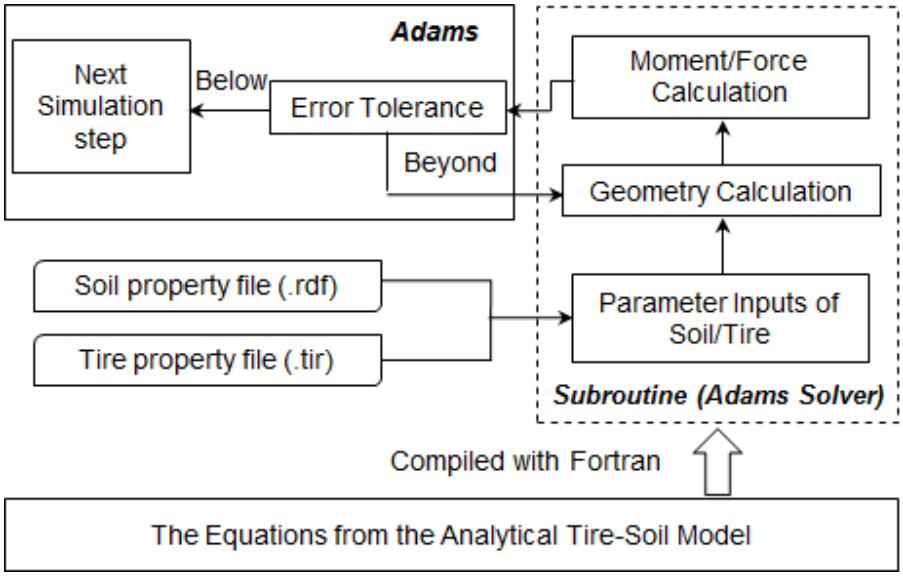

Fig. 4.5: Flow chart of the subroutine integrated in Adams

4.3 Simulations performed with Adams

As an example of a typical off-road tire, a bias tire in Fig. 4.6, which is specified with the mark of Bridgestone 10.00-20 and mounted on a Volvo excavator (EW 180B), is studied in this dissertation. As listed in Table 4.1, the parameters measured for the inflation pressure of 700 kPa at Volvo Construction Equipment Konz, are defined in the tire property file for the simulation initialization.

Fig. 4.6: Bridgestone 10.00-20 tire

Table 4.1: Tire parameters defined in the tire property file

Unloaded radius r [m]		Vertical stiffness K_t [kN/m]	Width b_t [m]
0.531		1050	0.28
Moment inertial [kg mm^2]		Damping Coefficient D_t [kN s/m]	Weight m_t [kg]
I_x, I_z	I_y		
6.976	12.434	48.6	95

The soil studied in the analytical model is a type of upland sandy loam. The wet bulk density is 1468 kg/m^3, and the moisture content is 49.4%. The other parameters for the pressure-sinkage and shear stress-displacement relationships cited from the Wong's publication-'Terramechanics and Off-road Vehicle Engineering' are listed in Table 4.2.

Table 4.2: Soil parameters defined in the soil property file [20]

k_c [kpa/m^{n-1}]	k_φ [kpa/m^n]	n [-]	c [kpa]
65.5	1418	0.97	2.2
ϕ [degree]	K_x [mm]	K_y [mm]	c_s [kN s/m]
39.4	61	20	0.28

4.3.1 Examination of soil damping effects

To demonstrate the effects of implementing soil damping on the dynamic behavior of a tire running through soil, the simulations with two tire-soil interaction models for a

rigid and a deformable tire were performed. One model takes into account the soil damping stress, and the other model uses the quasi-static pressure-sinkage equation without soil damping stress in the radial direction.

To study the soil compaction, the forces and the moments developed on the contact patch, the simulation was divided into two steps. In the first step, the position and the boundary conditions of the tire center were defined in such a way that the clearance of the tire bottom and the soil surface was zero and the tire only had the vertical degree of freedom. A constant load of 30 kN including the gravitational force was applied to the tire center and the simulation time was set to one second. In the second simulation step, a constant driving torque of 4 kNm to provide the tire propulsion and a lateral force of 12 kN were defined. The simulation time was set to 1 second as well. The simulation results are presented in the following figures. It should be noticed that R. means “rigid tire” and D. means “deformable tire”.

As displayed in Fig. 4.7, the amplitudes of the tire sinkage, the vertical and longitudinal force curves for the new analytical model considering the soil damping effect are significantly smaller, and the variations of those curves last shorter due to the soil damping effect. Due to the smaller area of the tire-soil interface, the sinkage is larger and the drawbar pull is much lower for the rigid tire.

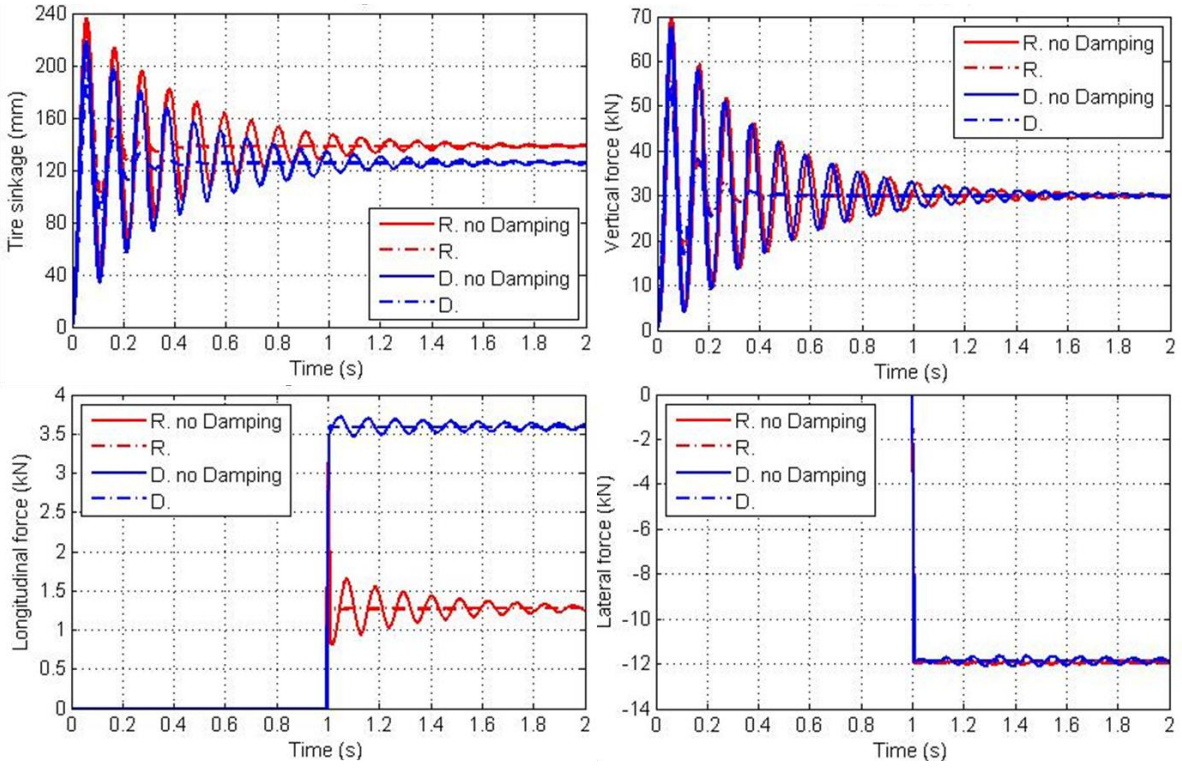

Fig. 4.7: Soil compaction and forces on the tire

As displayed in Fig. 4.8, the amplitudes of the rolling resistance and the anti-aligning torque curves are smaller for the model taking into account the soil damping effect. Since larger soil compaction causes more energy dissipation, the rolling resistance for the rigid tire is larger.

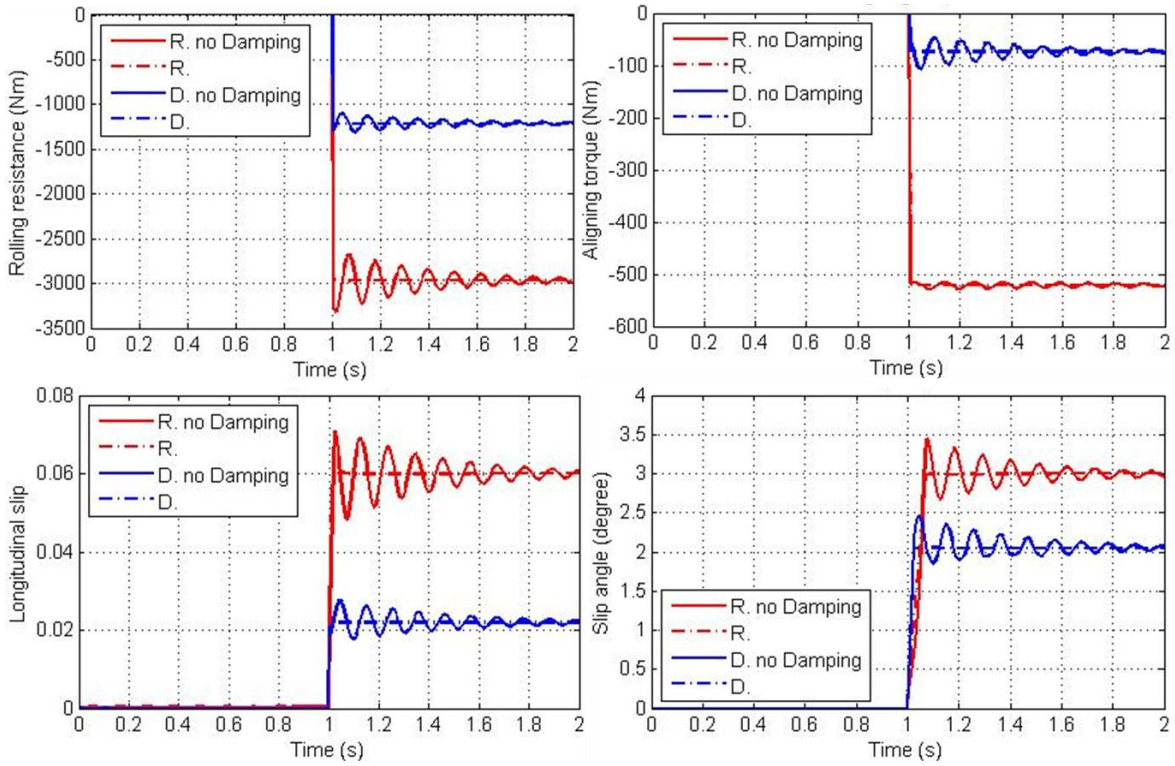

Fig. 4.8: Rolling resistance and anti-aligning torque on the tire

4.3.2 Simulation of soil compaction

The soil compaction is affected by several factors such as the inflation pressure, the shape and size of the tire, the wheel load, and the number of passes. Two groups of simulations as shown in Fig. 4.9 were performed to study the soil compaction for both the rigid and deformable tires in the same size and weight at different wheel loads.

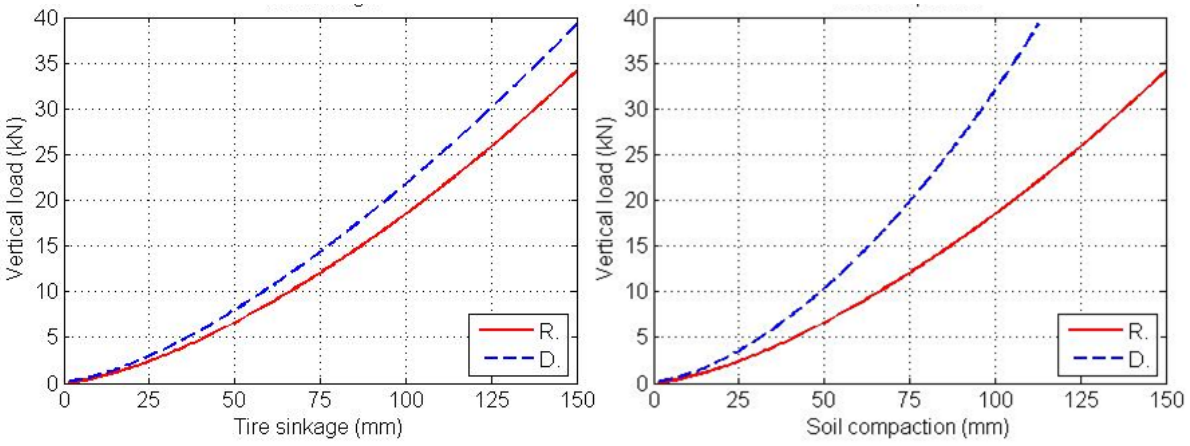

Fig. 4.9: Tire sinkage and soil compaction at different wheel loads

It is noticed that the slopes of the tire sinkage/soil compaction-vertical force curves tend to increase with the increasing of the soil sinkage/soil compaction. At the same wheel load, tire sinkage and soil compaction are larger for the rigid tire. To minimize the soil compaction, the wheel load should be uniformly distributed over the largest possible area [136]. Due to larger contact area and more uniform contact stress underneath the deformable tire, the stress on the contact patch is smaller resulting in less tire sinkage and soil compaction.

As displayed in Fig. 4.9, the curves of the tire sinkage/soil compaction-wheel load relationship are non-linear. A custom equation in the form of ax^n is selected to fit the curves. The coefficients in the equation for the curve fitting are listed in Table 4.3. Since the coefficient of determination R^2 is near to 1, the fitting quality is high [137].

Table 4.3: Coefficients in the custom equation

Tire sinkage-wheel load	*a* [kN/mm^n]	*n* [-]	R^2
Rigid tire	0.01902	1.494	0.9999
Deformable tire	0.02755	1.449	0.9999
Soil compaction-wheel load	*a* [kN/mm^n]	*n* [-]	R^2
Rigid tire	0.01902	1.494	0.9999
Deformable tire	0.01746	1.631	0.9999

The derived equations for calculating the wheel load at specified tire sinkage and soil compaction for the rigid tire is presented by Eq. (4.19) and for the deformable tire is presented by Eq. (4.20) and (4.21). It should be noticed that the tire sinkage is the sum of tire deformation f_0 and soil compaction z_e.

$$F_{zr} = 1.902 \times 10^{-2} z_e^{1.494} \tag{4.19}$$

$$F_{zd1} = 2.755 \times 10^{-2} \left(z_e + f_0 \right)^{1.449} \tag{4.20}$$

$$F_{zd2} = 1.746 \times 10^{-2} z_e^{1.631} \tag{4.21}$$

The comparison of the simulation and predicted results with the fitted equations is demonstrated in Fig. 4.10. It should be noticed that the abbreviation of ‘Pre.’ means prediction. The curve fitting method could restore the simulation results such as the wheel load, the tire sinkage and the soil compaction with certain simple equations, and a simplified tire-soil interaction model to predict the tire mechanical behavior in

the vertical direction could be derived based on the equations to fit the curves of simulation results.

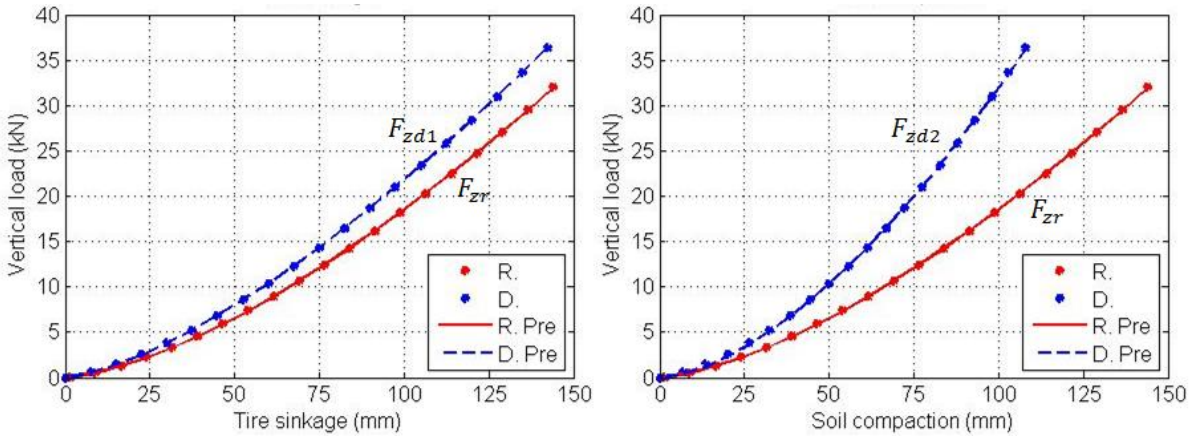

Fig. 4.10: Simulation results and fitting curves of tire sinkage and soil compaction

4.3.3 Simulation of pure longitudinal slip

The longitudinal force (driving or braking) is generated due to the longitudinal slip developed between the tire and the ground. The relationship of the longitudinal slip and the longitudinal force is of great interest to the researchers, who are involved in the design of driver assistance [138] and stability control systems [139]. For the tire-road interaction, the common longitudinal slip-force curve indicates that a peak force value occurs at low values of longitudinal slip [140-141]. There is little data of this curve for the tire-soil interaction. The simulation object in this section is to study the tire slipping behavior when running through deformable soil.

The accelerating and braking operation are the common working conditions for the tire. The longitudinal slip s_x defined in Eq. (4.22) indicates that a slip ratio of -1 means full sliding; a slip ratio of 0 means pure rolling; a slip ratio of 1 means full spinning.

$$s_x = \begin{cases} R_e\omega / v_x - 1 & (R_e\omega < v_x) \\ 1 - v_x / R_e\omega & (R_e\omega > v_x) \end{cases} \tag{4.22}$$

Where

R_e effective rolling radius ω rotation velocity

v_x tire longitudinal velocity

Different longitudinal velocities and a constant angular velocity on the tire center were defined to generate different longitudinal slips, and two constant wheel loads were applied on the tire center in the simulations. No steering action was defined

indicating that the slip angle is 0. Fig. 4.11 and 4.12 display the tire sinkage, soil compaction, drawbar pull/braking force and rolling resistance generated on the rigid and the deformable tire – soil interaction interface.

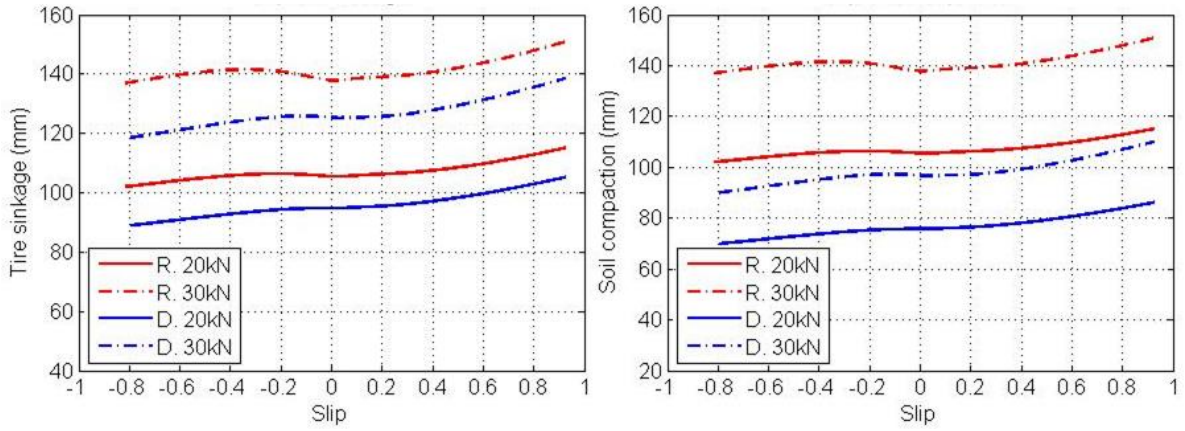

Fig. 4.11: Tire/soil deformation at different wheel loads and longitudinal slips

The tire sinkage and soil compaction curves indicate that when the tire is in the acceleration mode, a larger longitudinal slip between the tire and the soil causes larger tire sinkage and soil compaction; when the tire is in the braking mode, larger longitudinal slip results in less tire sinkage and soil compaction. At the same wheel load and longitudinal slip, the tire sinkage and the soil compaction is less for the deformable tire.

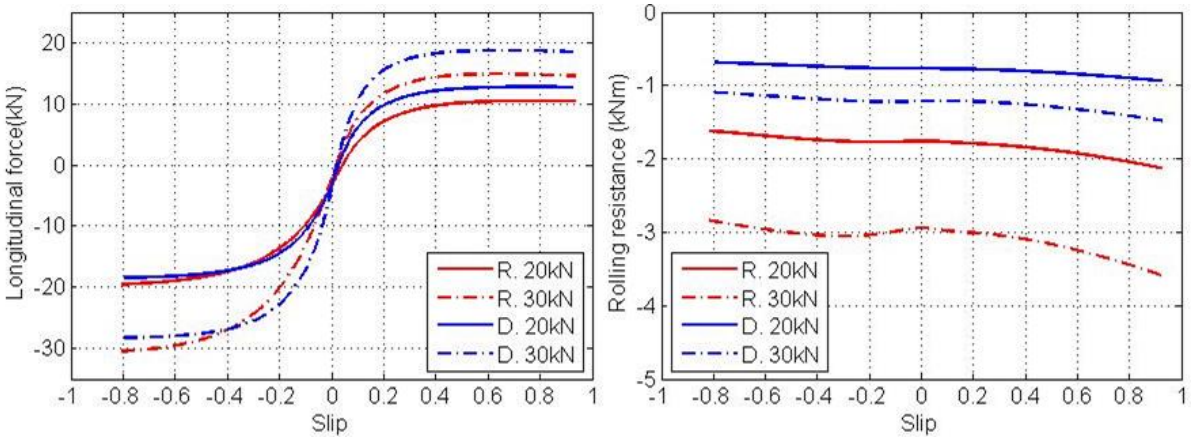

Fig. 4.12: Longitudinal force/rolling resistance at different wheel loads and longitudinal slips

The longitudinal force curve presents the features that as the slip increases, the longitudinal force becomes larger and reaches a maximum value, and as the slip increases further, the longitudinal force remains the same. A larger wheel load leads to a larger longitudinal force. When the tire is in the acceleration mode, the drawbar

pull that can be obtained from the contact patch is larger for the deformable tire at the same wheel load and longitudinal slip.

The rolling resistances curves indicate that, when the tire is in the acceleration mode, larger longitudinal slips result in more rolling resistances due to the fact that more energy is dissipated caused by the larger soil compaction; when the tire is in the braking mode, larger longitudinal slips cause less rolling resistances due to the fact that less soil compaction is observed and less energy is dissipated by the compaction resistance. Larger wheel loads causing more soil compaction lead to more rolling resistances. More rolling resistance is observed for the rigid tire because of more dissipated energy caused by the larger soil compaction.

To fit the tire force and moment curves, a simplified form of Pacejka's magic formula (MF) model was used. The MF model was first proposed for car tires [142] and further modified for motorcycle tires [143]. Since the curves of the longitudinal slip – longitudinal force relationship are similar to those derived from the MF tire model, this model appears to be feasible to fit these curves. The basic equation and shape of the MF model is presented as follows, and the independent variable x is either longitudinal slip ratio s_x or lateral slip angle α.

$$Y(x) = D\sin\left[C\arctan\left(B\left(x+S_h\right) - E\left(B\left(x+S_h\right) - \arctan\left(B\left(x+S_h\right)\right)\right)\right)\right] + S_v \tag{4.23}$$

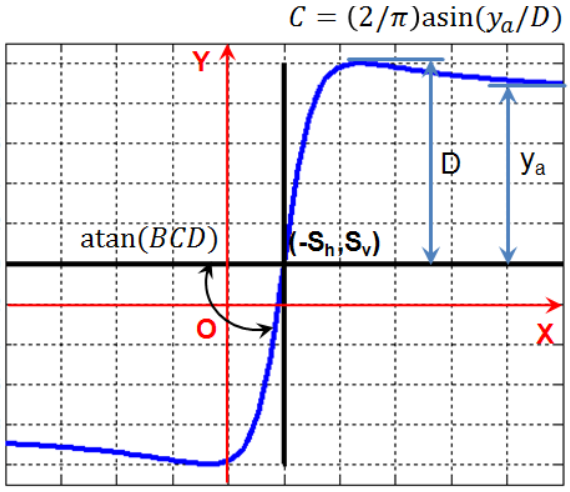

Fig. 4.13: Curve shape of the magic formula equation

D named as the peak factor, determines the peak value of the magic formular equation. *C* named as the shape factor, determines the part used of the sinusioidal function. *B* named as the stiffness factor, stretches the curve. *E* named as the curvature factor, can modify the characteristic around the curve peak. It is noticed that the curve slope at the point of ($-S_h$, S_y) is equal to the value of BCD.

$$f_x = F_x / F_z \tag{4.24}$$

As listed in Table 4.4, the coefficients in the MF model for the longitudinal force are determined with the regression function in Matlab. The coefficients of determination which are close to 1 indicate that the fitting quality is high and the regression is reasonable. Fig. 4.14 provides a better view of the curve fitting by comparing the simulation and predicted results.

Table 4.4: Coefficients in the MF model for the longitudinal force

Paramters	**Rigid tire**		**Deformable tire**	
	Wheel load		**Wheel load**	
	20 kN	30 kN	20 kN	30 kN
D	6.531	14.905	19.062	16.159
C	0.139	0.063	0.047	0.055
B	3.889	3.939	5.561	6.304
E	1.0990	1.1260	1.0490	1.052
S_h	0.034	0.067	-0.037	-0.0304
S_v	-0.2170	-0.2480	-0.1370	-0.153
R^2	0.9999	0.9999	0.9999	0.9999

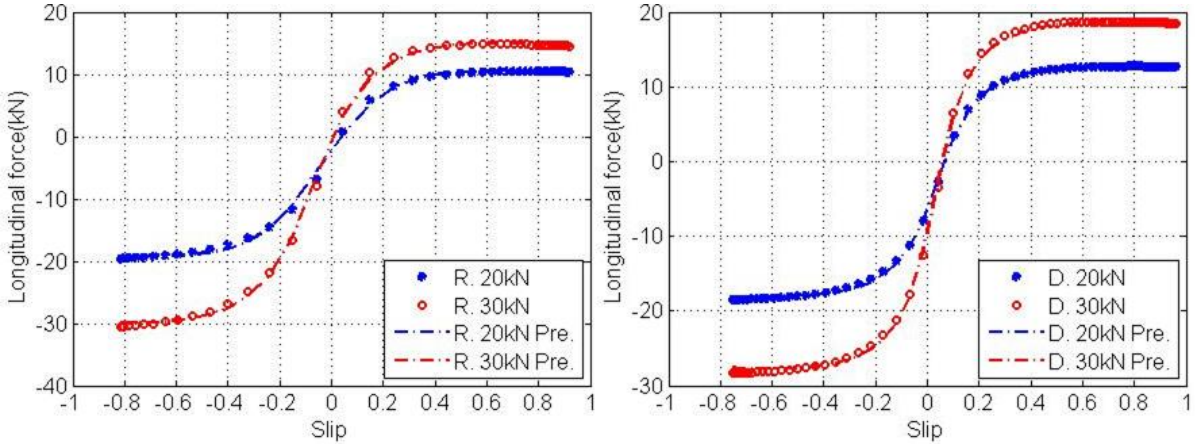

Fig. 4.14: Simulation results and fitting curves of longitudinal force

4.3.4 Simulation of pure lateral slip

The slip angle is the angular difference between the direction in which a tire is pointing and the actual travelling direction of the tire. It is defined as the arctangent of

the ratio of the lateral velocity of the tire contact center point (v_y) to the absolute value of the tire translational velocity (v_x), presented in Eq. (4.25).

$$\tan\alpha = v_y / |v_x| \tag{4.25}$$

The lateral force known as the side or cornering force is the necessary force to hold a vehicle through a turn. Considering the lateral deflections of the tread elements, they may slide across the contact area. Any tread slipping or creeping is accompanied by a reduction in the lateral deformation of carcass. After the tread elements have passed through their contact area, the tire returns to the undeformed condition. As a result of the tire carcass and tread deforming in this manner, an angular difference is created between the direction where the tire is being aimed and the direction where it actually travels [144]. As shown in Fig. 4.15, the slip angle – lateral force curve for the tire-hard ground interaction is sorted into three regions: linear/elastic, transitional and frictional [145].

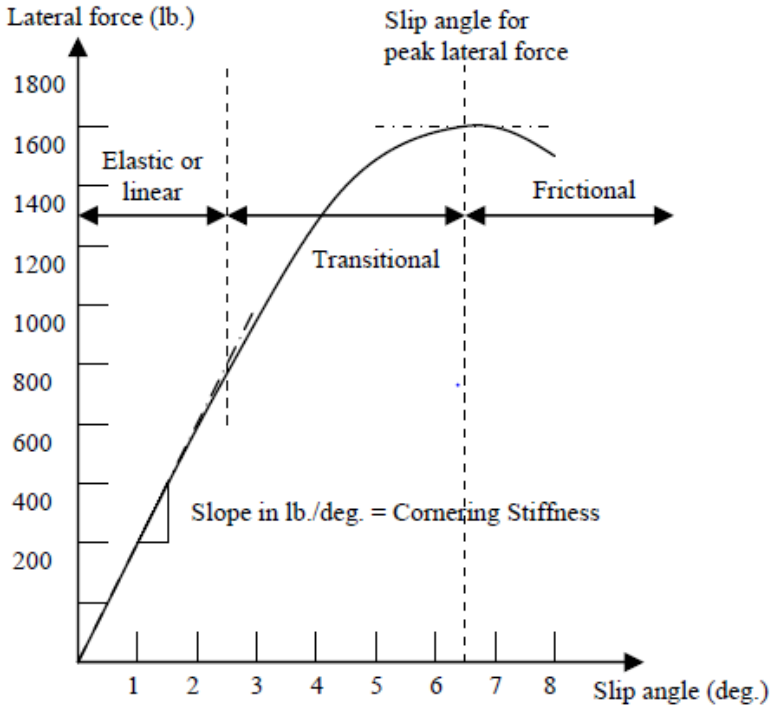

Fig. 4.15: Typical lateral force versus slip angle [145]

For the tire – rigid road interaction, the self-aligning torque generates a restoring torque on the tire to realign the traveling direction with the heading direction when the slip angle is non-zero. It helps the steered tire to return to the original position after a turning on the road. For the tire-soil interaction, the self-aligning torque enlarges the slip angle. The self-aligning torque is defined as the product of the lateral force and the pneumatic trail.

Different lateral velocities, constant longitudinal and angular velocities on the tire center were defined to generate different slip angles, and two constant wheel loads were applied on the tire center in the simulations. The tire was set in the free rolling mode indicating that the longitudinal slip equals to 0. The simulation results of lateral force and anti-aligning torque are displayed in Fig. 4.16.

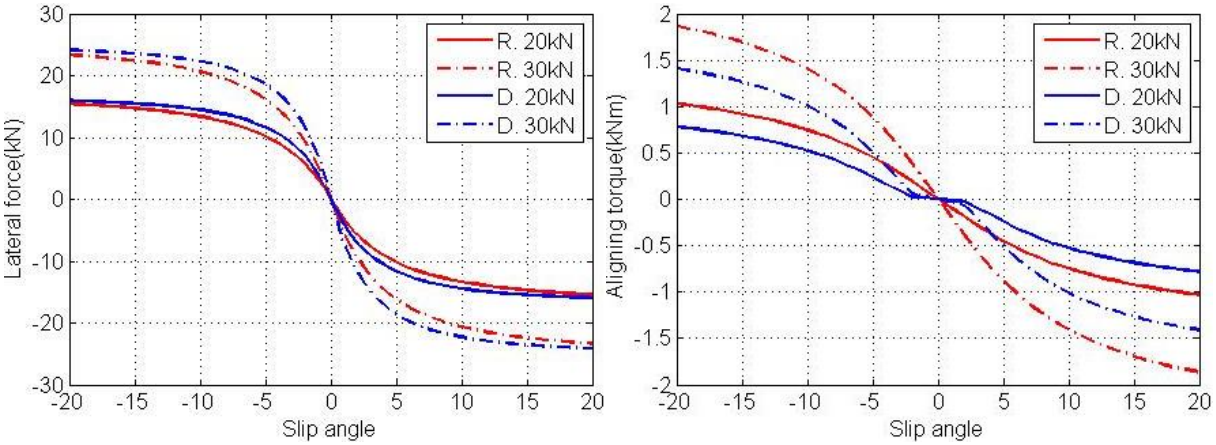

Fig. 4.16: Lateral force/anti-aligning torque at different wheel loads and slip angles

The non-linear curves present the features that as the slip angle increases, the lateral force and the anti-aligning torque become larger. The friction coefficient determines the up limit until a large slip angle occurs. When the tire is not completely sliding, the lateral force is not fully dependent on the friction coefficient, and it is affected by the tire cornering stiffness as well.

Larger wheel loads result in larger lateral forces and aligning torques. The lateral forces generated on the rigid and deformable tire – soil contact patch are similar. However the anti-aligning torque on the deformable tire is remarkably smaller than that on the rigid tire due to the reason that the pneumatic trail for the deformable tire is smaller. A larger soil compaction for the rigid tire results in a larger pneumatic trail. It should be noticed that the anti-aligning torque tends to increase the slip angle.

The equation of the MF model was applied to fit the lateral force and the anti-aligning torque curves for the rigid and deformable tire. The dependents for the curve regression are presented in Eq. (4.26) and (4.27).

$$f_y = F_y / F_z \tag{4.26}$$

$$f_z = M_z / F_z \tag{4.27}$$

As listed in Table 4.5 and 4.6, the coefficients in the MF model for the lateral force and the anti-aligning torque are determined with the regression function in Matlab as

well. The coefficients of determination which are near to 1 indicate that the fitting quality is high and the regression is reasonable. Fig. 4.17 and 4.18 provides a better view of the curve fitting by comparing the simulation and predicted results.

Table 4.5: Coefficients in the MF model for the lateral force

Parameters	**Rigid tire**		**Deformable tire**	
	Wheel load		**Wheel load**	
	20 kN	30 kN	20 kN	30 kN
D	-0.845	-0.857	-0.842	-0.851
C	1.788	4.517	2.873	3.314
B	3.421	1.155	2.222	1.910
E	1.134	2.704	1.505	1.723
S_h	0	0	0	0
S_v	0	0	0	0
R^2	0.9999	0.9999	0.9999	0.9999

Table 4.6: Coefficients in the MF model for the anti-aligning torque

Parameters	**Rigid tire**		**Deformable tire**	
	Wheel load		**Wheel load**	
	20 kN	30 kN	20 kN	30 kN
D	-3.215	-2.762	-1.266	-1.842
C	0.4052	0.8283	1.025	1.271
B	4.269	4.909	2.599	2.879
E	0.8782	0.6967	0.9793	0.9094
S_h	0	0	0	0
S_v	0	0	0	0
R^2	0.9999	0.9999	0.9999	0.9999

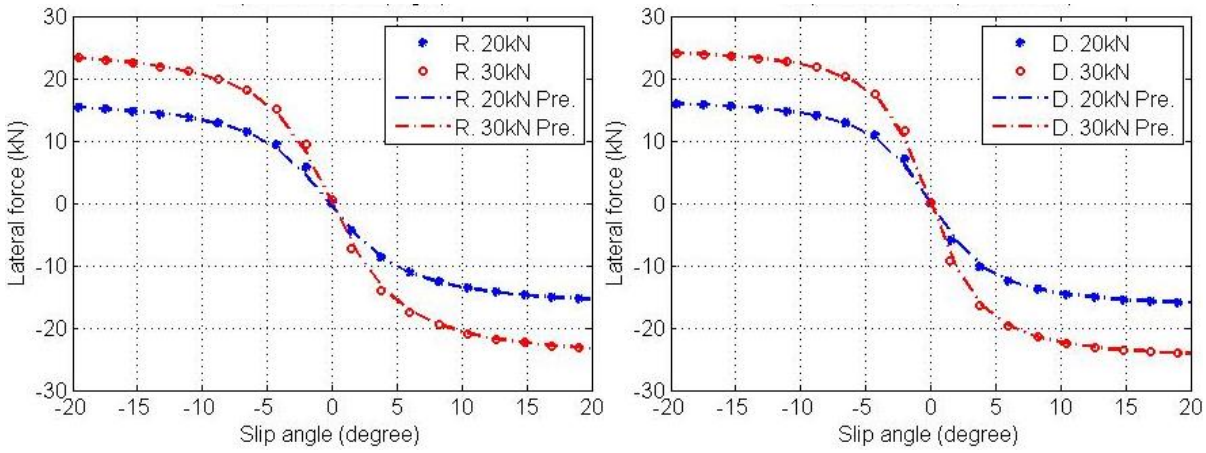

Fig. 4.17: Simulation results and fitting curves of lateral force

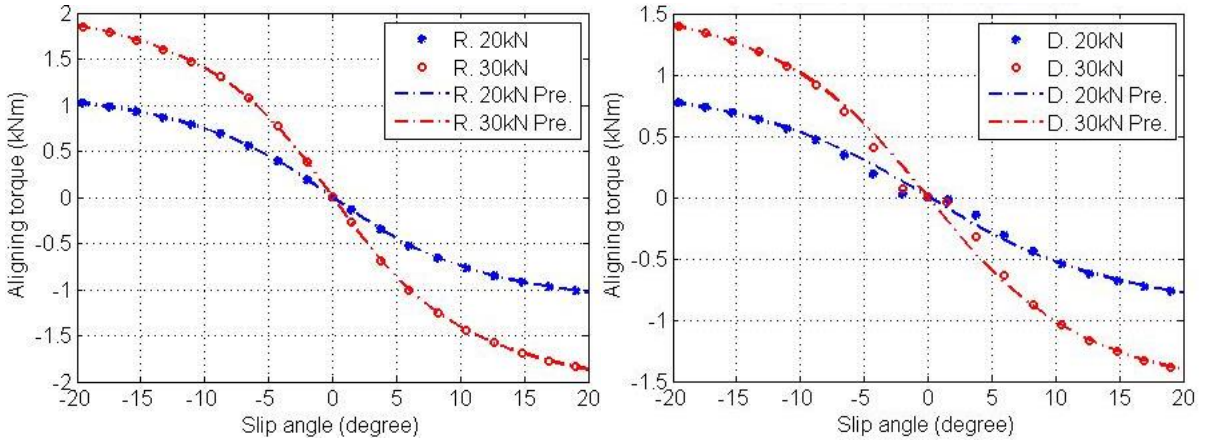

Fig. 4.18: Simulation results and fitting curves of anti-aligning torque

4.3.5 Simulation of combined slip

Longitudinal force, lateral force and aligning torque exhibit a strong sensitivity to a wide variety of operating conditions such as temperature, inflation pressure, wheel load, longitudinal slip and slip angle. Two coupled components (longitudinal slip and lateral slip angle) determine the combined tire slipping. For the study of the mechanical characteristics of tires running through soil during the combined slipping, these two components are altered in the tire-soil interaction simulation.

Three sets of lateral slip angles were defined by setting the lateral velocity on the tire center where the longitudinal slip is adjusted from braking lock to acceleration. Three sets of longitudinal slips were defined by setting the rotational velocity on the tire center where the slip angle ranges from -20° to 20°. The simulation results of the tire combined slipping at the 30 kN wheel load are illustrated in the following figures.

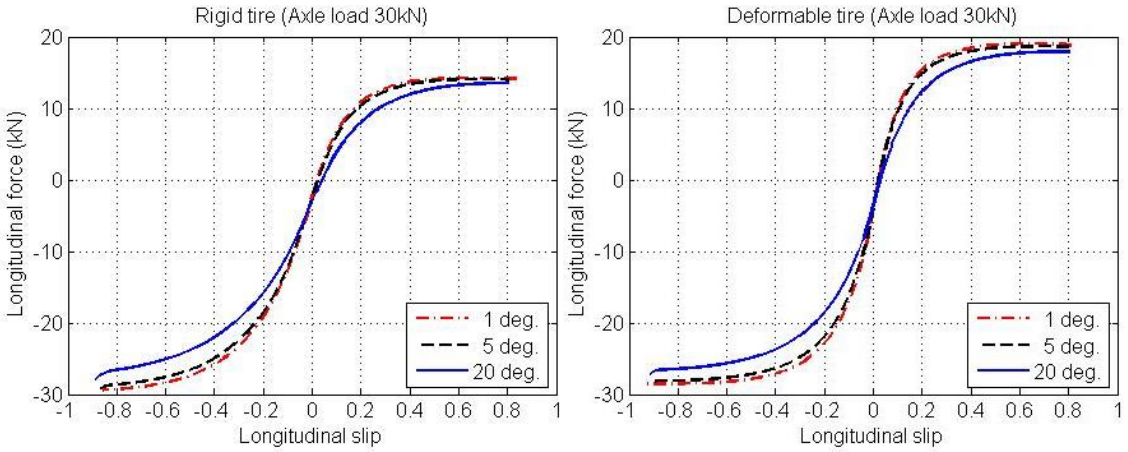

Fig. 4.19: Longitudinal force at constant slip angles and different longitudinal slips

As shown in Fig. 4.19, the longitudinal force decreases, as the applied lateral slip angle increases for the rigid and deformable tire. Since the lateral slip angle increases, the shear stress on the tire-soil contact interface becomes larger in the lateral direction, which results in the decrease of the stress and force in the longitudinal direction.

It is also observed that at the longitudinal slip of 0, an additional traction force as result of bull dozing effect is required to overcome the soil obstacle in front of the tire. For the operating conditions such as full accelerating and full braking lock, the absolute value of the longitudinal force is of great difference. When the tire accelerates on the soft soil, the soil is pushed to the tire rear region at the contact patch, and a “small hill” is formed at the back. As the slip between the tire and the soil becomes larger, more contact stress is generated leading to larger drawbar pull. When the tire brakes on the soft soil, not only the small hill formed in front of the tire but also the contact stress generated by the slip hinder the tire movement, hence the braking force is larger than the drawbar pull.

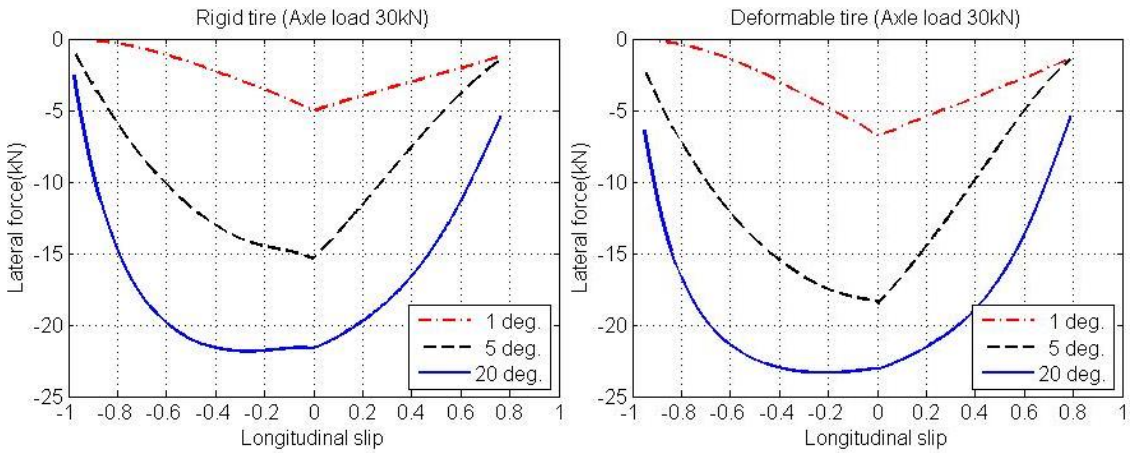

Fig. 4.20: Lateral force at constant slip angles and different longitudinal slips

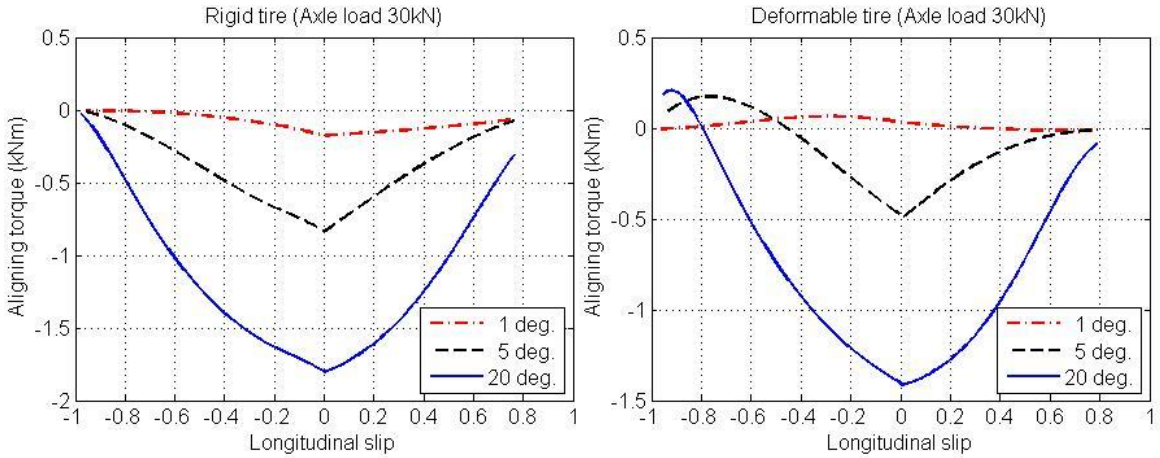

Fig. 4.21: Anti-aligning torque at constant slip angles and different longitudinal slips

As shown in Fig. 4.20 and 4.21 at constant lateral slip angle, the magnitudes of lateral force and anti-aligning torque become less when the longitudinal slip increases and the lateral slip angle decreases. As the longitudinal slip between tire and soil increases, the friction force generated on the contact patch decreases in the lateral direction leading to the decreasing of the lateral force and the anti-aligning torque.

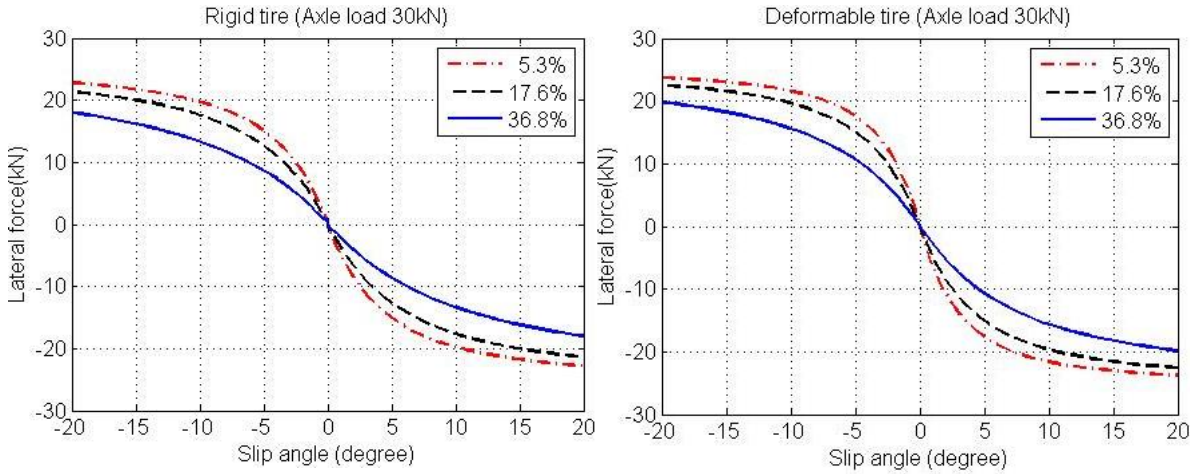

Fig. 4.22: Lateral force at constant longitudinal slips and different slip angles

As shown in Fig. 4.22, the lateral forces decrease, as the applied longitudinal slip increases for the rigid and deformable tire. Since the longitudinal slip increases, the shear stress on the tire-soil contact interface becomes larger in the longitudinal direction, which results in the decreasing of the stress and force in the lateral direction.

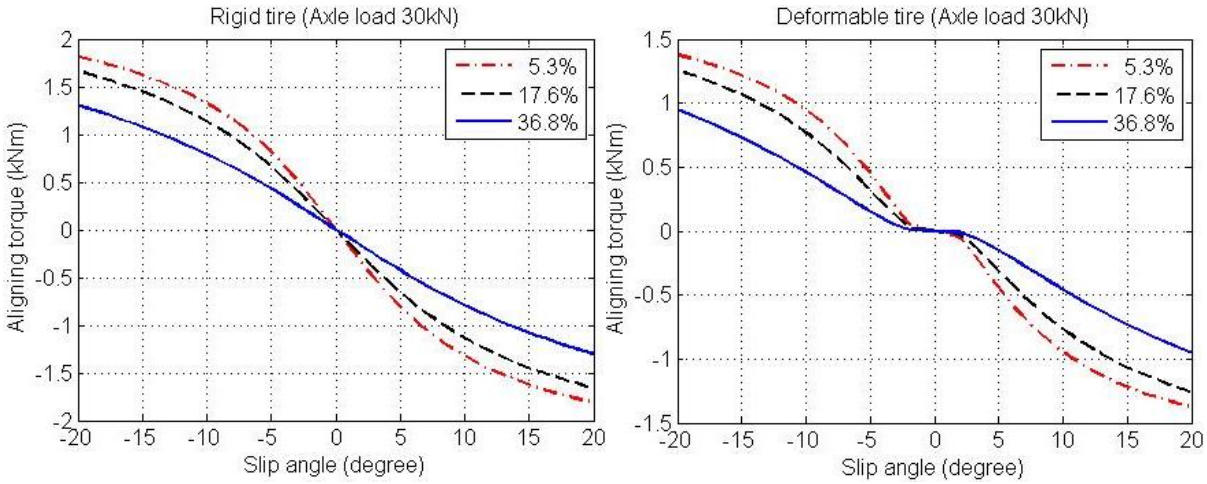

Fig. 4.23: Anti-aligning torque at constant longitudinal slips and different slip angles

As shown in Fig. 4.23, the anti-aligning torque decreases, as the applied longitudinal slip increases for the rigid and deformable tire. The decreasing of the anti-aligning torque is caused by the decreasing of the lateral force at larger longitudinal slips.

The tire dynamic behavior presented by the longitudinal/lateral forces and the anti-aligning torque during the combined slipping is displayed in the following figures.

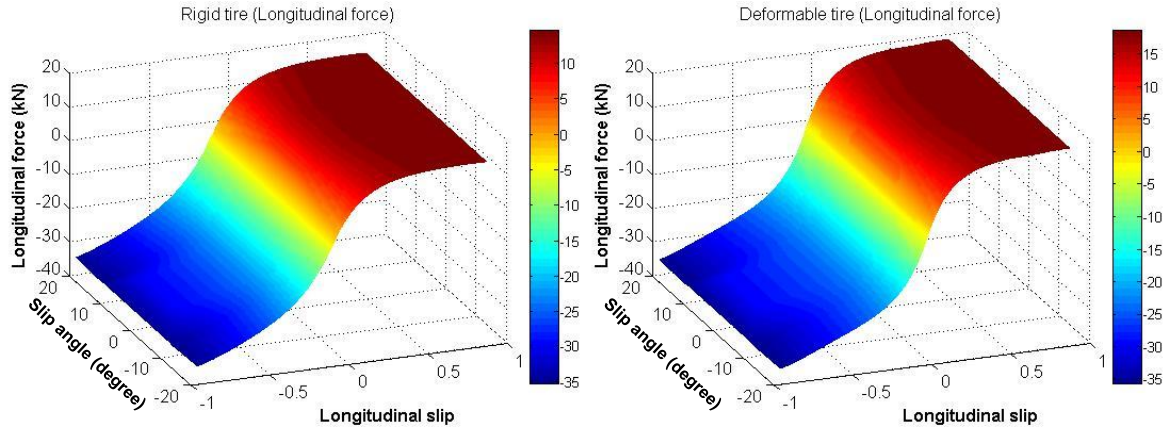

Fig. 4.24: Longitudinal force during the combined slipping

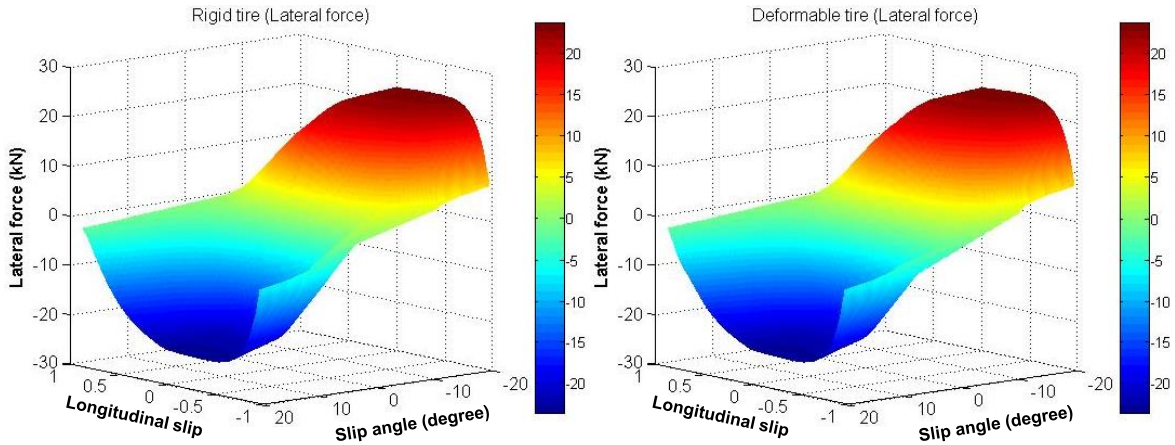

Fig. 4.25: Lateral force during the combined slipping

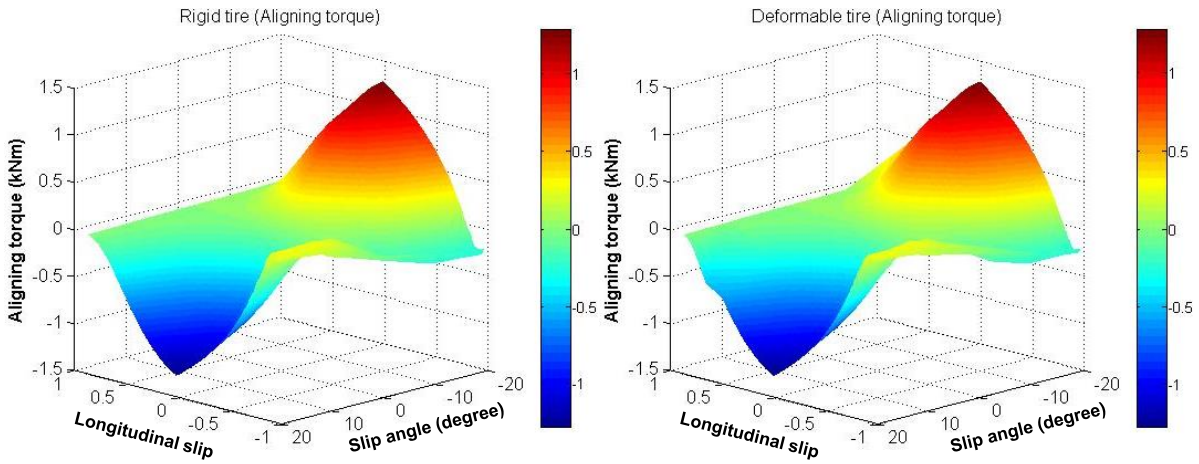

Fig. 4.26: Anti-aligning torque force during the combined slipping

4.4 Conclusion

In this Chapter, the KIMA analytical tire-soil interaction model for rigid and deformable tires was developed as user-defined subroutines in MBS software-Adams. With this model it is possible to predict the tire static and dynamic performance when operating on the soil in Adams.

To study the effect of wheel load on the soil compaction, the simulations of tire sinking were performed in this chapter. It is observed that for the same wheel load the deformable tire caused less soil compaction than the rigid tire. The relationships of the wheel load-tire sinkage/soil compaction for the rigid and deformable tire were established, with which tire sinkages or soil compactions can be predicted under specified wheel loads.

The longitudinal slip is critical to the longitudinal force developed along the contact patch. To study its influence on the tire accelerating and braking behavior, different longitudinal slips were defined in the simulations of tire pure longitudinal slipping. The simulation results at the specified wheel loads of 20 and 30 kN were compared and analyzed. Using the MF formula model for the curve fitting, the equations of the longitudinal slip – longitudinal force relationship for the rigid and deformable tire can be developed. The lateral slip angle is an important factor that impacts the lateral force and the anti-aligning torque developed on the contact patch. It is usually applied as a criterion to evaluate the tire cornering performance. The simulation results for the rigid and deformable tire at the specified wheel loads of 20 and 30 kN were presented. Using the MF model for the curve fitting, the equations of the slip angle – lateral force and anti-aligning torque relationship were derived from the

simulations of tire pure lateral slipping. An empirical MF tire model can be established based on the equations of the fitting curves derived from simulation results and this simple empirical model can be integrated into the MBS software for the storage of simulation results as look-up tables and further applied in the vehicle-soil simulation.

The simulations under the operating condition of combined slipping at the wheel load of 30 kN were carried out to study the effects of the combination of the longitudinal slip and the lateral slip angle on the mechanical characteristics of the tire-soil interaction.

5 Tire-Soil Interaction Modeling with FEM

With the FEM, the tire and the soil are supposed to be continuums comprised of a large number of small finite elements. The stress and displacement of each node on the finite elements are calculated as the material properties, the load and boundary conditions are defined. During the recent years, the FEM has been widely applied in the research of tire-soil interaction. The FE models developed in the past decade for the study of tire-soil interaction are either two dimensional or three dimensional. Two-dimensional models were mainly designed for the rigid tires applied on the planetary rovers, as their geometry is axial-symmetric and limited stress or strain occurs due to the applied forces. 3D models were developed for deformable tires mounted on off-road vehicles, and the simplifications such as tread structure with complex geometries is neglected or the belt and carcass for the reinforcement are not considered in the tire models, were proposed. Taking in to account the tread structure and the inner layers of the tire, non-linear 3D tire-soil interaction models were developed for the study of the mechanical characteristics of tire-soil interaction with Abaqus. The models and the simulation results are presented in this chapter.

5.1 Introduction of FE tire models

A pneumatic tire is a flexible structure of toroid shape filled with compressed air. Generally pneumatic tires are categorized into bias-ply tires and radial-ply tires according to the cord direction. The structures of the bias-ply and radial ply tire are displayed in Fig. 5.1. The most important structural element of a tire is the carcass. The carcass is a number of inner plies that supports weight and absorbs impact, and it has to resist fatigue caused by the constant flexing and compression. It is made up of a number of layers of flexible cords with high elasticity moduli encased in a matrix of low modulus rubber compounds. The belt is made of steel wire or textile fabric. It acts as reinforcement, reducing the impacts sustained from the road and helping to maintain stability by widening the tread in contact with the road. Cords are made of fabrics of natural, synthetic, or metallic compositions. The cords in the belt and the carcass layers are oriented at specified angles to maintain the desired response to loading. Each cord is consisted of many filaments twisted together, which produces a nonlinear response to the loading. The bead serves as the foundation for the carcass and provides adequate tire seating on the rim. It is composed of a bead wire and a rubber core. The inner liner is a special air-tight rubber lining resisting air diffusion

and replacing the inner tube within a tire. The sidewall adds rigidity to the structure, protecting the carcass and improving the ride quality by allowing the tire to expand and compress. The tread is a kind of rubber/composite compound formulated to provide traction. Tread patterns are featured with the geometric shape of grooves, lugs, and voids.

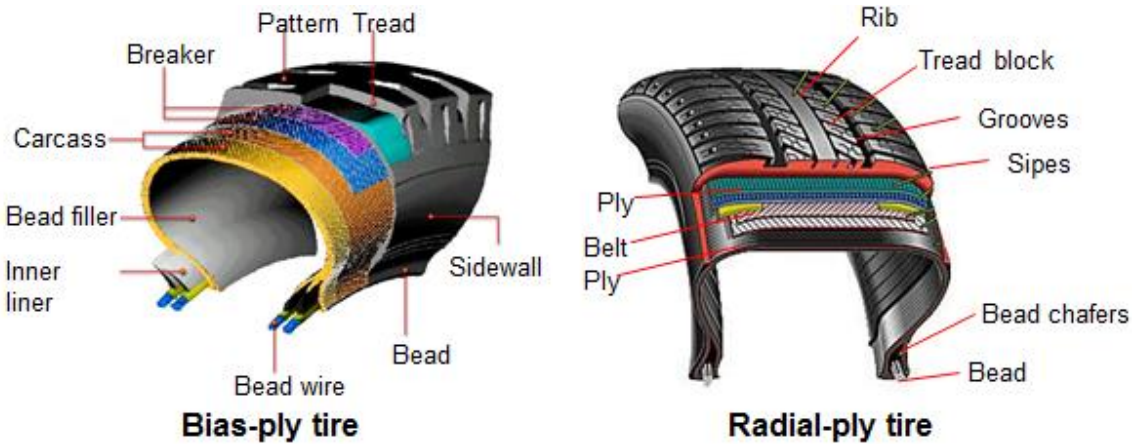

Fig. 5.1: Structure of bias-ply and radial-ply tire [146-147]

The bias-ply tire adopts the ply cords which extend diagonally across the carcass from bead to bead in the angle range of 30-40 degrees. The cords in the adjacent plies are arranged at opposite angles forming a crisscross pattern. The main advantage of this structure is allowing the entire tire body to flex easily which results in better gripping, better clean out, and better conformity to rough and rocky soil; the disadvantages are increased rolling resistance, less control and traction at high speed. The radial-ply tire adopts the ply cords which extend radially from beads and across the tread. The cords are parallel to each together with crown angle of 90 degrees. Radial ply tires which have more flexible sidewalls than bias-ply tires produce a larger and more stable ground contact area, a softer ride and lower rolling resistance; the disadvantages are poor transport handling, higher price and decreased self-cleaning ability on the off-road. For the off-road vehicles such as excavators, the bias-ply tires are mainly used.

5.1.1 Structure of FE tire models

For this work, a Bridgestone 10.00-20 bias tire was sliced into small pieces for the identification of the tire geometry and the inner layer position. As shown in Fig. 5.2, the corresponding FE tire model is comprised of six components. Modeled with solid elements, the tire body and the sidewall serve as a host for the inner layers. The tread patterns for providing traction and braking force were modeled with solid

elements. Belts and carcass in the ring geometry were modeled with shell elements embedded inside the tire body.

In Abaqus rebar elements are used to define layers of uniformly spaced reinforcing bars in shell, membrane and solid elements. The fiber cords modeled as rebar elements were embedded in the shells (carcass and belt). The bead, which prevents the tire from popping out from the rim, was modeled with solid elements embedded inside the tire. The rim is relatively stiff, and the stress distribution is not interested. To improve the computation efficiency, it was modeled with rigid elements.

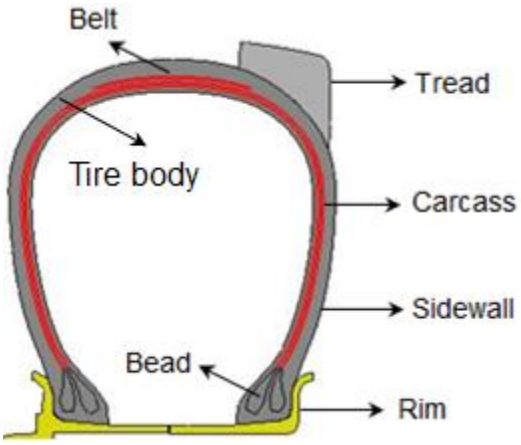

Fig. 5.2: FE tire structure

As displayed in Fig. 5.3, two different FE tire models (uneven-spaced and even-spaced model) were developed for different simulations. The uneven-spaced tire model was used to study tire sinkage and soil compaction, and the even-spaced tire model was used to study the tire pure longitudinal and lateral slipping performance.

As displayed in Fig. 5.3.a, the uneven-spaced tire model has the characteristics that the bottom tire elements (including the inner layers) are 3 times finer as those of the rest of the tire regions, as 90 nodes were distributed on the ¼ tire circumferential edge at the bottom, and 90 nodes were distributed on the rest of the tire circumferential edges. The element size of the tread at the bottom is 4 mm, and the element size of the rest of the tread is 8 mm. As only the bottom part of the tire came into contact with the soil during the sinking process, finer elements were used in the tire bottom region for more accurate contacting computations.

As displayed in Fig. 5.3.b, the even-spaced tire model has the characteristics that the nodes are evenly distributed along the tire edges, and each tire circumferential edge is assigned with 360 nodes, it is designed for the simulation of tire rolling as the tire crown interacts with the soil during the rotation. The tread element size is 4 mm.

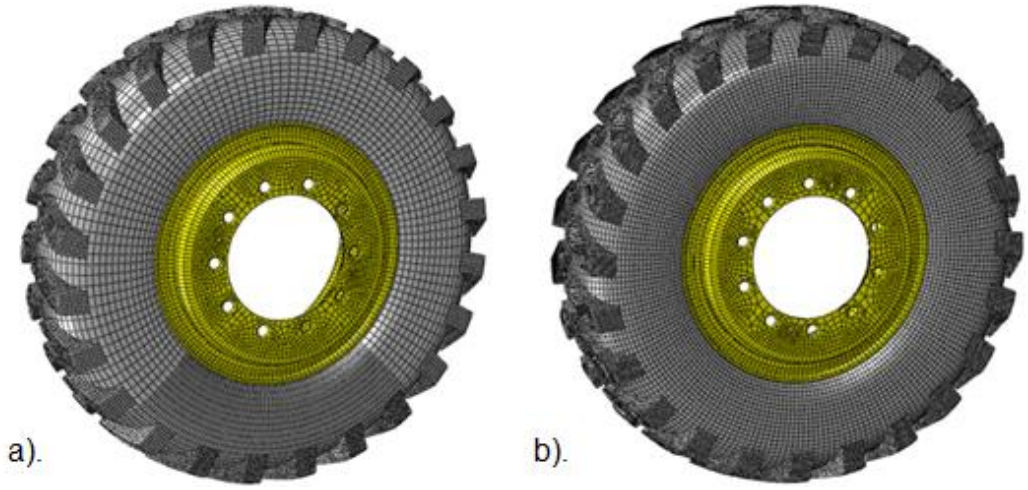

Fig. 5.3: Uneven-spaced and even-spaced tire model

The element type of C3D8R was selected for the solid elements of the rim, the tire body, the sidewall, the tread, and the bead. C3D8R is an 8-node linear brick, 3D solid element with reduced integration and hourglass control. C3D6R is a 6-node linear triangular prism, 3D solid element with reduced integration. Complex geometries can be difficult to mesh completely with hexahedrons (C3D8R); hence wedge and tetrahedral elements (C3D6R) are necessary. The element type of S4R is selected for the shell elements of the belts and the carcass. S4R is a 4-node, quadrilateral, 3D shell element with reduced integration and large-strain formulation.

The element number and type of the uneven and even-spaced tire models are summarized in Table 5.1 and 5.2.

Table 5.1: Element number and type of the uneven-spaced tire model

	Type	**Element Number**	**Node number**	**Minimum Size**
Rim	C3D8R	5137	11050	15 mm
	C3D6	664		
Sidewall	C3D8R	19800	30060	5 mm
	C3D6	720		
Tread	C3D8R	46986	67277	4 mm
	C3D6	2352		8 mm
Belt	S4R	3240	2880	8 mm
Carcass	S4R	29880	30960	5 mm
Bead	C3D8R	2880	7200	4 mm

Table 5.2: Element number and type of the even-spaced tire model

	Type	Element Number	Node number	Minimum Size
Rim	C3D8R	5137	11050	15 mm
	C3D6	664		
Sidewall	C3D8R	39600	60120	5 mm
	C3D6	1440		
Tread	C3D8R	144000	189960	4 mm
	C3D6	5088		
Belt	S4R	5760	6480	8 mm
Carcass	S4R	54000	55440	5 mm
Bead	C3D8R	5760	14400	4 mm

As the elements and nodes of the even-spaced tire model are twice more than those of the uneven-spaced tire, much more computer memory is required for performing the simulations. The computer used for the FEM simulations has the memory of 48 GB and 8 CPUs at the frequency of 3.2 GHz. With the application of the uneven-spaced tire model in the tire sinking simulation, the computation time is reduced by approximately 40%, and the discrepancy of the simulation results such as the stresses on the contact patch and the reacting forces is around 1.5%.

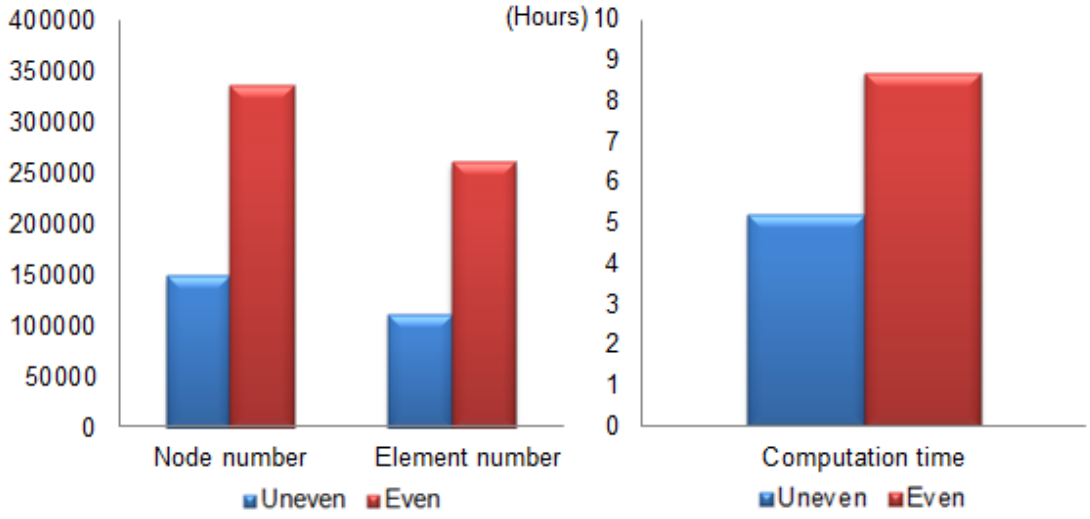

Fig. 5.4: Computational time comparison of uneven/even-spaced tire model

5.1.2 Materials of FE tire models

Tires are made from wide ranges of materials, such as rubber, synthetic fabric with high tensile strength and steel. The main materials of rims are steel and light alloys.

Wang [148] and Bolarrinwa [149] applied the Neo-Hookean model for the rubber hyperelastic property in the tire modeling. Ghoreishy [150] selected the Mooney-Rivlin model for the rubber components in a steel-belted radial tire.

Rubber is handled as a hyperelastic material since it is volumetrically incompressible due to the high bulk modulus. The constitutive models for rubber-like materials are available in Abaqus. The hyperelastic behavior is described in terms of the strain energy potential which defines the strain energy stored in the material per unit of volume in the initial configuration [151]. The neo-Hookean form is used for the prediction of the tire rubber stress-strain behavior. The neo-Hookean strain energy density U is:

$$U = C_{10}\left(\overline{I_1} - 3\right) + \left(J - 1\right)^2 / D_1 \tag{5.1}$$

$$\overline{I_1} = J^{-2/3} I_1 \tag{5.2}$$

$$J = \lambda_1 \lambda_2 \lambda_3 \tag{5.3}$$

$$C_{10} = \mu_0 / 2 \tag{5.4}$$

$$D_1 = 2 / K_0 \tag{5.5}$$

Where

C_{10} material constant

D_1 material constant

$\overline{I}_1$ the first invariant of the deviatoric part of the left Cauchy-Green deformation tensor

I_1 the first invariant of the left Cauchy-Green deformation tensor

J volume ratio λ_i principal stretches

K_0 bulk modulus μ_0 shear modulus

The material parameters of the sidewall and the tread are displayed in Table 5.3.

Table 5.3: Parameters of rubber material

Component	Density [kg/m^3]	C_{10} [MPa]	D_1 [MPa^{-1}]
Sidewall	890	0.226	0.10
Tread	850	0.981	0.03
Belt/carcass layer	1100	0.503	0.04

Carcass and belt layers are made of cord-rubber composites which display the mechanics of anisotropy and nonlinearity. The modeling of the cord-rubber composites determines the quality of the simulation results. Murat [152] applied steel cord reinforcements at the belt area of all-terrain tires and the carcass area of truck tires for the improvement of the tire lifetime. Meschke [153] used cord-reinforced elements for the 3D analysis of car tires.

The cord-rubber composites are comprised of laminated shells and rebar elements in Abaqus. The rubber laminated shells are used to describe the belt and carcass layers, and the steel rebar elements are used to describe the reinforcing cords, as shown in Fig. 5.5. The stiffness calculation for the rebar elements uses the same integration points as that for the underlying rubber shell elements. To define rebar elements, it is required to specify the cross-section area (A_R) of each rebar, the rebar spacing in the plane of the shell (S), the position of the rebar in the thickness direction measured from the shell mid-surface (P_R), and the angle α between the default local 1-direction and the rebar. The materials of the rebar elements are defined in Table 5.4.

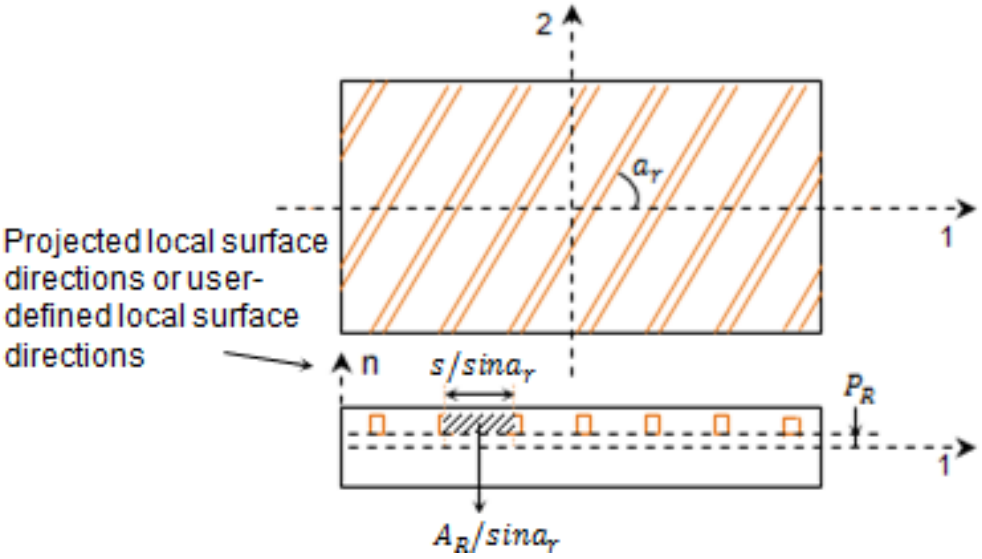

Fig. 5.5: Rebar elements in a 3D shell

Table 5.4: Material of cords in the belt and carcass layers

Parameters	**Belt cords**		**Carcass cords**			
A_R [mm^2]	0.332	0.332	0.385	0.385	0.385	0.385
S [mm]	1.27	1.27	1.27	1.27	1.27	1.27
P_R [mm]	0.1	0.1	0.1	0.1	0.1	0.1
α [°]	40	-40	50	-50	50	-50
Density [kg/m^3]	3500	3500	2000	2000	2000	2000
Young's Modulus [MPa]	4950	4950	550	550	550	550
Poisson's Ratio	0.35	0.35	0.35	0.35	0.35	0.35

The rim and the bead feature with the elastic properties. The material definition is presented in Table 5.5.

Table 5.5: Material of rim and bead

Component	Density [kg/m^3]	Young's Modulus [MPa]	Poisson's Ratio
Rim	7150	201000	0.3
Bead	6000	15000	0.3

5.1.3 Constraints of FE tire models

To define the rim as a rigid body, it is required to specify a reference point and rigid regions with the "Rigid body" constraint. A rigid body is an assembly of nodes and elements whose motion is determined by the motion of a single node, which is the rigid body reference point. The elements of the rigid body don't deform but can undergo large motions. The computation of the rigid body is more efficient than that of deformable finite elements, although some computational effort is required to update the motion of the rigid body. For the simulation with Abaqus/Explicit, the time increment is dependent on the element size and the material. The stable time increment in a stiff region may lead to a relatively large global time increment. By applying a rigid body instead of a deformable body, the computational efficiency is improved while the result accuracy is not remarkably affected.

To embed the belt and carcass layers and the bead in the sidewall, it is required to specify embedded regions and a host with the “Embedded element” constraint. The nodes of the embedded elements and the host elements are checked to build geometric relationships. If a node of embedded elements is inside of a host element, the node is constrained with the host element and the values of the displacement are obtained by interpolation according to the host element.

To create a loading or motion point on the tire center, it is required to specify the tire center point as a reference point, which is coupled with the rim surfaces by the “Coupling” constraint. This constraint couples the motion of an assembly of the nodes on surfaces to the motion of a reference node. The loading on the reference node is transmitted to the coupling nodes through weight factors, and the resultant loading at the coupling nodes is equivalent to the loading at the reference point. The motion of the coupled nodes is constrained to that of the reference node.

5.2 Introduction of FE soil models

Soil is a three-phase material consisting of solid soil particles, liquid water and gas. Soil physical properties include permeability, which refers to the ability of a soil to transmit water or air; water-holding capacity, which refers to the quantity of water that the soil is capable of storing; porosity, which refers to the amount of air space or void space between soil particles; soil texture, which is mainly classified into clay, silt, sand and gravel according to the grain size; soil structure, which is usually classified into platy, prismatic, blocky and granular soil according to the arrangement of aggregates [154].

Clay consists of particles smaller than 0.002 mm. Silt consists of particles smaller than 0.063 mm and larger than 0.002 mm. Sand consists of particles smaller than 2 mm and larger than 0.063 mm. Gravel consists of particles smaller than 63 mm and larger than 2 mm. Clay has good water and nutrient holding capacity, but the lack of large pore space restricts water and air movement indicating low permeability. Clay is soft and prone to compaction. Silt has a smooth or floury texture. Lying on the bottom of a lakeshore, silt is light and quite compressible. Sand and gravel particles can transfer compressive stresses, but any tensile stresses can’t be transferred between sand and gravel particles.

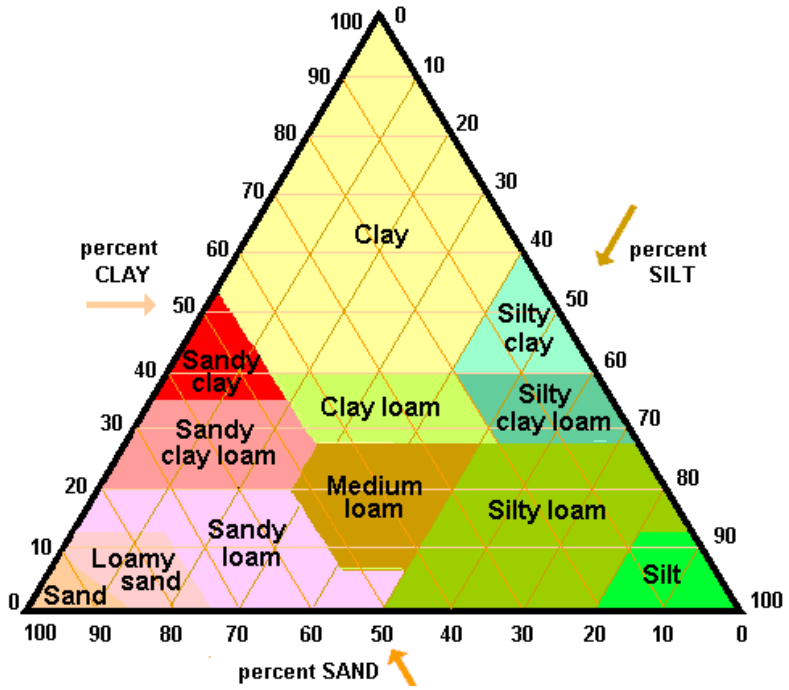

Fig. 5.6: Soil textural triangle (United States Department of Agriculture) [155]

5.2.1 Structure of FE soil models

Two FE soil models were developed in different dimensions. One model in the dimension of 1 m×0.8 m×0.3 m is used for the soil compaction simulations, the other model in the dimension of 2 m×1 m×0.3 m is used for the tire slipping and cornering simulations. The global element size is 10 mm.

As shown in Fig. 5.7, the contact regions have fine elements in the size of 5 mm, and the other regions have coarse elements in the size of 10 mm. The coarse elements which are not close to the contact regions don't play an important role in the simulation. Therefore the element size is increased for sparing memory and improving computation efficiency.

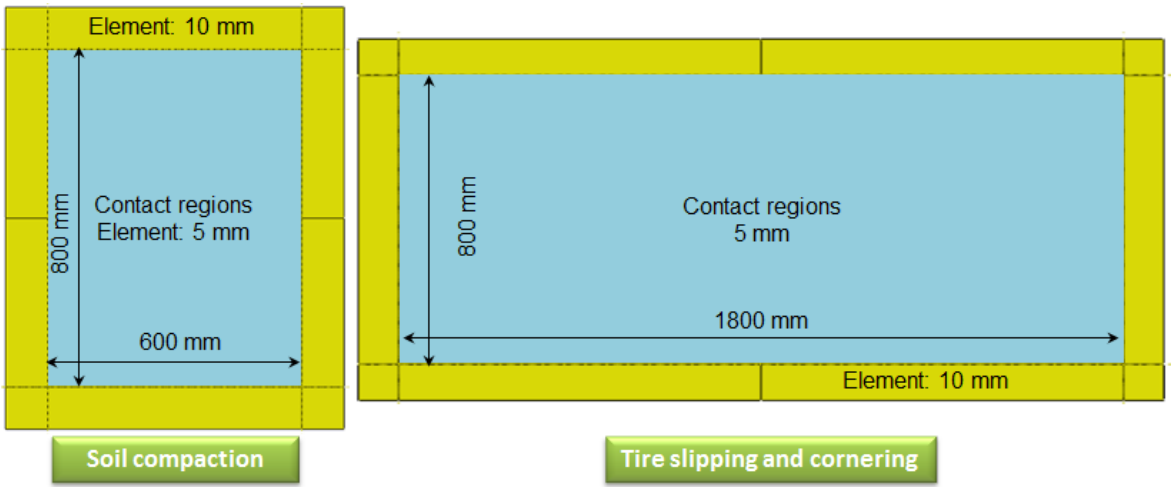

Fig. 5.7: Soil model dimensions

The element type of C3D8R is selected for the solid soil elements. The number of soil elements and nodes are presented in Table 5.6.

Table 5.6: Element number and type of the soil models

	Type	Element Number	Node number	Minimum Size
Soil compaction	C3D8R	1134000	1173966	5 mm
Tire slipping and cornering	C3D8R	2307357	2225664	5 mm

5.2.2 Materials of FE soil models

Soils usually display non-linear mechanical characteristics which can be presented with the elasto-plastic constitutive models in Abaqus. The constitutive models are capable of modeling soil strain-stress behavior before and after soil failure. Two separated elastic and plastic behaviors are involved in displaying soil mechanical characteristics. The critical state of soil failure (yield space) determined by the constitutive models is used for distinguishing the soil stress state. If the stress state is inside the yield space, the soil experiences recoverable deformation indicating that the soil is elastic. If the stress state is outside the yield space, the soil experiences irrecoverable deformation indicating that the soil is plastic.

To represent the soil plastic behavior, several constitutive models are introduced in Abaqus. The prevailing constitutive models are the Mohr-Coulomb (MC) model, the Drucker-Prager (DP) model and the Cam-Clay (CC) model.

Based on plotting Mohr's circle in the plane of the maximum and minimum principle stresses, the MC model is the most commonly applied failure criterion in the geotechnical engineering. The MC model indicates that the material can bear more compression stress than tensile stress before the failure occurs [151]. In the equations describing the MC model (see Fig. 5.8), the second principal stress is not under consideration. Due to the uncontinuous connection at the transition corner in the deviatoric plane, the calculation of the plastic increment is difficult to handle.

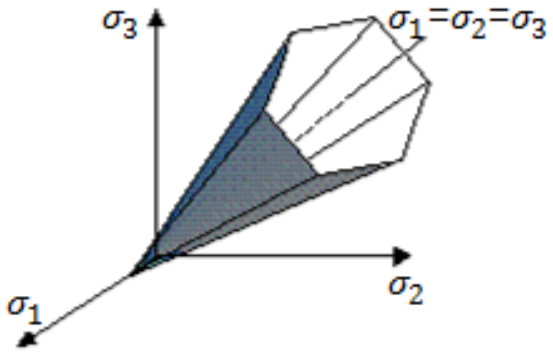

Fig. 5.8: Mohr-Coulomb yield surface [156]

The DP model (sometimes also known as the extended von Mises model) modifies the MC yield function to avoid the singularities associated with the transition corners. Unlike the MC model, the DP yield surface is smooth and plotted as a cylindrical cone in the principal stress space. The DP model can be used to simulate the behavior of rock and granular soil such as sand and gravel [151].

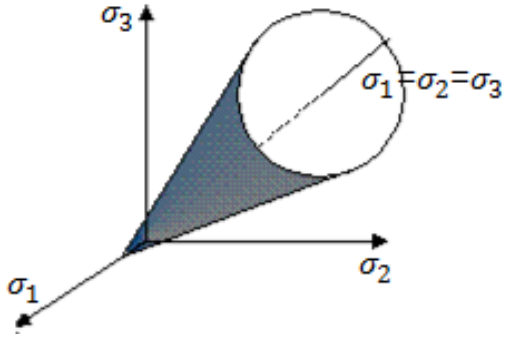

Fig. 5.9: Drucker-Prager yield surface [156]

Roscoe [157, 158] applied the strain hardening theory of plasticity to establish a stress-strain model known as the CC model for the consolidated clay. The CC model (see Fig. 5.10) describes the inelastic behavior by the yield functions depending on the three stress invariants. An associated flow is assumed to define the plastic strain rate for soil dilatant behavior, and a strain hardening theory which is responsible for the size of the yield surface according to the inelastic volumetric strain.

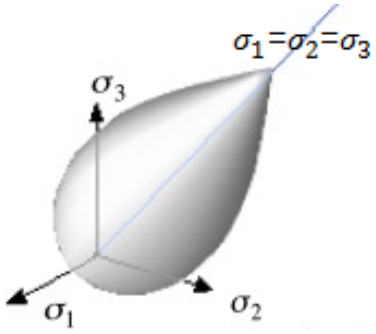

Fig. 5.10: Cam-Clay yield surface [159]

Chiroux [160] used the Young's modulus and the Poisson's ratio to define the soil elasticity, and the "cap plasticity" model to define the soil plasticity in the study of the 3D rigid tire-deformable soil interaction. For the study of cone penetration in the layered soil, Tekeste [161] considered the soil as a non-linear elasto-plastic material which was modeled using the DP model with hardening options. Jozsa [162] applied the same model as Chiroux for the soil elasticity, and the Mohr-Coulomb model for the soil plasticity. It was concluded that the MC model was feasible in the stability simulation. However the soil deformation obtained from the simulation was not accurately predicted compared to the experimental results, the soil plastic model considering the hardening effect could present more precise soil deformation.

The elasticity parameters such as the Young's modulus and the Poisson's ratio were defined in the FE soil model. As an extension of the DP model, the modified Drucker-Prager/Cap (MDPC) model has an additional cap yield surface which is formulated to account for the development of inelastic strains under isotropic compression, to control volume dilatancy and to provide hardening/softening as a function of the inelastic volume. Three segments (a pressure-dependent DP shear failure, a compression cap and a smooth transition region between the shear failure and the cap) consist of the yield surface in the MDPC model shown in Fig. 5.11. This model is able to precisely capture the soil mechanical characteristics under compression and has been used to simulate the responses of a wide range of geologic materials.

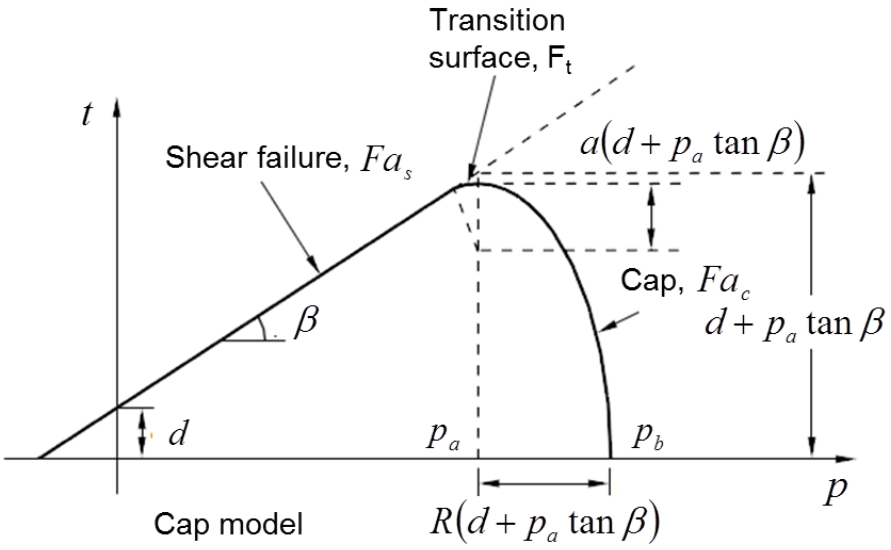

Fig. 5.11: Modified Drucker-Prager yield surface on the meridional plane

$$Fa_S = t - p_e \tan\beta - c \tag{5.6}$$

$$Fa_c = \sqrt{\left(p_e - p_a\right)^2 + \left(\frac{R_S t}{1 + a - a/\cos\beta}\right)^2} - R_S\left(c + p_a \tan\beta\right) = 0 \tag{5.7}$$

$$t = \frac{q}{2}\left[1 + \frac{1}{K_R} - \left(1 - \frac{1}{K_R}\right)\left(\frac{I_3}{\sigma_v}\right)^3\right] \tag{5.8}$$

$$p_e = -\frac{1}{3}\sum_{i=1}^{3}\sigma_i \tag{5.9}$$

$$\sigma_v = \sqrt{\frac{\left(\sigma_1 - \sigma_2\right)^2 + \left(\sigma_2 - \sigma_3\right)^2 + \left(\sigma_1 - \sigma_3\right)^2}{2}} \tag{5.10}$$

$$I_3 = \sigma_1\sigma_2\sigma_3 \tag{5.11}$$

Where

Fa_c cap failure

Fa_s shear failure

t deviatoric stress

p_e equibalent pressure stress

R_s cap eccentricity

K_R flow stress ratio

The hardening/softening effects are presented by the user-defined function which connects the hydrostatic compression yield stress to the volumetric inelastic strain.

The soil parameters defined in Abaqus are displayed in Table 5.7 and 5.8.

Table 5.7: Parameters for soil elasticity and plasticity

Young's Modulus [MPa]	Poisson's ratio	Cap eccentricity R_S	Initial yield surface position $\varepsilon_{vol}^{in}\big\vert_0$
50.5	0.25	0.1	0.001
Soil cohesion [MPa]	Friction angle β [°]	Transition surface radius α	Flow stress ratio K_R
0.113	14.56	0.03	1

Table 5.8: Parameters for soil hardening effect

Yield stress [MPa]	0.02	0.025	0.063	0.13	0.24	0.42	0.61	0.93	2.52
Volumetric inelastic strain	0	0.005	0.01	0.02	0.03	0.04	0.05	0.06	0.1

5.3 Introduction of contact definition

The contact pairs in the FE tire-soil interaction models include rim-sidewall and tread-soil. To formulate the contact behavior in the normal direction, the “hard” contact prohibiting the transfer of tensile stress across the contact interface, was selected in Abaqus. In the “hard” contact, it is defined that when the surfaces are in contact, any contact pressure can be transmitted between them; when the surfaces separate, the contact pressure reduces to zero. To formulate the contact behavior in the tangential direction, the Coulomb friction model transmitting shear stress across the contact interface, was selected. The Coulomb friction model calculates the maximum allowable frictional stress across a contact interface based on the contact pressure between the contacting pairs. In the sticking status, the frictional stress can rise up to a certain magnitude across the contact interface before the contacting pairs start sliding. The critical shear stress defined by the product of contact pressure and friction coefficient determines when the nodes stick or slip on the contact surfaces. An additional sticking stiffness was applied inside the sticking region by default. Constant friction coefficients were assumed to 0.8 for the rim-sidewall contact and 0.6 for the tread-soil contact.

To define a contact pair, it is required to assign the master and the slave surfaces interacting with one another. For the assignment of the master and slave surface, it is preferred that if a surface of a soft body contacts a surface of a stiff body, the soft surface is chosen as the slave surface; if the stiffness difference is hard to be distinguished, the smaller surface is chosen as the slave surface.

As shown in Fig. 5.12, the contact pairs in terms of master and slave surfaces were assigned in the FE tire models. The rim is stiffer than the sidewall, hence it is selected as master surface and the sidewall is assigned as slave surface. To formulate the contact, the surface to surface discretization considers the geometry of both the master and slave surfaces in the contact region. Contact conditions are

enforced in an average sense over the slave surface. The contact direction is determined by averaging the normal direction of the slave surface in the region surrounding a slave node.

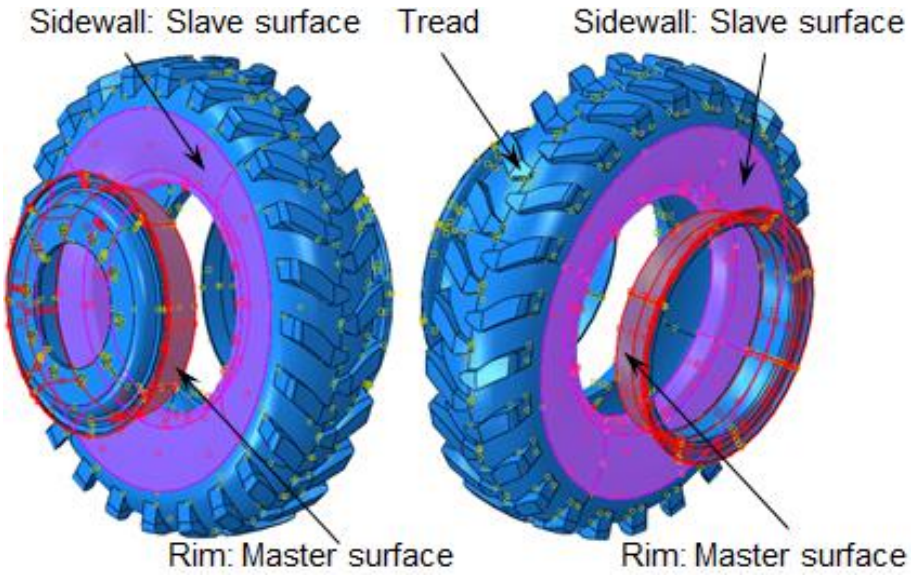

Fig. 5.12: Rim-sidewall contact

To use the contact pair algorithm for the definition of the tread-soil contact, it is required that every selected contact surface has to be continuous. However each tread surface is separated and another contact algorithm should be used. The general contact algorithm using sophisticated tracking algorithms ensures that all proper contact pairs are enclosed and enforced, and the penalty method for controlling the sticking stiffness is selected by default. By using the general contact, it isn't necessary to specify any contact pairs.

5.4 Explicit and Implicit Methods in Abaqus

To find solutions to partial differential equations, these equations are completely eliminated or rendered into an approximating system of ordinary differential equations, which are numerically integrated using standard mechanical procedures. Generally Abaqus/Standard is applied for the analysis of quasi-static simulations, and Abaqus/Explicit is applied for the analysis of dynamic simulations.

Explicit methods calculate the state of a system at a later time from the state of the system at the current time, while implicit methods find a solution by solving an equation involving both the current state of the system and the later one. In some cases where the application of explicit methods requires impractical small time steps to keep the error in the bounded result, the implicit method is more practical, accurate

and less time consuming with larger time steps. However whether to use explicit or implicit methods is dependent on the specific problems investigated.

Implicit methods are provided in Abaqus/Standard using the Hilber-Huges-Taylor operator for the integration of motion equations, while in Abaqus/Explicit uses the central-difference operator. In an implicit dynamic analysis the integration matrix must be inverted and a set of non-linear equilibrium equations must be solved at each time increment. In an explicit dynamic analysis displacement and velocities are calculated in terms of quantities that are known at the beginning of an increment, therefore the global mass and stiffness matrices needn't to be formed and inverted, which means that each increment is relatively inexpensive compared to the increments of the implicit scheme. The size of time step in an explicit dynamic analysis is limited due to the conditional stability of central difference. However there is no limitation on time step size due to unconditional stability of the Hiber-Huges-Taylor operator in the implicit method.

5.5 Simulations performed with Abaqus

In this work, the simulations performed with Abaqus consist of "Tire assembling", "Tire inflating", "Tire loading", "Soil compaction", "Pure longitudinal slip", and "Pure lateral slip".

In the "Tire assembling" simulation, the two separated rim parts were moved towards each other until the specified positions were reached so that the rim holds the tire preventing it from popping out. In the "Tire inflating" simulation, the tire center was fixed indicating any degrees of freedom were constrained, and constant inflation pressures were applied to the inner face. In the "Tire loading" simulation, vertical displacements were defined on the tire center so that the tire moved towards a rigid plate at the bottom, and the relationship between tire deformation and vertical load was established.

In the "Soil compaction" simulation, a translational displacement in the vertical direction was defined on the tire center leading to the soil compaction. The relationship of tire deformation/soil compaction-vertical load was established. In the "Pure longitudinal slip" simulation, a constant rotational velocity and various longitudinal velocities were defined on the center to generate different slip ratios. The slip – longitudinal force relationship was established. In the "Pure lateral slip" simulation, constant rotational and longitudinal velocities were defined to ensure that

the longitudinal slip equals to zero. Lateral velocities were defined to generate different slip angles for the study of the slip angle – lateral force relationship.

Since the first three groups of simulations are quasi-static equilibrium computations and involved with small element deformations, it is optimal to perform such simulations with the Abaqus/Implicit. The last two groups of simulations are quasi-static (soil compaction) and dynamic (pure longitudinal/lateral slip) computations, and involved with large element deformation, it is optimal to perform such simulations with the Abaqus/Explicit. To improve the simulation stability and efficiency, the coupling of Abaqus/Implicit and Explicit were also applied. As shown in Fig. 5.13, the simulation results including the stress, strain and parts positions from the Abaqus/Implicit were imported to the tire-soil interaction models in the Abaqus/Explicit as initial state.

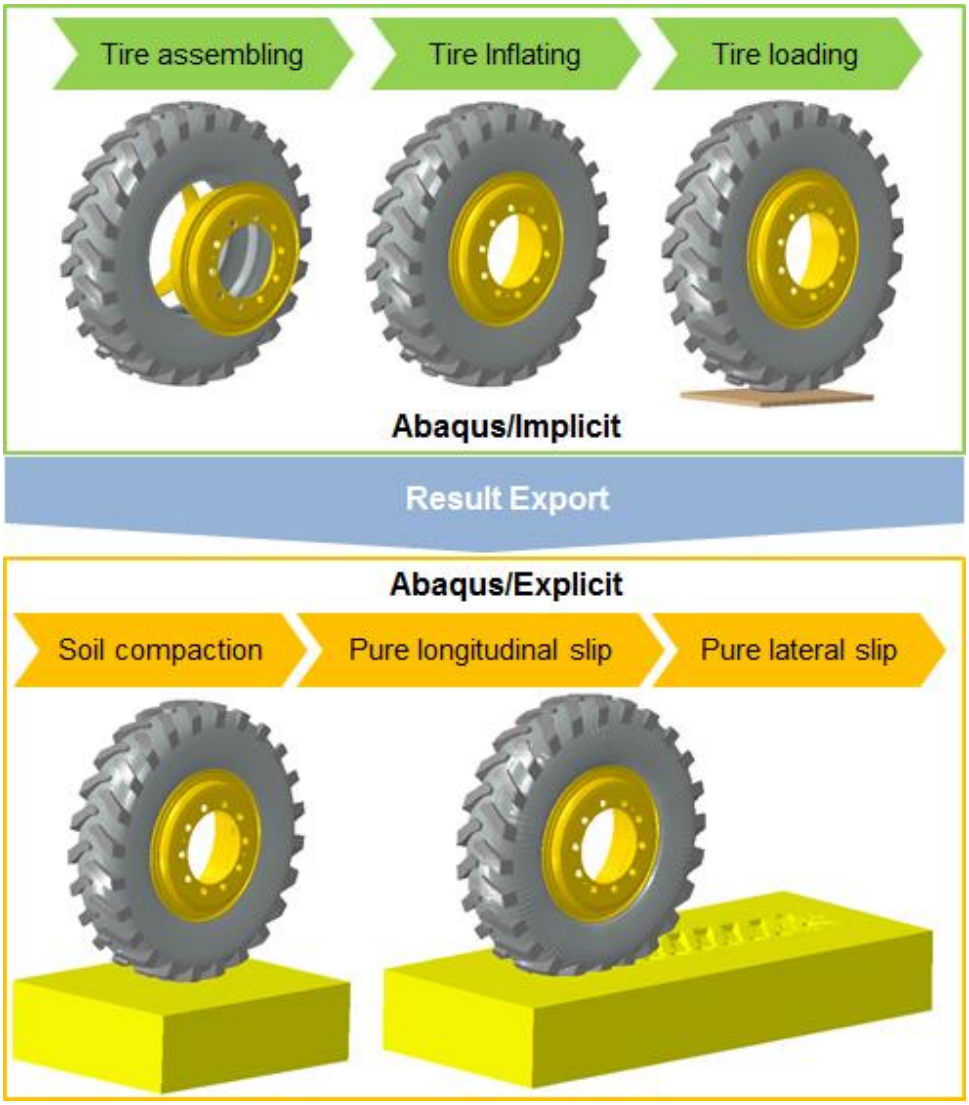

Fig. 5.13: Flow chart of simulation procedures

5.5.1 Simulation of tire assembling

The FE tire models were developed based on the geometry of the unassembled tire. It is impossible to get converged solutions if the tire is in the assembled status. To simulate the tire assembling, the rim was separated by two parts moving towards each other as displayed in Fig. 5.14. The distance between the tire center and the separated rim parts is 200 mm.

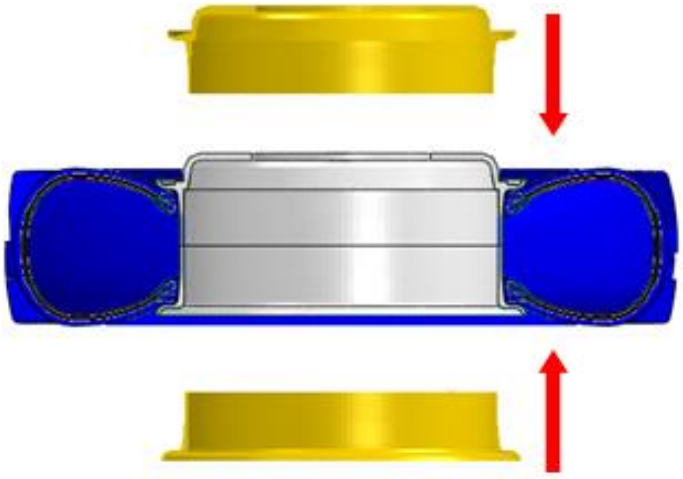

Fig. 5.14: FE model of tire assembling

The pre-load applied on both sides of the rim to keep the tire from popping out is displayed in Fig. 5.15. In this figure, it is observed that when the rim displacement is around 188 mm, the rim parts are in contact with the tire sidewall; as the displacement of the rim parts increases further to 199 mm, the pre-load generated by the response of the tire sidewall is linearly proportional to the rim displacement.

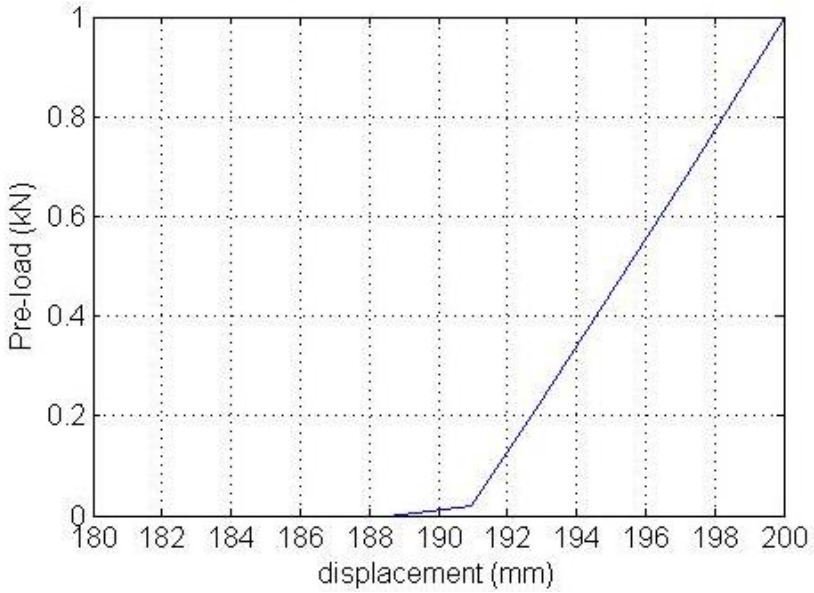

Fig. 5.15: Pre-load due to tire assembling

According to the simulation results, the bead plays an important role in preventing the tire from escaping from the rim, since it bears the maximum stress. The simulation results for the uneven-spaced and even-spaced FE tire model are compared in the Fig. 5.16.

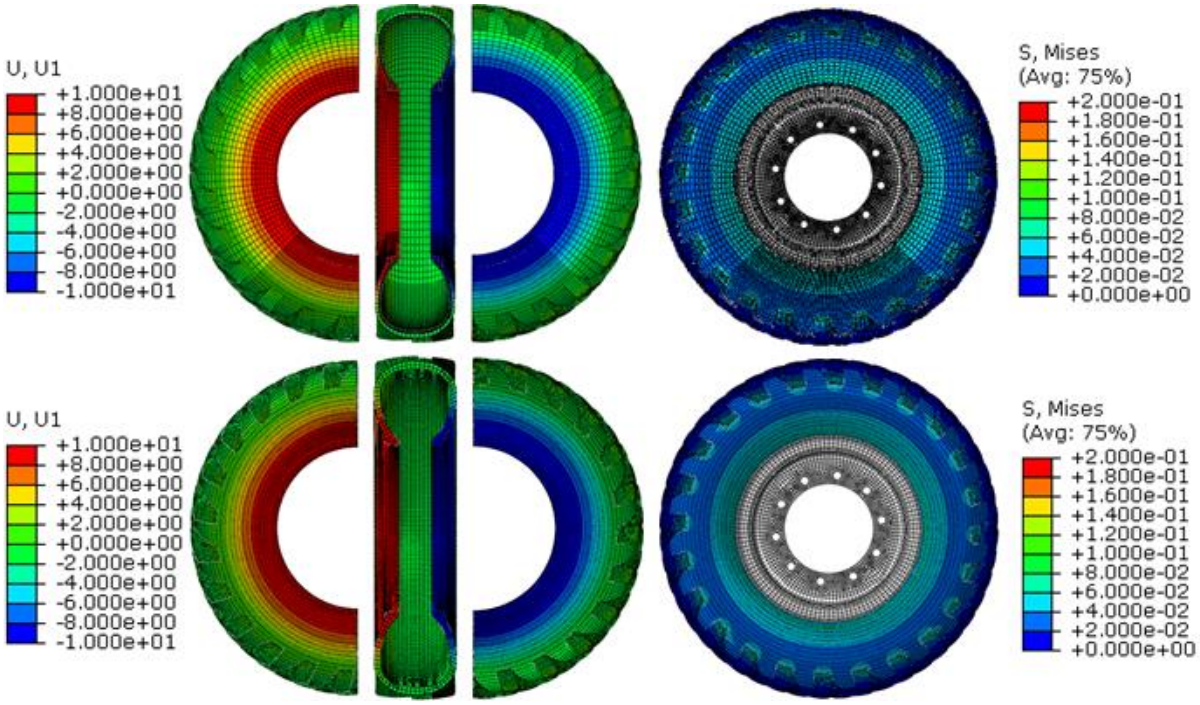

Fig. 5.16: Simulation results for uneven-spaced and even-spaced FE tire model

As these two FE tire models have the same structure and material properties, the sidewall deformation, stress distribution and pre-load caused by the rim compression are the same. However the memory required by the even-spaced FE tire model is twice more than that required by the uneven-space FE tire model. The computation time for these two tire models is compared in Fig. 5.17.

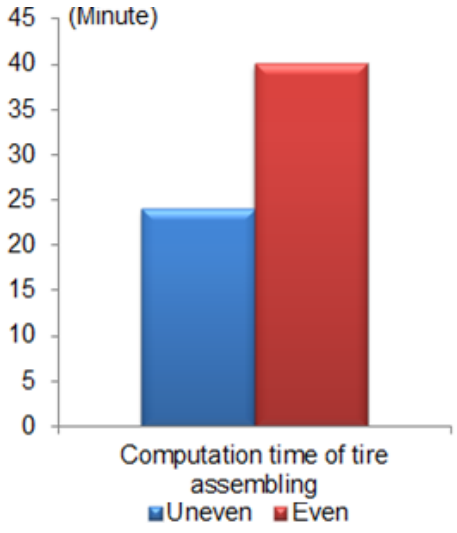

Fig. 5.17: Computational time of tire assembling simulation

5.5.2 Simulation of tire inflating

As the simulation started, the final part status in the tire assembling simulation, which included stress, strain, position and material properties, was transferred to the tire inflating model as initial status. The rim which was separated in the last mentioned simulation was integrated as one object by coupling these two rim parts. Constant inflation pressures were uniformly distributed on the tire cavity side.

Both the uneven and even-space tire models were used for the tire inflating simulation. The simulation results with these two models at the inflation pressure of 500 and 700 kPa are presented in the following figures.

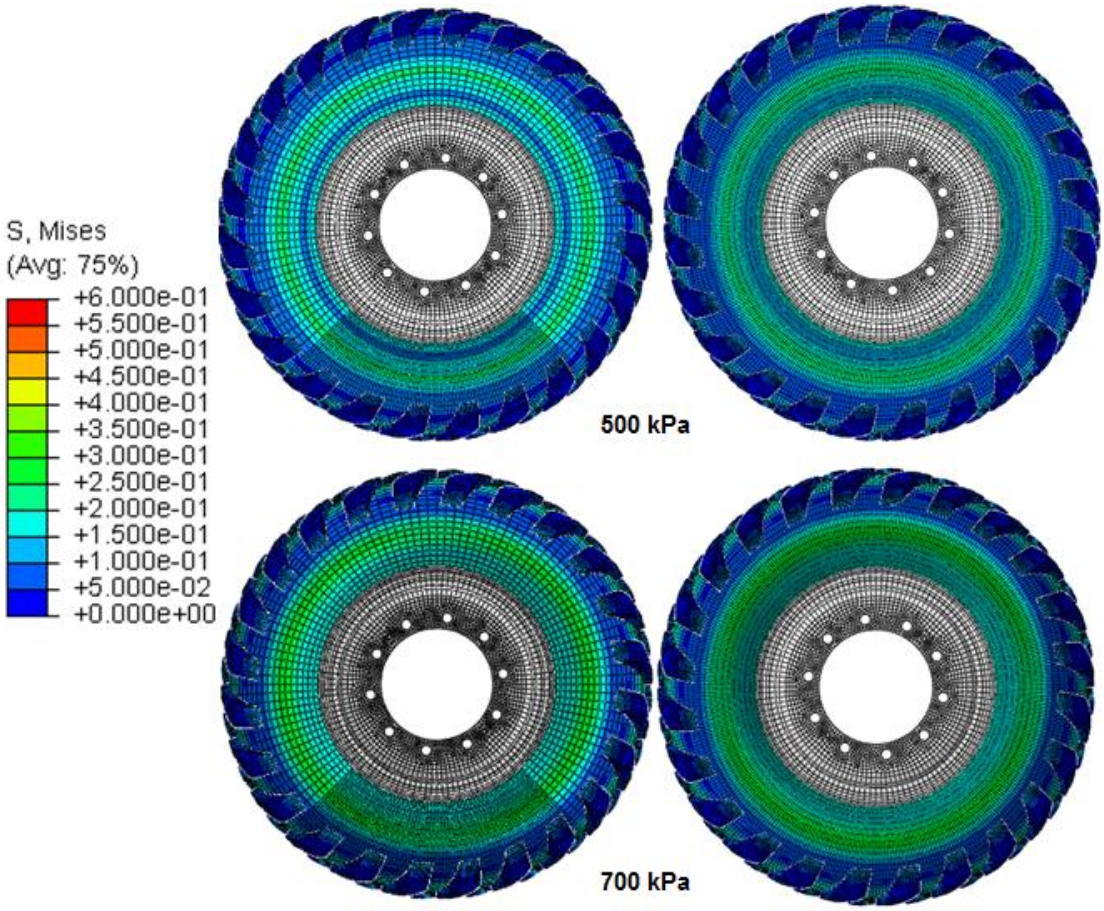

Fig. 5.18: Von Mises stress distribution in the uneven and even-spaced tire models

As shown in Fig. 5.18, the von Mises stress developed in the sidewall and tread for the uneven and even-spaced tire models is quite similar. At the inflation pressure of 500 kPa, the majority of the von Mises stress is approximately 0.18 MPa; at the inflation pressure of 700 kPa, the majority of the von Mises stress is approximately 0.22 MPa.

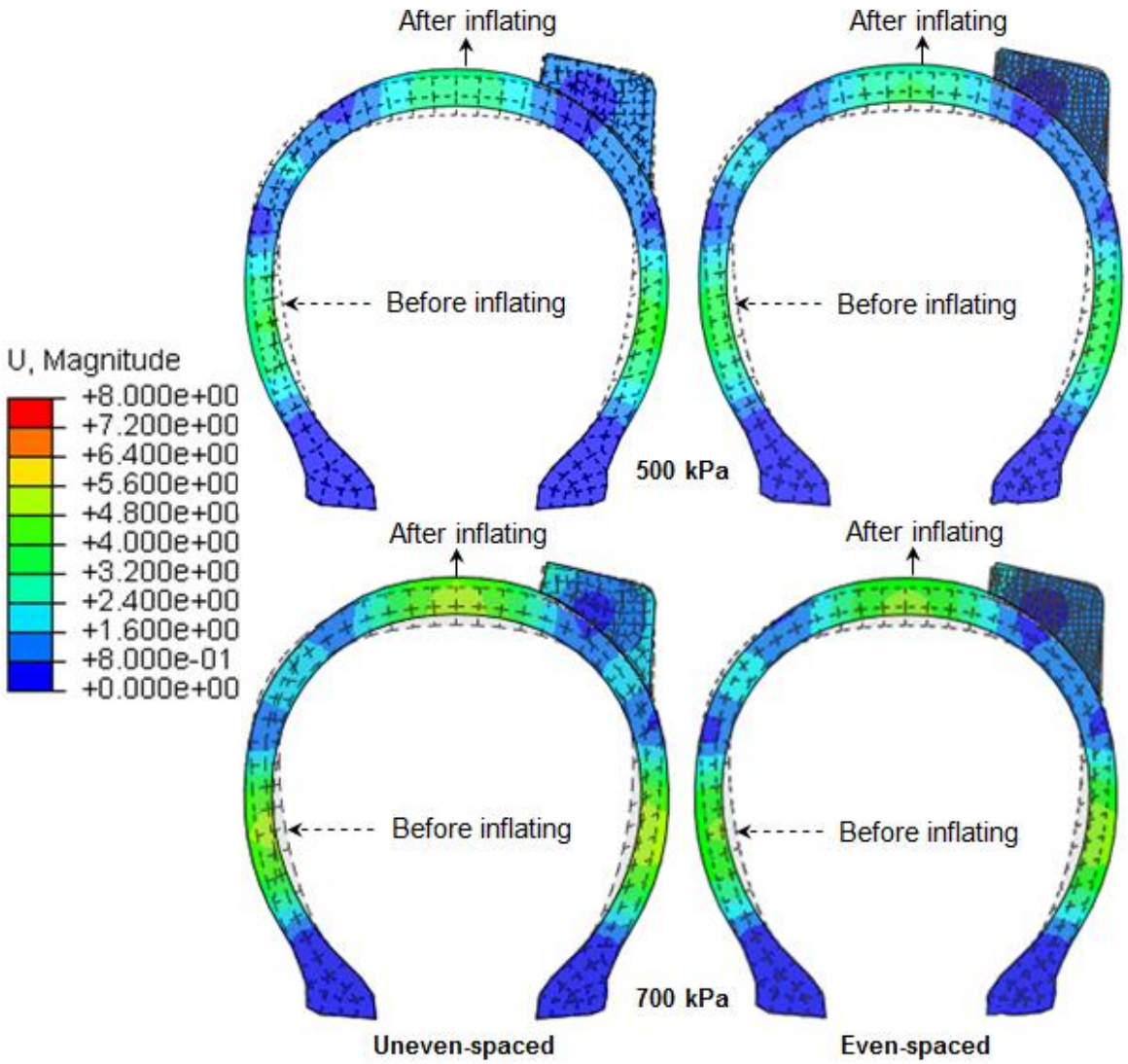

Fig. 5.19: Deformation of the uneven and even-spaced tire models

As shown in Fig. 5.19, the dotted line represents the tire contour before inflating, and the solid line represents the tire contour after inflating. At the inflation pressure of 500 kPa, the tire sidewall expansion is approximately 4.0 mm at the left and right side, the tire shoulder expansion is approximately 3.6 mm at the top; at the inflation pressure of 700 kPa, the tire sidewall expansion is approximately 4.8 mm at the left and right side, the tire shoulder expansion is approximately 4.5 mm at the top. At the inflation pressure of 500 and 700 kPa, the deformation for the uneven and even-spaced tire model is in good quantitative agreement.

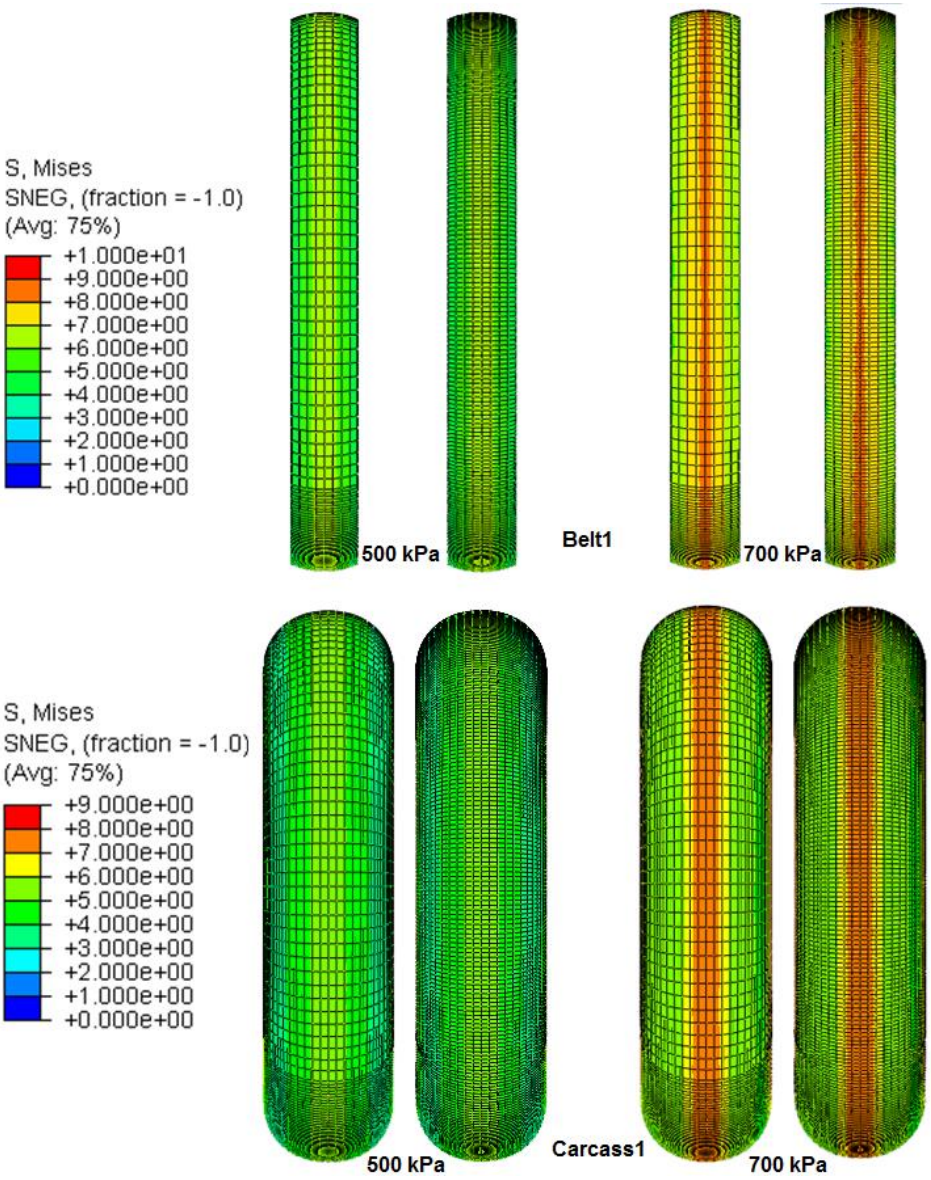

Fig. 5.20: Von Mises stress distribution in the belt and carcass

The von Mises stress distribution at the first belt and the first carcass layer is presented in Fig. 5.20. Compared to the tire sidewall, the belt and the carcass layer endure larger stress. At the inflation pressure of 500 kPa, the maximum von Mises stress at the first belt and the first carcass layer is approximately 6.5 MPa, and approximately 9 MPa at the inflation pressure of 700 kPa. At both inflation pressures, the belt and carcass stress distribution for the uneven and the even-spaced tire model is in good quantitative agreement.

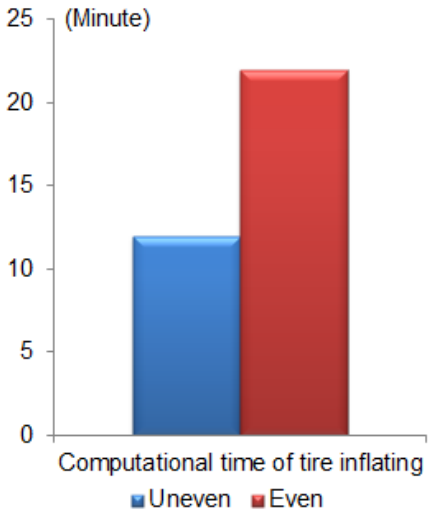

Fig. 5.21: Computational time of tire inflating simulation

The computation time of the tire inflation simulation for the uneven and even-spaced tire model is 12 and 23 minutes respectively. Concluded from the figures mentioned above, the uneven-spaced tire model is more efficient without degrading the accuracy of simulation results.

5.5.3 Simulation of tire loading

In the simulation of tire loading, a hard plate in the dimension of 1 m × 0.8 m × 0.03 m was placed underneath the tire as displayed in Fig. 5.22, and the finite element size of the hard plate was 5 mm. The tire inflation pressure applied on the tire cavity side was assumed to be constant regardless of the changing volume caused by the tire deformation. Before a vertical load was applied to the tire center, a contact simulation step was required to solve convergence problems. In the contact simulation step, a vertical displacement defined on the tire center enforced the tire moving downwards until the contact between the tire and the hard plate occurred.

Fig. 5.22: FE model for the tire loading simulation

The simulation results at the inflation pressure of 500 and 700 kPa are presented in the following figures.

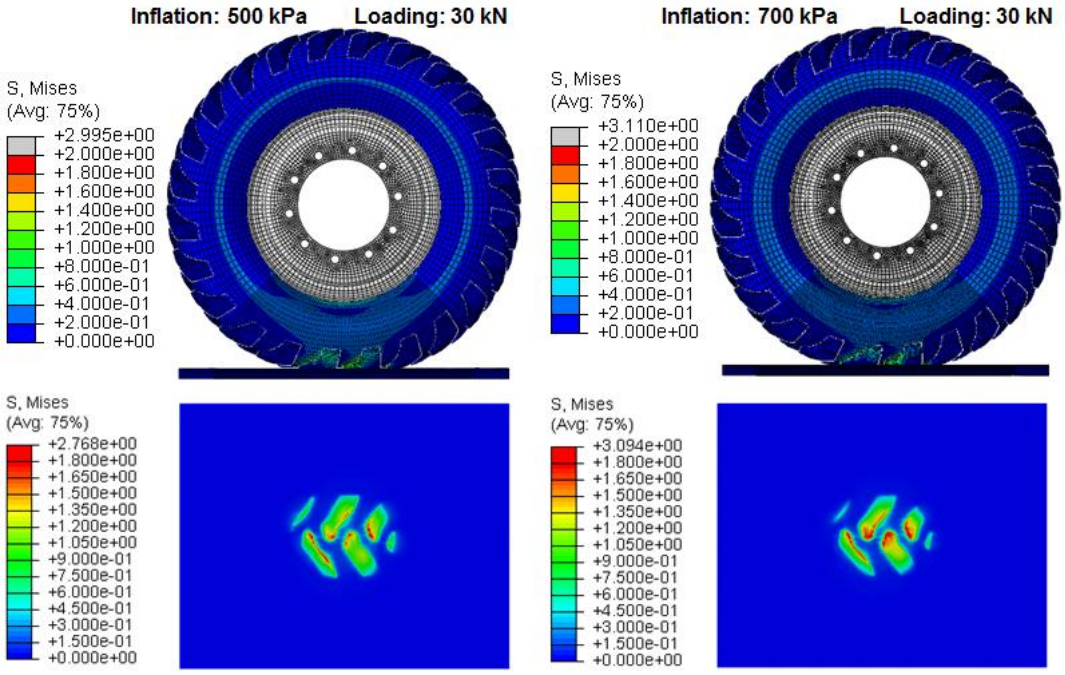

Fig. 5.23: Von Mises stress in the tire loading simulation

Fig. 5.23 indicates that the maximum von Mises stress in the uneven-spaced tire and hard plate is larger at the larger inflation pressure for the same wheel load. The bottom tire part which is near to the tire – rigid plate interaction interface endures larger von Mises stress.

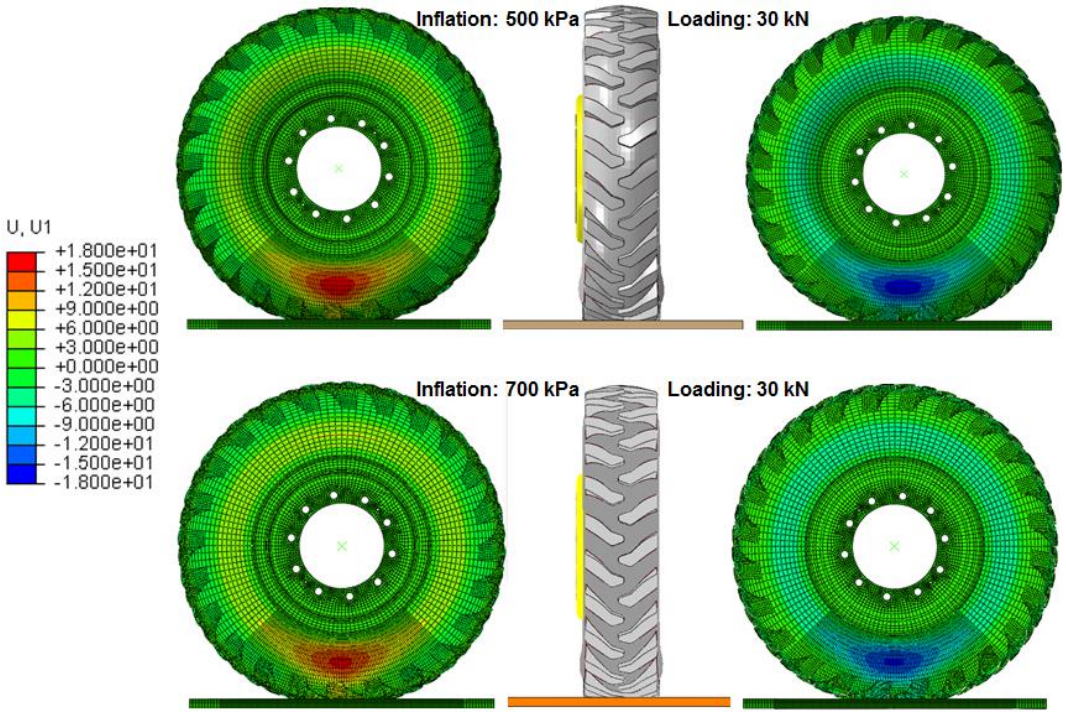

Fig. 5.24: Tire lateral deformation in the tire loading simulation

The tire deformation in the lateral direction is displayed in Fig. 5.24. The lateral tire deformation is approximately symmetric to the tire central plane. At the wheel load of 30 kN, the maximum tire deformation for the inflation pressure of 500 and 700 kpa is 17.98 and 16.62 mm in the lateral direction respectively. At the same wheel load, the lateral tire deformation is larger for lower inflation pressures.

The customed equations in the form of ax^n are applied to fit the curves in Fig. 5.25 and 5.26. Eq. (5.12) and (5.13) are used for predicting tire deformation at specific wheel loads; Eq. (5.14) and (5.15) are used for predicting contact area at specific wheel loads. The coefficients in the equations obtained from the curve fitting are listed in Table 5.9. Since the coefficients of determination R^2 are near to 1, the fitting quality is high. With the equations of the fitting curves, simulation results such as the tire deformation, the contact area and the wheel load for the inflation pressure of 500 and 700 kPa can be restored as look-up tables which could be applied to determine the wheel load as the tire deformation or the contact area are known. Furthermore a simplified tire – hard ground interaction model to predict the tire mechanical behavior in the vertical direction could be derived based on the equations of the fitting curves.

$$F_z = 0.1506\ f_0^{1.444} \tag{5.12}$$

$$F_z = 0.1978\ f_0^{1.45} \tag{5.13}$$

$$F_z = 1.879\times10^{-5}\ A_c^{1.424} \tag{5.14}$$

$$F_z = 3.756\times10^{-5}\ A_c^{1.381} \tag{5.15}$$

Where

f_0 tire deformation A_c contact area

F_z wheel load

Table 5.9: Coefficients in the stiffness and contact pressure equation

Inflation pressure [kpa]	**Tire deflection-Wheel load**			**Contact area-Wheel load**		
	a [kN/mm^n]	n	R^2	a [kN/mm^{2n}]	n	R^2
500	0.1506	1.444	0.9991	1.879×10^{-5}	1.424	0.9973
700	0.1978	1.450	0.9995	3.756×10^{-5}	1.381	0.9985

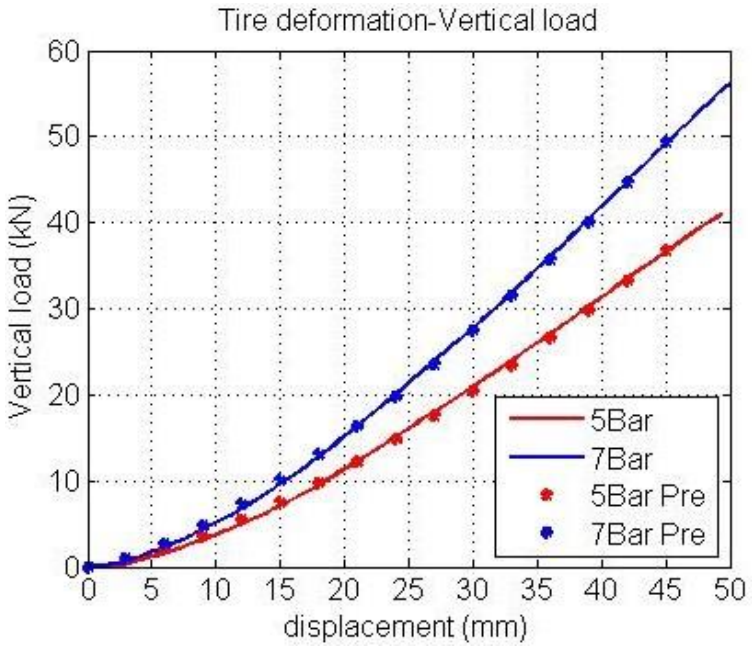

Fig. 5.25: Tire vertical stiffness at the inflation pressure of 500 and 700 kPa

The curve of the tire deformation and wheel load relationship is nonlinear, which indicates that the tire vertical stiffness varies with the tire vertical deformation. Fig. 5.25 displays that the stiffness increases with the vertical deformation and the inflation pressure. The points represent the predicted tire stiffness curves obtained from the derived equations.

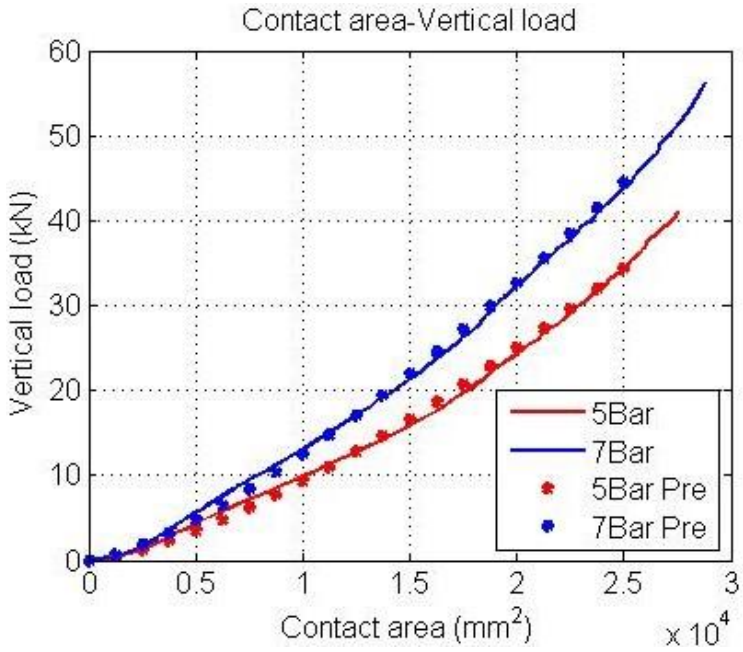

Fig. 5.26: Relationship of contact area and vertical load

The curve of the contact area and wheel load relationship is nonlinear as well. Fig. 5.26 indicates that with the increasing of wheel load and the decreasing of

inflation pressure, the contact area tends to increase. The points represent the predicted contact area-wheel load curves obtained from the derived equations.

5.5.4 Simulation of soil compaction

In the simulation of soil compaction, a soft soil model in the dimension of 1 m × 0.8 m × 0.3 m was placed underneath the tire, and the minimum size of soil elements was 5 mm. The results (strain, stress, parts position) of the tire inflating simulation, which was performed before in Abaqus/Implicit, were imported into the initial step of this simulation. The tire inflation pressure applied on the tire cavity side was assumed to be constant regardless of the changing volume caused by the tire deformation. To simulate the tire-soil interaction, a vertical displacement (70 mm) defined on the tire center enforced the tire moving downwards, and the soil reacting forces was outputted for the further analysis. The simulation objects are to study soil compaction and tire deformation at various wheel loads for different inflation pressures.

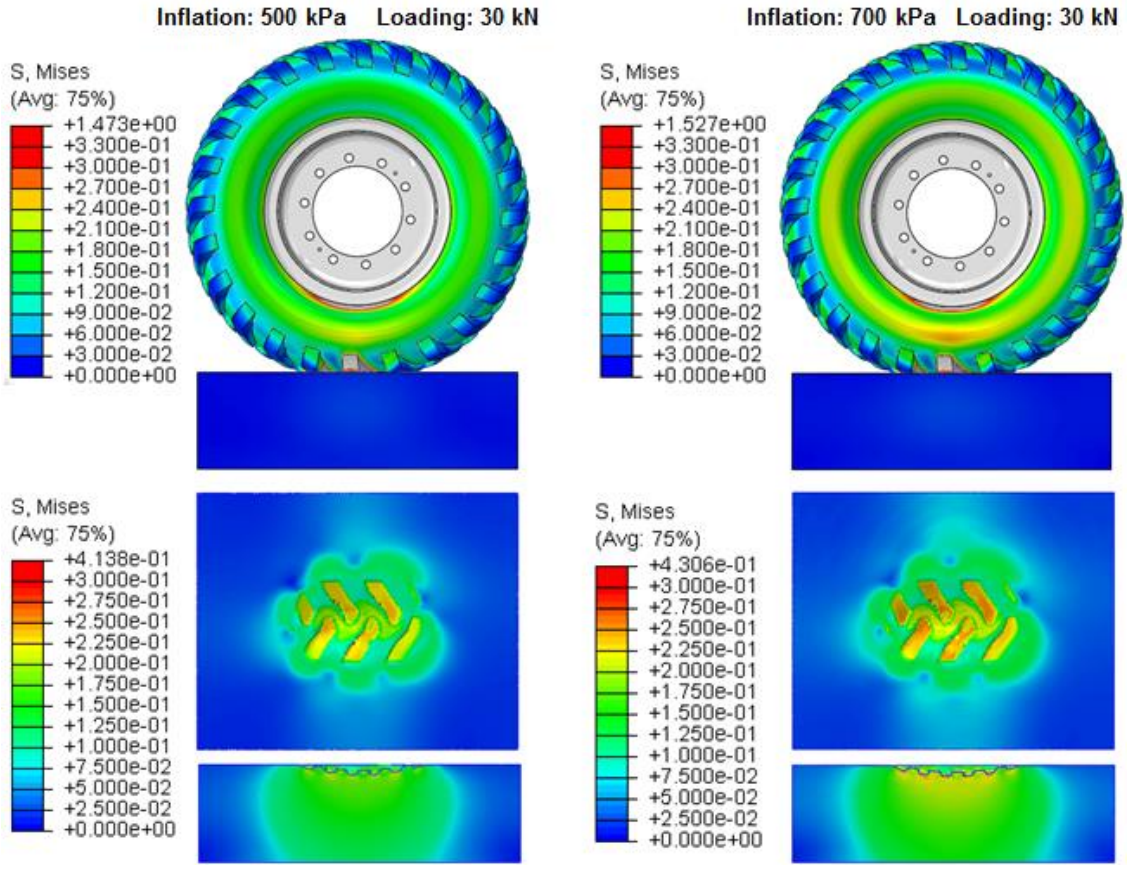

Fig. 5.27: Von Mises stress in the soil compaction simulation

As observed in Fig. 5.27, the von Mises stress locating around the tire-soil contact interface is larger than the other regions. At the same wheel load, the maximum von

Mises stress locating in the tire-soil interaction interface are larger for the larger inflation pressure.

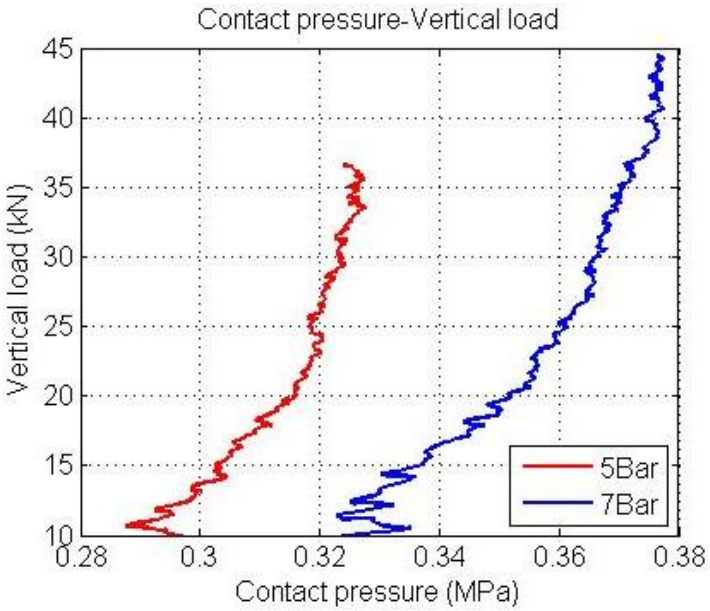

Fig. 5.28: Relationship of contact pressure and wheel load

The average contact pressure in the tire-soil interface increases with the wheel load and the inflation pressure. As observed in Fig. 5.28, the increasing rate of the contact pressure slows down as the wheel load increases.

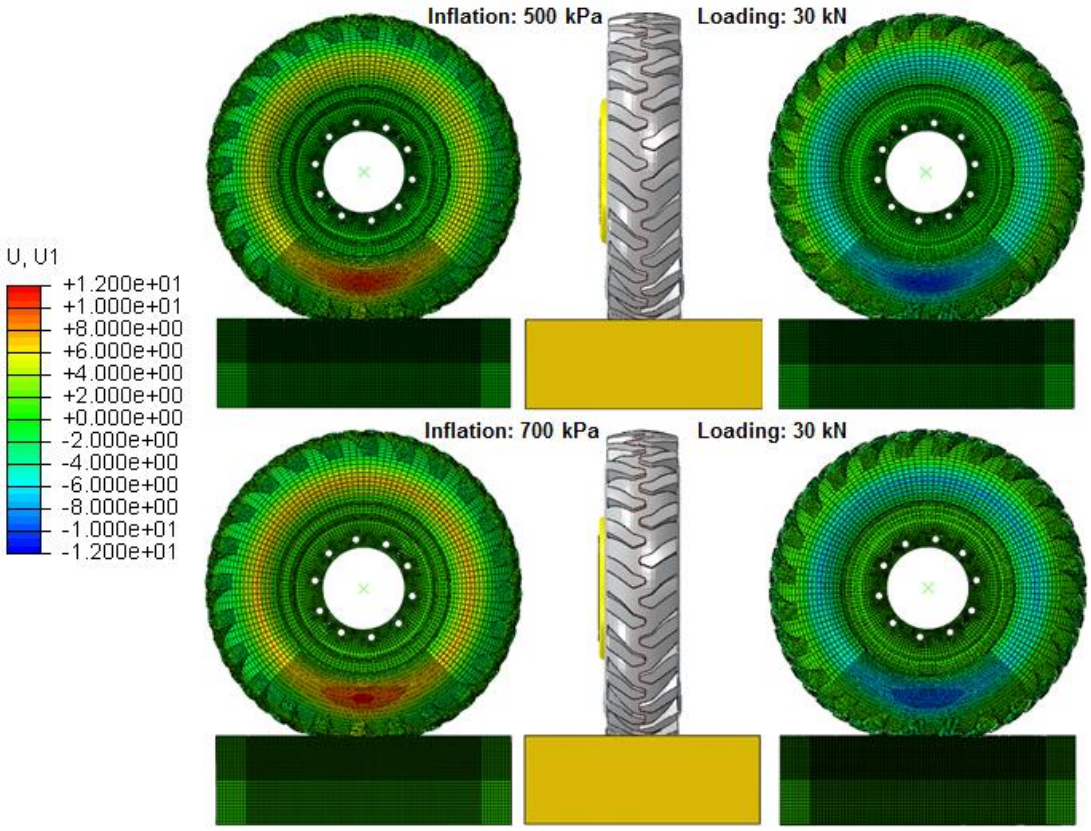

Fig. 5.29: Tire deformation in the soil compaction simulation

Fig. 5.29 shows that the tire deformation in the lateral direction is approximately symmetric to the tire central plane. At the larger inflation pressure, the tire tends to be stiffer, therefore it is noticed that the lateral deformation is remarkably less for the inflation pressure of 700 kPa.

The customed equations in the form of ax^n are applied to fit the curves in Fig. 5.30. The coefficients in the equation for the curve fitting are listed in Table 5.10. The coefficients of determination R^2 are near to 1, which means the fitting quality is high. With the equations of the fitting curves, simulation results such as the tire deformation and the soil compaction for the inflation pressure of 500 and 700 kPa can be restored as look-up tables and be applied to determine the wheel load as the tire deformation or the soil compaction are known. Furthermore a simplified tire-soil interaction model to predict the tire mechanical behavior in the vertical direction could be derived based on the equations of the fitting curves.

$$F_z = 0.378\ f_0^{1.405} \tag{5.16}$$

$$F_z = 0.434\ f_0^{1.506} \tag{5.17}$$

$$F_z = 0.401\, z_e^{1.299} \tag{5.18}$$

$$F_z = 0.323\, z_e^{1.297} \tag{5.19}$$

Where

f_0 tire deformation

z_e soil compaction

Table 5.10: Coefficients in the deformation-wheel load equation

Inflation pressure [kpa]	**Tire deformation-Wheel load**			**Soil compaction-Wheel load**		
	a [kN/mm^n]	*n*	R^2	*a* [kN/mm^n]	*n*	R^2
500	0.378	1.405	0.999	0.401	1.299	0.994
700	0.434	1.506	0.999	0.323	1.297	0.999

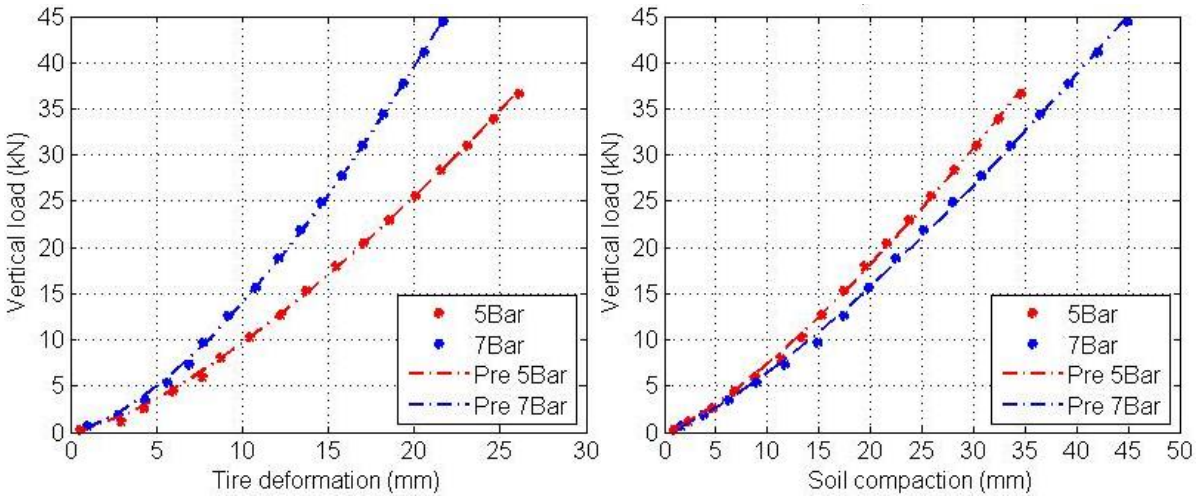

Fig. 5.30: Relationship of tire deformation/soil compaction and wheel load

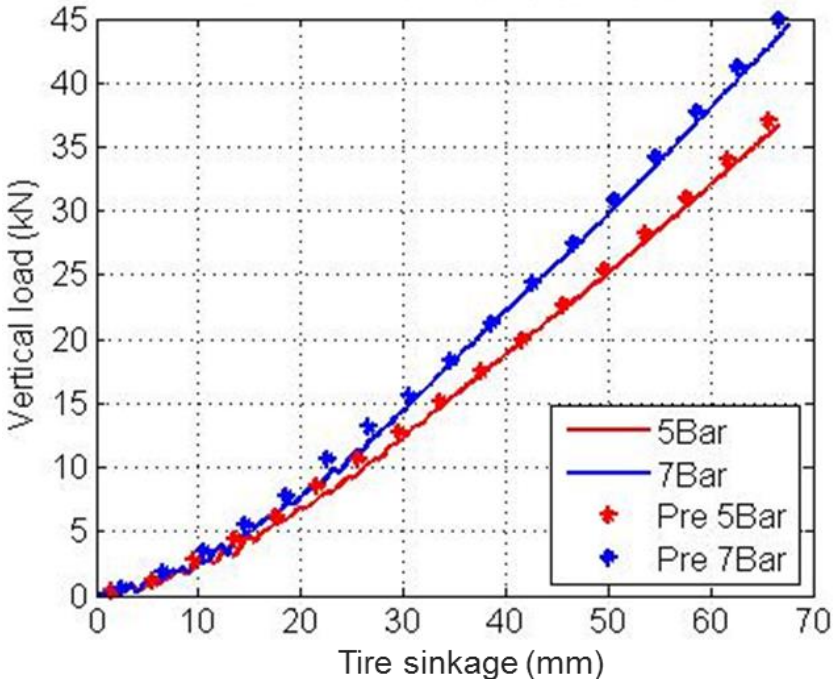

Fig. 5.31: Relationship of total deformation and wheel load

As shown in Fig. 5.30 and 5.31, the curves of the tire deformation/soil compaction/total deformation – wheel load relationship are nonlinear. As mentioned before, the tire tends to be stiffer when the inflation pressure increases, which results in less tire deformation and more soil compaction. The points in the figures are the predicted results obtained from the derived equations.

5.5.5 Simulation of pure longitudinal slip

In the simulation of pure longitudinal slip, a soft soil model in the dimension of 2 m × 0.8 m × 0.3 m was placed underneath the tire, and the minimum size of the soil elements was 5 mm. Constant tire inflation pressures were applied on the tire cavity

side, and constant wheel loads were applied on the tire center. To simulate the pure longitudinal slip, a constant rotational velocity of 2 rad/s and various translational velocities in the longitudinal direction were defined on the tire center for generating different longitudinal slips. The simulation objects are to study the influence of longitudinal slip on the tire mobility such as longitudinal force at various wheel loads for different inflation pressures.

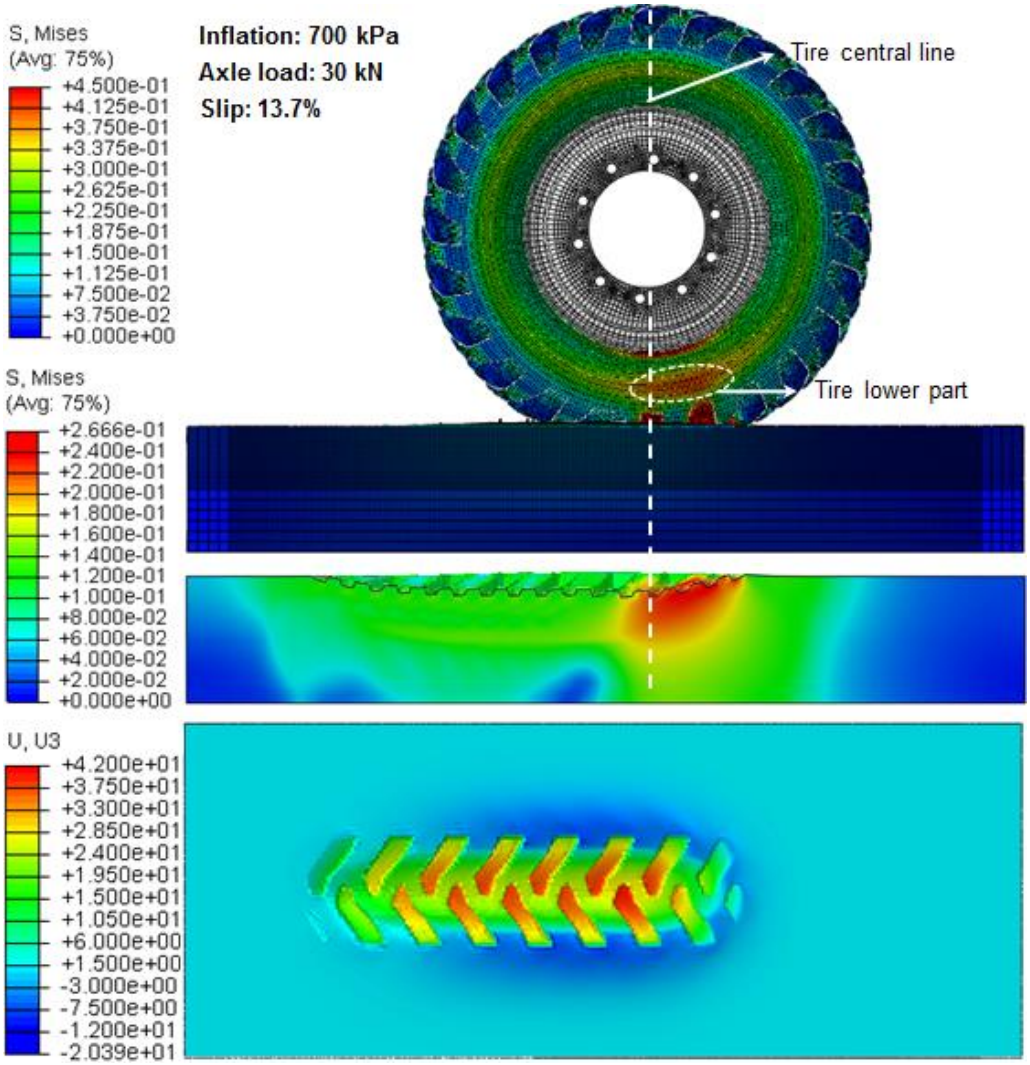

Fig. 5.32: Von Mises stress and soil deformation in the pure slipping simulation

As observed in Fig. 5.32, larger von Mises stresses locate around the lower tire region marked with the white circle which is near to the tire-soil contact interface. The maximum von Mises stress on the tire-soil contact interface is not directly at the tire bottom but in front of the tire central line. Due to the larger contact stress, the soil deformation is larger compared to that in the soil compaction simulation at the same wheel load and inflation pressure.

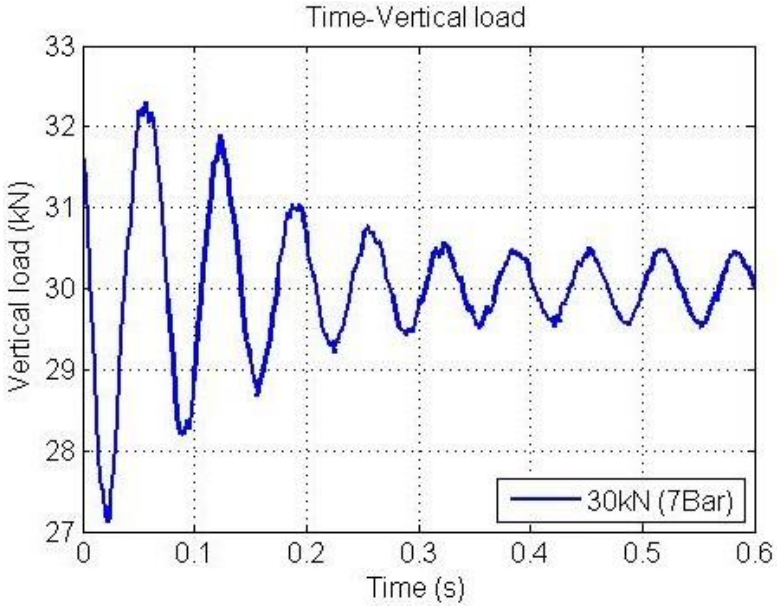

Fig. 5.33: Variation of vertical force along time axis at the 13.7 % slip

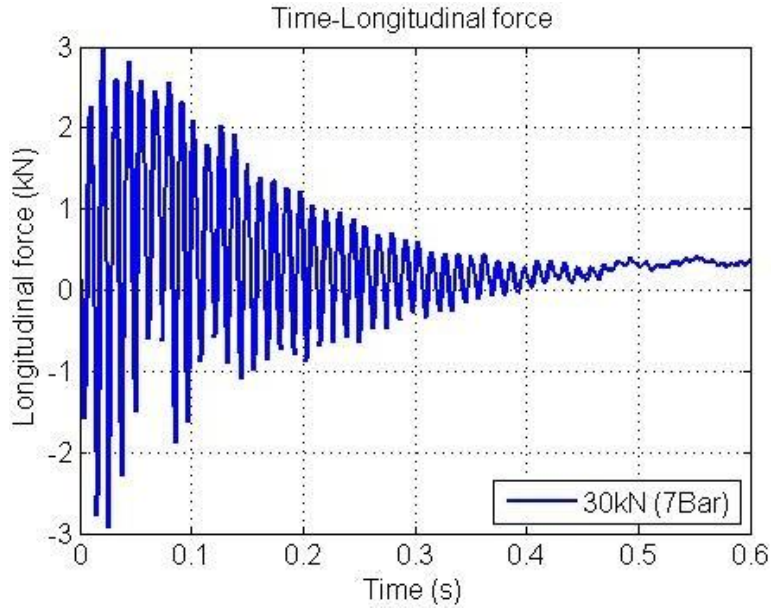

Fig. 5.34: Variation of longitudinal force along time axis at the slip of 13.7 %

As the tire starts rotating, vibrations are observed in the vertical and the longitudinal direction, as displayed in Fig. 5.33 and 5.34. As the simulation time increases, the amplitudes of the vertical and the longitudinal force decrease due to the damping effect of the tire-soil contact.

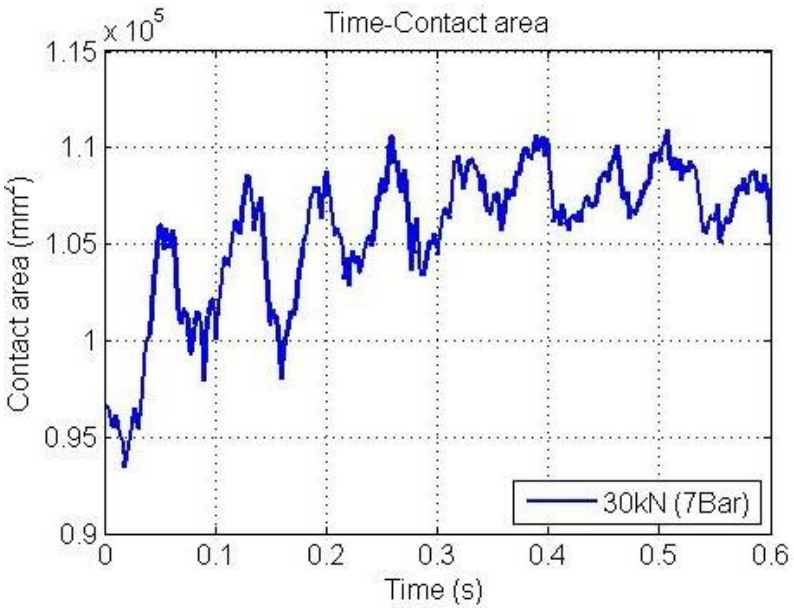

Fig. 5.35: Variation of contact area along time axis at the slip of 13.7 %

As observed in Fig. 5.35, the contact area increases during the transition from standing to slipping. The relative movement between the tire and the soil introduces more shear stresses which enlarge the contact pressure on the tire-soil contact interface and results in the increasing of the soil compaction and the contact area.

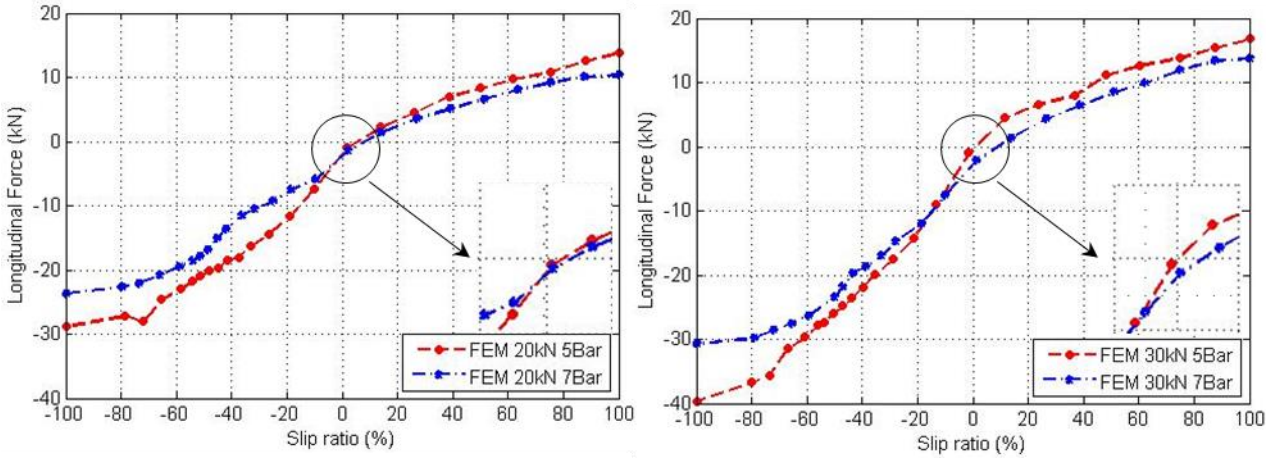

Fig. 5.36: Relationship of longitudinal slip – longitudinal force

Fig. 5.36 shows that at a slip equal to 0, additional traction force is required to overcome the soil obstacle in front of the tire. For the operating conditions such as full sliding and full spinning, the absolute values of the longitudinal forces are remarkably different. When the tire accelerates on the soft soil, the soil is pushed to the tire rear region at the contact patch, and a “small hill” is formed behind the tire. As the slip between the tire and the soil becomes larger, more shear stress in the contact patch is generated leading to a larger drawbar pull. When the tire brakes on

the soft soil, not only a “small hill” is formed in front of the tire but also the shear stress is generated by the slip hinder the tire movement, hence the magnitude of the braking force is larger than that of the drawbar pull at the same magnitude of longitudinal slip. It is also noticed that for the lower inflation pressure, drawbar pull and braking force generated in the contact patch are larger due to the larger contact area.

The Magic Formula (MF) model as displayed in chapter 4.3.3 (refer to Eq. (4.23) and (4.24)), was applied to fit the curves of the longitudinal slip – longitudinal force. The paramters of the MF equation and the coefficients of determination are displayed in Table 5.11. As the coefficients of determination are near to 1, the derived equations are reliable and the fit goodness is high. Fig. 5.37 provides a better view of the fit quality by comparing the simulation and predicted results.

Table 5.11: Coefficients in the slip ratio – longitudinal force equations

Paramters	**Inflation pressure**		**Inflation pressure**	
	500 kPa		700 kPa	
	Wheel load		**Wheel load**	
	20 kN	30 kN	20 kN	30 kN
D	1.574	1.061	0.777	0.647
C	0.477	0.477	7.896	10.501
B	2.932	2.932	0.216	0.177
E	-0.0955	-0.0955	111.6	165.7
S_h	0.161	0.161	0.164	0.122
S_v	-0.449	-0.386	-0.411	-0.342
R^2	0.998	0.998	0.997	0.999

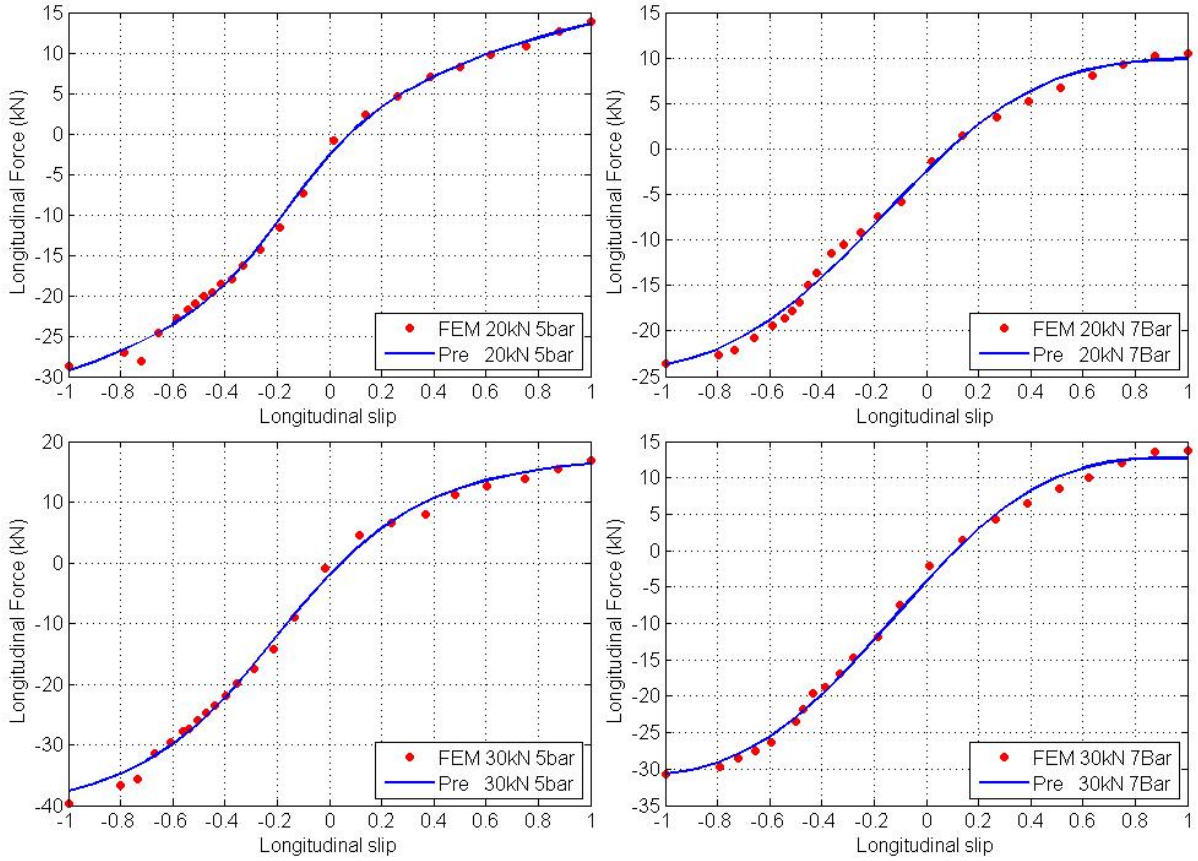

Fig. 5.37: Comparison of the longitudinal slip – longitudinal force relationship

5.5.6 Simulation of pure lateral slip

In the simulation of pure lateral slip, the soft soil model in the dimension of 2 m × 1.0 m × 0.3 m was placed underneath the tire, and the minimum size of soil elements was 5 mm. Constant tire inflation pressures were applied on the tire cavity side, and constant wheel loads were applied on the tire center. To simulate the tire pure lateral slip, a constant rotational velocity of 2 rad/s, a constant translational velocity of 1.05 m/s in the longitudinal direction and various lateral velocities were defined on the tire center for generating different lateral slips. The simulation objects are to study the lateral slip influence on the tire mobility such as lateral force at various wheel loads for different inflation pressures.

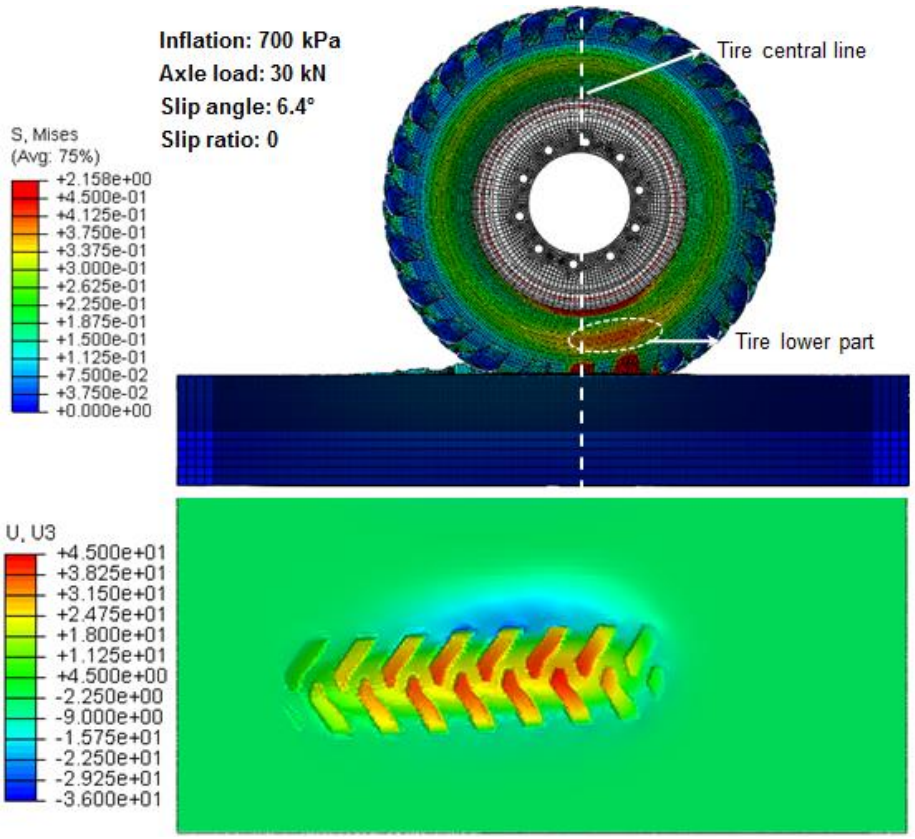

Fig. 5.38: Von Mises stress and soil deformation in the pure cornering simulation

As observed in Fig. 5.38, near to the tire-soil contact interface, the lower tire region marked with the white circle endures larger von Mises stresses than the rest of the tire. The position of the maximum von Mises stress on the tire-soil contact interface is in front of the tire central line. Due to the larger contact stress, the soil deformation is larger compared to that in the soil compaction simulation at the same wheel load and inflation pressure.

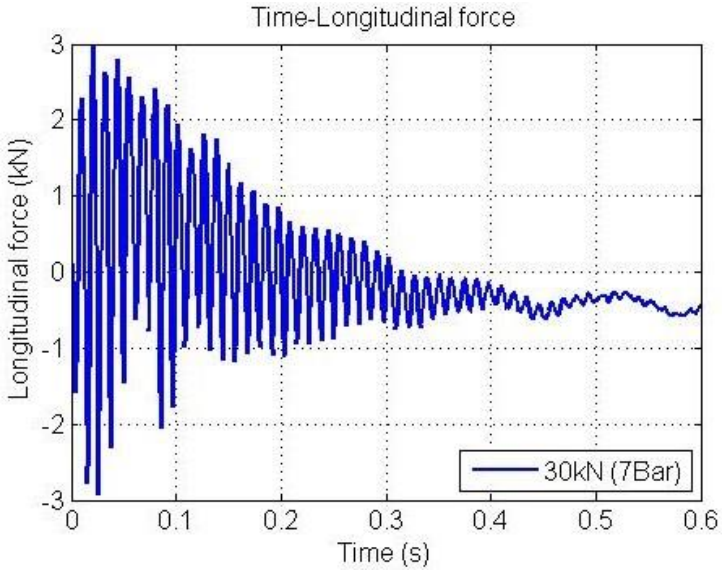

Fig. 5.39: Variation of longitudinal force along time axis at the 6.4° slip angle

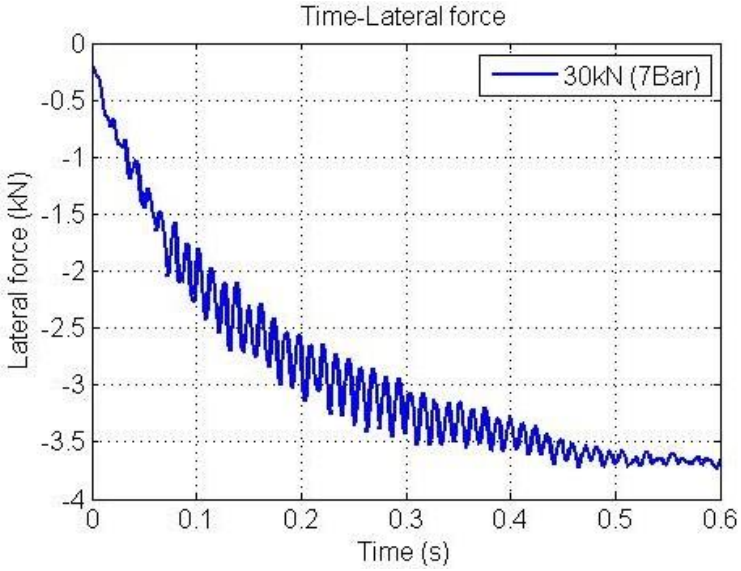

Fig. 5.40: Variation of lateral force along time axis at the 6.4° slip angle

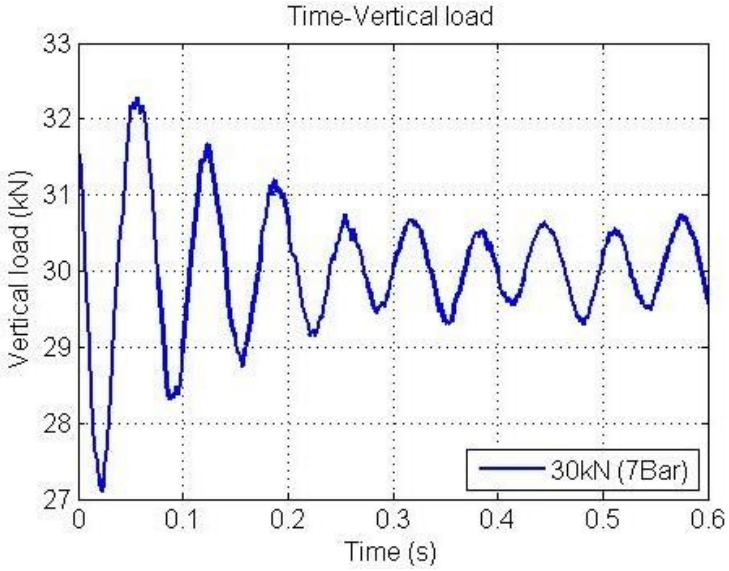

Fig. 5.41: Variation of vertical force along time axis at the 6.4° slip angle

As the tire starts rotating, the vibrations are observed in the vertical and the longitudinal direction displayed in Fig. 5.39, 5.40 and 5.41. With the elapsing of the simulation time, the amplitudes of the vertical, longitudinal and lateral force decrease due to the energy absorption caused by soil compaction. Deduced from the curve tendency, the magnitudes of the stabilized forces in the longitudinal and the lateral direction are estimated as 0.48 and 3.72 kN.

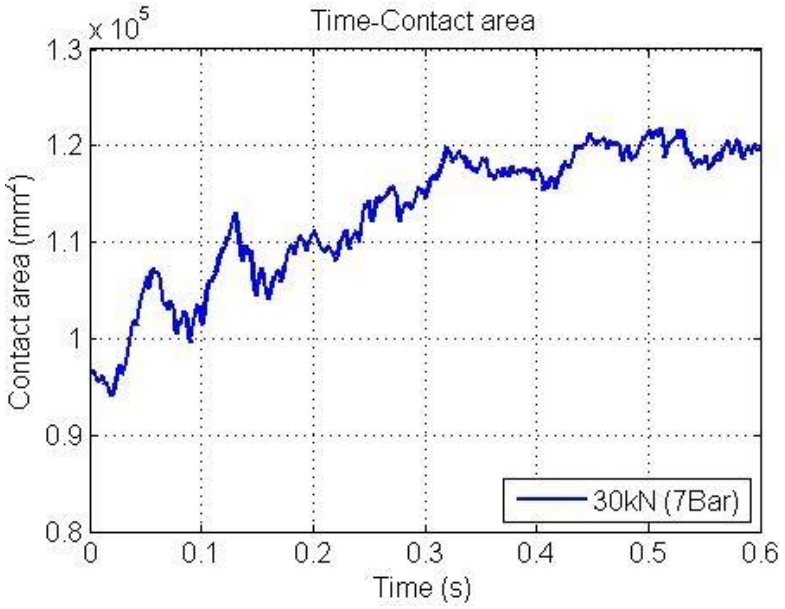

Fig. 5.42: Variation of contact area along time axis at the 6.4° slip angle

As observed in Fig. 5.42, the contact area increases during the transition from standing to cornering. The relative movement between the tire and the soil generates more shear stresses which enlarge the contact pressure in the tire-soil contact interface and lead to the increase of the soil compaction and the contact area.

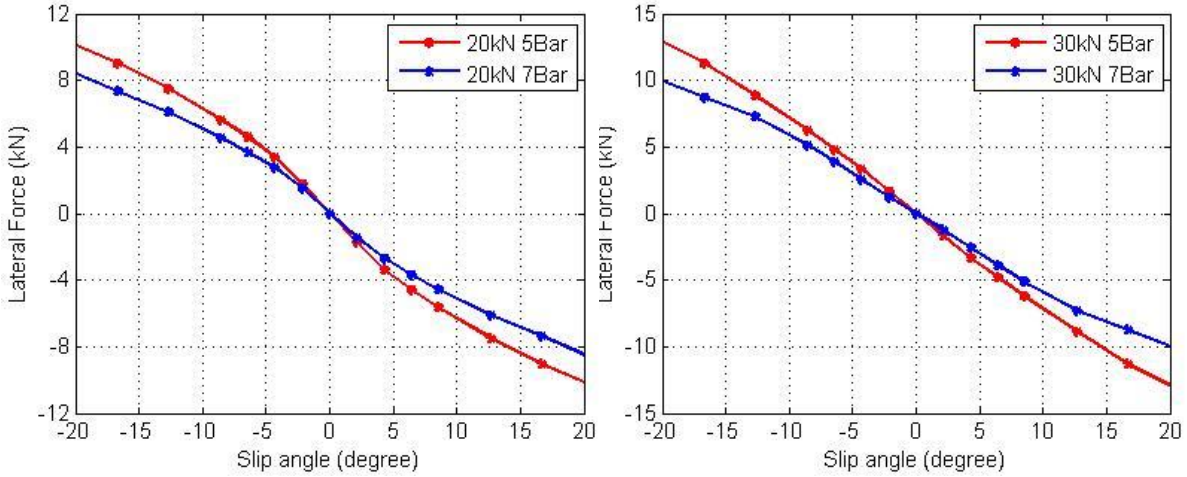

Fig. 5.43: Relationship of slip angle – lateral force

As displayed in Fig. 5.43, it is noticed that lateral force is determined by the wheel load, the slip angle and the inflation pressure. As the wheel load increases and the inflation pressure decreases, the area of the tire-soil interaction interface becomes larger leading to more lateral force. As the slip angle increases, the increasing of the relative movement between the tire and the soil in the lateral direction as well as the bulldozing resistance on the tire side face leads to a larger lateral force.

With an item introduced to account for the bulldozing resistance, Eq. (5.20) and Eq. (4.26) were established to fit the curves of the slip angle – lateral force. The equation paramters and the coefficients of determination for the specified operating conditions are displayed in Table 5.12. As the coefficients of determination are near to 1, the derived equations are reliable and the fit goodness is high. Fig. 5.44 provides a better view of the curve fitting by comparing the simulation and predicted results.

$$Y(x) = D\sin\left[C\arctan\left(Bx - E\left(Bx - \arctan(Bx)\right)\right)\right] + A(\tan x)^n \tag{5.20}$$

Table 5.12: Coefficients in the slip angle – lateral force equations

Paramters	**Inflation pressure**		**Inflation pressure**	
	500 kPa		700 kPa	
	Wheel load		**Wheel load**	
	20 kN	30 kN	20 kN	30 kN
D	12.3880	11.3720	12.400	9.8550
C	0.338	0.329	0.3630	0.339
B	0.030	0.023	0.022	0.0240
E	-18470	-36420	-34850	-23300
A	0.779	0.6760	0.7270	0.644
n	0.585	0.6140	0.700	0.7560
R^2	0.999	0.999	0.999	0.999

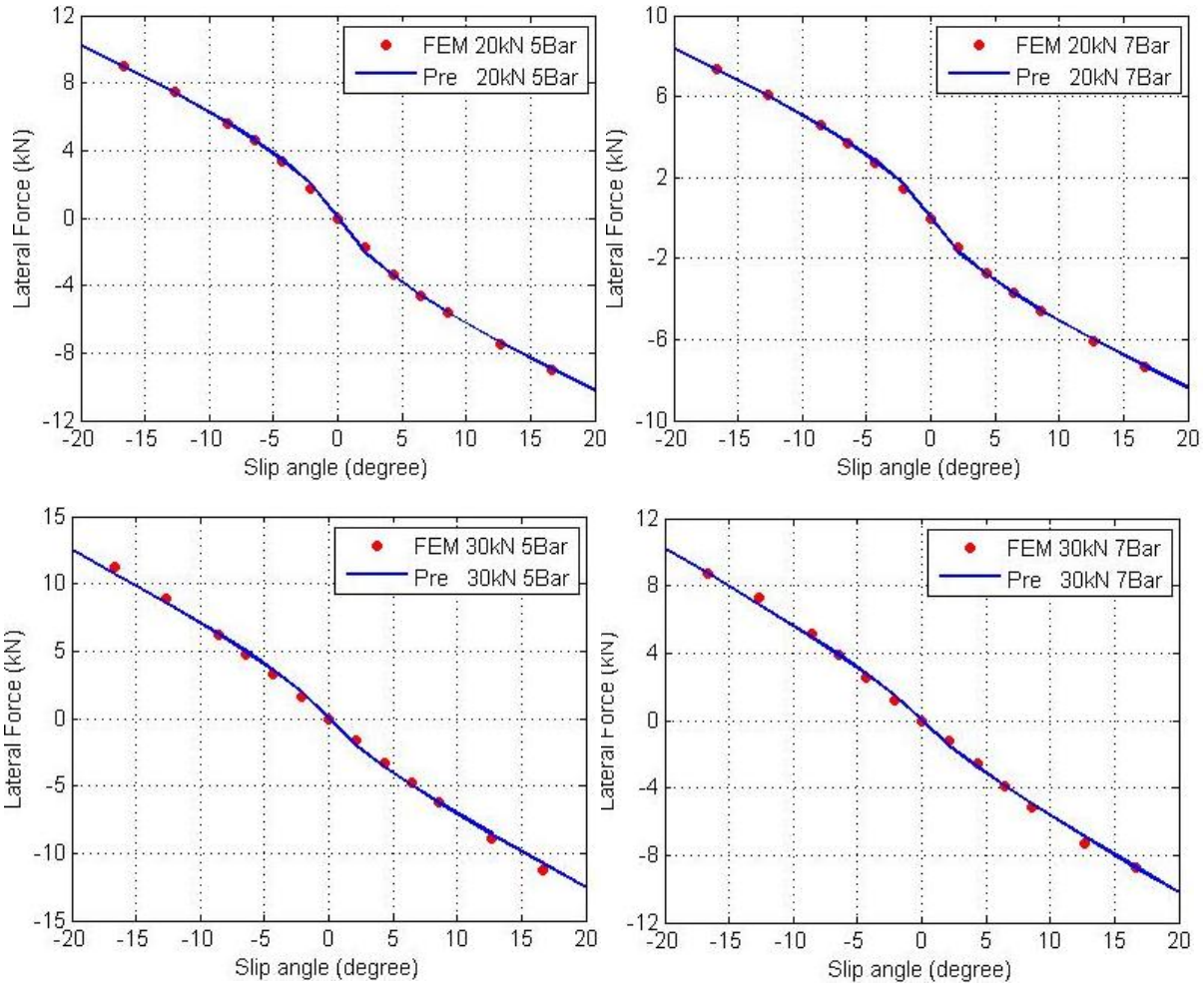

Fig. 5.44: Comparison of the slip angle – lateral force relationship

5.6 Conclusion

In this chapter, the FE models and the corresponding simulation results were described to study the tire-soil interaction under different operating conditions with the FEM software-Abaqus. In the simulation of assembling and inflating the tire, the stress and strain distributions within the tire were studied. In the simulation of tire loading and soil compaction, the stress distributions within the tire and the contact patch, and the tire/soil deformations were compared for two different inflation pressures at the wheel load of 30 kN. In the simulation of pure longitudinal and lateral slip, the development of the longitudinal and lateral reacting forces from the soil was investigated for different longitudinal slips and slip angles.

Using the exponential equation, the tire vertical stiffness and the soil compaction-wheel load relationship at the inflation pressures of 500 and 700 kPa were concluded based on the simulation results. Using the MF equation, the slip ratio – longitudinal

force and slip angle – lateral force relationships at the wheel loads of 20 and 30 kN, the inflation pressures of 500 and 700 kPa were derived from the simulation results.

Maintaining an appropriate inflation pressure is significant for reducing soil compaction, enhancing tire drawbar coefficient and improving steering performance. For lower inflation pressures, the tire tends to be softer indicating that more contact area and less soil compaction appear, and therefore the longitudinal and lateral forces are larger due to the larger contact area.

6 Experiments and FE Model Validation

In the previous chapters an analytical model integrated into a MBS program and FE models were presented, and the simulations for the analysis of the tire-soil interaction were discussed. As the objective of this dissertation is to provide reliable models for the prediction of the tire-soil interaction, therefore experiments which are similar to the operating conditions defined in the simulations were conducted. Simulation and experimental results are compared for the validation of the FE models.

6.1 Single wheel tester coupled with an excavator

As displayed in Fig. 6.1, a single wheel tester was designed and built to measure the tire deformation as well as the forces in the vertical, longitudinal and lateral directions. The single wheel tester can be connected to a versatile quick fit of an excavator arm for the outdoor tests. In each direction two force sensors were mounted on the single wheel tester to measure the force, and a laser senor was mounted on the frame to measure the tire and soil deformations. The tire was fixed to a flange which was welded with a thick steel tube. Inside the tube, two taper roller bearings mounted on the tire axle allow the tire to rotate.

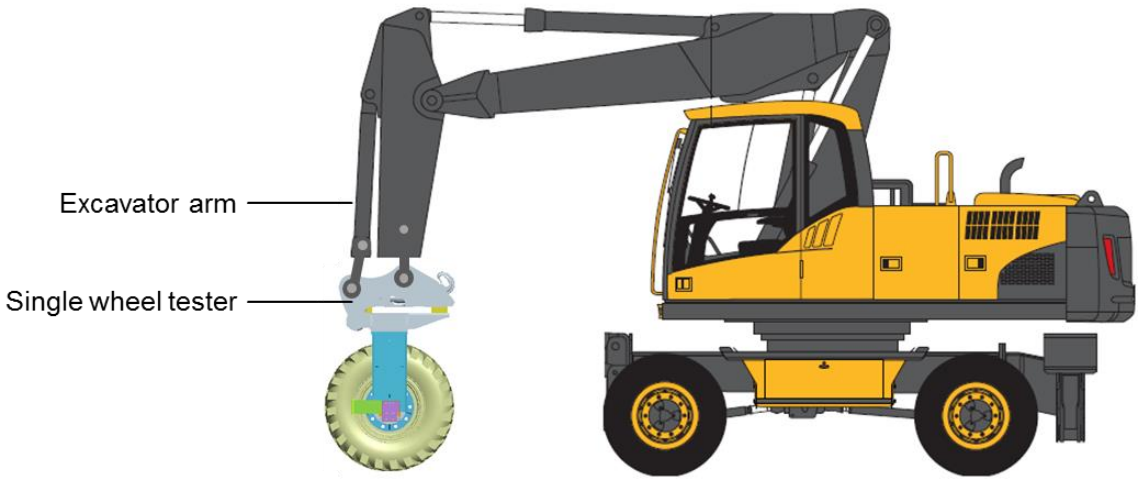

Fig. 6.1 Schematic diagram of the single wheel tester

Three sets of tests were conducted for the model validation as follows:

1. Static test of the tire-steel plate contact: a hydraulic cylinder in the excavator arm pushes the single wheel tester downwards. The vertical force appears when the steel plate at the bottom comes into contact with the tire. To validate the FE tire models, the tire vertical stiffness and the contact stress at the inflation pressures of 500 and 700 kPa are measured and compared with the simulation results.

2. Static test of the tire-soil contact: the single wheel tester is mounted on an excavator arm. The hydraulic cylinders for controlling the movement of the excavator arm and boom can change the location of the single wheel tester. As the single wheel tester moves downwards until the tire comes into contact with the soil, the vertical loads on the tire and the soil deformations at the inflation pressures of 500 and 700 kPa are measured and compared with the simulation results.
3. Dynamic test of the tire-soil contact: under constant vertical loads (34 and 41 kN), the single wheel tester is pushed forward at a constant velocity (0.25 m/s) by the excavator. The soil reacting forces and the soil deformations are measured and compared with the simulation results.

6.1.1 Design of the single wheel tester

The single wheel tester consists of two parts: the coupling connector and the wheel carrier. The function of the coupling connector is to provide connections between the single wheel tester and the excavator.

The coupling connector can be connected to the quick fit device of the excavator via two axles and a hook. The two axles can be hold by the two claws of the quick fit. To fix the coupling connector, a lever extended by the hydraulic cylinder inserts into the hook. The function of the quick fit is to allow the customers to use a wide variety of buckets from different manufacturers. The design of the quick fit device and the coupling connector are illustrated in Fig. 6.2.

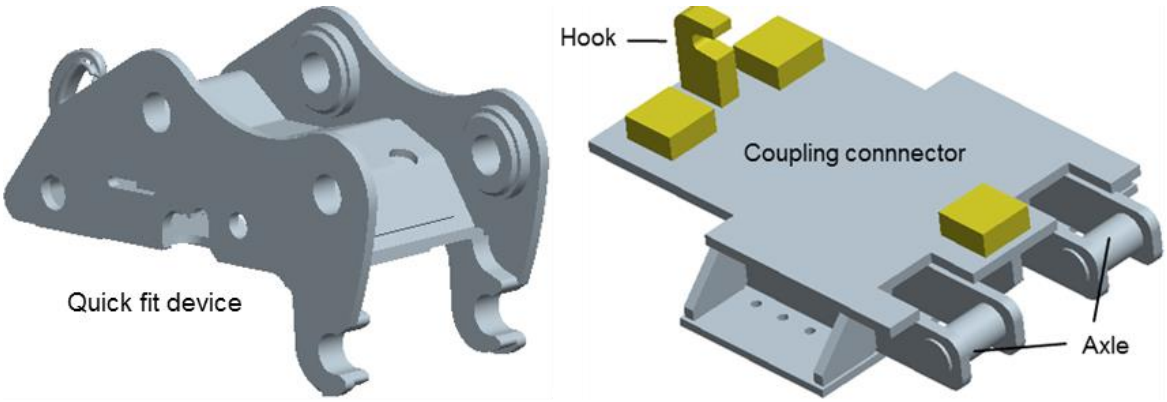

Fig. 6.2: Quick fit of the excavator and the coupling connector

The wheel carrier is designed for the carrying of the tire and the measuring of the reacting forces. The rim of the experimental tire is linked to the bushing in the green color with bolts. Inside the bushing, two taper roller bearings are placed through the

axle, and the position of the axle is fixed by the constraints of the load cells. The load cells installed in the specific positions can measure the forces in three directions separately. The design of the wheel carrier is displayed in Fig. 6.3.

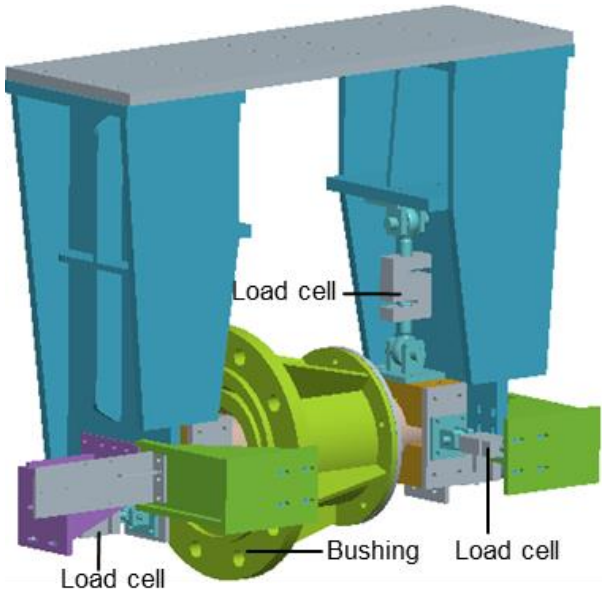

Fig. 6.3: Structure of the wheel carrier

The assembled single wheel tester consisting of the quick fit device, the coupling connector, the wheel carrier and the excavator tire, is presented in Fig. 6.4. The wheel carrier and the coupling connector are connected by bolts.

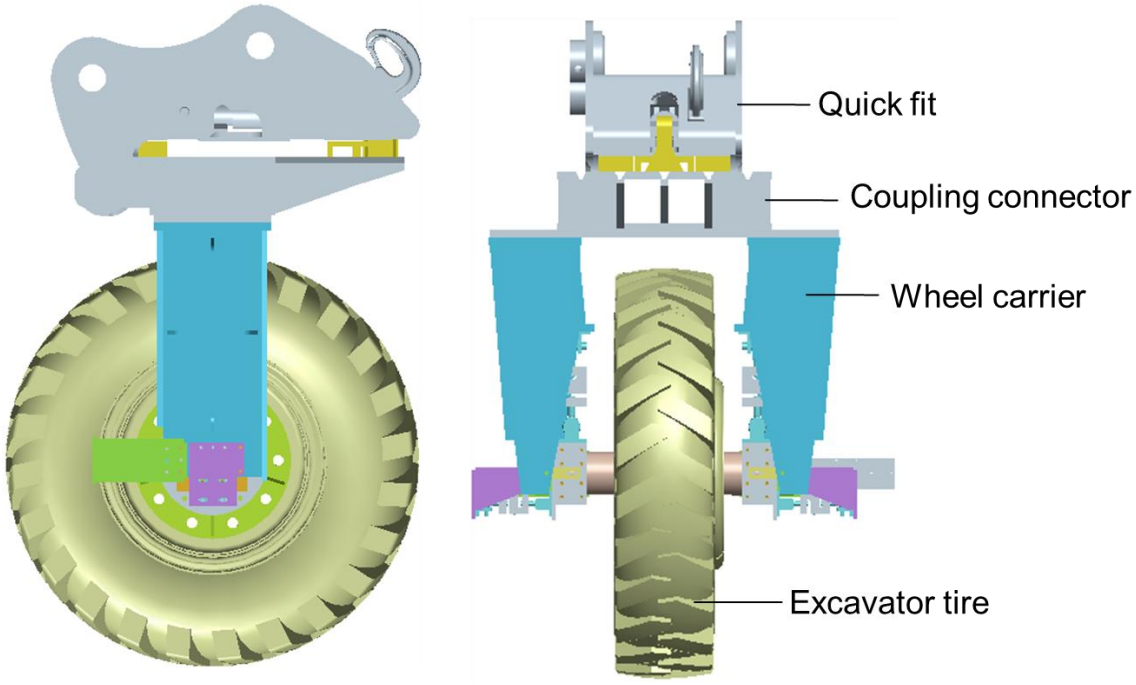

Fig. 6.4: Structure of the assembled single wheel tester

6.1.2 Principles of force measurement

The dynamic tire load, the net traction force and the lateral force which are perpendicular to each other are required to be measured simultaneously during the experiments. The force measured via the load cell in one direction shouldn't be interfered by the forces in the other directions. To comply with this requirement, swivel heads were used and connected to the load cells via screw threads. The swivel heads allow the load cell to move freely except for the direction along the central line of the screw thread. Therefore the load cell can only bear the tension and compression force in the direction of the central line as illustrated in Fig. 6.5.

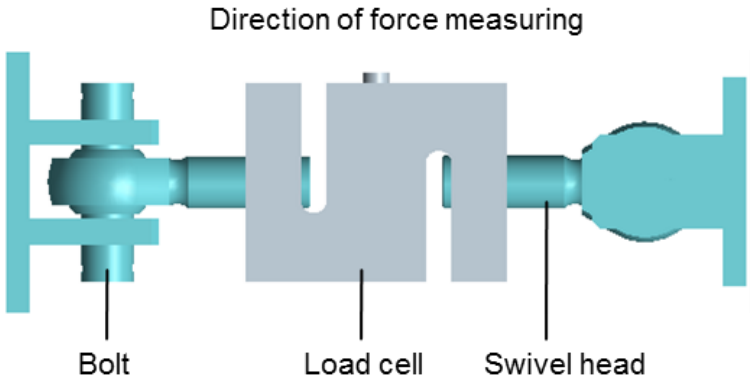

Fig. 6.5: Structure of the load cell group

Six load cells were used for the measurements of the forces in the three directions. Two load cells were applied in each direction to guarantee the balance and the stability of the single wheel tester. As illustrated in Fig. 6.5, S-form load cells for the measurement of the tension and compression forces from the Bosche Company were employed.

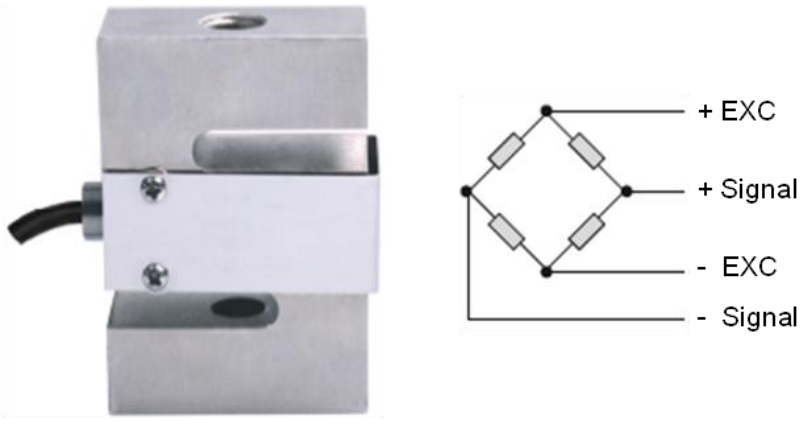

Fig. 6.6: S-form load cell

The four strain gauges applied inside the load cells are connected in a form of the full bridge. The voltage output of the bridge can be calculated. The technical features of the load cells are summarized as follows [163].

Table 6.1: Technical data of the load cells [163]

	K-DEE-C3-0500	**K-DEE-1000**	**K-DEE-A-5000**
Accuracy	0.04%	0.04%	0.04%
Nominal load [kg]	500	1000	5000
Isolation resistance [MΩ]	>5000	>5000	>5000
Supply voltage [V]	5-12	5-12	5-12
Temperature [°C]	- 30…70	- 30…70	- 30…70
Material	alloy steel	alloy steel	alloy steel
Number	2	2	2
Mounting direction	lateral	longitudinal	vertical

6.1.3 Calibration of the load cells

Before applying the load cells, the relationship of the voltage output and the load should be identified. As presented in Fig. 6.7, an additional device for the force measurement (Dynafor) is used to measure the force acting on the load cells. As presented in Fig. 6.8, the NI 9237 bridge module from National Instruments Corporation was applied, as it has four RJ-50 receptacles that provide connections for four half or full bridges and an external excitation voltage source [164]. The voltage outputs from the load cells are received and saved with the programs in Labview.

The tension force exerting on the Dynafor can be directly displayed on the monitor. The displayed value has to be recorded manually.

Fig. 6.7: Dynafor for the measurement of the tension force

The pins AI+ and AI-, EX+ and EX- were connected to those of the load cells.

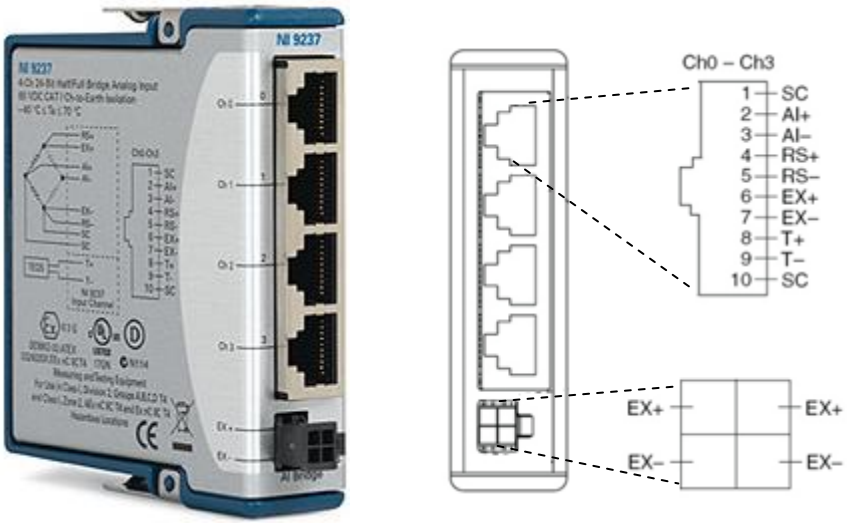

Fig. 6.8: Structure of the NI 9237

The NI cDAQ9172 is an I/O module that provides customers the interface for the application of Labview. The NI 9237 can be inserted into any slot of the NI cDAQ9172 as analog input. The configurations of data acquisition with the NI cDAQ9172 can be defined in Labview.

Each group of the two same load cells was calibrated separately. The linear regression in the form of $y=kx+b$ was used. The parameters for the regression equation and the coefficients of the determination are presented in Table 6.2. The coefficients of the determination near to 1 indicate the fit goodness is high.

Table 6.2: Conclusion of the parameters for the regression

	K-DEE-C3-0500		**K-DEE-1000**		**K-DEE-A-5000**	
	A	B	A	B	A	B
k [kN]	4.926	4.931	9.894	9.922	19.779	19.719
b [N]	-1.74	-10.24	-64.99	-31.57	-72.40	-108.80
R^2	0.9994	0.9991	0.9989	0.9991	0.9988	0.9981

6.1.4 Laser distance sensor

The laser distance sensor, ILD1700-750 from Micro-Epsilon was applied to measure the soil deformation. The ILD1700-750 sensor uses the principle of optical

triangulation, as a visible modulated point of light is projected onto the target surface. The diffuse element of the reflection of the light spot is imaged on a high-sensitivity resolution element (CCD) by a receiver optical element positioned at a certain angle to the optical axis of the laser beam [165]. From the output signal of the CCD element, a digital signal processor (DSP) in the sensor calculates the distance between the light spot on the measured object and the sensor. The distance is linearized and outputted via an analog or digital interface. The output signal and the term definition are displayed in Fig. 6.9.

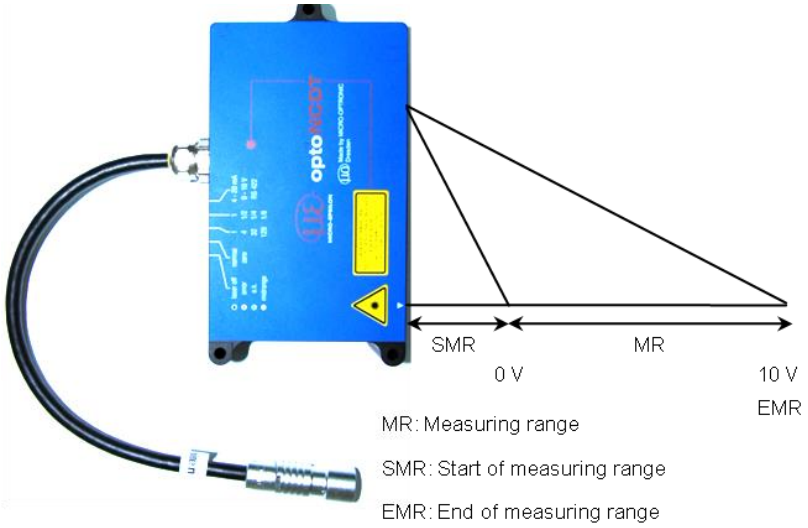

Fig. 6.9: Term definition for ILD1700-750

The measurement frequency of the sensor has to be reduced for dark or bright objects, when a longer exposure time is required. The technical data is presented in Table 6.3.

Table 6.3: Technical data of ILD1700-750 [165]

ILD 1700-750	
Measuring range [mm]	750
Start of measuring range (SMR) [mm]	200
Reference distance (MBM) [mm]	575
End of measuring range (EMR) [mm]	950
Linearity	±0.1%
Resolution [µm]	50
Programmable measurement frequency [Hz]	2500, 1250, 625, 312.5
Operating temperature [°C]	0…+50
Power supply U_B [V]	24 (11…30V)
Measurement output (Selectable)	0…+10 V, 4…20 mA

The ILD 1700-750 can output the measurement values either via the analog output or the RS422 serial interface. The voltage output is selected in the tests. The calculation of the distance *x* based on an outputted value U_{out} is presented by Eq. 6.1.

$$x = U_{out} \times MR / 10 \tag{6.1}$$

6.1.5 3D Kinect camera

The 3D camera Kinect was originally designed for the player-game interaction in computer game environments [166]. Due to the capability of capturing geometric data, the camera has attracted the interest of researchers from other fields including mapping and 3D modeling [166-168].

As displayed in Fig. 6.10, this device consists of a RGB Camera, an infrared camera, a laser projector and multi-array microphone. The device has a horizontal field view of 57°, a vertical field view of 43° and an operating distance range between 0.4 m and 5 m. The produced data streams with the RGB and Infrared camera are at a frame rate of 30 Hz. The device captures color images with the RGB camera and depth data with the infrared camera simultaneously. The integration of color data and depth leads to a colored point cloud that contains about 300,000 points in each frame. Khoshelham [169] found that the depth resolution decreased with the operating

distance, for example the point spacing in the depth direction could be as large as 70 mm at the maximum range of 5 meters. To maintain adequate accuracy, the data should be acquired within the measuring range of 1-3 m. The depth resolution is about from 1.5 to 3 mm in this measuring range.

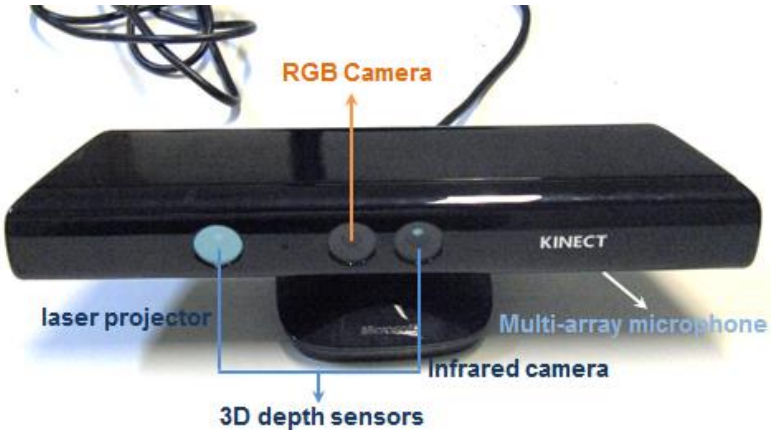

Fig. 6.10: Kinect for windows

A non-commercial software ReconstructMe was applied together with the Kinect device to scan objects for the measurement of the contour geometry. The data such as the coordinates of each point of the scanned objects were saved with the software and imported to Matlab for post-processing. Depth measurement with this device is presented in Fig. 6.11. Random deformation points were chosen and measured with a vernier. The results were compared with those from the camera, and good agreements (less than 5% discrepancy) were observed.

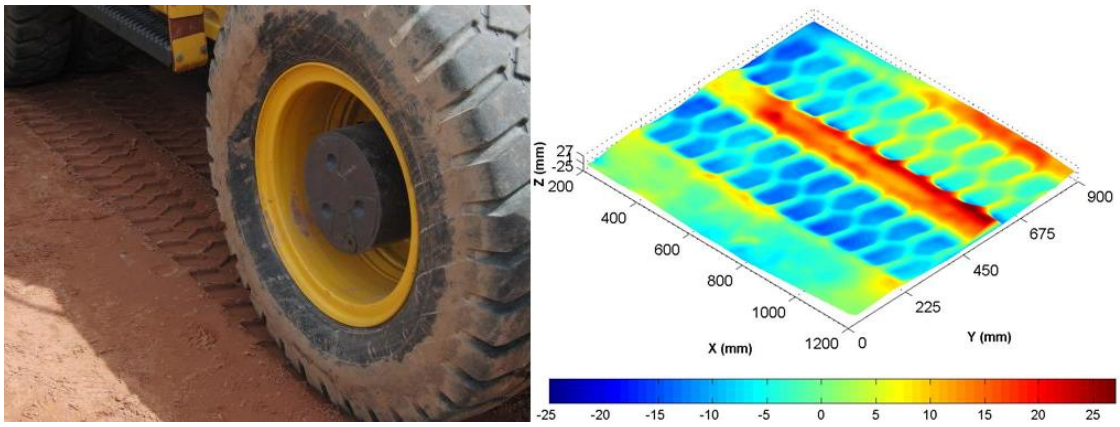

Fig. 6.11: Soil deformation measured with Kinect

6.1.6 Pressure measurement film

Prescale is a kind of extremely thin color film developed in Fuji, which can be used for the measurements of pressure distributions and the identification of pressure

values. The pressure range of Prescale is from 0.2 to 300 Mpa. There are two different structures of Prescale: Two-sheet and Mono-sheet type.

For the Two-sheet type, one film is coated with micro-encapsulated color-forming material and the other film is coated with the color-developing material. For the Mono-sheet type, the color-developing material is coated on a polyester base with the micro-encapsulated color-forming material layered on top. When the pressure applied on the Prescale is larger than the bearing capacity of microcapsules on the color-forming layer, the color-forming materials are released and red patches appear on the color-developing layer. The Prescale has eight different pressure measuring ranges as presented in Table 6.4, and the technical data of the Prescale is displayed in Table 6.5. To analyze the distribution and magnitude of the pressure, the affiliated software FPD-8010 and a scanner are utilized.

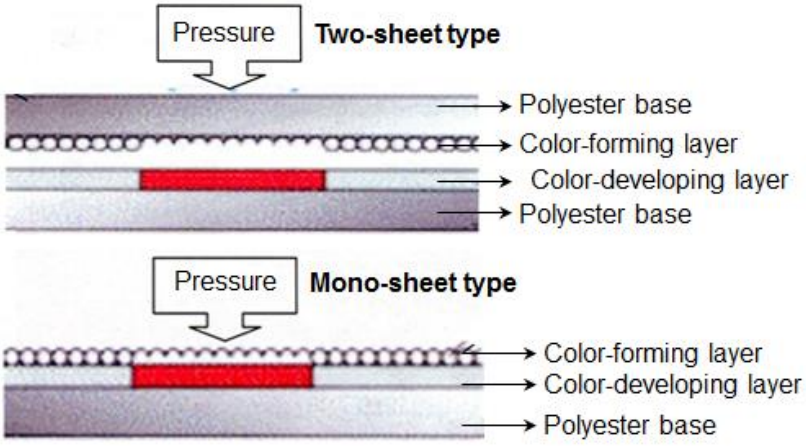

Fig. 6.12: Two types of the Prescale structure [170]

Table 6.4: Eight different pressure measuring ranges [170]

Prescale type	**Pressure measuring range [MPa]**
Extreme Low	0.05-0.2 (Two-sheet)
Ultra Super Low	0.2-0.6 (Two-sheet)
Super Low	0.5-2.5(Two-sheet)
Low	2.5-10 (Two-sheet)
Medium (MW)	10-50 (Two-sheet)
Medium (MS)	10-50 (Mono-sheet)
High	50-130 (Mono-sheet)
Super high	130-300 (Mono-sheet)

Table 6.5: Technical data of the Prescale [170]

Temperature (°C)	Humidity (%)	Accuracy (%)	Resolution (µm)
20-35	35-85	±10	5-15

6.2 Validation of the FE tire models

To validate the FE tire models developed in Abaqus, the tire stiffness and the contact stress at different wheel loads and inflation pressures were measured. As displayed in Fig. 6.13, the single wheel tester was connected to the excavator quick fit device. Different wheel loads generated by the hydraulic cylinders in the excavator arm, were measured through the load cells in the vertical direction. The tire deformation is measured through the laser distance sensor mounted on the tire frame. The contact stress was measured through the Prescale films laid on the weight scale at the bottom.

Fig. 6.13: Experiments for the validation of the FE tire model

6.2.1 Tire vertical stiffness

As compared in Fig. 6.14, the tire vertical stiffness obtained from the simulations is in accordance with that obtained from the experiments at the inflation pressures of 500 and 700 kPa.

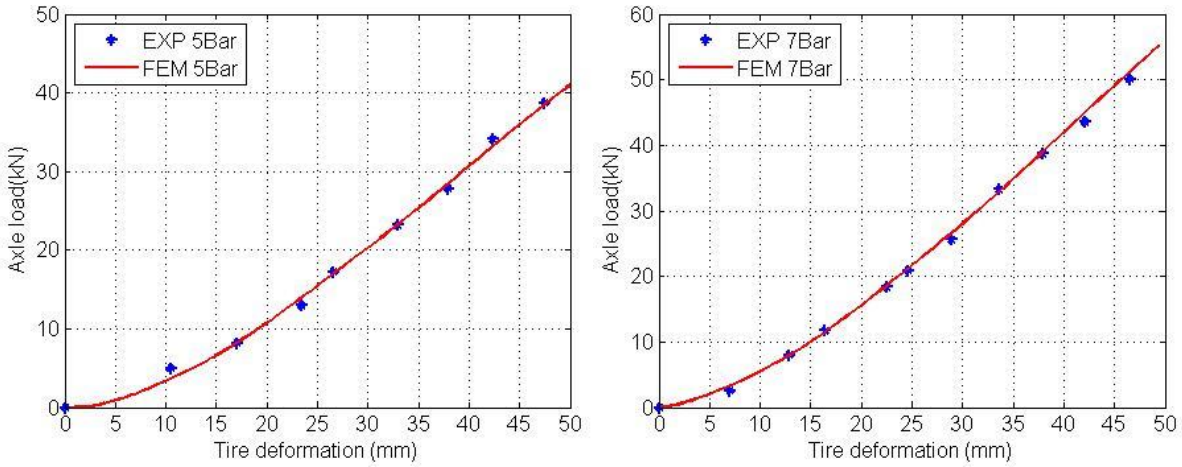

Fig. 6.14: Comparison of tire vertical stiffness

6.2.2 Stress distribution on the tire-steel plate contact interface

Under the operating conditions of inflation pressures of 500 and 700 kPa and the wheel load of 20 kN, four tire footprints appear on the Prescale film as illustrated in Fig. 6.15. By analyzing the contact stress from the Prescale film (right column) and the FEM simulation (left column), it is noticed that for the inflation pressure of 700 kPa, the contact area is less resulting in larger contact stresses at the wheel load of 20 kN.

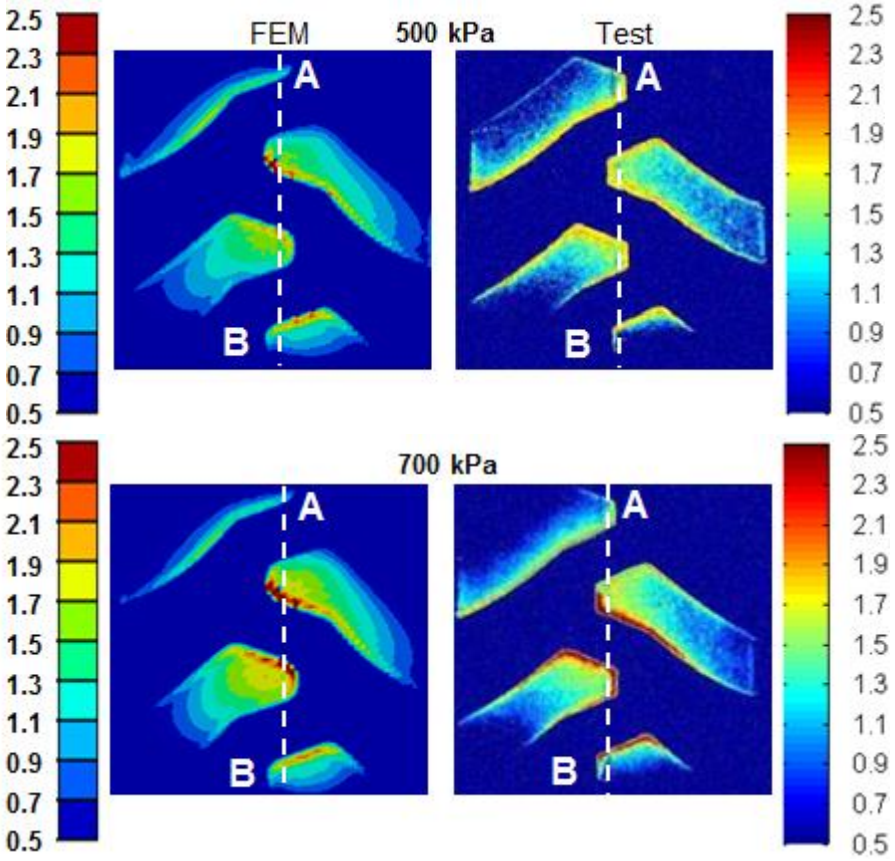

Fig. 6.15: Contact stress at the wheel load of 20 kN

The contact stresses in the regions near to the tire central line AB are larger than those distributed in the other contact regions. As presented in Fig. 6.16, the tendency of the stress along the tire central line AB from the Prescale film and the FEM simulation is identical. The stress curves similar to the shape of the character M indicate that the contact stress on the tread edges is larger. The average stress along the central line AB from the tests and the FEM simulation are 1.15 and 1.31 MPa for the inflation pressure of 500 kPa, 1.33 and 1.56 MPa for the inflation pressure of 700 kPa. The simulation and experimental results of the contact stresses are in good quantitative agreement with each other.

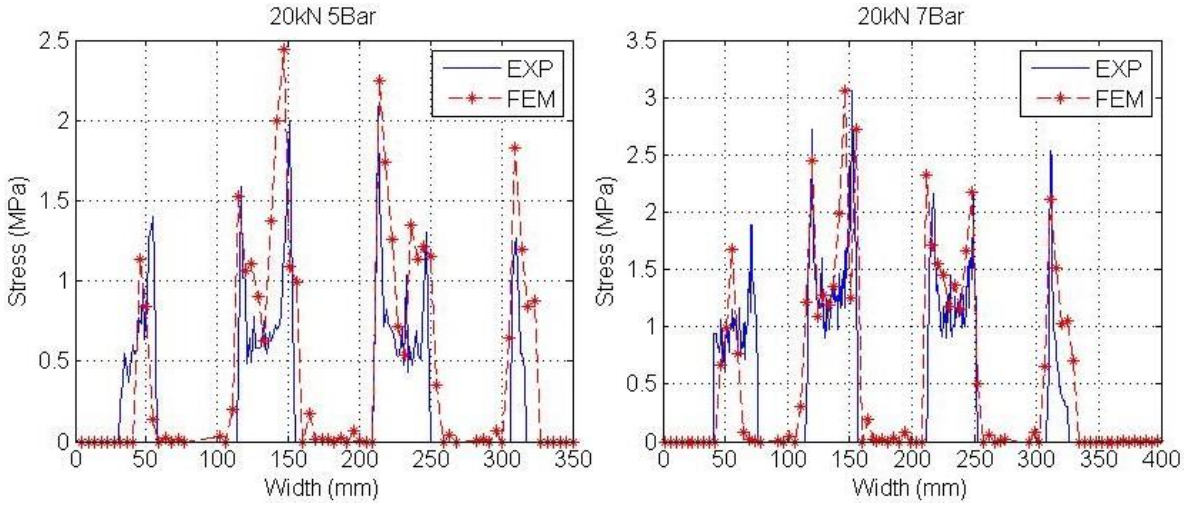

Fig. 6.16: Contact stress along the tire central line at the wheel load of 20 kN

Under the operating conditions of inflation pressures of 500 and 700 kPa and the wheel load of 30 kN, the stress distribution on the steel plate is illustrated in Fig. 6.17. By analyzing the contact stress from the Prescale film and the FEM simulation, it is observed that for the inflation pressure of 700 kPa, the contact area is less resulting in larger contact stresses at the wheel load of 30 kN.

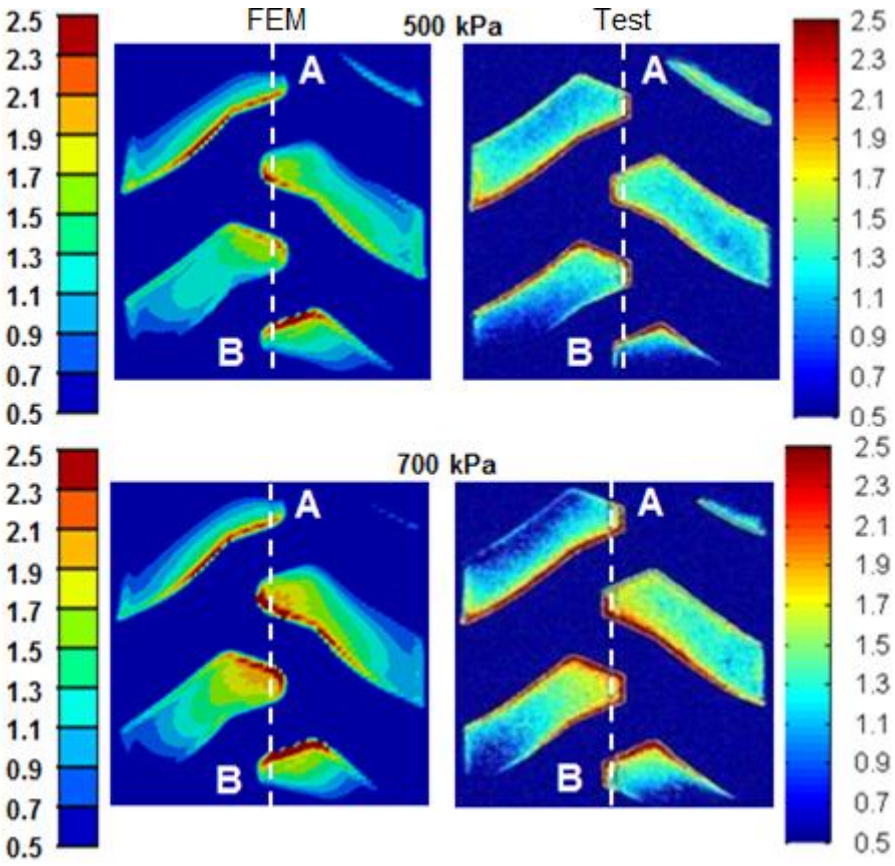

Fig. 6.17: Contact stress at the wheel load of 30 kN

The contact stresses in the regions near to the central line AB are larger than those distributed in the other contact regions. As displayed in Fig. 6.18, the tendency of the stress along the tire central line AB from the Prescale film (right column) and the FEM simulation (left column) is identical. The stress curves similar to the shape of the character M indicate that the contact stress on the tread edges is larger. The average stress along the central line AB from the tests and the FEM simulation are 1.25 and 1.42 MPa for the inflation pressure of 500 kPa, 1.41 and 1.77 MPa for the inflation pressure of 700 kPa. The simulation and experimental results of the contact stresses are in good quantitative agreement with each other.

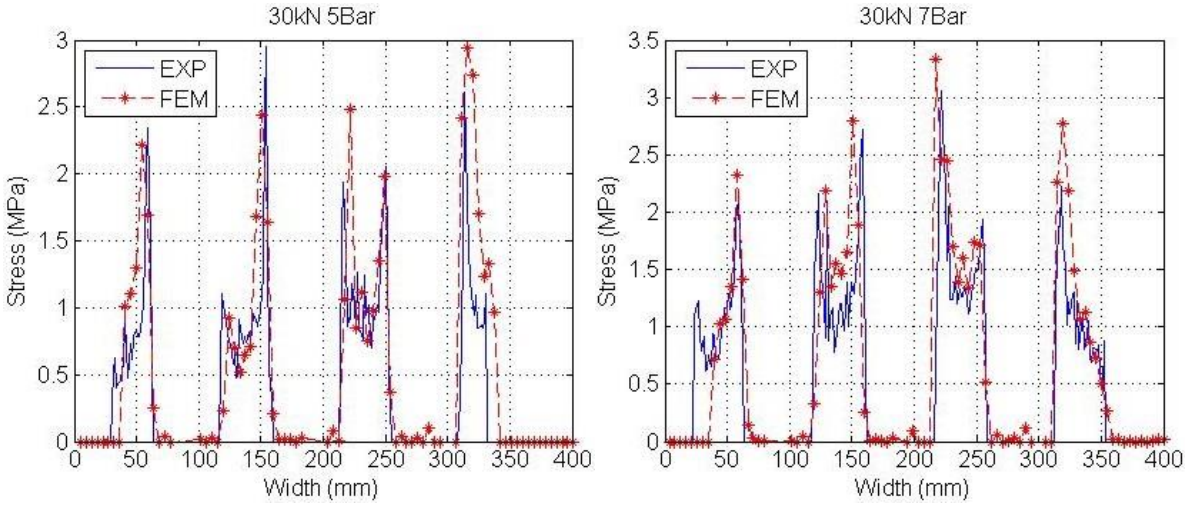

Fig. 6.18: Contact stress along the tire central line at the wheel load of 30 kN

Under the operating condition of inflation pressures of 500 and 700 kPa and the wheel load of 40 kN, six tire footprints appear on the Prescale film as illustrated in Fig. 6.19. By analyzing the contact stress from the Prescale film (right column) and the FEM simulation (left column), it is observed that for the inflation pressure of 700 kPa, the contact area is less resulting in larger contact stresses at the wheel load of 40 kN.

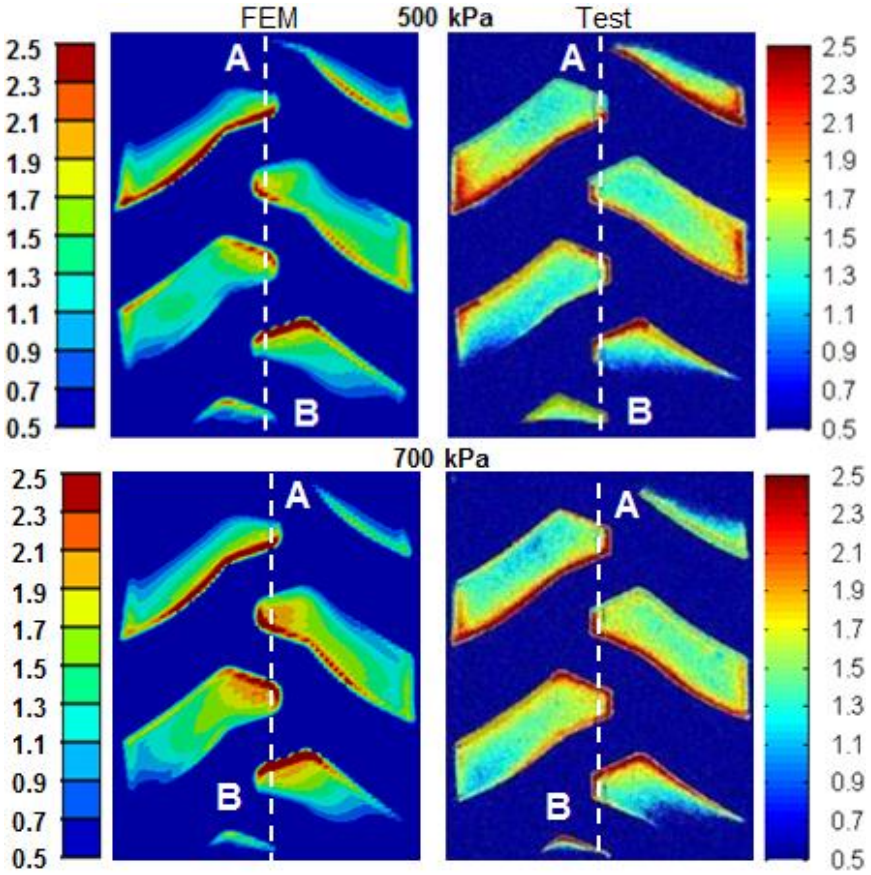

Fig. 6.19: Contact stress at the wheel load of 40 kN

The contact stresses in the regions near to the tire central line AB are larger than those distributed in the other contact regions. As presented in Fig. 6.20, the tendency of the stress along the tire central line AB from the Prescale film and the FEM simulation is identical. The stress curves similar to the shape of the character M indicate that the contact stress on the tread edges is larger. The average stress along the central line AB from the tests and the FEM simulation are 1.33 and 1.59 MPa for the inflation pressure of 500 kPa, 1.49 and 1.99 MPa for the inflation pressure of 700 kPa. The simulation and experimental results of the contact stresses are in good quantitative agreement with each other.

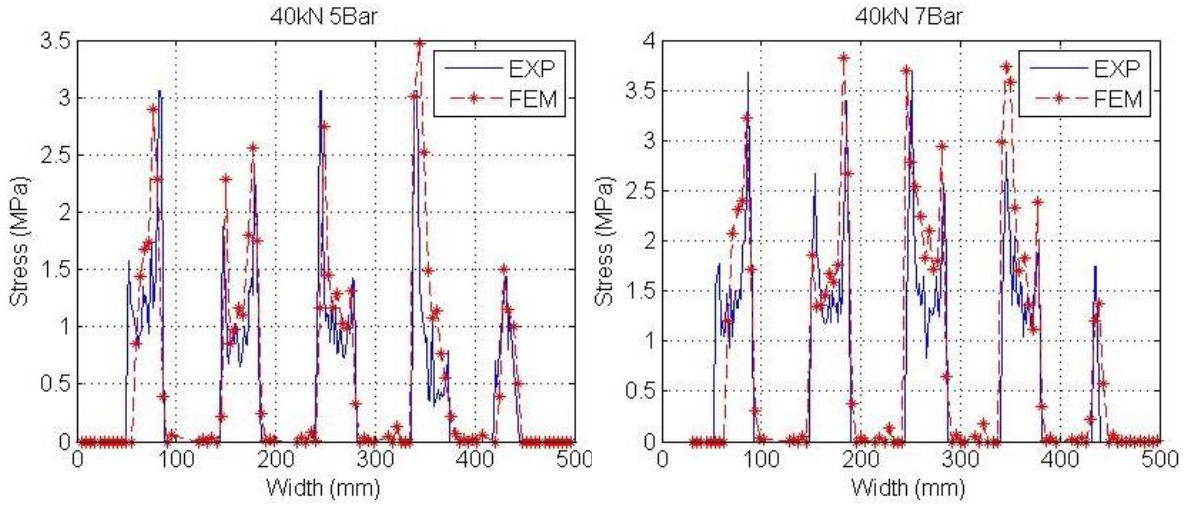

Fig. 6.20: Contact stress along the tire central line at the wheel load of 40 kN

6.3 Identification of the parameters of the FE soil model

Soil samples were collected after the preparation of the test field. The parameters such as moisture and bulk density dominate the soil mechanic properties. As the soil is a type of elasto-plastic material, the Young's modulus and the Poisson's ratio are required to describe the elasticity; the soil cohesion, the friction angle and other parameters are required to describe the plasticity presented by the Modified Drucker-Prager/Cap model.

As displayed in Fig. 6.21, a triaxial instrument is comprised of a distance senor for measuring the soil axial deformation, a force senor for measuring the axial load, surrounding water for providing the side pressure, and a volume meter for measuring the volume changing. To measure the parameters mentioned above, several tests were carried out with the triaxial instrument at the Division of Soil Mechanics and Foundation Engineering, TU Kaiserslautern. Soil samples were taken out of the sample collector and formed in the column with the dimension of 35.5 mm in

diameter and of 75.5 mm in length. The soil sample was enclosed in a thin rubber membrane, which sealed it from the surrounding water. After the preparation was finished, the soil sample was consolidated until the water was squeezed out.

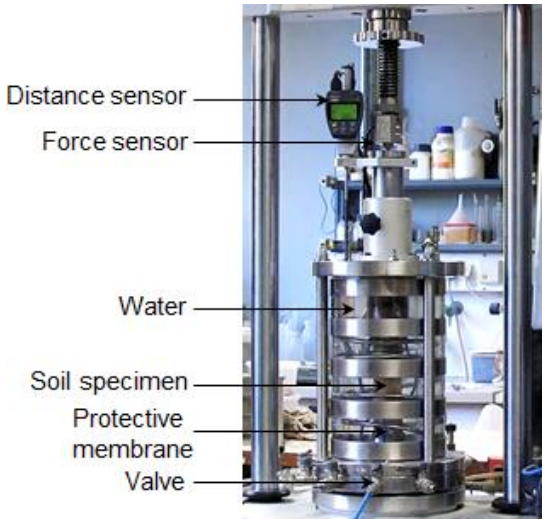

Fig. 6.21: Triaxial test instrument for the soil parameter identification

For the identification of the Young's modulus, the loading-unloading tests were conducted. At the beginning of the triaxial test, a hydrostatic pressure was applied on the axial and radial surface of the soil sample. More axial load was forced on the axial surface until the soil sample reaches the strain of 3%, and then the axial load was withdrawn. The axial load was applied again until the fully plastic deformation occurred. The water pressure and the axial pressure when the fully plastic deformation takes place are recorded for the calculation of soil cohesion and friction angle. The volumetric strain was measured as well to identify the Poisson's ratio. The experimental data are demonstrated in Fig. 6.22 and 6.23.

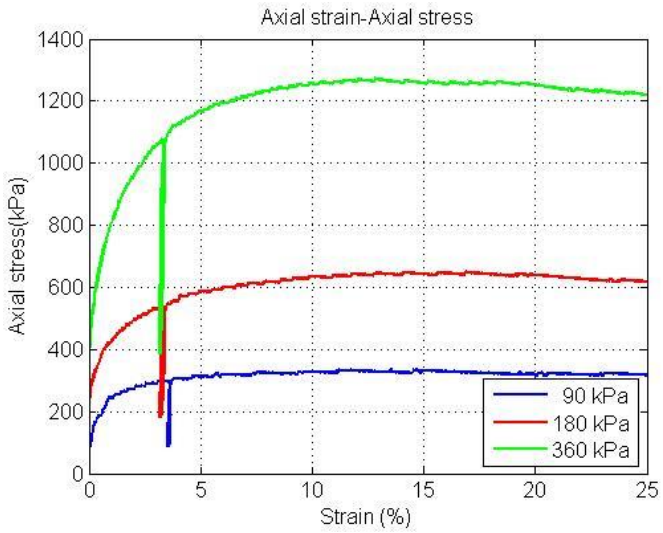

Fig. 6.22: Relationship of axial strain and stress

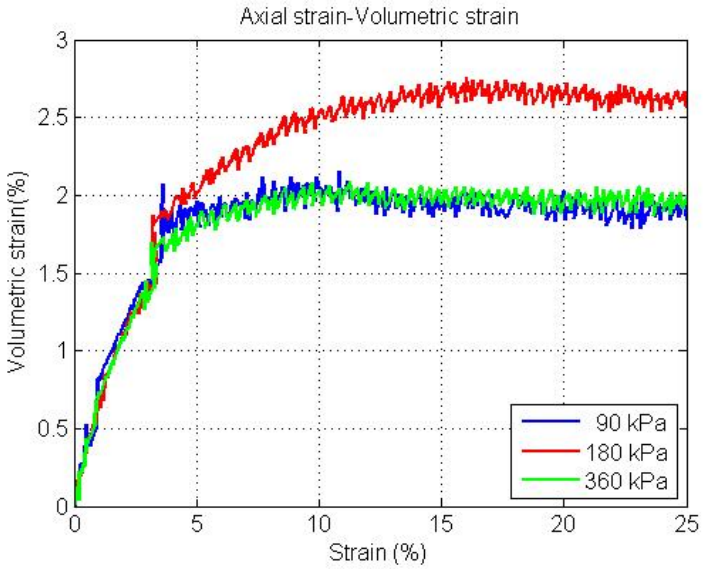

Fig. 6.23: Relationship of axial and volumetric strain

Concluded from the stresses measured where the soil failure takes place, the Modified Drucker-Prager/Cap model was established as displayed in Fig. 6.24. The measured soil parameters are presented in Table 6.6.

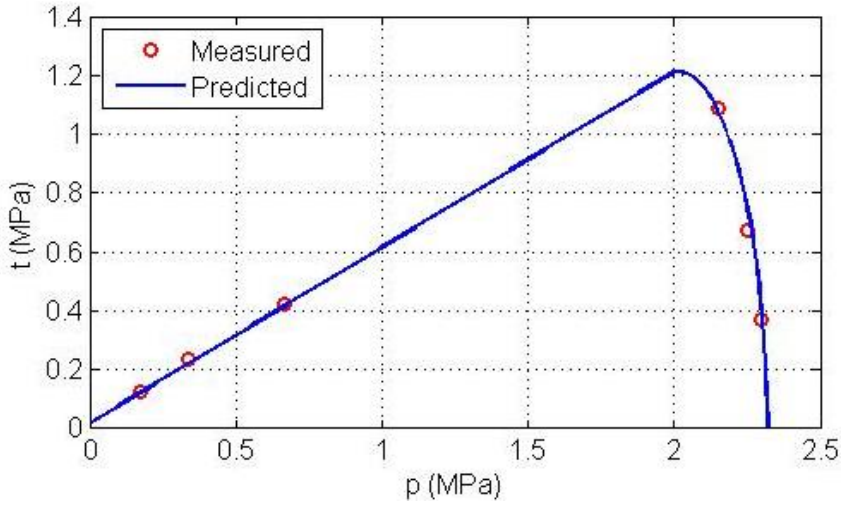

Fig. 6.24: Modified Drucker-Prager/Cap model

Table 6.6: Summary of soil parameters

Density [kg/m^3]	Moisture [%]	Young's Modulus [MPa]	R_s	K
1742	4.32	137.1	0.248	1
Poisson's ratio	Soil cohesion [kPa]	Friction angle [°]	P_b [MPa]	a
0.328	12.74	39.2	2.32	0.01

It should be noticed that the soil parameters are measured for the validation of the FE tire-soil interaction model, and are different from those defined for the FE soil model in chapter 5. Simulations with the measured soil parameters were carried out for the comparison of the simulation and experimental results.

6.4 Validation of the FE tire-soil interaction models

To validate the tire-soil interaction model, the soil deformation and the forces generated on the tire-soil contact interface were measured and compared with the simulation results. The validation experiments included the static and dynamic tests of the tire-soil contact. In the static tests of the tire-soil contact, the total deformation comprised of tire deflection and soil deformation was measured at different wheel loads and inflation pressures. In the dynamic tests of the tire-soil contact, the soil reacting forces in the vertical and longitudinal direction were measured at different wheel loads and inflation pressures.

6.4.1 Static tests of the tire-soil contact

As displayed in Fig. 6.25, the hydraulic cylinders in the excavator arm pushed the single wheel tester downwards, and the single wheel tester moved downwards until the tire came into contact with the soil. The load cells were used to measure the tire vertical loads; the laser distance sensor was used to measure the total deformation; the 3D Kinect camera was used to measure the soil plastic deformations (tire footprints).

Fig. 6.25: Tire sinking test

The total deformation and wheel load relationships obtained from the tests and simulations are presented in Fig. 6.26. It is observed that the total deformation is

larger at the smaller inflation pressure. However the soil deformation is less at the smaller inflation pressure, which is displayed in the following figures.

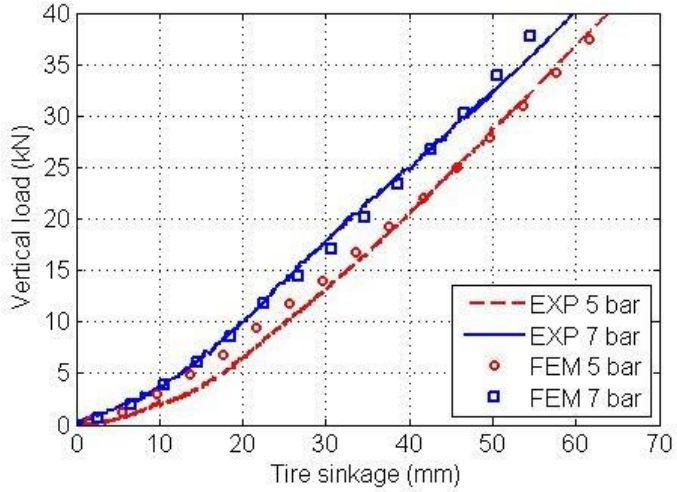

Fig. 6.26: The total deformation and wheel load relationship

The soil plastic deformations at different wheel loads and the inflation pressures of 500 and 700 kPa are displayed in Fig. 6.27 and 6.28. It should be noticed that the pictures in the first low are the simulation results, and the pictures in the second low are the experimental results. The pictures in the 1st, 2nd and 3rd row are soil plastic deformations at the wheel loads of 20, 30 and 40 kN respectively.

As displayed in Fig. 6.27, the shape and the depth of the tire footprints obtained from the simulations and the experiments are in good qualitative agreement at the inflation pressure of 500 kPa. When the wheel load is applied, the soil sinks and plastic deformations appear in the simulation. In the reality the soil which is underneath the tire is compacted by the wheel load; except for the vertical movement the soil tends to escape from the tire-soil contact patch which results in the increase of the soil height. This phenomenon can be observed in this figure, as the major plastic deformation is around -5 mm for the FE simulations and around 5 mm for the experiments. When the wheel load increases, the soil plastic deformation tends to increase due to the larger contact stress. At the inflation pressure of 500 kPa, the maximum plastic deformations obtained from the simulations and the experiments are 17.4 and 16.8 mm for the wheel load of 20 kN, 21.6 and 19.8 mm for the wheel load of 30 kN, 31.1 and 29.6 mm for the wheel load of 40 kN.

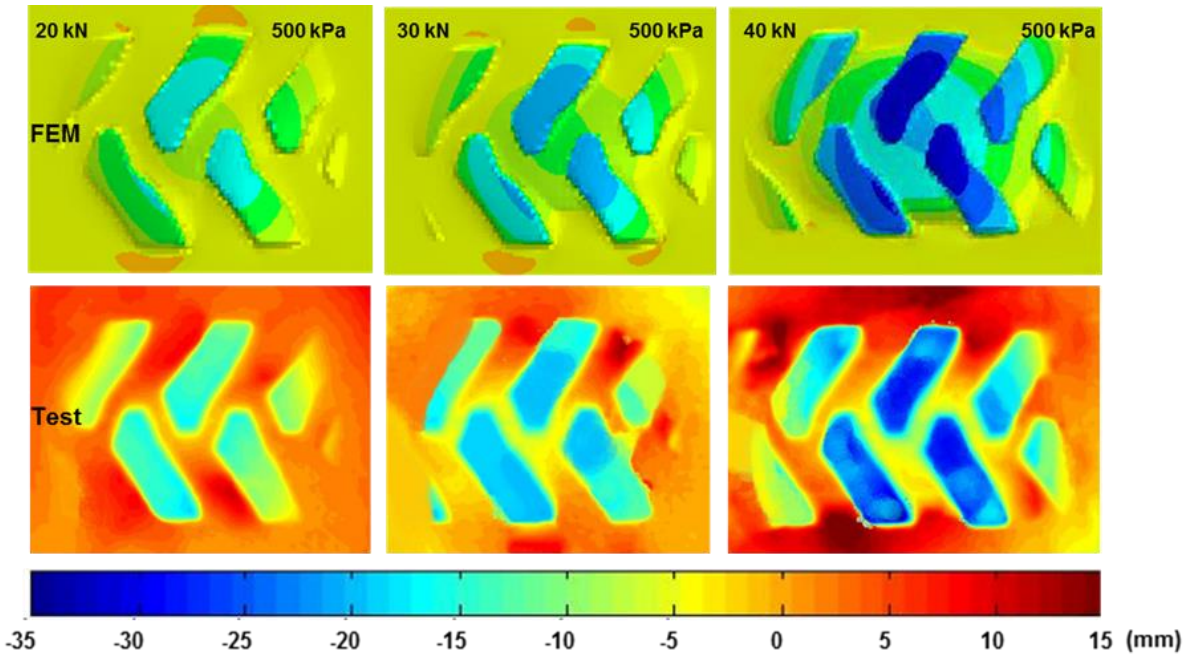

Fig. 6.27: Soil plastic deformation at the inflation pressure of 500 kPa

As displayed in Fig. 6.28, the shape and depth of the tire footprints obtained from the simulations and the experiments are in good qualitative agreement at the inflation pressure of 700 kPa. When the wheel load is applied, the soil sinks and plastic deformations appear in the simulation. In the reality the soil which is underneath the tire is compacted by the wheel load; except for the vertical movement the soil tends to escape from the tire-soil contact patch which results in the increasing of the soil height. This phenomenon can also be observed in this figure, as the major plastic deformation is around -6 mm for the FE simulations and around 7 mm for the experiments. When the wheel load increases, the soil plastic deformation tends to increase due to the larger contact stress. At the inflation pressure of 700 kPa, the maximum plastic deformations obtained from the simulations and the experiments are 21.3 and 20.8 mm for the wheel load of 20 kN, 26.6 and 25.5 mm for the wheel load of 30 kN, 34.7 and 34.8 mm for the wheel load of 40 kN.

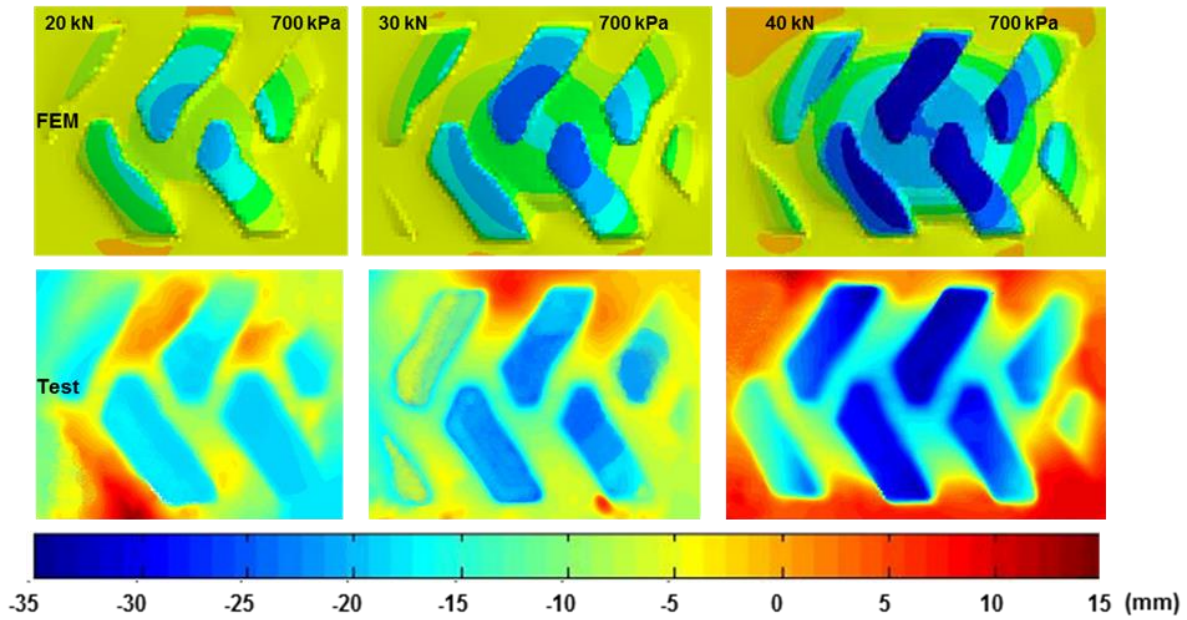

Fig. 6.28: Soil plastic deformation at the inflation pressure of 700 kPa

Concluded from Fig. 6.27 and Fig. 6.28, the soil plastic deformation is influenced by the wheel load and the inflation pressure. As the wheel load and the inflation pressure increase, the soil plastic deformation tends to increase due to the increasing of the stress on the tire-soil contact interface.

6.4.2 Dynamic tests of the tire-soil contact

As displayed in Fig. 6.29, the front excavator wheels hung in the air so that the gravitational force of the excavator and the single wheel tester was supported by the rear excavator wheel and the single wheel at the front. Hence a constant wheel load was applied on the single wheel tester. To generate various constant wheel loads, it was only required to adjust the arm and boom extension. After the adjustment of the wheel load, the excavator started to push the single wheel tester forward at a constant velocity (0.25 m/s), and the soil reacting force were measured via the load cells mounted in three different directions. Some segments of the soil plastic deformations (tire footprints) were scanned through the 3D Kinect camera.

Fig. 6.29: Tire rolling tests

For the following figures from Fig. 6.30 to 6.34, it should be noticed that the figures on the left side present the tire footprints obtained from the simulations, and those on the right side present the tire footprints obtained from the experiments.

As displayed in Fig. 6.30, the shape and geometry of the tire footprints obtained from the simulations and the experiments are quite similar. The average depths of the tire footprints from the simulations and the experiments are around 28.3 and 27.5 mm at the wheel load of 34 kN and the inflation pressure of 500 kPa. The simulation and experimental results of the soil plastic deformation underneath the tire are in good quantitative agreement with each other.

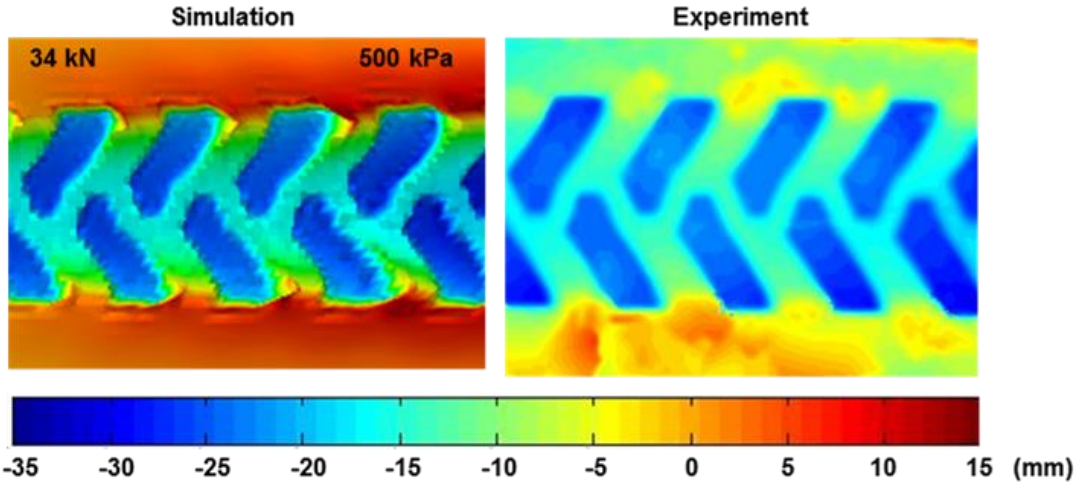

Fig. 6.30: Tire footprint at the wheel load of 34 kN and the inflation pressure of 500 kPa

As displayed in Fig. 6.31, the shape and geometry of the tire footprints obtained from the simulations and the experiments are quite similar. The average depths of the tire footprints from the simulations and the experiments are around 31.7 and 32.4 mm at the wheel load of 41 kN and the inflation pressure of 500 kPa. The simulation and experimental results of the soil plastic deformation underneath the tire are in good quantitative agreement with each other.

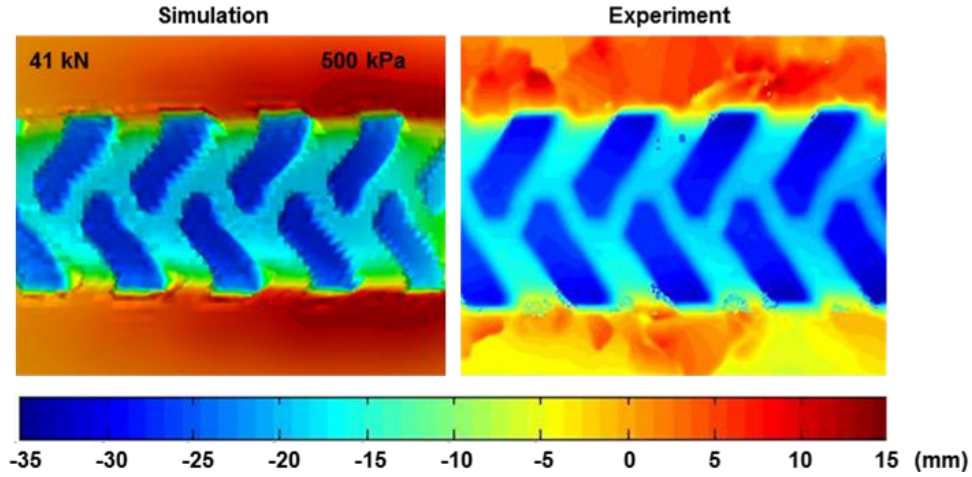

Fig. 6.31: Tire footprint at the wheel load of 41 kN and the inflation pressure of 500 kPa

As displayed in Fig. 6.32, the shape and geometry of the tire footprints obtained from the simulations and the experiments are quite similar. The average depths of the tire footprints from the simulations and the experiments are around 30.5 and 31.8 mm at the wheel load of 34 kN and the inflation pressure of 700 kPa. The simulation and experimental results of the soil plastic deformation underneath the tire are in good quantitative agreement with each other.

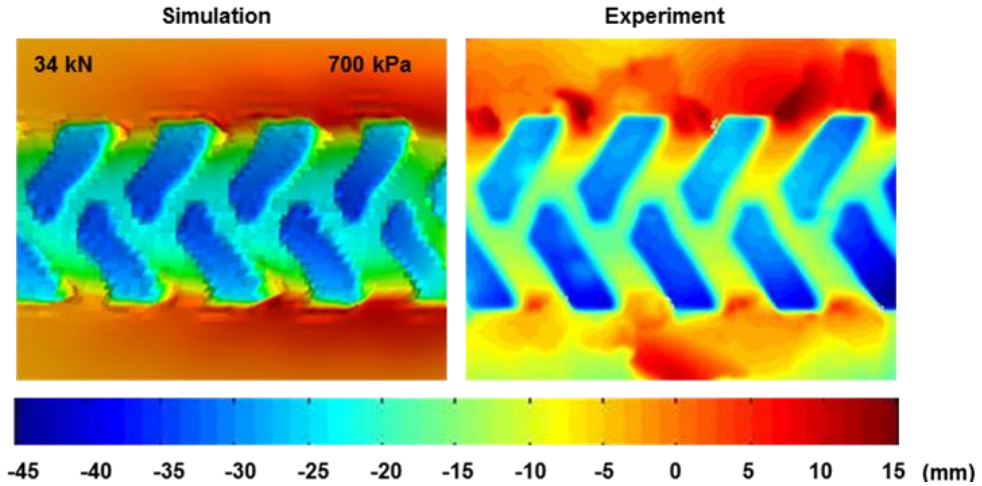

Fig. 6.32: Tire footprint at the wheel load of 34 kN and the inflation pressure of 700 kPa

As displayed in Fig. 6.33, the shape and geometry of the tire footprints obtained from the simulations and the experiments are quite similar. The average depth of the tire footprints from the simulations and the experiments are around 40.1 and 39.2 mm at the wheel load of 41 kN and the inflation pressure of 700 kPa. The simulation and experimental results of the soil plastic deformation underneath the tire are in good quantitative agreement with each other.

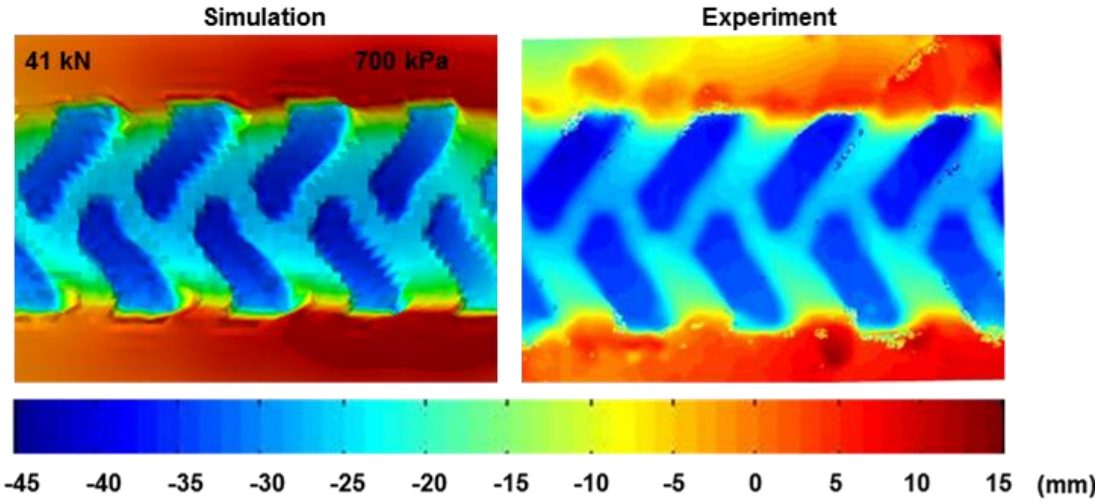

Fig. 6.33: Tire footprint at the wheel load of 41 kN and the inflation pressure of 700 kPa

Concluded from the figures illustrating the tire footprints, the soil plastic deformation tends to increase with the wheel load and the inflation pressure. For the same wheel load, the soil compaction is larger at larger inflation pressures. The simulation results are in good qualitative agreement with the experimental results.

When the excavator begins to push the single wheel tester, the direction of the longitudinal force acting at the tire bottom is opposite to the tire moving direction. The torque generated by the longitudinal force rotates the tire. As the translational velocity is constant in the longitudinal direction, the longitudinal force increases along with the time until a stabilized magnitude is reached.

As displayed in Fig. 6.34, the tendency of the vertical and longitudinal forces obtained from the simulations and the experiments are in accordance with each other. The stabilized longitudinal forces from the simulations and the experiments are 6.38 and 6.23 kN at the wheel load of 34 kN and the inflation pressure of 500 kPa.

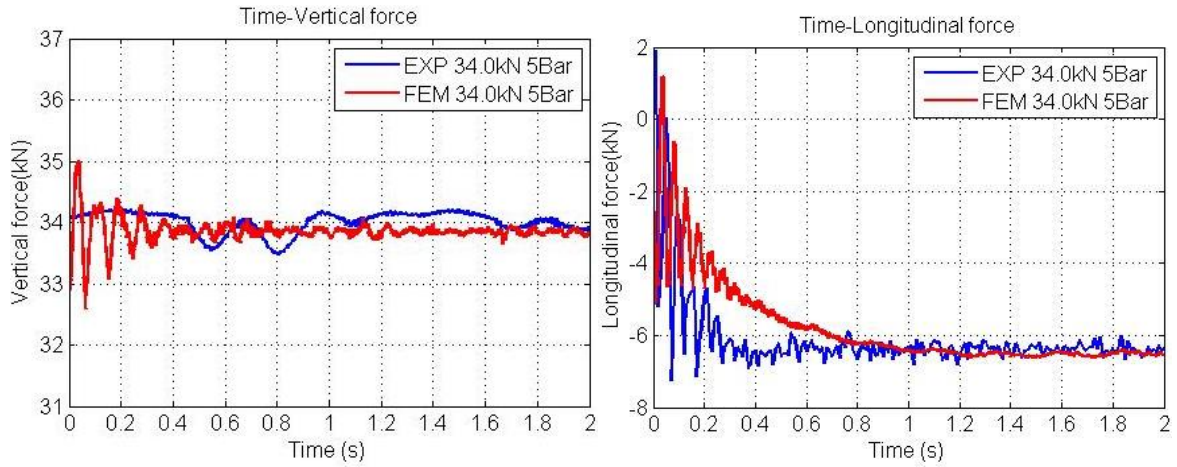

Fig. 6.34: Vertical and longitudinal reacting force at the wheel load of 34 kN and the inflation pressure of 500 kPa

As displayed in Fig. 6.35, the tendency of the vertical and longitudinal forces obtained from the simulations and the experiments are in accordance with each other. The stabilized longitudinal forces from the simulations and the experiments are 9.76 and 9.55 kN at the wheel load of 41 kN and the inflation pressure of 500 kPa.

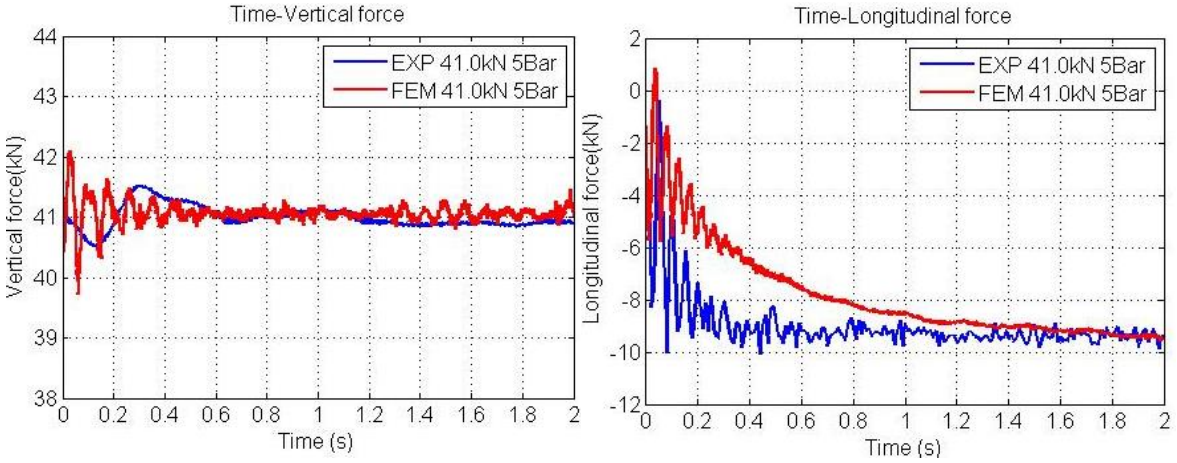

Fig. 6.35: Vertical and longitudinal reacting force at the wheel load of 41 kN and the inflation pressure of 500 kPa

As displayed in Fig. 6.36, the tendency of the vertical and longitudinal forces obtained from the simulations and the experiments are in accordance with each other. The stabilized longitudinal force from the simulations and the experiments are 7.14 and 6.97 kN at the wheel load of 34 kN and the inflation pressure of 700 kPa.

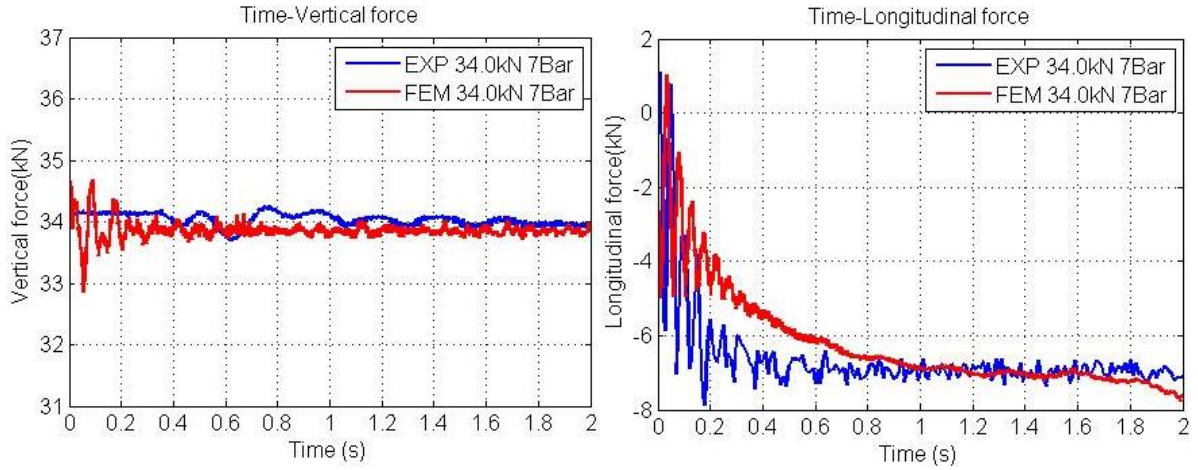

Fig. 6.36: Vertical and longitudinal reacting force at the wheel load of 34 kN and the inflation pressure of 700 kPa

As displayed in Fig. 6.37, the tendency of the vertical and longitudinal forces obtained from the simulations and the experiments are in accordance with each other. The stabilized longitudinal force from the simulations and the experiments are 9.87 and 10.08 kN at the wheel load of 41 kN and the inflation pressure of 700 kPa.

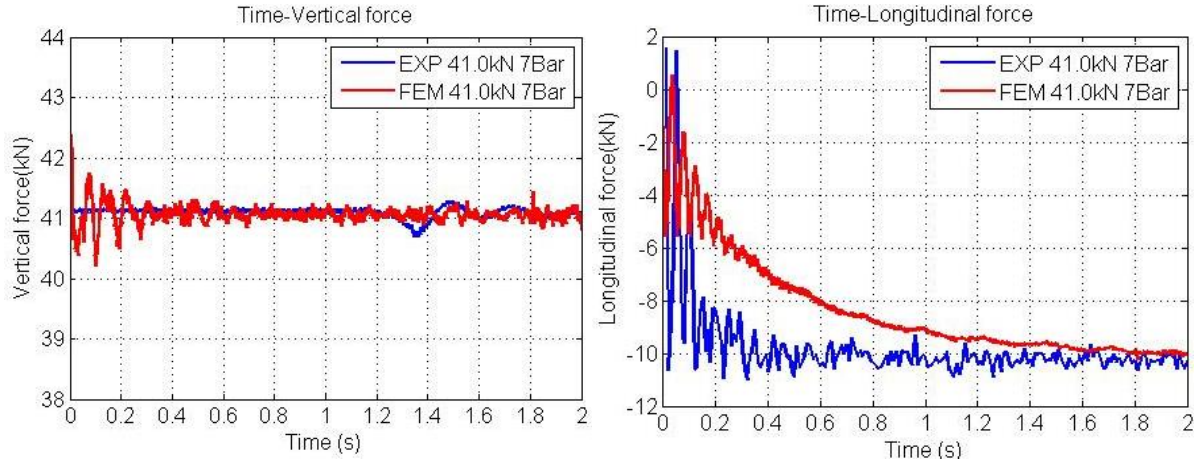

Fig. 6.37: Vertical and longitudinal reacting force at the wheel load of 41 kN and the inflation pressure of 700 kPa

Observed in the figures illustrating the comparison of the experimental and simulation results, the average vertical force is generally in good quantitative agreement. The difference of these forces obtained from the experiments and the simulations are caused by the following reasons:

1. In the simulations the soil surface is flat; however the test field is not exactly flat. There are some ups and downs in small amplitudes.
2. It's possible that the soil in different sections of the test field has slight different characteristics, such as grain size and soil moisture

The variations of the longitudinal force decrease along the time axis. The final stabilized longitudinal forces obtained from the experiments and simulations are in good quantitative agreement. However the transient characteristics of the longitudinal forces aren't exactly the same. The stabilizing development of the forces obtained from the experiment is faster than those obtained from the simulations, and the oscillations of the experimental longitudinal force are larger. This difference can be explained as follows:

1. There is a small amount of gravel in the soil of the test field. In the simulations, the soil which is a type of homogeneous material, doesn't take into account any gravel or small stones. Therefore the stiffness of the actual soil in the test field is slightly larger, and the development of the stabilized longitudinal forces is faster.
2. The test field is not exactly flat, and it causes the oscillations of the longitudinal forces.

6.5 Conclusion

In this chapter, the single wheel tester for the validation of the FE tire and soil models was introduced. Six load cells and a laser distance sensor were mounted on the single wheel tester and calibrated for the measurement of the reacting forces and the tire deformation. Prescale films were applied for the measurement of the stress inside the tire-ground contact. A 3D Kinect camera was used to capture the geometry data of the soil plastic deformation.

The FE tire models were validated by measuring the tire stiffness and the contact stress, and a good consistency was observed between the simulation and the experimental results. The parameters such as Young's modulus, Poisson's ratio, soil cohesion and friction angle were identified through triaxial tests to fit the FE soil model. The FE tire-soil interaction models were validated through two sets of tests. The static tests of the tire-soil contact is to measure the soil compaction at different wheel loads and inflation pressures, and the dynamic tests of the tire-soil contact is to measure the development of the forces generated on the tire-soil interaction interface at different wheel loads and inflation pressures. The experimental results obtained from these two sets of tests are in accordance with the simulation results.

7 Comparison of the Analytical and FE Simulations

The objectives of the simulations described in this chapter were to compare the results obtained from the analytical and the FE models. The soil parameters in the FE model were identified through the triaxial tests in the laboratory, as mentioned in chapter 6.3. A number of simulations were performed with Abaqus to identify the soil parameters for the analytical model. One group of simulations similar to the pressure-sinkage tests were conducted for the derivation of the cohesive and frictional moduli, the sinkage exponent, and the soil damping coefficient which were used in the pressure-sinkage model. The other group of simulations similar to the shear box tests were performed for the derivation of the soil cohesion, internal friction angle and shear displacement moduli which were used in the shear stress-displacement model.

7.1 Simulations of the pressure-sinkage tests

In the simulation, eight different steel plates in the length of 280 mm and different widths ranging from 60 mm to 200 mm were forced to penetrate into the soil. The sinkage and normal pressure were outputted for the post-processing. The FEM model of the pressure-sinkage tests is illustrated in Fig. 7.1. The vertical sinkage of 20 mm was defined on the steel plate.

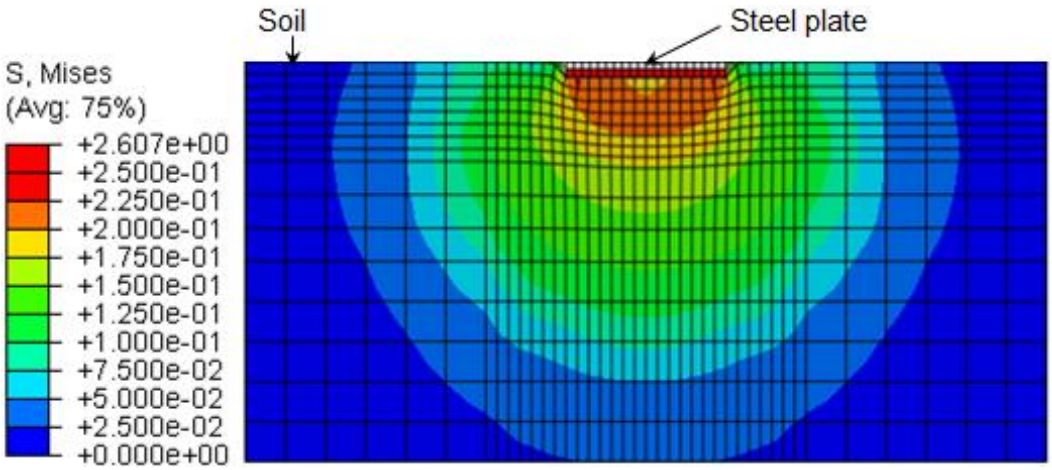

Fig. 7.1: FEM model of the pressure-sinkage tests

The soil model has the dimensions of 1 m in length, 1 m in width and 0.5 m in depth. The widths of the plates are 60 mm, 80 mm, 100 mm, 120 mm, 140 mm, 160 mm, 180 mm and 200 mm. The pressure-sinkage relationships for different loading steel plates are illustrated in Fig. 7.2.

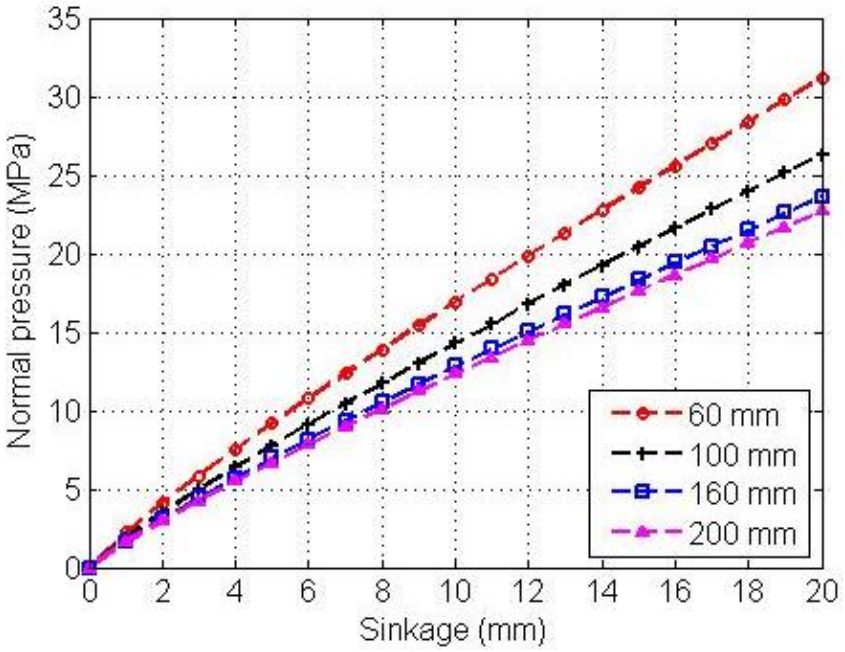

Fig. 7.2: Pressure-sinkage relationships for different plates

Eq. 7.1 was applied to fit the simulation results using non-linear regression. The plate width and the sinkage were handled as independent variables, and the normal pressure was handled as a dependent variable. The regression results for the parameters of the pressure-sinkage model are listed in Table 7.1.

$$p = \left(k_c / b + k_\phi\right) z^n + c_s v_r / A_c \qquad 7.1$$

Table 7.1: Parameters obtained from the pressure-sinkage tests

Cohesive modulus k_c [kPa/m^{n-1}]	Cohesive modulus k_Φ [kPa/m^n]	Sinkage exponent n	Damping coefficient c_s [Ns/m]
51.6	1358.7	0.882	412.6

7.2 Simulations of the shear box tests

The simulations which are similar to the shear box tests were performed for the derivation of the soil cohesion, internal friction angle and shear displacement modulus of the shear stress-displacement model. In the simulation, six different normal pressures (100, 120, 140, 160, 180 and 200 kPa) were applied on the steel plate 1 which is on the topsoil surface. The lateral displacement of 80 mm was defined on the steel plate 2. Hence the steel plate 2 pushes the soil until the specified position is reached, and the shear stresses between the soil layers are developed.

The shear stresses and the displacement were outputted for the post-processing. The FEM model of the shear box tests is illustrated in Fig. 7.3.

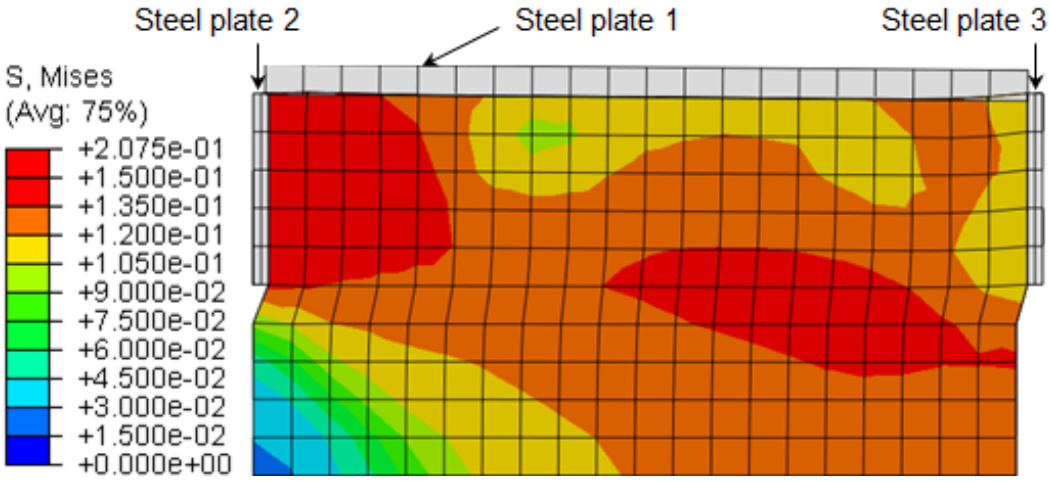

Fig. 7.3: FEM model of the shear box tests

The soil model has the dimensions of 1 m in length, 1 m in width and 0.5 m in depth. The steel plate 1 has the dimensions of 1 m in length and 1 m in width. The steel plate 2 and 3 has the dimensions of 1 m in length and 0.25 m in width. The relationships of the shear stress-displacement at different normal pressures are illustrated in Fig. 7.4.

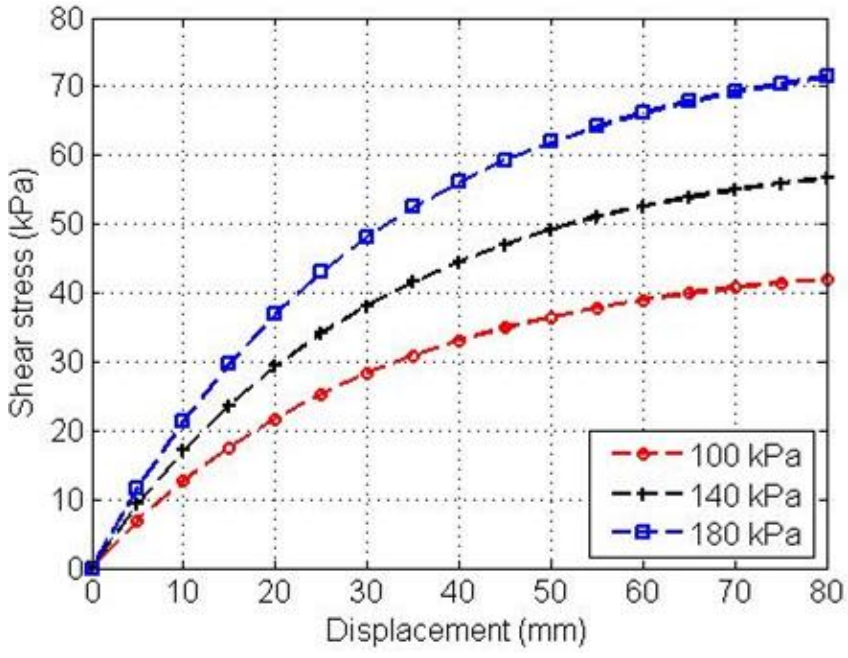

Fig. 7.4: Shear stress-displacement relationships at different normal pressures

Eq. 7.2 was applied to fit the simulation results using the non-linear regression. The normal pressure and the displacement were handled as independent variables, and

the shear stress was handled as a dependent variable. The regression results for the parameters of the shear stress-displacement model are given in Table 7.2.

$$\tau = \left(c + \sigma \tan\phi\right)\left(1 - e^{-j/K}\right) \qquad 7.2$$

Table 7.2: Parameters obtained from the shear box tests

Soil cohesion c [kpa]	Internal friction angle ϕ [°]	Shear deformation modulus K_x, K_y [mm]
5.8	21.6	43.7

7.3 Simulations performed with the analytical and FE model

Two simulation groups (tire sinking and rolling at the inflation pressure of 700 kPa and the wheel load of 30 kN) were performed with the analytical and the FE model. The simulation results with these models were compared. It should be noticed that the tire and the soil in these models correspond to the same tire and soil parameters.

In the analytical model, constant tire stiffness was defined at each constant inflation pressure. The tire stiffness in the FE model increases with the wheel load and the inflation pressure. At the same wheel load, more soil compaction and less tire deformation are observed for the tire which has larger stiffness.

As displayed in Fig. 7.5, the curves of the tire sinkage-wheel load relationships obtained from the analytical and the FE model have the same tendency: the curve slope is getting larger at larger tire sinkages. When the wheel load exceeds 35 kN, it is observed that the tire sinkage is larger for the FE model.

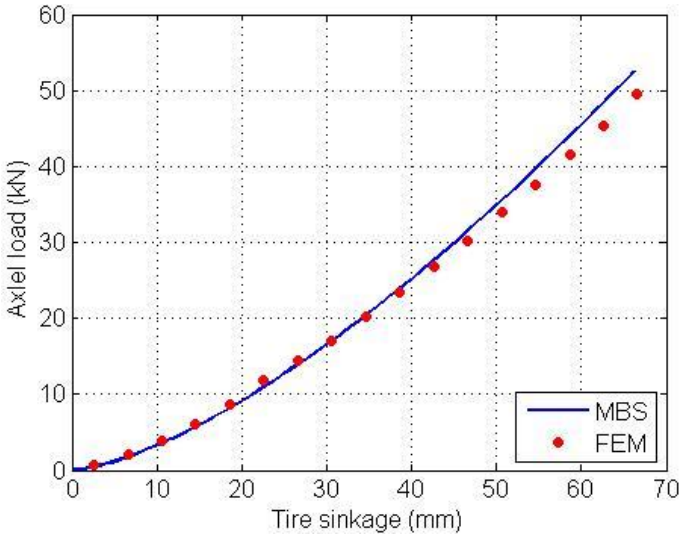

Fig. 7.5: Tire sinkage and wheel load relationship

The curves of the longitudinal and the lateral force at different longitudinal and lateral slips obtained from the analytical and the FE model are displayed in Fig. 7.6 and 7.7. As observed in Fig. 7.6, the tendency of the longitudinal forces developed on the tire-soil contact patch is similar along the axis of the longitudinal slip for the analytical and the FE simulations. However the amplitude of the longitudinal force at the same longitudinal slip is larger for the FEM simulations. One of the major differences between the analytical and the FE tire model is that the FE model considers the tread patterns but the analytical model doesn't. tread patterns are of great importance to the traction performance of the tire. From the comparison it is noticed that tread patterns have a positive influence on the tire traction performance: the traction and braking forces, which can be provided on the soil are larger for the tires with tread patterns.

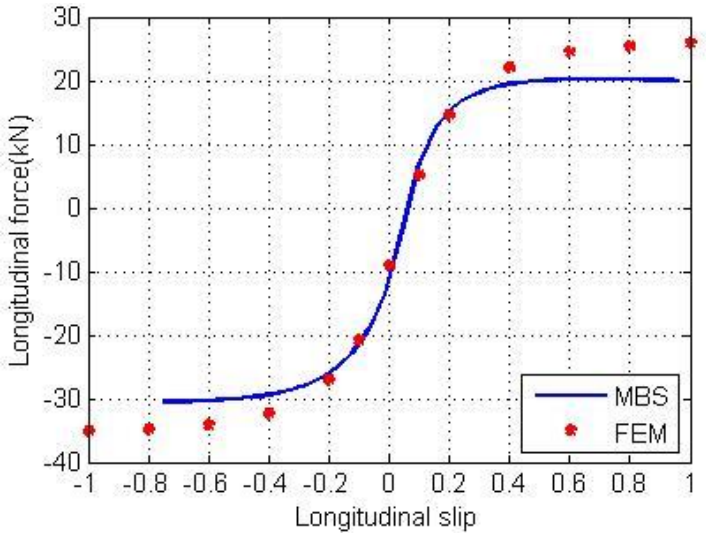

Fig. 7.6: Longitudinal slip and longitudinal forces relationship

As observed in Fig. 7.7, the tendency of the lateral forces developed on the tire-soil contact patch is similar along the axis of the slip angle for the analytical and the FE simulations. However the amplitude of the lateral force at the same slip angle is larger for the FEM simulations as well. Since the soil deformation is relatively little compared to the tire diameter, it is assumed that the lateral bulldozing resistance can be ignored in the analytical tire-soil interaction model. The bulldozing and friction resistance on the sidewall are simulated through the FE tire-soil interaction models. At small slip angles the amplitudes of the lateral forces are similar, but as the slip angle increases the differences of the lateral forces are obvious. This phenomenon is explained as follows: the contact stress on the tire-soil interface increases with the slip angle. As the slip angle becomes larger, the contact stress becomes larger which

leads to more soil deformation. More soil deformation could result in larger bulldozing resistance; therefore the lateral forces obtained from the FE models are larger.

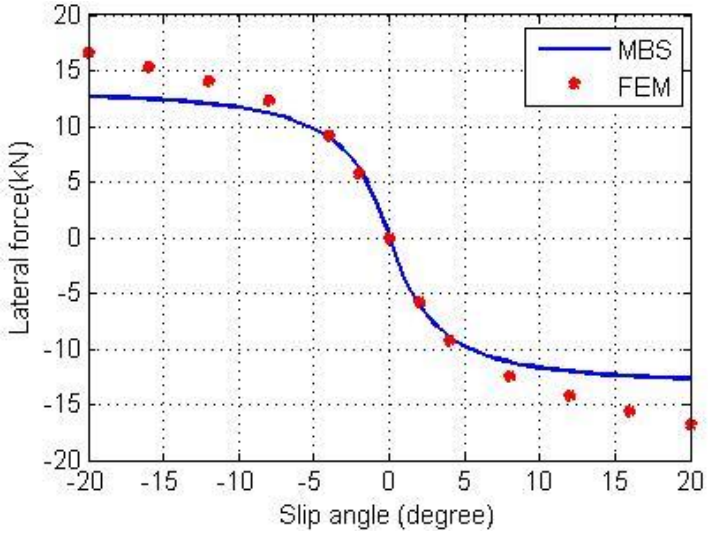

Fig. 7.7: Slip angle and lateral force relationship

7.4 Conclusion

The conversion of the FE soil model to the analytical soil model was realized through the simulations of the pressure-sinkage and shear box tests. The parameters in the analytical model were derived through the non-linear regressions.

The simulations with the application of the analytical and FE models were carried out. Under the same operating conditions, the simulation results such as the tire sinkage, the longitudinal and lateral forces obtained from these two models were compared and analyzed. It is observed that the simulation results of the tire sinkage-wheel load relationship are similar, and those of the longitudinal slip/slip angle – longitudinal/lateral force are different due to the simplifications proposed in the analytical model such as the bull dozing resistance and the tire tread are neglected.

8 Summary and Outlook

This dissertation is dedicated to providing reliable simulation models for the tire-soil interaction. Analytical models which could be integrated in Multi-Body Simulation (MBS) software have the advantages that the computational efficiency is high and these models could be applied in the simulations of vehicle-soil interaction. However the stress analysis inside the tire-soil interaction interface is not available with the analytical models. Finite element (FE) models provide opportunities to study stresses not only inside the tire-soil interaction interface, but also in the tire and soil models. Besides the geometrical features of tires such as tread patterns and inner reinforcement layers could be considered in the FE models. These two methods (analytical and finite element methods) were applied to model the tire-soil interaction.

For the analytical model, the major objective is to study the geometry of the contact contour and the stress on the tire-soil interface. Empirical equations such as the sinkage-pressure and shear stress-displacement relationships were used to predict the normal and tangential stresses on the tire-soil interface. Due to the fact that these empirical equations are derived from quasi-static experiments, the influence of the penetrating velocity on the soil mechanical characteristics is not considered. In the normal direction, the sinkage-pressure relationship which is similar like a non-linear spring was applied to link the quasi-static radial stress to the tire sinkage. To account for the dynamic radial stress, dampers parallel to the non-linear springs were added. A substitute circle larger than the unloaded tire was adopted to model the contact contour of the deformable tire. The forces and moments developed on the tire-soil interface were calculated by integrating the stresses in the longitudinal, lateral and vertical directions along the contact contour. The equations accounting for the forces and moments were compiled as subroutines in the MBS software Adams. A number of simulations were carried out to study the soil damping effect, the soil compaction, the reacting forces and moments for the rigid and deformation tires under different operating conditions. Exponential equations were applied to fit the soil deformation/tire deflection-wheel load curves, and the Magic Formula (MF) models were applied to fit the longitudinal slip – longitudinal force and the lateral slip-lateral force/anti-aligning torque curves.

For the FE model, the major objective is to develop a precise tire structure, to select appropriate element sizes and types for the tire and soil components, to define

proper constraints and contacts, and to choose appropriate models for the material description. The tread structure and the inner layers consisting of the cord-rubber composites were considered in the FE tire model. The elasto-plastic model was used to present the FE soil model which exhibits the elastic and plastic properties. Two FE tire models (uneven-spaced and even-spaced tire model) were established for different simulation usages. The uneven-spaced tire model was used for the study of soil compaction, as only the tire bottom interacts with the soil; the even-spaced tire model was used for the study of dynamic behaviors when the tire rotates. The uneven-spaced tire model could improve the computational efficiency without degrading the accuracy of the simulation results. The simulation procedure is in the following sequence: tire assembling, tire inflating, tire loading, soil compacting, pure longitudinal slip and pure lateral slip. The simulations in the first three steps were performed with the Abaqus/Implicit module, and those in the rest steps were performed with the Abaqus/Explicit module. The simulation results such as the stress distribution, the tire/soil deformation and the forces generated on the tire-soil interface were analyzed. Exponential equations were applied to fit the soil deformation/tire deflection-wheel load relationships, and the MF models were applied to fit the longitudinal slip – longitudinal force and the lateral slip-lateral force curves.

A single wheel tester pushed forward by an excavator is capable of measuring the tire deformation and the forces in the longitudinal, lateral and vertical direction. Experiments were carried out for the validation of the FE tire-soil interaction models. The tire stiffness and the distribution of the contact stress were measured to validate the FE tire models. The soil compaction and the soil reacting forces at different wheel loads and inflation pressures were measured to validate the FE tire-soil interaction models.

The parameters of the FE soil model were measured through the triaxial tests. To identify the parameters of the analytical soil model, the simulations similar to the pressure-sinkage and shear box tests were carried out with Abaqus. The simulation results of the analytical and the FE tire-soil interaction models such as tire sinkage, vertical and longitudinal forces were compared.

The summarized results of this dissertation are presented as follows:

1. Non-linear springs and dampers were applied to describe the stress in the tire radial direction; the shear stress-displacement relationship was applied to describe the stress in the tangential direction. Drawbar pull, lateral force, vertical

force, rolling resistance, anti-aligning torque can be predicted in the analytical rigid/elastic tire-deformable soil interaction models. These models can improve the prediction of tire dynamic behaviors.

2. Tire performance such as drawbar pull, cornering force and anti-aligning torque at different slipping conditions were investigated with the analytical tire-soil interaction models. The analytical models are capable of providing quantitative understanding and prediction of the tire-soil interacting forces and moments.
3. Two FE tire models (uneven and even-spaced tire model) were developed for different simulations. Taking into account the tread structure and the inner reinforcement layers, the FE tire model is more similar to the real tire. The Modified Drucker-Prager/Cap model and the elastic model were applied to describe the soil.
4. The soil compaction and wheel load relationship at different inflation pressures was investigated with the FE uneven-spaced tire-soil interaction model. The impact of the inflation pressure and the wheel load on the soil compaction is different at different soil depths. The inflation pressure is more dominate for the topsoil compaction, and the wheel load is more dominate for the compaction of the lower subsoil. The tire dynamic performance such as drawbar pull and cornering force at different slipping conditions was investigated with the FE even-spaced tire-soil interaction model. Lower inflation pressure brings some advantages such as larger drawbar pull, braking force and cornering force, and less rolling resistance in contrast.
5. The FE tire models were validated by measuring the tire stiffness and the contact stress under the support of the single wheel tester. The FE tire-soil interaction models were validated by measuring the forces generated on the tire-soil interface. A good qualitative agreement was observed between the simulation and experimental results.
6. Simulations were carried out with the analytical and FE tire-soil interaction models, and simulation results were compared and analyzed. It was observed that tire behaviors predicted with these two models could be different. The longitudinal and lateral forces predicted with the FE model are larger compared to those predicted with the analytical model.

7. With the analytical and FE tire-soil interaction models, it's possible to evaluate the tire/soil deformation and the forces/moments developed on the tire-soil interface. However the analysis of the tire transient behavior and the stress/strain distribution is only available with the FE models.
8. By using the validated FE model as a reference, the accuracy of the analytical model such as the predicted results of longitudinal/lateral forces and anti-aligning torques can be determined. By comparing the simulation results from the analytical and FE model, it is noticed that the differences of these results are in an acceptable range. The analytical model can be further applied in the simulations of the vehicle-soil interaction.

The work which should be done in the future are addressed as follows.

In the analytical models, the camber angle, the bulldozing resistance, the multi-pass effect and the tread structure were ignored. Empirical equations are required to account for those effects on the tire-soil interaction models. The tire hysteresis behavior isn't considered either in these models. In order to more accurately predict the tire transient behavior more efforts have to be focused on the tire dynamic properties.

In the FE models, the soil is assumed as a continuum, and the study object is a kind of sandy clay. For the pure sand which is comprised of small particles in different sizes, the FE method is not appropriate due to the fact that there is limited cohesive force between the sand particles. The discrete element method could be a better choice for the study of the tire-sand interaction. The friction coefficients of the tire/rim and tire/soil contact in the tangential direction are assumed to be constant. However the friction coefficient is influenced by many factors such as slip rate, temperature and normal pressure. More research should be done for the identification of the friction coefficient.

To fully validate the tire-soil interaction modes, more experiments for different longitudinal slips and lateral slip angles should be carried out.

9 Literature

[1] Chan, B. J..: *Development of an Off-Road Capable Tire Model for Vehicle Dynamics Simulations*. PhD dissertation, Virginia Polytechnic Institute and State University, 2008.

[2] Frey, N. W.: *Development of a Rigid Ring Tire Model and Comparison among Various Tire Models for Ride Comfort Simulations*. Master thesis, The Clemson University, 2009.

[3] Slade, J. L.: *Development of a New Off-Road Rigid Ring Model for Truck Tires Using Finite Element Analysis Techniques*. Master thesis, The Pennsylvania State University, 2009.

[4] Gibbesch, A.; Schäfer, B.: *Multibody System Modelling and Simulation of Planetary Rover Mobility on Soft Terrain*. In: Proceedings ISAIRAS 2005 Conference, Munich, 2005.

[5] Xia, K.; Yang, Y.: *Three-dimensional Finite Element Modeling of Tire/Ground Interaction*. Int. Journal for Numerical and Analytical Methods in Geomechanics, 36 (2012), 498-516.

[6] Zheng, D.: *Prediction of Tire Tread Wear with FEM Steady State Rolling Contact Simulation*. Tire Science and Technology, 31 (3) (2003), 189-202.

[7] Han, Y. H. et. al.: *Fatigue Life Prediction for Cord-Rubber Composite Tires Using a Global-Local Finite Element Method*. Tire Science and Technology, 32 (1) (2004), 23-40.

[8] Collins, J. G.: *Forecasting trafficability of soil*. Technical Memo 3-331, Vicksburg, Miss: USA Corps of Engineers Waterways Experiment Station, 1971.

[9] Voorhees, M. L.; Walker, P. N.: *Tractionability as a function of soil moisture*. Transactions of the ASAE, 20 (5) (1977), 806-809.

[10] Wells, L. G.; Tresuwan, O.: *The response of various soil strength indices to changing water content*. ASAE Paper No. 77-1055 (1977), St. Joseph, Mich.: American Society of Agricultural Engineers.

[11] Ayers, P. D.; Perumpral, J. V.: *Moisture and density effect on cone index*. Transactions of the ASAE, 25 (5) (1982), 1169-1172.

[12] Perumpral, J. V.: *Cone penetrometer applications-a review*. Transactions of the ASAE, 30 (4) (1987), 939-944.

[13] Bekker, M. G.: *Introduction to terrain-vehicle systems*. Ann Arbor, Michigan: The University of Michigan Press, 1969.

[14] Anderson, G., Pidgeon, J. D.; Spencer, H. B.: *A new hand-held recording penetrometer for soil study*. Journal of Soil Science, 31 (2) (1980), 279-296.

[15] Olsen, H. J.: *Electronic cone penetrometer for field test*. Proceedings of the 9th International Conference of the International Society for Terrain-Vehicle Systems, 1987.

[16] Herrick, J. E.; Jones, T. L.: *A dynamic cone penetrometer for measuring soil penetration resistance*, Soil Science Society of America Journal, 66 (2002), 1320-1324.

[17] Bekker, M. G.: *Theory of land locomotion*. Ann Arbor, Michigan: The University of Michigan Press, 1956.

[18] Bekker, M. G.: *Off-the-road locomotion. Ann Arbor, Michigan*: The University of Michigan Press, 1960.

[19] Bekker, M. G.: *Mechanics of locomotion and lunar surface vehicle concepts*. Transactions of SAE, 72 (1964), 549-569.

[20] Wong, J. Y.: *Terramechanics and Off-Road Vehicle Engineering*. Printed and bound in the UK, 1989.

[21] Freitag, D. R.: *A dimensional analysis of the performance of pneumatic tires on soft soils*. Technical Report No. 3-688, Vicksburg, Mississippi, USA: US Army Engineer Waterways Experiment Station, 1965.

[22] Turnage, G. W.: *Performance of soils under tire loads; application of test results to tire selection for off-road vehicles*. Technical Report No. 3-666, Vicksburg, Mississippi, USA: US Army Engineer Waterways Experiment Station, 1972.

[23] Turnage, G. W.: *A synopsis of tire design and operational considerations aimed at increasing in-soil tire drawbar performance*. Proceedings of the 6th International Conference of the International Society for Terrain-Vehicle Systems, 1978.

[24] Wismer, R. D.; Luth, H. J.: *Off-road traction prediction of wheeled vehicles*. Journal of Terramechanics,10 (2) (1973), 49-61.

[25] Wismer, R. D.; Luth, H. J.: *Off-road Traction Prediction for Wheeled Vehicles*. Transactions of ASAE, 17(1) (1974): 8-10.

[26] Rula, A. A; Nuttall, J.: *An Analysis of Ground Mobility Models (ANAMOB)*. Technical Report M-71-4. U. S. Army Engineer Waterways Experiment Station. Vicksburg, Mississippi, 1971.

[27] Reece, A. R.; Peca, J. O.: *An assessment of the value of the cone penetrometer in mobility prediction*. Proceedings of the 7th International Conference of the International Society for Terrain-Vehicle Systems, A1-A33, 1981.

[28] Gee-Clough, D.: *A comparison of the mobility number and Bekker approaches to traction mechanics and recent advances in both methods*. Proceedings of the 6th International Conference of the International Society for Terrain-Vehicle Systems, 1978.

[29] Grecenko, A.; Prikner, P.: *Progress in tire rating based on soil compaction potential*. Journal of Terramechanics, 46 (2009), 211-216.

[30] Bernstein, E.: *Probleme zur experimentellen Motorplugmechanic*. Der Motorwagen 16.heft, 1913.

[31] Goriatchkin, B. P.: *Theory and Development of Agriculture Machinery*, Moscow, 1936.

[32] Reece, A. R.: *Principles of soil-vehicle mechanics*. Proceedings of the Institution Mechanical Engineers, 180 (1965), 45-67.

[33] Meirion-Griffith, G.; Spenko, M.: *A modified pressure-sinkage model for small, rigid wheels on deformable terrains*. Journal of Terramechanics, 48 (2) (2011), 149-155.

[34] Wong, J. Y.: *An introduction to terramechanics*. Journal of Terramechanics, 21(1) (1984), 5-17.

[35] Wong, J. Y.: *On the study of wheel-soil interaction*. Journal of Terramechanics, 21 (2) (1984), 117-131.

[36] Janosi, Z.: *An analysis of pneumatic tire performance on deformable soil*. Proceedings of the 1st International Conference on the Mechanics of Soil-Vehicle Systems. Edizioni Minerva Tecnica, Troino, Italy, 1961.

[37] Janosi, Z.; Hanamoto, B.: *The analytical determination of drawbar pull as a function of slip for tracked vehicles in deformable soils*. Proceedings of the 1st International Conference on the Mechanics of Soil-Vehicle Systems, Torino, Italy, 1961.

[38] Wong, J. Y.; Preston-Thomas, J.: *On the characterization of the shear stress-displacement relationship of terrain*. Journal of Terramechanics, 19 (4) (1983), 107-127.

[39] Wong, J. Y.: Evaluation of soil strength measurements. NRCC Report No. 22881, National Research Council of Canada, 1983.

[40] Kacigin, V. V.; Guskov, V. V.: *The basis of tractor performance theory*. Journal of Terramechanics, 5 (3) (1968), 43-66.

[41] Oida, A.: *Study on equation of shear stress-displacement curves*. Report No. 5, Japan: Farm Power and Machinery Laboratory, Kyoto University, 1979.

[42] Wills, B. M. D.: *The measurement of soil shear strength and deformation moduli and a comparison of the actual and theoretical performance of a family of rigid tracks*. Journal of Agricultural Engineering Research, 8 (2) (1963), 115-131.

[43] Kiebre, R.: Ph.D. Thesis, *Contribution to the modelling of aircraft tire-road interaction*, Upper Alsace University, 2010.

[44] Fiala, E.: *Lateral forces on rolling pneumatic tires*. In Zeitschrift V.D.I. 96 (29) (1954), 114.

[45] Tielking, J. T.; Mital, N. K.: *A comparative evaluation of five tire traction models*. Technical Report UM-HSRI-PF-74-2, Highway Safety Research Institute, Ann Arbor, Michigan, 1974.

[46] Bernard, J. E.; Segel, L.; Wild, R. E.: *Tire shear force generation during combined steering and braking maneuvres*. SAE 770852, 1977.

[47] Sakai, H.: *Theoretical and experimental studies on the dynamic cornering properties of tires*. International Journal of Vehicle Design, 2 (1981), 1-4.

[48] Sakai, H.: *Study on cornering properties of tire and vehicle*. Tire Science and Technology, TSTCA, 18 (3) (1990),136-196.

[49] Pacejka, H. B.: *Tire and Vehicle Dynamics, 2nd edition*. SAE International, ISBN 0768017025, 2005.

[50] Bakker, E.; Nyborg, L.; Pacejka, H. B.: *Tire modelling for use in vehicle dynamics studies*. SAE paper 870421, Society of Automotive Engineers, 400 Commonwealth Drive, Warrendale, PA 15096, USA, 1986.

[51] Bayle, P.; Forissier, J. F.; Lafon, S.: *A new tire model for vehicle dynamic simulations*. In: Proceedings of Automotive Technology International, 1993.

[52] Pacejka, H. B.; Bakker, E.: *The magic formula tire model, tire models for vehicle dynamic analysis*. Proceedings of the 1st International Colloquium on Tire Models for Vehicle Dynamic Analysis, Lisse, 1-18, 1993.

[53] Pacejka, H. B.: *The role of tire dynamic properties. Seminar on Smart Vehicles*, Proceedings: Vehicle System Dynamics, Special Issue, Delft, February 1995.

[54] Pacejka, H. B.; Besselink, I. J. M.: *Magic formula tire model with transient properties*. Proceedings of the Berlin Tire Colloquium, Vehicle System Dynamics Supplement 27, Lisse, 145-155, 1997.

[55] Pacejka, H. B.: *Tire Mechanics and Vehicle Dynamics*. Elsevier Science, 2002.

[56] Schlippe, B.; Dietrich, R.: *Das Flattern eines bepneuten Rades (Shimmying of a pneumatic wheel)*. In: Bericht 140 der Lilienthal-Gesellschaft für Luftfahrtforschung, 1941.

[57] Fromm, H.: *Kurzer Bericht über die geschichte der Theorie des Radflatterns*. Bericht 140 der Lilienthal Gesellschaft, 1941.

[58] Van Oosten, J.; Pacejka, H. B.: *SWIFT-Tire: An accurate tire model for ride and handling studies also at higher frequencies and short road wavelengths*, ADAMS Users' Conference, Orlando, 19-21 June, 2000.

[59] Gipser, M.: *FTire: a physically based application-oriented tire model for use with detailed MBS and finite-element suspension models*. Vehicle System Dynamics, 43 (2005), 76-91.

[60] Gallrein, A.; Bäcker, M.: *CDTire: a tire model for comfort and durability applications*. Vehicle System Dynamics, 45 (2007), 69-77.

[61] Wong, J. Y.; Reece, A. R.: *Prediction of rigid wheel performance based on the analysis of soil-wheel stresses - Part I. Performance of driven rigid wheels*. Journal of Terramechanics, 4 (1) (1967), 81-98.

[62] Wong, J. Y. ; Reece, A. R.: *Prediction of rigid wheel performance based on the analysis of soil-wheel stresses - Part II. Performance of towed rigid wheels*. Journal of Terramechanics, 4 (2) (1967), 7-25.

[63] Yoshida, K. et. al.: *Terramechanics-based analysis and traction control of a lunar/planetary rover*. In Proceedings of the Int. Conf. on Field and Service Robotics FSR '03, Yamanashi, Japan, 2003.

[64] Yoshida, K. and Ishigami, G.: *Steering characteristics of a rigid wheel for exploration on loose soil*. In Proceedings of the 2004 IEEE Int. Conf. on Intelligent Robots and Systems IROS '04, Sendai, Japan, 2004.

[65] Karafiath, L.; Nowatzki, E.: *Soil Mechanics for off-road vehicle engineering*. Trans Tech Publication, Clausthal, Germany, 1978.

[66] Irani. R. A.; Bauer R. J.; Warkentin, A.: *A dynamic terramechanic model for small lightweight vehicles with rigid wheels and grousers operating in sandy soil*. Journal of Terramechanics, 48 (2011), 307-318

[67] Krenn, R.; Hirzinger, G.: *SCM-A Soil Contact Model for Multi-Body System Simulations*, 11th European Regional Conference of the International Society for Terrain-Vehicle Systems, Bremen, October 5-8 2009.

[68] Wong, J. Y.: *Performance of the Air Cushion-Surface Contacting Hybrid Vehicle for Overland Operation*. in Proc. Institution of Mechanical Engineers, 186 (1972), 50-72.

[69] Wong, J. Y.: *Theory of ground vehicles*. New York, NY: John Wiley, 1978.

[70] Schmid, I.; Luderwig, J.: *Improved Calculation of Sinkage of a wheel on Soft ground*. Proc. 5th European Conference of the ISTVS, Budapest, 1991

[71] Harnisch, C. et al.: *A new tire-soil interaction model for vehicle simulation on deformable ground*. Vehicle System Dynamics, 43 (2005), 384-394.

[72] Chan, B. J.; Sandu, C.: *A Novel Wheel-Soil Interaction Model for Off-road Vehicle Dynamics Simulation*. Proceedings of ASME IDETC, 9th International Conference on Advanced Vehicle and Tire Technologies, Las Vegas, NV, 2007.

[73] Senatore, C.; Sandu, C.: *Off-road tire modeling and the multi-pass effect for vehicle dynamics simulation*. Journal of Terramechanics, 48 (2011), 265-276.

[74] Favaedia, Y. et. al.: *Prediction of tractive response for flexible wheels with application to planetary rovers*. Journal of Terramechanics, 48 (3) (2011), 199-213

[75] Adams documentation, *Adams/Tire tutorial*, MSC Software, Inc.; 2010.

[76] Perumpral, J. V.; Liljedahl, J. B.; Perloff, W. H.: *A numerical method for predicting the stress distribution and soil deformation under a tractor wheel*. Journal of Terramechanics, 8 (1971), 9-22.

[77] Yong, R. N.; Fattah, E. A.: *Prediction of wheel-soil interaction and performance using finite element method*. Journal of Terramechanics, 13(4) (1976), 227-240.

[78] Yong, R. N.; Fattah, E. A.; Boosinsuk, P.: *Analysis and prediction of tire-soil interaction and performance using finite elements*. Journal of Terramechanics, 15 (1) (1978), 43-63.

[79] Pi, W. S. *Dynamic tire/soil contact surface interaction model for aircraft ground operations*. Journal of Aircraft, 25(11) (1988), 1038-1044.

[80] Foster W.A.; Johnson C. E.; Raper R. L.: *Soil deformation and stress analysis under a rolling wheel*. Proceedings of the 5th North American ISTVS Conference/Workshop, Saskatoon, Canada, 1995

[81] Liu, C. H.; Wong, J. Y.: *Numerical simulations of tire-soil interaction based on critical state soil mechanics*. Journal of Terramechanics, 33 (1996), 209-221.

[82] Aubel, T.: *FEM simulation of the interaction between elastic tire and soft soil*. In Proceedings, 11th International Conference of the ISTVS, Lake Tahoe, Nevada, 1993.

[83] Fervers, C. W.: *FE simulations of tire-profile effects on traction on soft soil*. In Proceedings, 6th European Conference of the ISTVS, Vienna, Austria, 1994.

[84] Fervers, C. W. *Effects of traction and slip, investigations with FEM*. In Proceedings, 7th European Conference of the ISTVS, Ferrara, Italy, 1997.

[85] Shoop, S. A. et. al.: *Finite element analysis of a wheel rolling in snow*. In: Proceedings of the 10th international conference on cold regions engineering. Lincoln, NH, August 1999.

[86] Darnell, I. *An efficient three-dimensional tire model for predicting spindle loads*. PhD dissertation, University of Michigan, 2001.

[87] Shoop, S. A.; Darnell, I.; Kestler, K.: *Analysis of Tire Models for Rolling on a Deformable Substrate*. Tire Science and Technology, 30 (3) (2002), 180-197.

[88] Zhang, X.; Rakheja, S.; Ganesan, R.: *Estimation of tire-road contact pressure distribution based on nonlinear finite element analysis*. International Journal of Heavy Vehicle Systems, 8 (3/4) (2001), 197-217.

[89] Poodt, M. P.; Koolen, A. J.; van der Linden, J. P.: *FEM analysis of subsoil reaction on heavy wheel loads with emphasis on soil pre-consolidation stress and cohesion*. Soil and Tillage Research, 73 (1/2) (2003), 67-76.

[90] Cui, K.; Defossez, P.; Richard G.: *A new approach for modelling vertical stress distribution at the soil/tire interface to predict the compaction of cultivated soils by using the PLAXIS code*. Soil and Tillage Research, 95 (1/2) (2007), 277-287.

[91] PLAXIS: *Finite element code for soil and rock analysis*. Balkema, Rotterdam, Netherlands, 1998.

[92] Mulungye, R. M.; Owende, P. M. O.; Mellon, K.; *Finite element modelling of flexible pavements on soft soil subgrades*. Materials and Design, 28 (2007), 739-756.

[93] Hambleton, J. P.; Drescher, A.: *Modeling wheel-induced rutting in soils: Indentation*. Journal of Terramechanics, 45 (2008), 201-211.

[94] Hambleton, J. P.; Drescher, A.: *Modeling wheel-induced rutting in soils: Rolling.* Journal of Terramechanics, 46 (2009), 35-47.

[95] Mohsenimanesh, A.; Ward, S. M.; Owende, P. O. M.; A. Javadi: *Modelling of Pneumatic Tractor Tyre Interaction with Multi-layered Soil*. Biosystems Engineering, 104(2) (2009), 191-198.

[96] Xia, K. M.: *Finite element modeling of tire/terrain interaction: Application to predicting soil compaction and tire mobility*. Journal of Terramechanics, 48 (2010), 113-123.

[97] Biris, S.; Ungureanu, N.: *FEM Model to study the influence of tire pressure on agricultural tractor wheel deformations*. Engineering for Rural Development, 10 (2011), 223-228.

[98] Pruiksma J. P.; Kruse, G. A. M.: *Tractive Performance Modelling of ExoMars Rover Wheel Design on Loosely Packed Soil Using the Coupled Eulerian Lagrangian Finite Element Technique*. 2011.
URL:http://robotics.estec.esa.int/ASTRA/Astra2011/Presentations/Session%202A/02_pruiksma.pdf

[99] Lee J. H.: *Finite element modeling of interfacial forces and contact stresses of pneumatic tire on fresh snow for combined longitudinal and lateral slips*. Journal of Terramechanics, 48 (2011), 171-197.

[100] Choi, J. H. et. al.: *Numerical investigation of snow traction characteristics of 3-D patterned tire*. Journal of Terramechanic, 49 (2) (2012), 81-93.

[101] Carillo, A. R. et. al: *Design of a large scale discrete element soil model for high performance computing systems*. in ACM/IEEE Conference on Supercomputing, 1996

[102] Ohkubo, S.; Oida, A.; Yamazaki, M.: *Application of DEM to find the interaction between tire and soil*. In Proc. 5th Asia-Pacific Regional Conf. ISTVS, Seoul, Korea, October, 1998.

[103] Oida, A; Ohkubo, S; Schwanghart H.: *Effect of tire lug cross section on tire performance simulated by distinct element method*. Proc. 13th Int. Conf. ISTVS, Munich, Germany, 345-352, 1999.

[104] Oida, A; Ohkubo, S.: *Application of DEM to simulate interaction between soil and tire lug*. Agricultural and Biosystems Engineering, 1 (1) (2000). 1-6.

[105] Tanaka, H. et. al.: *Simulation of soil deformation and resistance at bar penetration by the distinct element method*. Journal of Terramechanics, 37 (1) (2000), 41-56.

[106] Oida, A.; Momozu, M. *Simulation of soil behavior and reaction by machine part by means of DEM*. Agricultural Engineering International: the CIGR E-journal, 5 (2002).

[107] Nakashima, H.; Oida, A.: *Algorithm and implementation of soil-tire contact analysis code based on dynamic FE-DE method*. Journal of Terramechanics 41(2/3) (2004), 127-137.

[108] Nakashima, H. et al.: *FE-DEM Analysis of the Effect of Tread Pattern on the Tractive Performance of Tires Operating on Sand*. Journal of Mechanical Systems for Transportation and Logistics, 2 (1) (2009), 55-65.

[109] Nakashima, H. et al.: *Parametric analysis of lugged wheel performance for a lunar micro-rover by means of DEM*. Journal of Terramechanics, 44 (2007), 153-162.

[110] Fujii, H.: *An analysis of lugged wheel performance by DEM for the development of wheel for a lunar rover*. Unpublished Master of Agric. Sci. Thesis. Division of Environmental Science and Technology, Graduate School of Agriculture, Kyoto University, Kyoto; 2003.

[111] Khat, L. R.; Salokhe, V. M.; Jayasuriva. H.: *Experimental validation of distinct element simulation for dynamic wheel-soil interaction*. Journal of Terramechanics, 44 (2007), 429-437.

[112] Li, W. et. al.: *Trafficability analysis of lunar mare terrain by means of the discrete element method for wheeled rover locomotion*. Journal of Terramechanics, 47 (2010), 161-172.

[113] Knuth, M.A. et al.: *Discrete element modeling of a Mars Exploration Rover wheel in granular material*. Journal of Terramechanics, 49 (2012), 27-36.

[114] Meywerk, M.: *Technische Daten für Universelle Belastungsprüfeinrichtung*. 2004. URL: http://www.hsu-hh.de/meywerk/index_2UbdlHHDkiLuKYkL.html

[115] Kawase, Y.; Nakashima, H.; Oida, A.: *An indoor traction measurement system for agricultural tires*, Journal of Terramechanics, 43 (3) (2006), 317-327.

[116] Yahya, A. et al.: *UPM indoor tire traction testing facility*. Journal of Terramechanics, 44 (2007), 293-301.

[117] Tiwari, V. K.; Pandey, K. P.; Sharma A.K.: *Development of a tire traction testing facility*. Journal of Terramechanics, 46 (2009), 293-298.

[118] Ding, L. et.al. : *Experimental study and analysis on driving wheels' performance for planetary exploration rovers moving in deformable soil.* Journal of Terramechanics, 48 (2011), 27-45.

[119] Pytka, J.; Konstankiewicz, K.: *A new optical method for soil stress and strain investigation*. Soil and Tillage Research, 65 (2002), 243-251.

[120] Billington, W. P.: *The NIAE MkII Single Wheel Tester. Research Note.* Journal of Agricultural Engineering Research, 18 (1973.), 67-70.

[121] Upadhyaya, S. K.; Wulfsohn, D.: *An overview of traction research at University of California Davis*. California Agriculture. 43 (2) (1989), 15-17.

[122] Armbruster, K.; Kutzbach, H. D.: *Development of a Single Wheel Tester for Measurements on Driven Angled Wheels*. The 4th European Conference of ISTVS, Wageningen, Niederlande, 1989.

[123] Armbruster, K.; Kutzbach, H. D.: *Combined lateral and longitudinal forces on driven angled tractor tires*. Journal of Terramechanics, 28 (4) (1991), 331-338.

[124] Morhard, J.: *Untersuchungen im Bereich der Rad-Boden-Schnittstelle bei Maschinen zur Rasenpflege*, DRG Rasen, Oktober 2008.

[125] Nagaoka, A. K. et. al.: *Evaluation of a Single Wheel Testing Device with Mechanical Transmission*. In presentation at 2001 ASAE Annual International Meeting. 01-1166. Sacramento, CA. Sacramento Convention Center, 2001.

[126] Gill, W. R.; Vanden Berg G. E.: *Soil Dynamics in Tillage and Traction*. Agriculture Handbook 316. 377-378. Washington, D.C: U.S. Government Printing Office, 1968.

[127] Burt, E. C. et. al.: *A machine for testing tractor tires in soil bins*. Transaction of the ASAE, 23(3) (1980), 546-552.

[128] Way, T. R.: *Three Single Wheel Machines for Traction and Soil Compaction Research*. Agricultural Engineering International: the CIGR E-journal 4 (2009), 1-24.

[129] Monroe, G. E.; Burt, E. C.: *Wide frame tractive vehicle for controlled-traffic research*. Applied Engineering in Agriculture 5 (1) (1989), 40-43.

[130] Kavazanjian, E.; Mitchell, J. K.: *Time-dependent deformation behavior of clays*. Journal of Geotechnical and Geoenvironmental Engineering, ASCE, 106 (6) (1980), 611-630.

[131] Matesic, L.; Vucetic, M.: *Strain-Rate Effect on Soil Secant Modulus at Small Cyclic Strains*. Journal of Geotechnical and Geoenvironmental Engineering, ASCE, 129 (6) (2003), 536-549.

[132] Sheahan, T. C.: *A Soil Structure Index to Predict Rate Dependence of Stress-Strain Behavior*. Testing, Modeling and Simulation in Geomechanics, ASCE, Geotechnical Special Publication, 143 (2005), 81-97.

[133] Sorensen, K. K.; Baudet, B. A.; Simpson, B.: *Influence of Structure on the Time-Dependent Behaviour of a Stiff Sedimentary Clay*. Geotechnique, 57 (1) (2007), 113-124.

[134] Bekker, M. G.: *Prediction of design and performance parameters in agro-forestry vehicles*. NRCC Report No. 22880 (1983), National Research Council of Canada.

[135] Bekker, M. G.: *The effect of tire tread in parametric analyses of tire-soil systems*. NRCC Report No. 24146 (1985), National Research Council of Canada.

[136] Raper, R. L. et. al.: *The effects of reduced inflation pressure on soil-tire interface stresses and soil strength*. Journal of Terramechanics, 32 (1) (1995), 43-51.

[137] Steel, R. G. D.; Torrie, J. H., *Principles and Procedures of Statistics*, New York: McGraw-Hill, 1960, pp. 187, 287.

[138] Rossetter E. J.; Gerdes J. C.: *The Role of Handling Characteristics in Driver Assistance Systems with Environmental Interaction*. In Proceedings of the 2000 ACC, Chicago, IL, 2000.

[139] Van Zanten, A. T.: *Evolution of Electronic Control Systems for Improving the Vehicle Dynamic Behavior*. In Proceedings of the 61h International Symposium on Advanced Vehicle Control. 2002.

[140] Ray, L.: *Nonlinear Tire Farce Estimation and Road Friction Identification*. Simulation and Experiments, 33 (10) (1997), 1819-1833..

[141] Canudz-De-Wit; C.; Homwilz, R.: *Observers for Tire/Road Contact Friction Using Only Wheel Angular Velocity Inflation*. In Proceedings of the 38Ih Conference on Decision and Control, 3932-3937, 1999.

[142] Pacejka, H. B.; Bakker, E.: *The magic formula tire model*. Vehicle System Dynamics, 21 (1991), 1-18.

[143] De Vries, E. J. H.; Pacejka, H.B.: *Motorcycle tire measurements and models*. In Proceedings of the 15th IAVSD symposium: The Dynamics of Vehicles on Road and Tracks, Budapest, Hungary, 280-298, 1997.

[144] Nunney, M. J.: *Light and Heavy Vehicle Technology*. 2006.

[145] Milliken, W. F.; Milliken, D. L.: *Race Car Vehicle Dynamics*, SAE International, 1995.

[146] Tire identification diagram, 2012
URL: http://www.sturgeontire.com/images/glossary/sidewalls.jpg

[147] Diagram of Radial Tire Parts and Wear Signs, 2012
URL: http://www.abbsrytire.com/diagramtire.htm

[148] Wang, L. R.; Lu, Z. H.: Modeling Method of Constitutive Law of Rubber Hyperelasticity Based on Finite Element Simulations. Rubber Chemistry and Technology, 76 (1) (2003), 271-285.

[149] Bolarrinwa, E. O.; Olatunbosun, O. A.: *Finite Element Simulation of the Tire Burst Test*. Journal of Automobile Engineering, 218 (11) (2004), 1251-1258.

[150] Ghoreishy, M.: *Finite Element Analysis of the Steel-Belted Radial Tire with Tread Pattern under Contact Load*. Iranian Polymer Journal, 15 (8) (2006), 667-674.

[151] Abaqus 6.8.2 documentation, Simulia Software, Inc., 2009.

[152] Murat, B.: Lifetime Improvement of Radial Tires with the Help of Steel Cords, Rubber World, 228 (6) (2003), 28-32.

[153] Meschke, G.; Payer, H.J.; Mang. H.A.: *3D simulations of automobile tires: Material modelling, mesh generation and solution strategies*. Tire Science and Technology, 25 (3) (1997), 154-177.

[154] Whiting, D.: *Managing Soil Tilth*. Colorado State University Extension, 2011.
URL: http://www.cmg.colostate.edu/gardennotes/213.pdf

[155] The Textural Triangle, 2012
URL: http://www.oneplan.org/Water/*soil*-triangle.asp

[156] Plastic Models, 2012
URL: http://www.pisa.ab.ca/program/model/plastic/plastic.htm

[157] Roscoe, K. H.; Schofield, A. N. ; Thrairajah, A.: *Yielding of clays in states wetter than critical*, Geotechnique, 13 (3) (1963), 211-240.

[158] Roscoe, K. H.; Burland, J. B.: *On the generalized stress-strain behaviour of wet clay*. In Engineering Plasticity, Cambridge University Press, London, 535-609, 1968.

[159] Lee, J. Y.; Ahn, S. Y.: *Interactive visualization of elasto-plastic behavior through stress paths and yield surfaces in finite element analysis.* 47 (5) (2011), 496-510.

[160] Chiroux, R. C. et al.: *Three-dimensional finite element analysis of soil interaction with a rigid wheel*. Applied Mathematics and Computation, 162 (2005), 707-722

[161] Tekeste, M. Z.: *Non-linear Finite Element Analysis of Cone Penetration in Layered Sandy Loam Soil: Considering the Precompression stress state*, Computers in Agriculture and Natural Resources, 4th World Congress Conference, Orlando, Florida USA, 24-26 July 2006

[162] Jozsa, V.: *Effects of rarely analyzed soil parameters for FEM analysis of embedded retaining structures*. Proceedings of the 21st European Young Geotechnical Engineers' Conference, Rotterdam, 2011.

[163] Bosche: *Instruction manual of load cell*. 2010.
URL: http://www.bosche.eu/Prospekte/zugkraftwaegezelle_k-dee.pdf

[164] National Instruments: *NI 9237 Operating Instructions*. 2008.
URL: http://www.ni.com/pdf/manuals/374186e.pdf

[165] Micro-Epsilon: *Instruction manual of optoNCDT 1700*, Micro-Epsilon Inc, 2010.

[166] Herbst, E.; Ren, X.; Fox, D.: *Toward object discovery and modeling via 3-D scene comparison*. In Proceedings of IEEE International Conference on Robotics and Automation, Shanghai, China, 9-13 May 2011.

[167] Menna, F. et al.: *Geometric investigation of a gaming active device*. In Proc. SPIE 8085, Videometrics, Range Imaging, and Applications XI, Munich, Germany, 2011.

[168] Zollhöfer, M. et al., *Automatic reconstruction of personalized avatars from 3D face scans*. Computer Animation Virtual Worlds, 22 (2011), 195-202.

[169] Khoshelham, K.; Elberink, S. O.: *Accuracy and Resolution of Kinect Depth Data for Indoor Mapping Applications*, Sensors 2012 (2012), 1437-1454.

[170] Prescale, *Instruction manual of Pressure Measurement Film*, 2012.

Supervision of Thesis

The student research works which I supervised are partly used in the dissertation, and they are listed as follows:

Jiang, M. J.: Mechanische Analyse des Reifenprüfstandes mit Hilfe der Finite-Elemente-Methode, Projektarbeit, Lehrstuhl für Konstruktion im Maschinen- und Apparatebau, Nr. 635, 2011 (unveröffentlicht).

Jiang, M. J.: Mechanische Analyse statischer und dynamischer Kontaktprobleme zwischen pneumatischen Diagonalreifen und Boden mit Hilfe der Finite-Element-Methode, Masterarbeit, Lehrstuhl für Konstruktion im Maschinen- und Apparatebau, Nr. 645, 2011 (unveröffentlicht).

Zhou, Q.: Konstruktion eines Reifen Prüfstandes zur Verifikation von Simulations- und Messergebnissen, Studienarbeit, Lehrstuhl für Konstruktion im Maschinen- und Apparatebau, Nr. 660, 2011 (unveröffentlicht).

Bisht, B. S.: Concept design of a test rig for the investigation of tire/soil interaction, Projektarbeit, Lehrstuhl für Konstruktion im Maschinen- und Apparatebau, Nr. 659, 2012 (unveröffentlicht).

Guo, Y. F.: Investigation of tire cornering on a soft soil with the application of finite element method, Studienarbeit, Lehrstuhl für Konstruktion im Maschinen- und Apparatebau, Nr. 681, 2012 (unveröffentlicht).

Publications

Li, H.; Schindler, C.: Study of Tire-Soil Interaction with Analytical and Finite Element Method, Commercial Vehicle Technology Symposium, Kaiserslautern, 13-15 March, 2012.

Li, H.; Schindler, C.: Application of Analytical and Finite Element Method in Tire-Soil Modeling, International Journal of Heavy Vehicle Systems, 19 (4) (2012), 333-354.

Li, H.; Schindler, C.: Investigation of Tire-Soil Interaction with Analytical and Finite Element Method, Mechanics Based on Design of Structures and Machines, 41 (3) (2013), 293-315.

Li, H.; Schindler, C.: Three Dimensional Finite Element and Analytical Modelling of Tyre-Soil Interaction, Proceedings of the Institution of Mechanical Engineers, Part K: Journal of Multibody Dynamics, 227 (1) (2013), 42-60.

Li, H.; Schindler, C.: Analysis of Soil Compaction and Tyre Mobility with 3D Tyre-Soil Interaction Models, Proceedings of the Institution of Mechanical Engineers, Part K: Journal of Multibody Dynamics, (2013) (published online), DOI: 10.1177/1464419313486627

Curriculum vitae

Name Hao Li

School education

1990-1996	the 1st Elementary school of Yushan, Yushan
1996-1999	Qinglin junior middle school, Yushan
1999-2002	the 1st senior middle school of Yushan, Yushan

Higher education

2002-2006	Automobile Engineering, Beijing University of Aeronautics and Astronautics, Beijing, China Degree: Bachelor
2006-2009	Power Machinery and Engineering, Beijing University of Aeronautics and Astronautics, Beijing, China Degree: Master of Science

Occupation

From 2009	Doctoral candidate at the Chair of Design in Mechanical Engineering, TU Kaiserslautern